

INVESTIGATION INTO THE EFFECT OF MATERIALS MICROSTRUCTURE AND PROPERTIES ON MICRO-CUTTING PRECISION

Lorelei GHERMAN

MSc, Advanced Manufacturing Technologies

Thesis submitted to The University of Nottingham

for the degree of Doctor of Philosophy

October 2017

ABSTRACT

For the past decades, one of the major trends in industry has been micro-product manufacturing. Micro-parts are in high demand in many industries, including medical devices, electronics and automotive applications. The challenge in manufacturing micro-products is to achieve excellent surface quality in parts with sub-micron tolerances, whilst also maintaining low production costs.

Precision can be established based on parameters such as linear and dynamic stability, as well as process repeatability.

In micro-cutting, stability is influenced by variations of operating parameters which are considered constant in regular cutting. Such variations have been found in literature for shear angles and cutting forces as a result of the material anisotropy of single crystals. Models and experimental work for cutting force variation due to crystallographic orientation have been previously developed. However, the effects of the cutting force variation have not been sufficiently understood.

The aim of the current research is to improve micro-cutting precision based on crystallographic anisotropy models. This thesis achieves four objectives that contribute to a new understanding of micro-cutting by investigating linear and dynamic stability, and repeatability in single crystal investigations.

The first objective of this study has been to provide a better understanding of linear stability based on single crystal analytical models. Tool deflection and slope are modelled for the first time due to their proportionality with the cutting force. It is found that tool deflection varies by a factor of two for some crystallographic directions, negatively influencing the stability of the tool path. Cutting forces are also affected by the variation of tool deflection by a six Newtons difference. By providing this new tool deflection model, linear stability understanding is improved for cutting of single crystal materials.

The second objective has been to experimentally validate cutting force variation in single grain cutting, and to provide a comparison with multigrain results. Previous studies have investigated either turning, either orthogonal cutting, but they have not considered the evolution of the tangential and radial components of the cutting force during a 360° workpiece rotation. This is critical in order to assess crystallographic anisotropy effects on stability and material deformation mechanisms. The current research has analysed both cutting force components, which enable new models to be developed. The radial cutting force has been successfully found to validate the force profile in the anisotropic analytical model.

The third objective has been the development of new, single grain-specific cutting stability models. Classic stability analysis has been extended to include for the first time the variation of the cutting force and shear angle. The new models generate levels of critical depth of cut which vary widely from classic stability values, by 45% in analytically-based analysis and 70% in empirically-determined values. Based on this new knowledge, recommendations of new stability limits are made for manufacturers, in the direction of improving micro-cutting dynamic stability.

The final objective of this research has been to provide a new and comprehensive understanding of material deformation mechanisms, due to single crystal cutting effects on surface quality and repeatability of results. Material phenomena analysis is provided for chip formation, burr and ploughing formation, and dimensional accuracy of machined features. Different chip morphologies are characterised for the first time and correlated with anisotropic models. Based on chip typology, chips can be classified as desirable, acceptable or undesirable in cutting. The results show that for a third of the overall number of chips, the morphology is unsuitable for cutting operations. Burr formation has been identified to occur by a four-peak repeatability, which matches the crystallographic anisotropy repeatability; a correlation between chip and burr generating mechanisms is established for 79% of results. In terms of dimensional accuracy, channel width has been analysed. A four-peak pattern and 1.43 times channel dimension variation is found. The chip, burr and dimensional accuracy findings provide an improved understanding of surface quality parameters and repeatability. Based on these new empirical findings, the manufacturing process parameters can be adjusted for optimal micro-cutting.

In summary, the research presented in this thesis has investigated the effects of material microstructure properties on micro-cutting precision by developing new models for linear and dynamic stability. For the first time, the correlation between crystallographic anisotropy and surface quality, dimensional accuracy and repeatability have been assessed. These analyses contribute towards an improved understanding of material microstructure effects on micro-cutting precision, and have enabled the development of recommendations to improve micro-manufacturing results.

ACKNOWLEDGMENTS

This thesis would not have been possible without the help of several individuals who have extended their valuable knowledge and support throughout the duration of this research.

I would like to start by expressing my gratitude towards my supervisors, Prof Atanas A. Popov and Prof Svetan M. Ratchev. Atanas, thank you for the support and guidance you have provided throughout this research, for meeting and advising me, and for giving me the first insight into dynamics. This work would not have been possible without your many contributions and recommendations. Svetan, thank you for your valuable guidance in micro-manufacturing directions of studies and for enabling this research.

I have greatly benefitted from insightful yearly review discussions with Dr Simon Lawes, whom I would like to thank for all his kindness and help in discussing the cutting of materials and helping me outline the direction of this research.

A special thank you is owed to Dr Andrew Gleadall, who has contributed to the ideas in this research, from the first analytical models to developing this thesis, and to countless discussions (and a few times, critical thinking!) over the years which have helped me shape this study. I have learned much from you, which have helped me become a better person and a better researcher.

Profound gratitude is owed to my friends and colleagues, Dr Rupesh Patel, Dr Lavindra de Silva and Dr Jack Chaplin, who have read and helped me improve this thesis. In this respect, thank you for your many efforts and valuable knowledge in times of need. Rupesh, I am grateful to you for your friendship, endless support and for the innumerable occasions you have aided me in dynamics and Matlab pursuits.

Many thanks to Mark Strickland, Paul Wentworth, Jeremy Straw, Chris Cook, Joe Griffin, Otto Bakker and to Tom Buss, for helping facilitate all experimental and

machining pursuits, and for your continuous kindness, wisdom and support throughout this research.

I would like to express my gratitude towards Dave Shipley, Magda, and all my friends and colleagues, too many to mention, in the Institute for Advanced Manufacturing and in the Structural Integrity & Dynamics Research Group, who have helped me over the past years, and which whom I share cherished memories.

Thank you to Professor Donal McNally and my new friends in the Bioengineering Research Group, who have supported me with such kindness in completing this thesis.

One special mention goes towards my mentor, Professor Laurențiu Slătineanu, who was the first to show me what a wonderful path research can be, and who has ignited my passion for it. Thank you for all your guidance, optimism, kindness and never-ending support. This thesis wouldn't have happened without you, who have opened an entire realm of possibilities with your vision.

Lastly, I carry a great deal of gratitude towards my family, who has always supported me and has been by my side throughout exciting and challenging times. Heartfelt thankfulness is owed to my grandparents, Mărioara and Alexandru †, who have always supported me in scholarly pursuits, and have provided me with all the love a parent can carry for their child, and beyond. Everything I am, I owe to you. Deep gratitude is owed to Ionuț, my boyfriend, who has been by my side from the first day of this research. We have started this adventure together, and I cannot thank him enough for his love, patience and support throughout these years. I have been very lucky to have you, to have shared these moments with you. Despite thanking my family lastly, I dedicate this thesis to them, as they come first in my heart.

CONTENTS

ABSTRACT i

ACKNOWLEDGMENTS iv

CONTENTS vi

NOMENCLATURE x

LIST OF FIGURES xiii

1. INTRODUCTION 1

2. LITERATURE REVIEW 4

2.1. Introduction 4

2.1.1. Definition of micro-cutting 5

2.1.2. Differences between regular-scale and micro-cutting technologies 7

2.2. Micro-cutting specific phenomena 11

2.2.1. Chip formation 12

2.2.2. Ploughing and slipping 13

2.3. Crystallographic anisotropy in single grain materials 14

2.3.1. Shear formation in a single crystal 15

2.3.2. Cutting forces based on crystal orientation 16

2.3.3. Grain orientation-dependent material behaviour in cutting 18

2.3.4. Burr formation in single-crystal material cutting 21

2.4. Dynamic analysis in micro-cutting 24

2.4.1. Micro-cutting models 24

2.4.2. Operating parameter models. Speed, feed, rotation. 26

2.4.3. Cutting force models 26
2.4.4. Cutting stability analysis 27
2.5. Knowledge gaps and key challenges 30
2.6. Aims and objectives 31
3. RESEARCH METHODOLOGY 33
3.1. Scientific approach 33
3.2. Micro-cutting framework 34
3.3. Specific objectives 36
3.4. Thesis outline 42
4. CRYSTALLOGRAPHIC ANISOTROPY INFLUENCE ON CUTTING FORCES 45
4.1. Introduction 45
4.2. Method 46
4.2.1. The maximum work principle 47
4.2.2. Shear angle calculation 51
4.2.3. Cutting force calculation in an orthogonal process 57
4.3. Results & discussion 59
4.3.1. Cutting forces in turning 59
4.3.2. Slope in turning 64
4.3.3. Tool deflection in turning 69
4.3.4. Cutting stability lobes 74
4.4. Conclusions 77
5. MICRO-CUTTING FORCES EXPERIMENTAL INVESTIGATION 80
5.1. Introduction 80
5.2. Data acquisition equipment and procedures 81
5.3. Experimental program 83
5.3.1. Variables 84

5.3.2. Design of experiments/ Program 85
5.3.3. Experimental conditions 88
5.4. Preliminary test 89
5.5. Calibration of equipment 92
5.5.1. Cutting force calculation 92
5.5.2. Dynamometer calibration 93
5.6. Experimental results of orthogonal cutting of copper 102
5.7. Discussion 109
5.8. Conclusion 113
6. CUTTING STABILITY ANALYSIS 115
6.1. Introduction 115
6.2. Regenerative chatter study in turning 116
6.2.1. Self-generated vibration in micro-cutting 116
6.3. Micro-cutting stability analysis proposed procedures 118
6.3.1. Calculation of new cutting stability factor based on tool cutting edge radius-generated process instability 119
6.2.2. Instability generated by the variation in the cutting force 121
6.2.3. Instability generated by the variation in the shear angle within a single crystal material 90° rotation 130
6.2.4. Instability generated by the differences in the rake angles 133
6.3. Conclusion 135
7. CONTRIBUTIONS TO MATERIAL PHENOMENA UNDERSTANDING BY CONSIDERING EXPERIMENTAL INVESTIGATION OF SINGLE CRYSTAL COPPER ORTHOGONAL CUTTING 138
7.1. Introduction 138
7.2. Method of experimental analysis 140
7.3. Equipment and procedures 141
7.3.1. Equipment 141

7.3.2. Procedure 142
7.3.3. Method of analysis 143
7.4. Experimental program 145
7.5. Experimental results and analysis 146
7.5.1. Analysis of exit chip formation in single crystal cutting 146
7.5.2. Analysis of burr formation and plastic deformation in single crystal cutting 168
7.5.3. Analysis of channel dimensional accuracy in single crystal cutting .. 185
7.6. Recommendations for improving precision in single crystal micro-cutting 194
7.7. Conclusions and future work 195
8. CONCLUSIONS AND FUTURE WORK 200
REFERENCES 209
APPENDIX A. TABLES FOR DATA POINTS ANALYSED IN SINGLE CRYSTAL MICRO-CUTTING 220
APPENDIX B. 2ND PHASE SINGLE CRYSTAL 60 CHANNEL MICRO-MACHINING. CHIP RESULTS 241
APPENDIX C. DEPTH OF CUT AND SURFACE ROUGHNESS INVESTIGATION 244
APPENDIX D. CONSIDERATIONS REGARDING SLIP DISLOCATION IN A 24-CHANNEL SINGLE CRYSTAL TEST PIECE MACHINED AT 200 μM DEPTH OF CUT 246

NOMENCLATURE

α (°)	rake angle on the tool
β (°)	friction angle
γ_i (rad)	shear strain
δ (mm)	deflection
δ_{ij} (rad)	longitudinal and shear strains
ε_i (rad)	longitudinal and shear strains
ϵ_{ij} (rad)	strain tensor in the crystallographic coordinate system
ϵ_s (rad)	strain tensor – material
ϵ_w (rad)	strain tensor – workpiece
ζ_1	damping ratio
ζ_2	damping ratio
θ (°)	workpiece orientation angle
Θ (°)	slope
θ_1 (°)	flexibility in the machine tool
θ_2 (°)	flexibility in the machine tool
θ_f (°)	re-calculated orientation angle
θ_i (°)	initial orientation angle
µm	micrometre
σ_{ij} (N/m^2)	stress tensor

τ_{ij} (N/m^2)	shear stress tensor
ϕ (°)	shear angle
ψ	phase shift of the transfer function
ω_{n1} (rad/s)	first natural frequency of the machine tool
ω_{n2} (rad/s)	second natural frequency of the machine tool
a (mm)	the depth of cut
a_{lim} (mm)	the maximum axial depth of cut for chatter–free machining
(*abc*), (*pqr*) and (*def*)	crystal coordinates
(*abc*) , (*uvw*) and (*hkl*)	cutting system coordinates
a_{ki}, a_{lj}	slip system cosines
b_i and n_j	direction cosines
BUE	build-up edge
E (N/m^2)	Young's modulus
E_s	shear plane coordinates
f.c.c.	face-centred cubic
F_c (N)	horizontal cutting force
F_f (N)	thrust force
F_s (N)	shear force
F_u (N)	friction force
G	real part of the transfer function
H	imaginary part of the transfer function
h_0 (mm)	intended chip thickness
k_1 (N/m)	stiffness
k_2 (N/m)	stiffness

K_f (Pa)	cutting constant
I (m^4)	second moment of area
l, m and n	direction cosines of the normal ON
micro-EDM	micro-electrical discharge machining
N	iteration of stability lobes
P	the coordinate transformation matrix
S_n (N/m^2)	normal stress acting on a plane
S_s (N/m^2)	resultant shear stress
S_x, S_y and S_z (N/m^2)	stress acting on the X, Y and Z directions
t (s)	present time
T	one spindle revolution period
T_θ	coordinate transformation matrix for the orientation angles
T_ϕ	coordinate transformation matrix
V (mm/s)	cutting speed
V_c (mm/s)	chip velocity
$y(t)$ (mm)	chip thickness during a specified time interval
W_f (N·m)	friction work
W_p (N·m)	plastic work
W_t (N·m)	total work

LIST OF FIGURES

Chapter 2

Figure 2.1. The range of part and feature size machining capability. From Shanahan (2013), Figure 2

Figure 2.2. Predictive models for machining operations for practical application. (Luttervelt et al., 1998), Figure 1, p. 589

Figure 2.3. Size effects resulting from small ratio of the uncut chip thickness to tool edge radius (Cheng and Huo, 2013), Chapter 2, Figure 2.6., p. 26

Figure 2.4. Differences related to the rake angle in micro and regular scale cutting. From Gherman et al. (2017), Chapter 4, Figure 4.4., p. 107

Figure 2.5. The minimum chip thickness effect in micromachining (Filiz et al., 2007), Figure 1, p. 1089

Figure 2.6. Schematic of the effect of the minimum chip thickness (Chae, Park and Freiheit, 2006), Figure 7, p. 320

Figure 2.7. Shear angle and cutting force variation on the (001), (110) and (111) crystallographic planes. From Lee and Cheung (1999) Figures 2 and 3, p.219

Figure 2.8. Surface texture in polycrystalline material. From Donatus (2015): a. Figure 2, p.93. b. Figure 9, p.97

Figure 2.9. Material removal mechanism and burr formation. From Gillespie (1974) Figure 3, p. 8; and Wan (2014), Figure 4, p. 30

Figure 2.10. Key aspects to be considered in micro-milling (in Câmara et al., 2012), Figure 2, p. 674

Chapter 3

Figure 3.1. Micro-cutting framework

Figure 3.2. Research approach

Chapter 4

Figure 4.1. Forces on infinitesimal tetrahedron. After Mendelson, 1968

Figure 4.2. Comparison between shear angle results for a 360° workpiece rotation, obtained by applying different methods: a. model with strain-rate plasticity, image from Figure 3b (Cheung et al., 2002); b. orthogonal cutting model, image from Figure 8 (Kota and Burak Ozdoganlar, 2008)

Figure 4.3. Orthogonal cutting processes coordinate system. From Kota (2011): Figure 2.1b, p.14

Figure 4.4. Turning cutting scheme. From Kota (2011): Figure 1.6a, p.8 and Figure 2.2, p.16

Figure 4.5. Cutting forces in an orthogonal cutting scheme. From Kota (2011): Figure 2.1a, p.14

Figure 4.6. Stereographic map of crystallographic orientation with (001) as principal axis

Figure 4.7. Matlab program validation of Kota's results for different crystallographic orientations: a. (001); b. (101); c. (102); d. (111); e. (112); f. (212); g. (213); h. (216)

Figure 4.8. Cutting force profiles: a. (001) plane and Kota's 110 μm depth of cut; b. (101) plane and Kota's 110 μm depth of cut; c. (001) plane and 25 μm depth of cut; d. (101) plane and 25 μm depth of cut.

Figure 4.9. Single crystal cutting scheme: a. turning, indication the orientation angle; b. slope effect in turning.

Figure 4.10. Slope for the (001) zone axis

Figure 4.11. Slope for the (111) zone axis

Figure 4.12. Cutting force calculated considering the slope difference. a. (001); b. (001) detail; c. (111); d. (111) detail

Figure 4.13. Difference in absolute values for the cutting forces obtained on (001) zone axis. a. real values; b. absolute values

Figure 4.14. Horizontal cutting forces differences and shear angle profile association: a. Difference in the horizontal cutting forces (001); b. Shear angles (001); c. Difference in the horizontal cutting forces (111); d. Shear angles (111)

Figure 4.15. Tool deflection effect in turning

Figure 4.16. Tool deflections calculated for different crystallographic orientations: a. (001) - (111) at 114.3 μm depth of cut; b. (112) - (216) at 114.3 μm depth of cut; c. (001) - (111) at 25 μm depth of cut; d. (112) - (216) at 25 μm depth of cut.

Figure 4.17. Comparison of tool tip deflections

Figure 4.18. Implementing the tool deflection subtraction in the uncut chip thickness value

Figure 4.19. Analysing the effect of amplitude in tool deflection: a. incremental steps for different chip thicknesses between 110 μm and 120 μm; b. incremental steps for different chip thicknesses between 25 μm and 15 μm; c. the absolute difference between cutting force values

Figure 4.20. Schematic representation of chatter formation in an orthogonal turning process

Figure 4.21. Normalised value of horizontal cutting force

Figure 4.22. Assessing the difference of shear angles' influence on stability lobes

Figure 4.23. Tool deflection effect on tool path

Chapter 5

Figure 5.1. Cutting parameters: a. channel depth and slipping tools used in experiment, with a 60° tool angle; b. cutting force profiles estimated for a 50 μm and 200 μm depth of cut

Figure 5.2. Cutting force components representation

Figure 5.3. Experimental set-up used in preliminary test on Hurco machining centre.

Figure 5.4. Aluminium support for enabling positioning of test piece in 24 orientations during micro-cutting. Dynamometer-aluminium support-test piece set-up, as in the experiment

Figure 5.5. Section view of channel. The width of the cut varies, as the slipping tool has an angled tip.

Figure 5.6. Test piece profile after cutting.

Figure 5.7. Individual force readings in multigrain copper cutting

Figure 5.8. Individual force readings in single grain copper cutting

Figure 5.9. Selection of signal ranges for cutting force calculation

Figure 5.10. Analysis of loads applied on different axes: a. calibration scheme; b. calibration results

Figure 5.11. Measurements and calculation of X and Y readings for 3 kg applied load

Figure 5.12. Force in dynamometer coordinate system at 3 kg applied load

Figure 5.13. Measurements and calculation of X and Y readings for 0.108 kg applied load

Figure 5.14. Force in dynamometer coordinate system at a 0.108 kg applied load

Figure 5.15. Zero Fx levels measurements in single crystal experiments

Figure 5.16. Force measurements in 100 N units of zero levels in various experiments

Figure 5.17. Zero load differences for manual rotation of table

Figure 5.18. Measurements on Hermle, with aluminium plate. Medium speed. Direction of rotation C+

Figure 5.19. Measurements on Hermle, no aluminium plate. Medium speed. Direction of rotation C-

Figure 5.20. Test piece after cutting of 24 channels.

Figure 5.21. Zero and loading levels during multigrain copper cutting of 50 µm depth of cut

Figure 5.22. Individual force readings in multigrain copper cutting at 50 µm

Figure 5.23. Zero and loading levels during multigrain copper cutting of 200 µm depth of cut

Figure 5.24. Individual voltage readings in multigrain copper cutting at 200 µm

Figure 5.25. Zero and loading levels during single grain copper cutting of 200 µm depth of cut

Figure 5.26. Individual cutting measurements in single crystal copper cutting at 200 µm

Figure 5.27. Cutting forces comparison for 200 µm depth of cut

Figure 5.28. Cutting forces obtained at 200 µm depth of cut

Figure 5.30. Single grain copper cutting forces

Figure 5.31. Duration of tool plunge and channel cutting phases

Figure 5.32. Comparison between the specific cutting energies obtained with Kota's tool geometry, and the tool used in the current study

Figure 5.33. Scheme of slipping on a (001) crystal plane inclined at 15°, 10° and 0°

Chapter 6

Figure 6.1. Regenerative chatter vibrations in orthogonal cutting, from Figure 4.1. in Altintas (2012) p.126

Figure 6.2. Cutting scheme: a. turning model assumes a perfectly sharp tool; b. regular tool, with a cutting tool edge radius R; c. detail of tool-workpiece contact zone

Figure 6.3. Feed force constant evolution in a 360° workpiece rotation

Figure 6.4. Investigation of the cutting stability lobes values for minimum, maximum and average (multigrain) cutting forces developed on the (001) plane

Figure 6.5. Cutting stability lobes generated for a 0° to 20° workpiece rotation generating an incremental cutting force variation

Figure 6.6. Cutting stability lobes generated for a 0° to 45° workpiece rotation with 5° increments

Figure 6.7. Cutting stability lobes generated with cutting forces measured in single grain copper cutting: a. Sector 1; b. Sector 2; c. Sector 3; d. Sector 4.

Figure 6.8. Cutting stability lobes generated with cutting forces measured in multigrain copper cutting: a. Sector 1; b. Sector 2; c. Sector 3; d. Sector 4.

Figure 6.9. Shear angle evolution in a 90° segment based on the analytical model described in Chapter 4: a. on the crystallographic planes (001), (111), (101), (112), (216) and (102); b. comparison of evolution and change of phase on planes (212) and (213)

Figure 6.10 Cutting stability analysis based on 5° increments of the shear angle obtain on a 90° workpiece rotation of a (001) oriented single crystal: a. orientations 0° - 50°; orientations 50° - 90°

Figure 6.11. Instability generated by the differences in the rake angles: a. differences at the level of Fc horizontal force estimations; b. differences at the level of ratios of Fc horizontal force; c. differences at the level of shear angle estimations; d. differences at the level of ratios shear angles.

Figure 6.12. Stability lobes variation with rake angle. From Afazov et al. (2013): Figure 16.a, p. 682

Chapter 7

Figure 7.1. Chapter outline

Figure 7.2. Selection of points representing material deformation on SEM images: Ploughing or lateral plastic deformation; b. Ploughing width; c. Channel dimensional accuracy; d. Burr width; e. Burr length

Figure 7.3. Differences between images taken at different points along the channel: a. channel 57, single crystal copper sample machined at 50 µm depth of cut; b. multigrain copper with a surface machined by EDM.

Figure 7.4. Chip adjacent to channels 1, 2 and 5 on the copper multigrain sample

Figure 7.5. Chips 1-4 formation in multigrain sample machined at 200 µm depth of cut

Figure 7.6. Tool entrance for channels 1-4 in multigrain sample machined at 200 µm depth of cut

Figure 7.7. Group 1 – Chips for channel 1 (0°), 7 (90°), 13 (180°), 19 (270°)

Figure 7.8. Group 2 – Chips for channel 2 (15°), 8 (105°), 14 (195°), 20 (285°)

Figure 7.9. Group 3 – Chips for channel 3 (30°), 9 (120°), 15 (210°), 21 (300°)

Figure 7.10. Group 4 – Chips for channel 4 (45°), 10 (135°), 16 (225°), 22 (315°)

Figure 7.11. Up: Group 5 – Chips for channel 5 (60°), 11 (150°), 17 (240°), 23 (330°). Left: Shear fronts detail and delimitation

Figure 7.12. Group 6 – Chips for channel 6 (75°), 12 (165°), 18 (255°), 24 (345°)

Figure 7.13. Tool entrance areas for channels 1 – 4 at 200 µm depth of cut

Figure 7.14. Chip morphology assessment at 50 µm depth of cut

Figure 7.15. Shear angle increments on the (001) plane for 6, respectively 15 increments on a 90° workpiece segment

Figure 7.16. Second experiment with 50 µm depth of cut

Figure 7.17. Classification of chip forms. Kluft et al. (1979) from: Altintas (2012) Figure 2.14, p. 34

Figure 7.18. Schematic of effect of strain difference on the two channel walls

Figure 7.19. Tool entrance for channels 1-4 in the first phase single crystal 60-channels experimental trial

Figure 7.20. Differences in chip thickness due to shear angle formation

Figure 7.21. Tool entrance for channel 10, 11, 12 and 13 in the second phase single crystal 60-channels experimental trial

Figure 7.22. Channels 1-4 in multigrain sample machined at 200 µm depth of cut

Figure 7.23. Multigrain copper disc machined at 50 µm depth of cut.

Figure 7.24. Microscope photos of multigrain, respectively single grain channels

Figure 7.25. Comparison between ploughing and burr formation

Figure 7.26. Plastic deformation assessment of single grain material phenomena in 50 µm deep channels

Figure 7.27. Correlation between burr formation and chip morphology

Figure 7.28. Microscope observation of top burr formation in 50 µm depth of cut single crystal cutting

Figure 7.29. Burr assessment of single grain material phenomena in 50 µm deep channels

Figure 7.30. Channel dimensions: a. comparison between a symmetrical channel width and one with a high variation due to ploughing phenomena occurring on one of the channel walls; b. method of measuring the channel width, and the left and the right dimensions from the centre of the channel

Figure 7.31. Channel dimensional accuracy measurements in 200 µm deep channels

Figure 7.32. Channel width data for single grain material channels machined at 50 µm depth of cut

Figure 7.33. Variation of shear angle and surface roughness with crystallographic cutting directions. From Zhou et al. (2001) Figure 7, p. 821; Figure 9, p. 822.

Appendix C

Figure C.1. Microscope vs. Interferometer channel depth assessment

Figure C.2. Tool tracks observed on surface roughness analysis

Figure C.3. Surface roughness and tool track estimations

Appendix D

Figure D.1. Slip dislocations prevalent in 50 μm single crystal channels: a. Channel 2, indicating overall slip dislocations, including on channel walls; b. Measurements of dislocation size at the bottom of the channel; c. Channel 1; d. Channel 3 detail; e. Channel 6.

Figure D.2. White-light interferometry analysis

Figure D.3. Slip dislocations observed on the bottom and walls of 200 μm single crystal channels: a. Channel 21; b. Channel 22; c. Channel 23.

Figure D.4. Correlation between dislocation slip lines observed in micro-machined channel and on the chips: a. channel 3; b. channel 2; c. channel 1; d. chip 3; e. chip 2; f. chip 1.

Figure D.5. Plane surface of chips emerging from channels 4 – 9

Figure D.6. Comparison of Fy force profile and slip dislocation numbers

Figure D.7. From: Kawasaki (1974) Figure 3, p. 143 and 4, p. 144. Orientation dependence of dislocation structures in cyclically deformed Cu-16 At. Pct Al alloy single crystals

Figure D.8. Dislocations identified on the under surface of the chip

CHAPTER 1

INTRODUCTION

Micro-manufacturing has been at the heart of developing flawless precision products for the past decades (Masuzawa, 1997). The importance of continuous development in micro-cutting technologies is led by the demand for a high number of micro-manufacturing applications, from the production of medical components, micro-electrical-mechanical-systems, micro-moulds, to sub-miniature actuators, micro-valves and motors (Harder, 2013).

Substantial efforts have been made in the direction of advancing micro-manufacturing technologies. In the past 15 years, the European Union has invested significant research funds in projects that will enable its top position in the micro- and nano-manufacturing area; a number of such projects are MASMICRO, 4M, Launch-Micro, Production4µ, EUPASS, Hydromel, HYTI, NANOSAFE2, Manudirect, Napolyde, PRONANO, NaPa, CHARPAN, NANOIMPRINT, NanoCMM, etc. (Qin et al., 2010).

In the United Kingdom, the Department of Trade and Industry has had a budget more than £90 million over six years for the program "Micro and nanotechnology initiative". This enabled businesses to develop based on the scientific track record in micro-scale sciences (Department of Trade and Industry, 2003).

In delivering micro-products designed for the medical, aviation or wearable devices industries, micro-cutting has focused on industry-driven challenges, in the form of part precision, excellent surface quality and mass production.

One promising technology that meets these demands is micro-cutting, as it enables high production rates and low operating costs. One main challenge in micro-cutting advances remains process precision.

In a small scale commercial setting, such as the laboratory in the Advanced Manufacturing Group at the University of Nottingham, achieving sub-micron tolerances is a complex task. With a high number of applications, ranging from medical products to wearable devices, technical staff have challenging operations to improve in order to perform precise micro-parts. One issue encountered is the lack of micro-cutting specific knowledge which can directly influence the industrial process; some factors which appear, but which the technical staff cannot account for, are instabilities, deflections, and repeatability of results.

This has led recent studies into understanding the complex differences between regular scale cutting and micro-cutting technologies which influence process precision.

One issue explored in literature has been the size effect (Weule, 2001), introduced in micro-cutting studies as the relative difference between the tool cutting edge radius and the uncut chip thickness. At regular scale, the cutting radius is much smaller than the depth of cut, and cutting is performed through a large number of grains, of varying sizes and orientations. However, in micro-cutting, the depth of cut is often smaller than the grain size. As such, micro-cutting is performed through individual grains, and the workpiece material properties can no longer be considered isotropic. Therefore, the microstructure properties gravely affect surface accuracy, precision and repeatability of the process.

One industrial concern is centred on generating products with a high surface finish from the first operation, and it is driven by the cost of manufacture and physical limitations of the micro-cutting scale. The implication is that burr formation has to be predicted and mitigated against before the cutting process, as burr removal becomes impossible for micron level features. Uneven surfaces which do not meet tolerances become scrap parts, and as a result excellent surface accuracy is a request from the first processing steps. These aspects reflect positively into productivity and low tool wear, decreasing the overall cost of micro-cutting operations.

As such, a better understanding of material micro-scale phenomena will lead to improving surface generation and accuracy in micro-cutting, while decreasing the cost

of the operation. This work sets out analytical models and correlating their effects with micro-cutting experiments, in order to contribute to a better understanding of the influence of material microstructure on micro-cutting precision, namely on stability and process repeatability.

This thesis aims to develop a better understanding of precision in micro-cutting, which will enable recommendations for improved micro-cutting industrial operations.

CHAPTER 2

LITERATURE REVIEW

2.1. Introduction

In the previous chapter, the direction of study has been formulated as improving micro-cutting precision. The large goal of this research is making micro-cutting into a process as precise as regular cutting. In this respect, micro-cutting could be developed, in the future, as a processing technology or into a specialised equipment which can be utilised with a high degree of confidence, so that even the lowest tolerances needed in micro-manufacturing can be achieved with great stability and repeatability, as it happens in regular cutting set-ups.

To achieve this, it is important to understand the differences between regular scale and micro-scale cutting, to address the specific micro-cutting challenges and to investigate the factors which can improve precision. By understanding how micro-cutting fits within the broader cutting technology, it is possible to identify the methods and analyses which need development with a micro-scale insight.

The current chapter is organised around micro-cutting specialty literature, which will help identify the knowledge gaps, and the methods which can be adopted in order to address them. Initially, micro-cutting is investigated from a broad perspective, of general machining concerns. This is followed by looking into the differences between regular and micro-level mechanical machining. The differences help identifying the micro-cutting specific challenges, and details the specialty literature in those fields.

Lastly, the knowledge gaps, key challenges and aims and objectives of this study are formulated, as driven by the literature survey.

2.1.1. Definition of micro-cutting

Defining micro-cutting can take into account several factors: either defining the machined feature size, either defining the conditions under which the process takes place.

Out of the two, this thesis focuses on cutting processes where micro-cutting specific phenomena (namely, size effects) take place, as illustrated in later sections. One such process is more representative of micro-cutting than just keeping the value of the depth of cut under a certain boundary.

If the machined feature dimensions were taken into account, different authors provide different figures. While there hasn't been a consensus on one threshold, it is useful to understand the level at which machining takes place.

Masuzawa (2000) initially defined mechanical micro-machining as the process taking place between 0 and 500 µm. However, according to Shanahan (2013), micro-cutting occurs when products with features of 1 to 25 µm are manufactured. Manufacturing products with features of 25 to 100 µm represents a machining area called meso-machining, while manufacturing features smaller than 1 µm represents nano-machining. These boundaries were defined in the industry annual trends report, as shown in Figure 2.1:

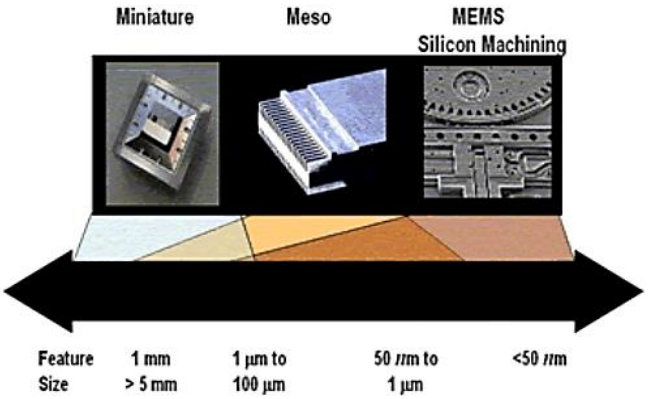


Figure 2.1. The range of part and feature size machining capability. From Shanahan (2013), Figure 2

Some micro-milling definitions (which is one type of micro-cutting) include values based on the tool diameter. For example, Özel et al. (2007) have used 6 mm tools in micro-milling experiments. Other have remarked that micro-milling tools can have a 3 mm diameter or smaller (Morcom, 2013).

Therefore, there is no consensus on a tool diameter threshold, or on a specific depth of cut. This makes micro-cutting challenging to define. As such, there are other factors considered, such as the relation between certain geometrical features of the tool (the cutting edge radius) and the uncut chip thickness, which are more relevant for the micro-cutting definition (Özel et al., 2007).

Another aspect to consider when defining micro-cutting is material properties. More recently, the boundary between meso- and micro-cutting was set up in relation with the material microstructure (Simoneau and Elbestawi, 2006c). The structure of the uncut chip thickness was correlated with the average grain size of the workpiece material. In this respect, if cutting occurs in a single grain material, it can be considered as 'micro-cutting'. In industry, material grains significantly vary, with some typical values for copper average grain size 20 µm – 50 µm. If micro-milling is performed, this grain can withhold 5-10 tool cuts before the tool exits the grain. As such, if larger material grains are considered, micro-cutting principles correlated with material microstructure can still be assumed. For example, phenomena occurring in a 50 µm long single crystal, being cut at with a 5 µm depth of cut, can be considered similar to that of a 500 µm long single crystal, being cut with a 50 µm chip thickness, due to the same single grain-specific phenomena.

Very precise tools of 1 mm diameter, having a sharp cutting edge radius, can perform very small depths of cut, at sub-micron level (Dornfeld and Lee, 2008). Many micro-milling and slipping tools (both micro-cutting technologies) have cutting edge radii of 5 µm – 15 µm. Some tools have radii of under 1 µm.

This establishes a relation between certain geometrical features of the tool and the minimum chip thickness which can be obtained with each tool. Based on Shanahan's definition, micro-cutting is the process performed at depths of cut between 1 µm - 25 µm. However, it is more appropriate to define it as an operation performed with a sharp cutting edge and a process which is dominated by single crystal cutting phenomena. If

the single crystal has higher physical dimensions, then the depth of cut can have a higher value as well, when looking at crystallographic anisotropy in micro-cutting.

As such, the definition of micro-cutting is considered as the relative dimension between cutting edge radius and the uncut chip thickness (one size effect).

2.1.2. Differences between regular-scale and micro-cutting technologies

In 1998, Luttervelt et al. have published an early report which indicated the problems and trends in modelling of machining operations. While not micro-cutting specific, the authors have provided a good framework for a machining application, as shown in Figure 2.2. Some important issues such as tool-workpiece interaction, burr and chip formation, arise from the framework and are to be discussed in a micro-cutting context.

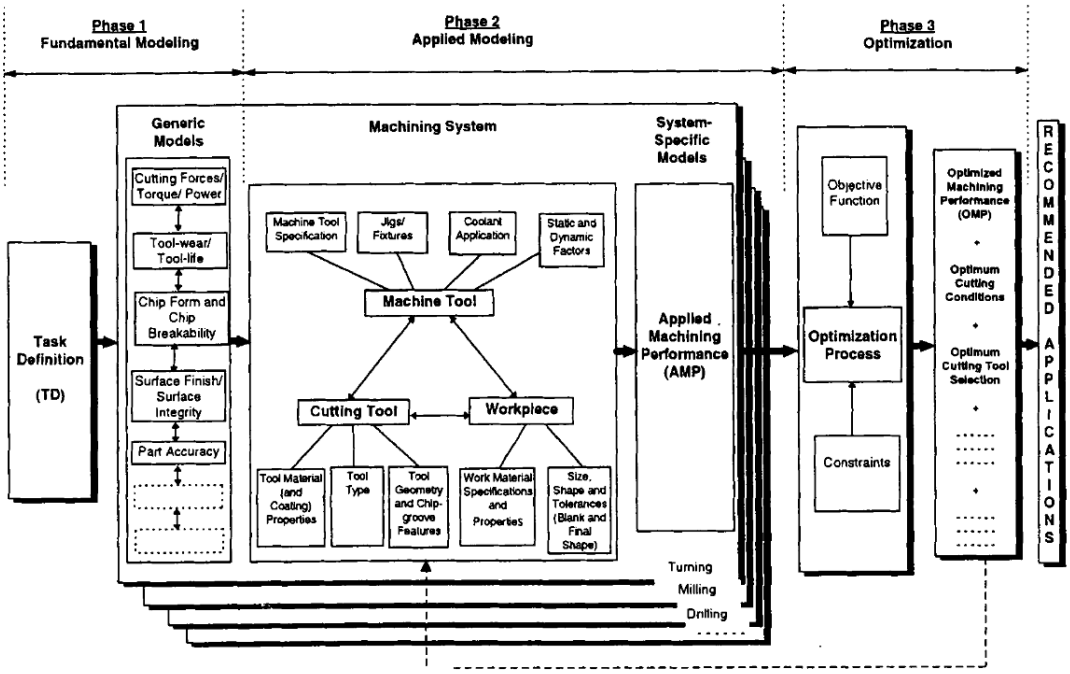


Figure 2.2. Predictive models for machining operations for practical application. (Luttervelt et al., 1998), Figure 1, p. 589

This schematic is relevant because it lists all the main categories that need to be considered in a cutting operation (machine-tool, cutting tool, workpiece), providing a good model for synthesising the most important parameters and succession of operations. By using them as a basis, specific micro-cutting factors (such as cutting tool edge radius, workpiece material properties) can be built in to develop a new,

micro-cutting specific framework. This illustration also helps highlight some important differences between regular-scale and micro-cutting technologies, which are presented in the following section.

Although they have similar kinematics, micro-cutting has distinct requirements, different parameters than regular cutting. For example, micro-cutting takes place at speeds higher than 20,000 rpm. The mechanics of micro-cutting are also different: in generating the workpiece surface, an important part is played by the material microstructure. However, the main difference between cutting and micro-cutting processes, beside the size order, is the uncut chip thickness (Cheng and Huo, 2013). Some of these differences are explored in the subsections below, in order to provide a good the level of understanding of the fundamental differences between regular scale and micro-scale cutting.

2.1.2.1. Differences related to the tool

One difference has been identified as the tool required to perform a micro-cutting operation. Unlike regular-scale cutters, which have 4 or six flutes, micro-tools are usually designed with only two or one flutes, to aid chip removal. In regular cutting, the cutting tool edge radius appears very sharp in comparison to the large uncut chip thickness (e.g. 100 μm radius compared to 20 mm depth of cut). However, in micro-cutting, the uncut chip thickness and the cutting edge are of comparable dimensions (under 100 μm); thus, the cutting edge radius must be sharper and should present improved mechanical properties. Due to the smaller area of the tool cutting edge, this is more prone to wear, and the improved mechanical properties would help to endure the high levels of thermal and mechanical stress induced by the high rotational speed.

2.1.2.2. Differences related to the machine tool

Beside the need for a specialised tool, specialised machining centres are also required in micro-cutting. There are two types of equipment that performs these operations: ultra-precision machining centres and micro-machines (such as micro-factories and

miniature machines). Unlike a regular machine tool, the machining centres require a higher stability, and they must act as dampers, to absorb the processing-induced vibrations. Thus, dissimilarities between regular and micro-cutting technologies lie also in the required machine-tools. Most micro-machine tools represent high rigidity ultra-precision equipment which run in a controlled environment, with constant temperature (Chae, Park and Freiheit, 2006). This ensures constant operating parameters, which improves tool life.

Although they execute the same kinematics (translation and rotation) as cutting equipment, the micro-cutting machining equipment must have an increased degree of stability, precision at sub-micron level, stiffness and must be perfectly aligned. They also should have a high degree of static and dynamic stiffness, of thermal stability, and compensation of positioning errors (Câmara et al., 2012). Due to the high speeds necessary, starting from 20,000 rpm and going beyond 50,000 rpm for some machining centres, such as the KERN Triton, the induced vibrations have high rates and the equipment has to act as a damper for them. These vibrations affect tolerances and the micro-machined generated surface. The main objective of precision machining studies is to improve the accuracy of this generated surface, to bring the geometry, dimensions and tolerances of the processed part closer to prescribed values.

2.1.2.3. Differences related to the uncut chip thickness

Some researchers have observed that a reduction in depth of cut values indicated a nonlinear specific cutting energy increase (Filiz et al., 2007). These size effects (deviations from proportional values of a process which occur in scaling the geometrical dimensions) represent the most important difference when comparing regular and micro-scale cutting, as illustrated in Figure 2.3.

In this image, the effects of the small ratio of the uncut chip thickness to tool edge radius are presented. In Figure 2.3a, the effect of the cutting tool edge radius is shown. These images indicate the difference between regular scale and micro-scale cutting. The main difference derives from the size of the radius compared to that of the uncut chip thickness. In regular cutting, the radius is signficantly smaller, and thus the tool has a high sharpness. However, in micro-cutting, the radius can be considered of a

similar size with that of the workpiece material average grain. This affects the effective tool sharpness, and thus, the shear zone formation.

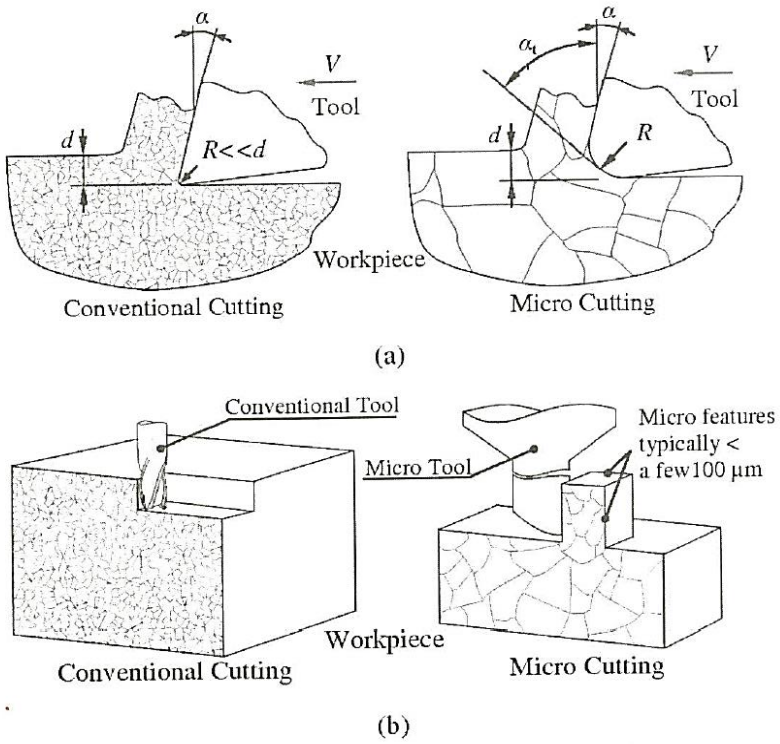


Figure 2.3. Size effects resulting from small ratio of the uncut chip thickness to tool edge radius (Cheng and Huo, 2013), Chapter 2, Figure 2.6., p. 26

In Figure 2.3.b, the difference between tools used at regular and micro-scale is presented. The micro-tool has a different geometry than the one used in conventional milling. Also, the relationship between the size of the cutter and that of the material grain size is indicated. The main difference in both sets of images is the size of the uncut chip thickness, which can create issues in terms of chip formation.

The relative scale between tool and grain size is reflected in the rake angles occurring at the chip-tool contact area (Figure 2.4.). While the cutting tool may have a sharp cutting edge radius, the relative scale difference makes the tool act as one with a negative rake angle, which is known to cause ploughing, rubbing and slipping phenomena.

At small cutting depths, phenomena of ploughing and slipping are more prone to occur due to free surface energy (Hesketh et al., 1993). Free surface energy can be defined as the excess energy at a material surface when compared to the material bulk, or the disruption of intermolecular bonds that occur when a surface is created, and represents

the work required to build an area of a particular surface. However, free surface energy is not analysed in this thesis. The phenomena analysis is concentrated at the micro-cutting level, with observations of ploughing and slipping, but does not involve phenomena of the molecular level.

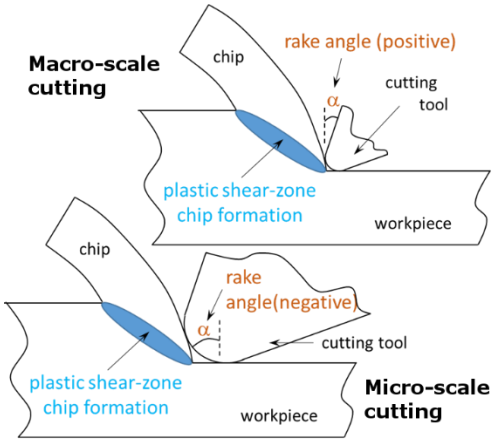


Figure 2.4. Differences related to the rake angle in micro and regular scale cutting. From Gherman et al. (2017), Chapter 4, Figure 4.4., p. 107

This concludes the analysis of differences between regular and micro-level cutting.

A few main points are drawn, and will be investigated in the following sections. Firstly, size effects dictate the conditions under which micro-cutting takes place. Thus, it is important to detail specific micro-cutting phenomena. Secondly, the tool-workpiece interaction is the main cause of micro-cutting lack of precision. And thirdly, due to the process taking place at grain-size level, it is important to address single crystal cutting. These three main points are investigated, in order to build the knowledge base needed for methodology.

2.2. Micro-cutting specific phenomena

The phenomena which happen at micro-scale cutting differ from those occurring in conventional cutting. One of the main differences is the relationship between the size of the uncut chip thickness and the cutting tool edge radius. In this subsection, chip formation, size effects, and the mechanisms that lead to shearing and ploughing are to be discussed.

2.2.1. Chip formation

In a cutting process, the size of the cutting depth can lead to slipping, ploughing and shearing phenomena. Out of these three effects, the most desirable phenomenon is shearing, as it leads to chip formation and, thus, to surface generation. One way to analyse the chip formation process is by cutting models, such as Merchant's slip-line model (Altintas, 2012). Ploughing and slipping are material phenomena which involve some elastic recovery, due to the fact that in chip removal, shearing involves mainly a plastic behaviour (Parmar, 2013). In slipping, the tool glides against the surface of the machined surface, while in ploughing, the material is not detached from the workpiece surface.

In a cutting process, a combination of these three phenomena takes place; however, at regular scale, shearing has a predominant behaviour (as the bulk of material is removed through material fracture), and ploughing and slipping can be ignored. In micro-cutting, the differences between the machined workpiece areas where these three phenomena take place are more obvious.

The reason is that in micro-cutting, one critical factor is the minimum chip thickness. This states that when the chip thickness is too low, compared to the tool edge radius, ploughing occurs; this causes the material to bulge, having negative effects on surface accuracy. This phenomenon also represents a lack of shearing or chip formation; the damaging effects are high burr formation, or impossibility of processing the material as intended in the operational steps.

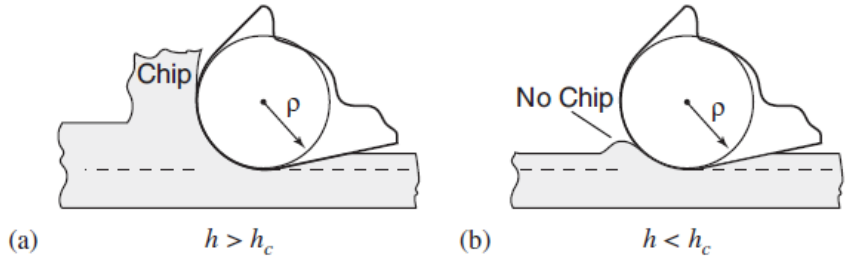


Figure 2.5. The minimum chip thickness effect in micromachining (Filiz et al., 2007), Figure 1, p. 1089

In Figure 2.5, an example of the material removal phenomena is given. This schematically presents the chip formation mechanism (Figure 2.5a) when the minimum chip thickness condition is satisfied, as in Figure 2.5 b.

Extensive studies have been made in the study of the uncut chip thickness and chip formation (Bissacco et al., 2006; Kang and Zheng, 2012; Malekian et al., 2012). The issue is that the simplifying assumptions affect the validity of the result. Along material consideration, this is why the ratio between minimum chip thickness and cutting tool edge radius varies from 5% to 40% and cannot be accurately determined.

The chip formation process depends on a sum of factors, such as tool geometry, workpiece material, cutting feeds and speeds, and depth of cut. The main driving factor of chip morphology is the shape of the tool, as it will dictate how the chip is formed. One important aspect to mention is that at micro-scale cutting, the depth of cut is close in value to that of the material grain size, which indicates that the chip will form differently than in regular scale cutting. As such, it is of interest to study the chip formation process in micro-cutting.

2.2.2. Ploughing and slipping

By correlating these three main material phenomena with the effects of the minimum chip thickness, one may observe the elastic deformation occurring in micro-cutting in Figure 2.6. The lower the cutting depth, the more likely it is slipping or ploughing will occur (Bissacco et al., 2006). When the uncut chip thickness is lower than the tool edge radius, elastic recovery has higher values (Figure 2.6 a, b). When the uncut chip thickness has value larger than the tool edge radius, the elastic recovery is minimal (Figure 2.6c).

Wang and Zheng (2002) have proposed an analytical force model with shearing and ploughing mechanisms for end milling. They stated that chip thickness varies with cutter rotation, thus manufacturers use the average cutting values, considering the lumped effects of two force generating mechanisms. The model proved accurate for end-milling, and could be further tested for more general micro-cutting principles, to determine whether size effects cause a difference in achieving the same results based on the model.

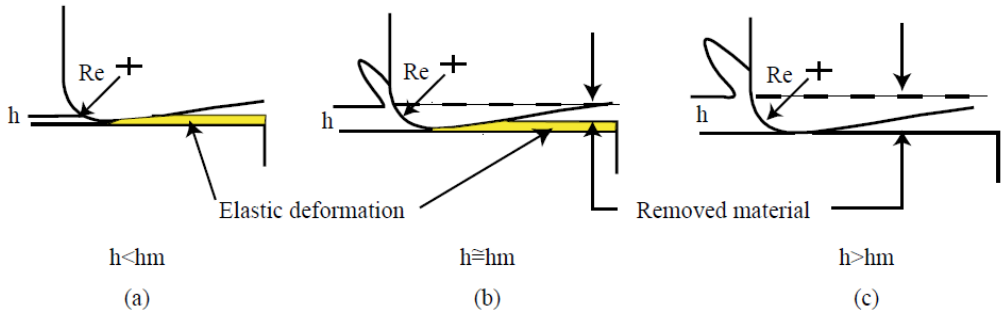


Figure 2.6. Schematic of the effect of the minimum chip thickness (Chae, Park and Freiheit, 2006), Figure 7, p. 320

At micro-cutting, low cutting forces occur, due to a small shear area (Câmara et al., 2012). The ploughing effect was associated with an increase of the cutting forces. Özel et al. (2011) have identified one method of minimising the ploughing action by having a low tool edge radius, thus a thinner initial chip thickness.

Endres et al. (1995) pointed out that, by decomposing machining force into separate chip removal and edge ploughing mechanisms, the dual-mechanism model provides better understanding of the cutting process and the physical mechanisms at work than the lumped model.

2.3. Crystallographic anisotropy in single grain materials

Material phenomena discussions have been centred, so far, around general mechanical deformation principles. However, it has been stated that, in micro-cutting, the material removal takes place at the same order of size or lower than the average material grain size. This brings into light specific issues, such as single grain material cutting. These are dictated by crystallographic anisotropy, as the material is homogenous (while in regular scale cutting, material can be considered heterogeneous).

By looking into single crystal cutting specialty literature, it is possible to extrapolate the findings to a micro-cutting process. As such, micro-cutting is again defined not only by the small depth of cut, but by the size effects (including cutting through individual material grains) which results from the process.

2.3.1. Shear formation in a single crystal

The study of shear band formation in single crystal materials has been the interest of research spanning from the 1960s and until present. This is of particular importance as the shear angle has a constant value in a regular cutting process; however, due to crystallographic anisotropy, the shear angle value varies with grain orientation.

The shear angle represents the angle made by the shear plane with the work surface. In the study of ductile materials cutting, the shear angle magnitude indicates the machinability of the material (Trent, 1991; Zorev, 1966). A large shear angle is associated with good surface finish, low cutting forces and continuous chip formation.

In the study of shear plane angle formation in single crystals, a few models have been developed based on crystallographic principles (Engel, 1986; Barrett and Massalski, 1980; Calladine, 1985; Schmid and Boas, 1968). The problem arising from these studies is that sometimes a competing number of shear planes can generate the same amount of plastic work, and modelling the exact ones which occur in cutting proved a challenge. Different approaches have been taken at this stage, but models have been validated only with limited success.

In order to tackle the issue of multiple shear planes competing, Zhou and Lee (1993) have proposed a microplasticity model which includes employing Bishop and Hill's maximum work principle. When different possible shear directions generate the same amount of plastic work, the authors have proposed and introduced an additional texture softening factor to determine the slip direction. Their approach was an improvement in a shear angle calculation; however, the shear angles had consecutive high and low peaks. In experimental studies, it has been seen (Cohen, 1982) that the shear angle values do not exhibit such large differences for incremental steps of cutting. As such, Zhou and Lee's models don't reflect well empirical findings.

A better example is found in Kota's orthogonal cutting model (2008), where shear angle calculation includes utilisation of the empirically-determined friction angle β. This prevents the model from being purely theoretical, and thus independent of experimental trials. He has corroborated his modelling findings with Cohen's experimental results, and both shear angle values and cutting force profiles match well. As such, Kota's orthogonal cutting model can be used to determine shear band

formation in single crystal cutting, and, further on, the cutting force developed during the process.

2.3.2. Cutting forces based on crystal orientation

In regular scale cutting, the cutting force is assumed to be constant. However, in micro-cutting, forces depend on crystallographic anisotropy. As such, it is important to define the correlation between individual grain orientations and the cutting forces associated with them. The implications are that all factors which normally depend on the cutting force (stability, repeatability, chip and burr formation) will no longer be valid in micro-scale cutting. The cutting force variation brings instabilities in the process. As a result, a critical step is to identify in which manner the cutting force changes due to single crystal material properties, and to investigate its implications on micro-cutting precision.

The first step is analysing cutting force models in single crystal cutting. In 1997, To et al. have found that cutting force evolution remains constant at different depths of cut. While it varied significantly on the (001), (110) and (111) crystallographic planes, those variations remained constant with crystallographic directions when several depths of cut were attempted. This is an important factor, and it states that cutting force is proportional with uncut chip thickness. This will allow future studies to employ various levels of cutting forces. It can be assumed that a force occurring at a higher depth of cut will be proportional with one occurring at a lower depth of cut, as long as they are generated on the same crystallographic direction. While this study has been in the direction of chip formation investigation, the research has not established models, repeatability or correlations between crystallographic anisotropy and chip behaviour.

In 1999, Lee and Cheung have continued their research by applying the procedure including texture softening factor (as shown in Figure 2.7) onto vibration generated by the workpiece material. Plane-strain orthogonal cutting has been defined as a succession of incremental strains happening one after another, and the shear band occurs between the top of the tool and the surface of the workpiece material.

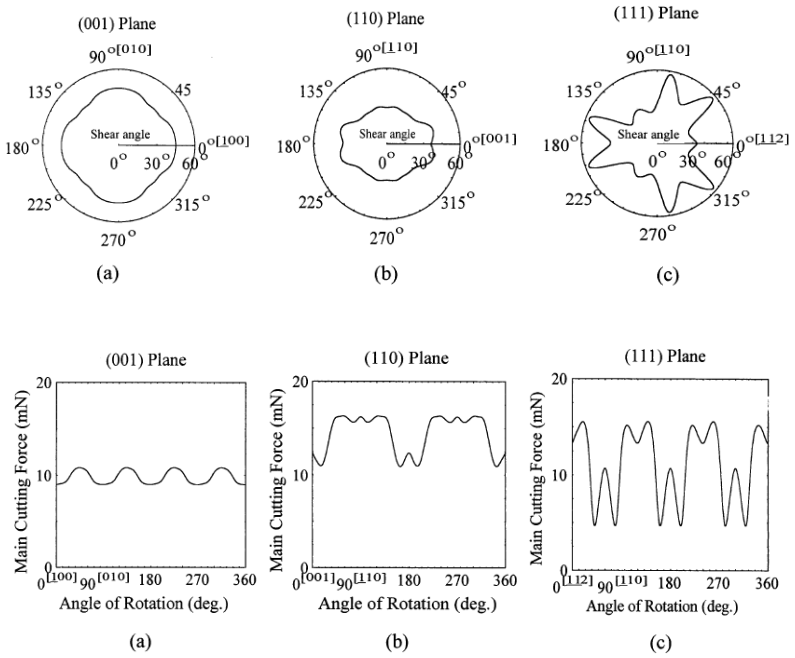


Figure 2.7. Shear angle and cutting force variation on the (001), (110) and (111) crystallographic planes. From Lee and Cheung (1999) Figures 2 and 3, p.219

In 2000, Lee, Cheung and To have applied the shear band formation model first developed in 1993 to single point diamond turning. They have described the strains and shears occurring on each of the five possible shear planes, starting with Reid's models for material science (1973). An initial observation of the shear angles and cutting forces plots indicate a small variation across shear angles results obtained on the (001) plane. Matched against experimental findings such as those made by Cohen in 1982, the shear angle and cutting forces variations (although experiencing a four-peak pattern) do not account for the much higher amplitude variation in cutting forces.

Later, in 2003, the authors have investigated the combined effects of crystallographic anisotropy and friction forces based on empirical analysis. While this was a minor contribution to the cutting force model developed inside a single grain, it is noteworthy to understand that in calculating shear angles, there are a number of additional factors that come into play. For example, some shear angle calculations include rake and friction angles. It is known that rake angles in micro-cutting often become negative (as shown in Figure 2.4), thus negatively influencing micro-cutting precision and causing ploughing phenomena to occur. An investigation of analytical models could prove useful to understand the variations of such factors in single crystals' shear band formation.

In 2008, Kota has proposed an algorithm based on orthogonal cutting principles stemming from Merchant's cutting theory (Altintas, 2012) for calculating the cutting forces necessary to cut through a single crystal rotated from 0° to 360°. His doctoral thesis in 2011 was based on the crystallographic anisotropy model of cutting forces in face-centred cubic metals, where he furthered his algorithm by including strain-rate plasticity in the model. The most important aspect is that unlike previous studies, the cutting force models provides a smoother profile in the force evolution. This is due to selection of the most appropriate shear plane as the one closer to the previous incremental step. In experimental single crystal studies, it can be seen that cutting forces have a smooth outline, without sudden jumps in values such as previously indicated by Lee, Cheung and To.

Experimentally, this is further validated by a number of studies, such as that conducted by Cohen (1982) in turning of single crystal copper and aluminium with different tool rake angles and cutting parameters. He has performed extensive studies on the evolution of shear angles, cutting forces and cutting energies in single crystal turning. Cohen's experimental results (1982) match well against Kota's orthogonal cutting model (2008). For this reason, Kota's model for cutting forces development in relationship with crystallographic anisotropy will be the one selected in this study.

2.3.3. Grain orientation-dependent material behaviour in cutting

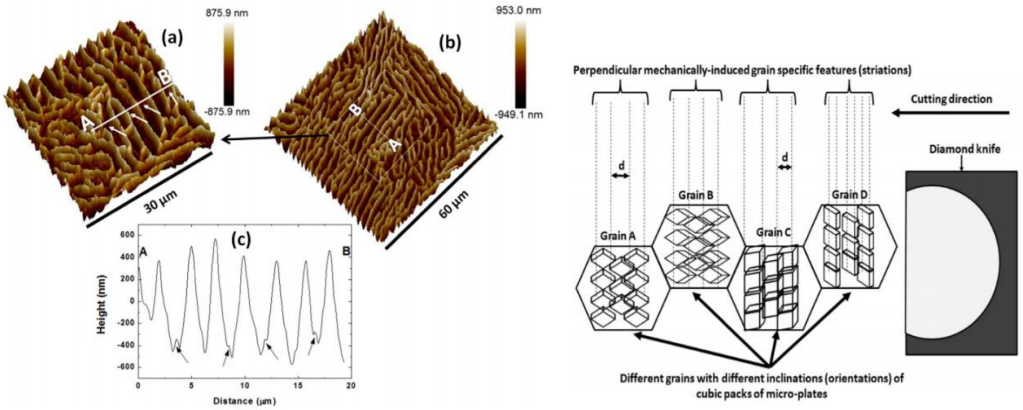
In order to address the knowledge gap identified above, that micro-cutting forces should be associated with specific material deformation mechanisms, one must have an insight in the material behaviour occurring in single grain machining (Zhou et al., 2014; Kelly and Knowles, 2012). The main paper in the field (Simoneau and Elbestawi, 2006a) is based on the idea that materials with different grain structures and phases (such as steel) have specific phenomena during the chip formation process. In the current study, this can be further extended to include the fact that grains with different orientations behave like different materials, and undergo different stresses and strains, which affect the chip formation process.

Simoneau and Elbestawi have investigated macro- and micro-scale cutting processes by performing orthogonal cutting by turning. The authors present experimental and

numeric results considering a number of factors: chip morphology, stress and shear, strain, temperature. The workpiece average grain size varied between 50 μm for pearlite and 5 μm for ferrite grains. When macro-scale cutting was performed, the chip was continuous and homogenous. When the uncut chip thickness reached or went under the size of the grains, specific microscale phenomena occurred. Simoneau assumed the hardness of grain A (ferrite) to be three times lower than of grain B (pearlite). This is an important assumption that can be expanded to the current research: different grains have different hardness depending on their crystallographic orientation. If an arbitrary grain orientation has a specific cutting force, then the grain has an arbitrary hardness. When looking at micro-cutting in multi-grain models, the model can be interpreted as Simoneau's model, and individual grains can act as different materials (in their case, grain type A and B).

Moriwaki and Okuda (1989) have done one of the most complete sets of experimental analysis on chip formation in fly cutting of copper known to this date. They have proposed depths of cut varying from 3 μm down to 0.0025 μm in order to understand the uncut chip thickness influence on chip formation in micro-cutting. The shortcoming of this study was that, whilst it was considering individual grains in the workpiece material, this was a multigrain type and thus a correlation between chip morphology and grain orientation could not be established.

Lee, To and Cheung (2000 and 2007) have investigated surface roughness in diamond turning of single crystal copper. Three crystallographic planes (001), (110) and (111) have been machined under various cutting conditions. A four-fold pattern has been identified on the first two planes, while a three-fold evolution of a 'cloudy' surface, indicating higher burr formation, has been observed in the latter plane. These have been associated with different elastic recovery sustained in a single crystal material. It is well-known that Young's modulus, elastic recovery, tensile strength all vary with crystallographic anisotropy. This was an important step in identifying the main cutting force profile 'zones' by looking at surface texture; however, only three-fold main profiles are identified (each 120°), which is not sufficiently detailed to address the correlation between the detailed cutting force profiles and the material deformation mechanisms.



a. b.

Figure 2.8. Surface texture in polycrystalline material. From Donatus (2015): a. Figure 2, p.93. b. Figure 9, p.97

Donatus et al. have studied the effects of structures caused by anodising and corrosion processes in the grains of the AA5083-O aluminium alloy, looking at chemical and mechanical phenomena. Mechanical processing has been performed through ultramicrotomy by micro-trimming the multigrain alloy with a diamond knife. They have found that the grain morphologies were dependent on grain orientation and had a sharp, ridge-like profile. They have also indicated that ridge-like profiles were probably caused by pack boundaries and the micro-layers which have created sharp micro-buckles. The most important finding was that the arrangement of micro-layers and mechanically-induced profiles were grain-specific, as illustrated in Figure 2.8. They reported that the features were mostly perpendicular to the direction of cutting, despite different inclinations of micro-layer packs; this is consistent with earlier studies done by Ramalingam and Black (1973). However, this study looked again at surface texture in a multigrain material, and as such surface quality was not analysed in a single grain material.

By looking at these investigations, it is found that some specific material behaviours appear in single grains, but a thorough understanding and correlation with crystallographic anisotropy has not been established yet. Nevertheless, this is a critical step in order to identify the surface quality which can occur when cutting through an individual single crystal with a known crystallographic orientation.

2.3.4. Burr formation in single-crystal material cutting

It has been previously mentioned that, in micro-cutting, deburring is a costly, if not impossible operation, due to the low depth of cut. Thus, burr formation must be better understood in a micro-cutting and, specifically to this study, single grain cutting processing operation.

As a material depending phenomenon, burr formation can be investigated in relation to the material microstructure from a wide array of considerations. Each grain orientation can present a higher or lower level of difficulty when being machined. Some grain orientations are thus 'soft orientations', and some are 'hard orientations'. This has not been studied in detail before, and is vital in understanding and improving micro-cutting precision.

The small size of the machined feature makes it difficult to coordinate subsequent deburring operations, while maintaining the feature geometry. There is a high risk in misaligning the part; after cutting, the test piece has to be investigated by optical means, microscopy or white-light interferometry. If burrs are observed, the part has to be oriented and clamped again on the machine tool, steps which introduce a number of errors: from clamping and unclamping to difficulties in getting the 'zero' value of the tool with respect to the top surface position, or positioning with microns in error against the initially machined feature. Machine tool limitations play their part in having difficulties in machining micron-level burr formation. For these reasons, in micro-cutting, deburring as a subsequent cutting operation is not always a possibility.

Micro-chips and micro-burrs are more difficult to remove from the surface of the machined test piece. In ductile materials, they tend to stick to the edges of the channels. Another problem lies in the fact that heated up material, due to the small size, tends to melt and thus bind with the surface of the test piece. Trying to remove the chips can further damage the test piece surface by scratching. For this reason, chip and burr formation has to be further understood in order to apply it to micro-cutting operations.

In order to investigate chip and burr formation in micro-cutting and single crystal machining, it is important to define what types of burr can be generally encountered. Gillespie's doctoral thesis (1973) stands as the foundation of burr formation characterisation techniques. Burr height is less important in material deburring operations than burr hardness, and burr thickness (width). In order to define burr, there

is a need to refer to the three basic mechanisms of burr formation: bending of chip, lateral extrusion of chip, and tearing of chip from the test piece surface.

Characterisation of known types of burr (Gillespie, 1973):

- Poisson burr (lateral flow deformation)

This type results from material bulging at the sides when compression ensues. The material becomes compressed up to the limit of permanent plastic deformation.
In order for this burr to occur, the tool needs not be perfectly sharp. Even with a slight tool radius, the tool will develop a built up edge (BUE), which would in effect increase the actual size of the tool radius. The high pressure on the tool flank can be ignored in this study, as it is more prone in materials with low modulus of elasticity. However, it would be noteworthy to observe if the tool flank induces different marks on different crystallographic orientations.

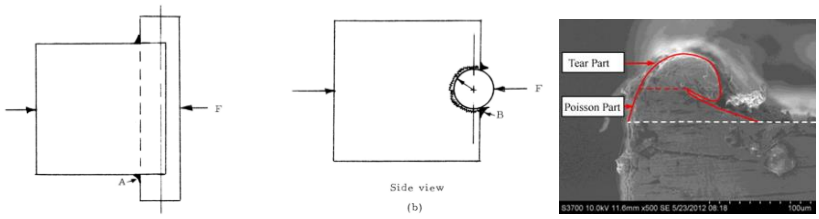


Figure 3. Bulging caused by indentation of cylinder.

a. b.

Figure 2.9. Material removal mechanism and burr formation. From Gillespie (1974) Figure 3, p. 8; and Wan (2014), Figure 4, p. 30

- Roll-over burr (bending)

It is created when the cutting tool exits the workpiece material, and the leftover material is pushed over the test piece edge, rather than sheared. In this study, it is also named the ‘exit chip’.

- Tear burr

Similar to punching operations, the material becomes torn rather than sheared. In this study, it is correlated with the adjacent behaviour on the lateral edges of the exit chip, where tearing is identified by highly serrated chip edges.

- Cut-off burr

Incomplete shearing of workpiece material can cause a cut-off projection of material.

One of the types of burr described above is the exit bur, looking like a partially detached chip at the end of a machined channel. Some early material investigation in single crystal machining have looked at these chips, as follows.

Detailed researches have been done in the 1970's about lamellae formation, shear front formation, and these classic principles have to be incorporated when analysing micro-chips and micro-burrs (Turkovich and Black, 1970; Black, 1972; Ramalingam and Black, 1973). However, most studies have been done in microtomy operations, inside scanning electron microscopes, at very low cutting speeds compared to speeds used in usual micro-cutting operations. Also, the tools used in order to observe and detach lamellae were sharp glass knives, which don't behave like micro-cutting tools in machining, don't possess the same strength, and have a far less complex geometry than slipping tools and micro-mills used in micro-cutting. Another limitation stems from the fact that chip morphologies have not been discussed or researched, leading to an incomplete image of chip formation mechanisms.

For this reason, the micro-chips and micro-burrs observed are lacking the complexity of more complicated, industrial operations. Ultimately, these models have to be able to be applied to industrial processes, to extend single grain considerations to multi-grain materials, in processes with speeds and feeds used in industrial micro-cutting. Microtomy studies lack this level of evidence. Next, this type of research has to include an increase of cutting speed and perform micro-cutting on a regular precision machining centre with specialised tooling, to take steps in the direction of approximating industrial factors.

In conclusion, it has been seen that burr formation and chip formation are material behaviour mechanisms which can reflect the quality of a product, or, effectively, how precise a cutting technology is. In micro-cutting, in particularly, burr and chip formation lack the level of understanding needed to address how surface quality varies with crystallographic anisotropy. This knowledge is fundamental in ensuring process precisions and micro-parts surface quality. As such, a high need arises in the developing a better understanding of burr and chip formation in single crystal cutting.

2.4. Dynamic analysis in micro-cutting

Thus far, micro-cutting specific concerns and material behaviour in single crystal machining have been discussed. The goal of this thesis is to improve precision in micro-cutting technologies.

One effect damaging to micro-cutting precision has been identified as burr formation (Pham et al., 2008). This depends as much on the material being machined, as on the operating parameters undertaken. Some materials are more prone to burr formation, such as ductile ones. However, in many cases, bur formation occurs as a results of process instabilities.

This refers to instabilities arising from the tool-workpiece interaction: some operating parameters (feed, cutting speed, depth of cut) can negatively affect surface precision. In order to assess the influence of operating parameters on the micro-cutting or single grain cutting process, a difference must be made between burr formation as a consequence of material behaviour, and burr formation as a result of process instability. The first can be addressed though experimental investigations of material deformation mechanisms. However, the second can be investigated through dynamic analysis.

The latter is developed in the following section, by looking at micro-cutting models, operating parameters, re-iterating cutting forces (but within a dynamic analysis context) and focusing on cutting stability models. This will help define the models which can be adopted in the investigation of stability and repeatability, which need to be updated in order to be applied to single crystal cutting, rather than a general cutting process.

2.4.1. Micro-cutting models

When analysing the size effects, one must take into consideration the entire micro-cutting subsystems: cutting tool, machining centre, tool-workpiece interaction, fixtures. Some authors have analysed the effects of some input factors, such as speeds, feeds and depths of cut, on surface roughness, cutting forces, and tolerances.

In order to better analyse the micro-cutting process, one may see the important aspects that were considered by Câmara et al. (2012) in his micro-cutting investigations, identified as input parameters in micro-milling (Figure 2.10). These aspects are synthesised in three subsections, namely workpiece material, tool characteristics and machine tool concerns. This schematic representation of the input factors that go into a micro-cutting process and it can be used as a model to define the process, and to highlight the properties that can affect the results.

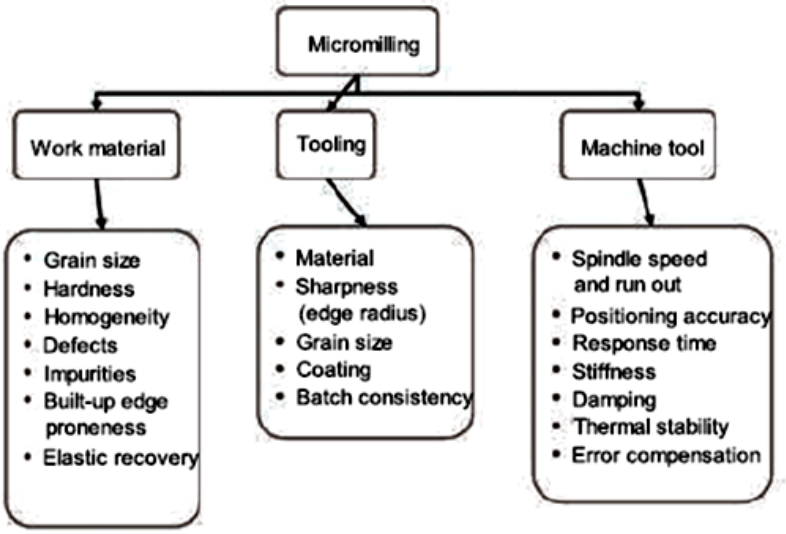


Figure 2.10. Key aspects to be considered in micro-milling (in Câmara et al., 2012), Figure 2, p. 674

Some models are based on simplifying assumptions, such as considering the cutting forces to be constant, or the cutting velocity to be constant. Other models look at adopting an orthogonal cutting model for the cutting force or a more complex, oblique cutting model (Karpat and Özel, 2006). The models adopted depend, for this reason, on what type of results are sought: surface roughness as an indicator of surface accuracy and process stability; material removal rate for productivity.

As different authors focus on different input parameters, no general model or exhaustive analysis of the micro-cutting process exists (Astakhov, 2005). Due to the complexity of the cutting processes, one strategy is to reduce the number of parameters that are varied. As such, an orthogonal cutting process is more useful in understanding stability, due to having a simpler development. Moreover, by adopting a constant depth of cut and cutting speed, one focus on material behaviour.

2.4.2. Operating parameter models. Speed, feed, rotation.

It is known that by using higher rates for cutting parameters, productivity can be increased. Also, the selection of optimal cutting operating parameters has proven good results in reducing burr formation (Câmara et al., 2012).

In papers that refer to burr formation, it was observed that a decrease in the value of the operating parameters (such as cutting force) is usually correlated with a decrease in surface quality - higher burr levels, higher surface roughness and higher tolerances (Weule, Huntrup and Trischler, 2001). These can be a result of the tool-induced vibration and of the elastic recovery of the test piece (Liu et al., 2005). Also, higher cutting speeds would require a highly stable machine tool, for which specialised design is required, considering dynamic effects (Huo and Cheng, 2006).

While the nominal surface accuracy and low depths of cut can be achieved at micro-cutting only at high speeds, these also present disadvantages. Higher cutting speeds lead to an increase in vibration; they also affect cutting edge sharpness and cutting tool life.

The problem arises from the fact that regular cutting operating parameters cannot be adopted with the same degree of confidence in micro-cutting in order to achieve good productivity and surface finish.

2.4.3. Cutting force models

One indicator of the stability of a cutting process is the cutting force. As the cutting force depends on: the position of the tool, the rotation of the spindle, the material of the workpiece, the clamping of the part, and furthermore, a constant cutting force is an indicator of a process running smoothly. However, if, for example, the cutting tool encounters inclusions or defects in the workpiece material, then the cutting force registers a spike. If the operating parameters are not chosen well, the cutting force will have high values and will lead to tool breakage. As such, it can be stated that the cutting force is the cutting parameters that ties together the entire cutting process subassemblies, and it indicates whether the process works well or is unstable.

For this reason, it is important to understand and identify methods through which cutting force modelling, and cutting stability, can be assessed.

A large body of work exists in the field of modelling cutting forces, as follows.

In regular scale cutting, some of the most well-known cutting models were given by Merchant, by Ernst and by Piispanen (Atkins, 2003). Lee and Altintas have worked on cutting forces models (1996) for helical end mills. They have taken into consideration shear and friction angles, along shear stress, in order to predict cutting forces, forced and chatter vibration and errors. The chip formation was analysed by means of true trochoidal motion of milling models, considering static displacements. Altintas' studies extended to mechanics and dynamics of ball end-milling (1996, 2011). The models proved accurate for ball end milling using helical cutters. The problem is that these studies tackle small areas of cutting technologies, too specific in their own issues to provide a more generalised understanding.

As such, a simpler cutting process, such as slipping or scratching, which involves just one feed motion of the tool and no rotations, is more appropriate in order to assess micro-cutting and single grain cutting forces.

2.4.4. Cutting stability analysis

It has been stated that, in micro-cutting, machining precision is a bigger issue due to the level of accuracy needed: a few microns in tool deflection could easily cause tool breakage and high burr formation (Suh and Liu, 2013; Zhang et al., 2015).

One classic method of analysing cutting precision is cutting stability analysis, as it indicates the range of operating parameters which generate vibration and instabilities in the process. This section explores these modelling techniques, in order to adopt the most appropriate for a micro-cutting or single crystal cutting process.

In his manufacturing automation book, Altintas (2012) has defined different principles for stability theory. In this respect, he differentiated between linear and non-linear parameters that lead to different types of stability analyses.

One definition is that linear stability theory, which is based on linear cutting parameters, can be used to analyse the stability of chatter vibrations. Previous work

done by Tobias (1965), Tlusty and Polacek (1965), and Merrit (1965) supports this type of investigation. Vibration generation can be investigated based on cutting force discontinuities: when the cutting force varies, so does the stability of micro-part formation (Tobias, 1965; Rao, 2011).

Altintas (2012) also mentions that nonlinear process parameters (such as the ones in turning and milling, which are nonlinear due to the dynamic effects of workpiece and tool rotations) are not used in linear stability analysis. One important nonlinearity in cutting is represented by nonlinear cutting constants. Thus, technologies like boring and turning have nonlinear dynamics due to the complexity of their respective cutting constants.

Based on these notions, two cutting stability analyses can be identified: one based on linear parameters (linear stability) and one on non-linear parameters.

As non-linear parameters occur in cutting processes that involve rotations, which generate dynamic (regenerative) effects, this will be considered a ‘dynamic’ analysis. For example, orthogonal cutting (where rotations are not involved in the analysis) will be considered linear; turning models and analyses will be considered non-linear and dynamic in nature.

Characterising stability analysis based on the linearity or non-linearity of the investigated cutting parameters is important in addressing the structure of future analytical steps, as developed in Chapter 3, methodology.

In terms of the negative effects of micro-cutting precision, tool deflection is mostly caused by vibrations occurring during cutting: spindle-induced and self-generated vibration. The spindle-generated vibration travels through the tool holder to the micro-tool tip, where it causes the tool to deflect (Cao and Altintas, 2007; Namazi et al., 2007; Thomson and Dillon Dahleh, 2014; Tobias, 1965). The vibration propagation through the machine subassemblies commands interest. Each subassembly (spindle, holder and tool) can be modelled as a multi-span beam.

Another important source of vibration is chatter, which represents a self-excited vibration occurring at the tool-workpiece interaction.

Between tool, tool holder and machine-tool spindle, resonances can occur at their natural frequencies. This results in a high occurrence of vibration, on multiple concomitant natural frequencies. When the tool is in contact with the workpiece surface, the vibration causes the tool to perform waviness at the machined surface. The undulation negatively affects the parameters of the cutting process when a consecutive cutting step is undertaken, due to the variability in the chip volume, cutting force, and pressure on the spindle. This variability is added onto the effect of the vibration already present.

Some of the causes of chatter are a lack of rigidity in either tool or workpiece. Others are that some exciting frequencies (produced by certain feeds and speeds) induce vibrations in the cutting system. For some tool geometries, these vibrations are also known to occur due to tool angles, dimensions or surface treatment. However, the common characteristic between these causes is that they become regenerative due to dynamic effects. Thus, the chip thickness depends on the relative position between tool and workpiece during the previous tool passage.

While chatter occurs at conventional cutting speeds, it is more distinctive at higher spindle speeds; as discussed in micro-cutting definitions, most micro-cutting speeds are high, reaching 50,000 rpm. As such, the spindle speed (and as such the cutting speed) is the main factor that affects regenerative vibration.

The cutting tool, tool holder, machine spindle or exciting frequencies can result in chatter, which produces a high chip thickness variation for each of the tool steps during consecutive cuts. This regeneration of surface waviness can grow up to the size of the uncut chip thickness, after which the tool jumps out of the cut.

Various tool geometry factors (such as tool wear, cutting tool edge radius or rake angle) increase chatter, thus affecting cutting stability and precision (Afazov et al., 2010, 2012 and 2013; Altintas et al., 2012; Jin and Altintas, 2013; Stepan et al., 2013; Szalai et al., 2004).

Tool wear results in a variable diameter during cutting, which affects not only chip formation, but the tool trajectory as well (Ding et al., 2010). The Newton-Rhapson method is used in cutting force equations to determine the tool diameter nonlinearities in time. A similar approach is used to model the cutting tool edge radius and rake angle variation in time. Cutting force equations are proposed for each model. Despite this, a

material microstructure has not been studied so far in correlation with self-generated vibrations, or in a general tool deflection model.

The importance of grain boundaries is explored in recent studies by modelling an orthogonal cut at a titanium grain boundary (Venkatachalam et al., 2015). Although this program serves well to understand the surface free energy, phenomena are more complex in micro-cutting. The tool trajectory, tool run-out and chatter greatly affect the tool-workpiece interaction and need a more complex model than classic orthogonal cutting, which does not include any cutting force variations.

There is a need for a better understanding of the material microstructure impact at depths of cut equal or less than the material average grain size (Matuszak, 2014). New cutting stability analytical models and empirical studies focusing on surface quality analysis are needed to provide information relevant to stable conditions of single crystal cutting, which would positively affect micro-cutting precision.

2.5. Knowledge gaps and key challenges

Based on the literature survey presented in this chapter, the knowledge gaps and key challenges in improving micro-cutting precision have been identified as:

- Knowledge gaps

1) Lack of understanding micro-cutting stability in correlation with material microstructure

Stability analysis in micro-cutting does not include crystallographic considerations and thus cannot be applied to micro-cutting operations.

2) Gap in understanding process repeatability factors in micro-cutting

Many parameters are a consequence of cutting forces; when they vary, this introduces instability in the process; micro-cutting specific parameters which can assess repeatability are lacking.

3) Deficit of characterisation of micro-cutting surface phenomena, such as burr formation and ploughing, in relation to material microstructure properties

Many studies have investigated burr formation and ploughing in micro-cutting, but few in correlation with the material microstructure. Characterisation of different chip morphologies due to crystallography properties have not been developed yet.

4) Lack of empirical data for micro-cutting surface phenomena repeatability in relation to crystallographic anisotropy

Micro-cutting needs more specific understanding of material behaviour at micro-scale, building on predicted material behaviour during cutting of single grain materials.

- Key challenges

1) Understanding of micro-cutting factors repeatability.
2) Developing new stability analysis that integrates material microstructure effects.
3) Discovering and explaining grain-orientation specific material phenomena, such as burr formation and ploughing.
4) Improving precision by establishing surface phenomena repeatability.

2.6. Aims and objectives

The main aim of the current research has been identified as improving micro-cutting precision based on investigations of the material microstructure properties and their effects in micro-cutting processes.

By achieving this goal, it would be possible to develop, in the future, a micro-cutting equipment or processing technique which enables the micro-cutting operation to take place with as much precision as a regular scale cutting process. This would, in effect, eliminate the size effects from the micro-cutting process.

The research proposed below has the potential to improve precision of micro-cutting by providing the first steps in generating micro-cutting specific analyses and validations.

As such, the specific objectives of this research are formulated as follows:

1. To provide a better understanding of linear stability based on single crystal analytical models.
2. To experimentally validate cutting force variation in single grain cutting, and to provide a comparison with multigrain results.
3. The development of new, single grain-specific cutting stability models.
4. To achieve a new and comprehensive understanding of material deformation mechanisms, by considering single crystal machining effects on surface quality and repeatability of results

CHAPTER 3

RESEARCH METHODOLOGY

3.1. Scientific approach

This thesis aims to improve micro-cutting precision. In order to understand what the goalposts are, a breakdown of these terms (improving, micro-cutting and precision) helps define both the area of focus and the methodology undertaken for it.

As such, to improve precision, the first step is to define, analyse, understand whether some parameters have an effect on precision or not, and ultimately to propose better machining strategies based on these findings.

Secondly, a difference must be made between regular cutting and micro-cutting processes. These arise from, but are not limited to:

- cutting tool edge radius: very sharp tools, where radii are often in the 5 – 10 μm range
- rake angles: what is a positive rake angle in regular cutting becomes a negative one for very small, micron-level depths of cut
- size effects: due to the small depth of cut, cutting is done at the same order of size, or smaller, than the average material grain size; this is perhaps the most important micro-cutting aspect, as it affects the entire process through material microstructure properties; grain size and orientation make the material behave like

a heterogeneous one, and cutting must be investigated by looking at individual grain machining.

And thirdly, precision can be defined as the property of a machining process which can be measured through stability and repeatability of results.

Based on these three terms, it is now possible to outline the area of study as defining, analysing (through modelling and experimental techniques) and deciding what parameters can improve the stability and repeatability of a micro-cutting process, by looking at micro-cutting relevant parameters such as material microstructure.

This would enable the developments of micro-cutting specific strategies for machining. Such strategies would ensure that a micro-cutting process can be undertaken with the same degree of confidence as a regular cutting process in terms of stability, repeatability, ultimately precision of results. Effectively, size effects would be removed from the cutting process, rendering it as easy to perform as a regular cutting process.

3.2. Micro-cutting framework

A few authors have proposed frameworks to analyse cutting processes, such as Luttervelt et al. (1998), as illustrated in Figure 2.4 for a general cutting process, and Câmara et al. (2012), as presented for micro-milling in Figure 2.8. A number of common points arise from the frameworks; with the exception of a few points, the micro-milling scheme could be applied to a general micro-cutting process. However, some important implications, such as size effects, broader considerations for tools, and the impact of the depth of cut on the process, are missing.

As such, this thesis develops a new, micro-cutting-specific framework, presented below in Figure 3.1.

The categories that are of most interest in micro-cutting are tooling, workpiece material, machine tool, and size effects. They are interconnected, and influence each other's influence to a high degree. Therefore, no category can be considered independent. For example, the interaction between the cutting tool and the workpiece material. While some definitions put the threshold of micro-cutting at machined features below 25 μm, the reality is that the threshold depends on the average grain

size and the tool geometry (rake angle and tool edge radius). For materials with a higher average grain size, such as 300 µm, cutting behaves in the same way at 10 µm as it does at 50 µm depth of cut, as it has to consider the individual grain orientation and crystallographic properties. As such, the 'size effect' dominates the cutting process, rendering it effectively into micro-cutting.

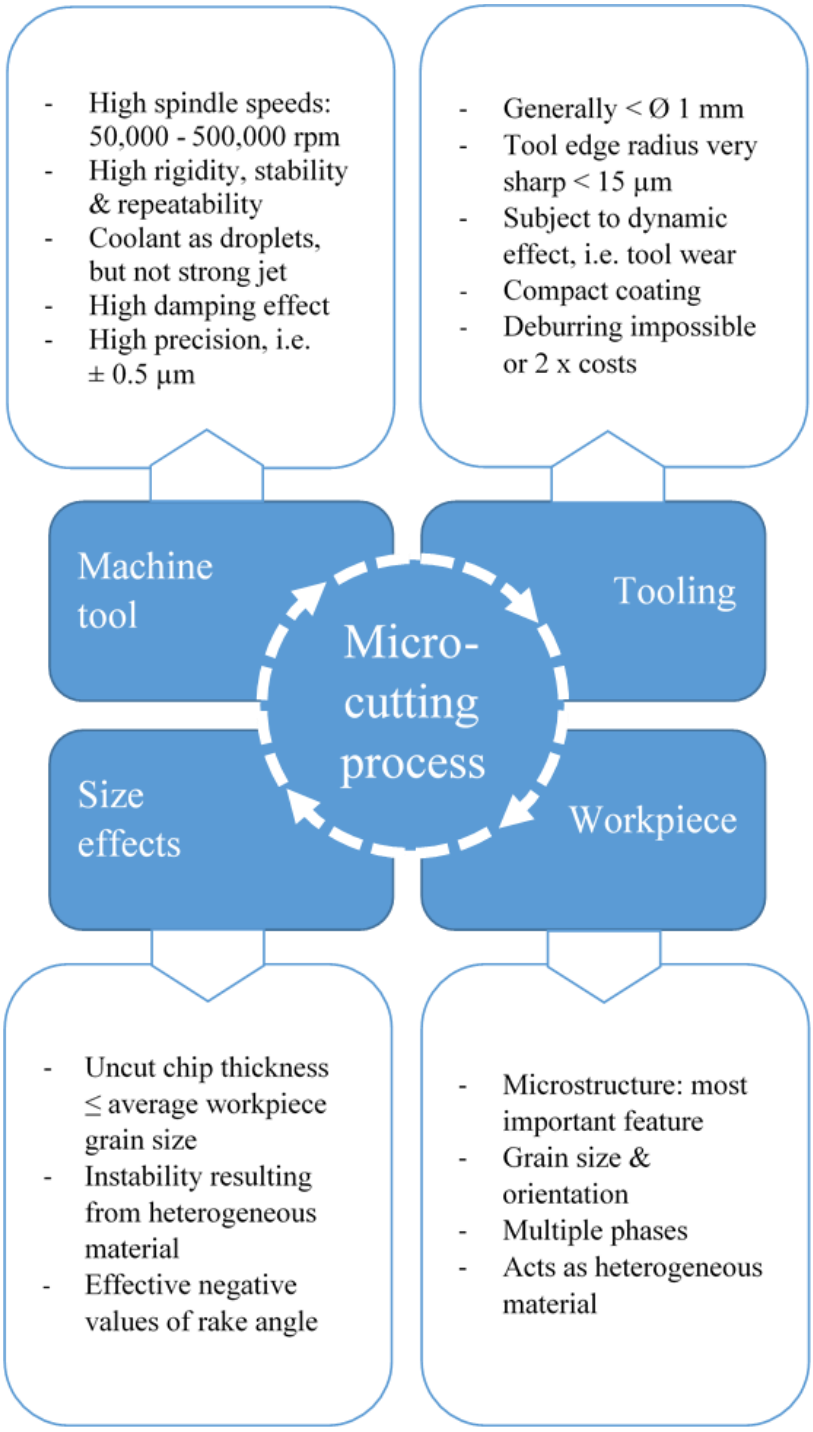


Figure 3.1. Micro-cutting framework

Another example stems from instabilities due to material microstructure. In a micro-cutting process, due to the variation of material properties, cutting forces can vary and negatively affect process stability.

By using this proposed framework, it is possible to look at the micro-cutting process as an assemble of interacting elements, and to develop a methodology based on this improved understanding. Hence, the following section deals with methodology in order to meet the objectives defined at the end of Chapter 2.

3.3. Specific objectives

The aim of the current chapter is to present the research methodology that addresses the aim and objectives formulated at the end of Chapter 2. A general plan for the research methodology is presented, while detailed steps of methodology are worked out in detail at the beginning of each chapter.

The first specific objective of the current research is to provide a better understanding of linear stability based on single crystal analytical models.

To achieve this, the research focuses on developing a program that can be used in the calculation of cutting forces. A number of studies have been identified in the literature survey as cutting force methods that are based on crystallographic anisotropy formulations (Kota, 2008; Zhou and Lee, 1993). The most appropriate analytical model has been selected as the orthogonal cutting procedure developed by Kota (2011).

The cutting force calculation is made with the maximum work principle (Hill, 1950), which employs shear strains in order to derive the stress state. Initially, strains and stresses in a single crystal have been defined in the material.

The second step in the analysis focuses on the formation of shear plane angles in single crystals (Engel, 1986; Barrett and Massalski, 1980; Calladine, 1985; Schmid and Boas, 1968). The maximum work principle was applied as the selection of the shear angles that would generate the most amount of plastic work (Reid, 1973).

The final steps is the calculation of orthogonal cutting forces based on Merchant's theory (Ernst and Merchant, 1941; Altintas 2012). This concludes the development of the Matlab program based on Kota's procedure (2011).

Next, new models are proposed to understand the effects of the material microstructure on linear stability. Some parameters that can affect linear stability are the tool position, namely the tool deflection and slope. A variation in the tool-workpiece relative position can be caused by tool deflection and can cause vibration (Wu, 2013). Tool deflection models are employed to obtain the new tool path and, consequently, the change in the cutting force evolution. The results indicate horizontal cutting force patterns for 360° rotations considering various tool deflection values.

The new models proposes their calculation based on the variation of cutting force values developing during cutting of a (001) crystallographic plane.

In order to meet the second objective of the current research, an experimental study is proposed. The goal is to empirically validate the cutting force variation due to crystallographic anisotropy, and to enable a comparative study with multigrain material cutting.

One of the topics of focus in the study has been to develop an experimental set-up that would allow cutting force acquisition. This comes in the light of the small forces developed in micro-cutting. The selected force acquiring equipment will be a dynamometer, due to enabling the measurement of X, Y and Z directions. Previous studies have either considered turning (Kota, 2011) as a succession of incremental orthogonal steps, either orthogonal cutting by performing slipping (Black, 1972). As such, the first type of set up enables the measurement of successive steps made on a 0° to 360° workpiece rotation. The advantage is that it offers a large number of data points, for many crystallographic directions, which provide a comprehensive image on the effect played by microstructure. In contrast, orthogonal cutting studies in slipping generally consider limited numbers of crystallographic directions, and cutting forces are analysed on a single direction. Moreover, this set up meets the theoretical orthogonal cutting assumptions that cutting force models are based on. The tool executes a straight feed motion, and no tool or workpiece rotations are involved. This vastly benefits experimental studies, as the experiment is much better controlled and

dynamic effects are avoided, thus providing an accurate analysis of linear stability. Based on these two known experimental set-ups, a compromise is made in the cutting process selection. The main aspects that are of interest are that orthogonal cutting is a cutting method closer to theoretical assumptions, while it also enables linear stability analysis (which turning experiments do not, due to complex cutting constants). The analytical model used for cutting forces is based on an orthogonal cutting procedure; whilst it is proposed by Kota for turning results, the model itself does not include any dynamic effects, thus it can be ruled as linear. Based on these considerations, a decision has been made in the selection of an appropriate cutting process that would validate the analytical model. Single crystal material samples will be machined by slipping, although a method of workpiece rotation that will enable a higher number of crystallographic directions to be studied is proposed.

Two methods used for workpiece rotation are considered as set-up. Both involve clamping the workpiece through a screw on the dynamometer top surface. The first method is proposed as clamping the dynamometer itself on an aluminium plate, which is then clamped on a rotating table. The rotating table allows manual rotation of the entire set-up at arbitrary angles. To ensure a high number of data points, the angle of rotation between machined channels would be 6°. This enables cutting of 60 channels on a test piece that has 12 mm in diameter and 2 mm thickness. However, due to the increased number of channels, channel overlapping is a reason for concern. The largest depth of cut which would assure that channel material deformation would not interfere with each other is estimated at 50 μm, based on CAD models of the workpiece. Smaller depths of cut would also enable performing large numbers of channel; however, at this depth of cut, the main issue is represented by the cutting force. It is estimated that the cutting force is in danger of being at the lower limit of dynamometer capabilities; thus, higher depths of cut would enable a higher force to be produced – whilst also trying to maintain the depth of cut in the range of micro-cutting definitions.

The second proposed method of workpiece rotation is by manually changing the position of the test piece. The test piece would be screwed onto the surface of a plate. A plate (smaller than the dynamometer, but larger than the workpiece) is designed, based on the profile of the dynamometer. The dynamometer has a number of holes which allow the plate to be clamped on. As such, a CAD model of the disc-shaped plate features all the possible clamping possibilities offered by the holes of the

dynamometer. It has been found that performing 24 holes on the plate would allow 24 workpiece positions, by clamping the plate on the dynamometer with four screws positioned at 90° apart. The plate would be manually unscrewed after each machined channel, and the test piece and plate assembly would be manually rotated by one position, then clamping it down with the 4 screws. Three things are important in the assessment of this rotation method. Firstly, it would enable a smaller number of channel than the previous method (60), but still much larger than most orthogonal cutting studies. Secondly, the machined channels could be in the range of 200 µm depth of cut, which would enable higher forces to be developed and thus overcoming the possible dynamometer limitation. Thirdly and most importantly, by manually rotating the workpiece and not changing the position of the dynamometer, errors introduced by manipulating the dynamometer or by introducing a large piece of equipment (the rotary table, which hosts its own positional errors) are avoided.

Based on these proposed experimental set-ups, experimental validation of cutting forces occurring in single crystal cutting is sought.

In order to address the third objective of the current research, cutting stability analysis has been considered for the development of new, single grain-specific stability models.

Cutting stability represents an analysis of the dynamic effects of machining processes. The main focus is establishing the operating conditions which will generate self-regenerated vibration, or chatter. This type of vibration does not occur as a result of machine-tool or tool-workpiece interaction vibration, but it stems from the generation of vibration introduced by each workpiece or tool rotation (the dynamic effects of the workpiece in turning, or the tool in milling). As such, cutting stability lobes are a type of nonlinear stability analysis, which investigates the effects of dynamic parameters on process precision.

Cutting stability lobes have been developed for classic cutting operations (such as turning) based on well-researched formulations (Schmitz and Smith, 2009; Altintas, 2012). However, it is known that the cutting parameters involved in the process, although dynamic in nature (due to the workpiece rotation), are taken as a constant value. Some of the parameters involved in the calculation which are used as constant

inputs in the model are the cutting coefficient, the cutting force and the shear angle (which is calculated based on the effects of the friction and rake angles).

New cutting stability models are proposed in order to study the effects of the linear variation of cutting forces and shear angles on the dynamic analysis of a cutting process. By doing this, a 'dynamic' analysis can assess whether the variation of the parameters identified in the cutting force analytical and experimental studies affects the process stability, and thus, micro-cutting precision.

As cutting coefficients depend on the cutting force and shear angle value in their formulation, it is possible to propose new cutting coefficients that include the variation of cutting parameters due to single crystal rotations. Moreover, cutting forces and shear angles depend on the influence of the rake angle of the tool, and a comparative study of various rake angles is proposed. It is important to determine whether a variation of the rake angle would introduce positional variations of the cutting forces (for example, if the cutting force profiles would occur at 5° apart), as this indicates a larger impact on process stability. If cutting forces follow the same pattern, but they occur on a different crystallographic position, this has to be factored in the new models to improve the micro-cutting precision.

In order to meet the fourth objective of this research, experimental analysis of single crystal machining effects on surface quality and repeatability of results is proposed, in order to enable a new and comprehensive understanding of material deformation mechanisms in single crystal materials.

The experimental analysis focuses on the surface quality analysis of the samples machined during the experimental validation of cutting force variation. This approach is undertaken in order to obtain a clear image in the correlation between measured cutting forces, and their observed effects.

Surface quality is to be investigated based on image analysis. Scanning electron microscopy is proposed as a means of obtaining images of the high number of channels observed: 24 and 60 channels performed in single grain and multigrain copper samples. The positions investigated with respect to the channel length are:

- the tool entrance area in the workpiece material (as this offers important information with regards to tool positioning);

- two points along the channel, to focus on burr and ploughing formation (two are necessary in order to ensure that the material behaviour observed remain constant throughout the channel, and thus findings from one image can be extrapolated to the entire length of the channel);
- the chip exit area, where exit burr formation (in this case representing one chip, which can be used to define different chip morphologies) is expected to form.

Additionally, white light interferometry can be used to further investigate aspects such as depth of cut and surface roughness.

Based on the SEM images, chip, burr and ploughing typologies can be identified and a correlation with the experimentally-determined cutting force is sought. Burr, ploughing width and channel dimension are to be measured with image analysis software. The most important factor to be considered is results repeatability; if a certain chip morphology is seen to occur on a crystallographic direction, then that morphology should also occur on other positions, at 90°, due to the cutting force pattern four-times repeatability in a single crystal oriented on the (001) plane.

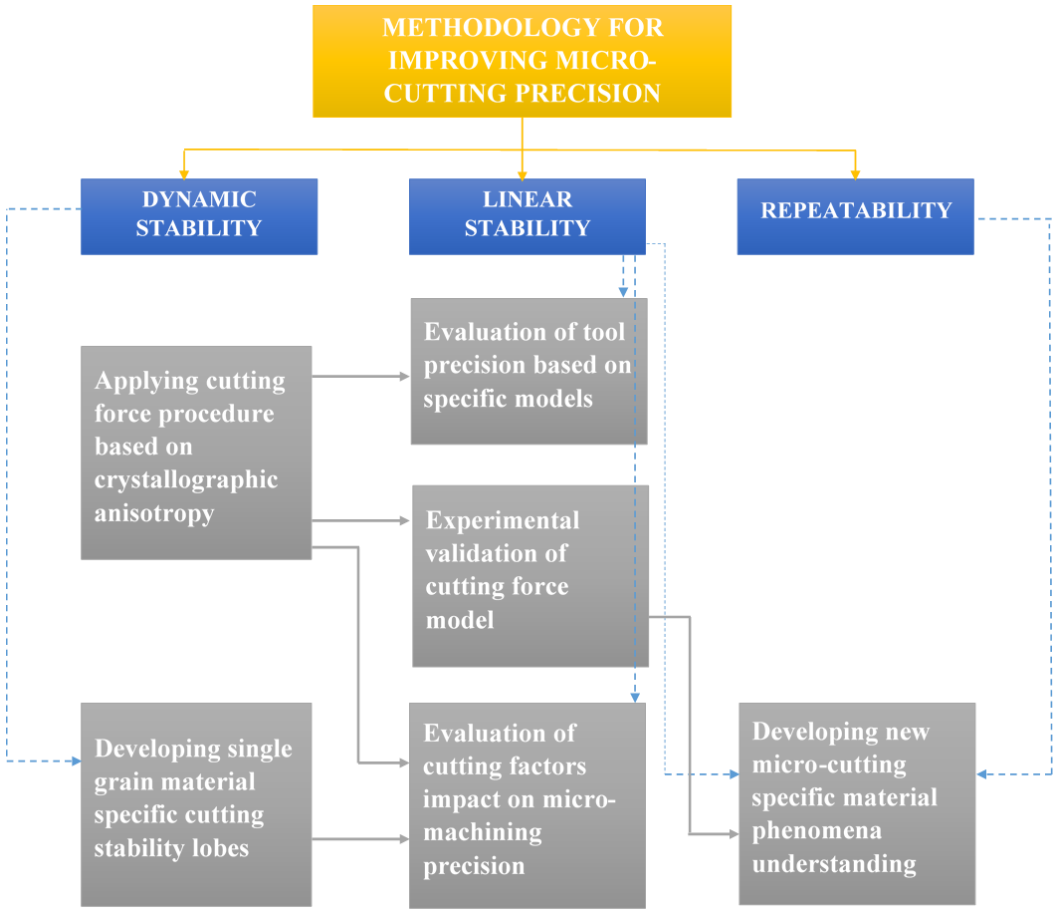


Figure 3.2. Research approach

Based on these assumptions, a correlation can be established between the crystallographic anisotropy and surface quality, which would enable a new and comprehensive understanding of material deformation mechanisms in single crystal materials.

The direction of analytical and experimental investigations (as explained in the objectives above) is represented in a schematic form in Figure 3.2. Furthermore, based on this research approach, it is possible to formulate the chapter outline that would enable meeting the aims and objectives and the current research. This is done in the following section.

3.4. Thesis outline

The layout of the following chapters, based on the research assumptions, is as follows:

Chapter 1

In the introductory chapter, a motivation for the selection of the topic of research, of improving micro-cutting precision, is laid out.

Chapter 2

In the second section, a literature survey is provided in order to define the problems in the chosen area of focus. Micro-cutting, material microstructure, stability and material phenomena are studied. Based on previous work, the knowledge gaps are identified, which helped formulate the aims and objectives of this study.

Chapter 3

Chapter 3 provides a framework for micro-cutting, to ensure detailed objective steps and justification for the chosen methodology. Following these, a plan for the next chapters can be designed.

Chapter 4

Initially, the development of a Matlab program for cutting force analytical modelling is provided. The program is necessary to obtain the cutting force variation due to single crystal material properties, and it will be based on previously-developed models in specialty literature. The machining operation assumed in the analysis is orthogonal

cutting, as it benefits the overall analysis due to the simplicity of tool path and motion in orthogonal cutting. This enables the study to focus on the influence of material microstructure on micro-cutting results. New models for linear stability will be provided for the calculation of tool deflection and slope variation in the cutting of single crystal face-centred cubic (f.c.c.) materials. New cutting force values introduced by tool deflection variation will be assessed. The emphasis in Chapter 4 is to develop the analytical model for cutting forces which will be used in all following chapters, and to take the first steps in assessing micro-cutting stability.

Chapter 5

In Chapter 5, the research focuses on experimental trials aimed at measuring the radial and tangential components of the cutting forces developed during single crystal copper micro-cutting. This is necessary in order to obtain a validation of the cutting force pattern generated on various crystallographic directions, as previously modelled in Chapter 4. Further experimental and analytical work will be possible if the cutting force variation is empirically determined. Due to the low level of cutting forces expected in micro-cutting, the first steps are aimed at gaining a good understanding of the cutting force acquiring equipment. Based on this understanding, an experimental set-up and procedure will be proposed. The same experiment will be undertaken for single crystal and multigrain samples, in order to allow a comparison between cutting force values in single versus multi-grain materials. A comprehensive study on the cutting force development is essential, as validating the force variation supports further investigation into the effect of material microstructure on micro-cutting precision.

Chapter 6

Cutting precision can be improved by dynamic stability analysis, which is developed for regular-scale cutting operations. Cutting stability lobes have been previously developed as a tool for calculating depths of cut at which regenerative vibration, chatter, does not occur. Chapter 6 is aimed at providing new cutting stability lobes which encompass crystallographic anisotropy effects. In classic stability, the cutting force and shear angle are considered constant. The new models will generate improved stability limits based on the variation of cutting force and shear angle developed on a (001) crystal plane. The new models will also enable a comparison between cutting stability lobes that are based on the analytical model in Chapter 4, versus the empirical

findings in Chapter 5. Furthermore, differences introduced by tool geometry in the cutting force and shear angle will be explored. This analysis is aimed at providing a better understanding of dynamic stability in single crystal cutting by studying the individual effects of material microstructure-influenced parameters. This analysis will also enable recommendations for manufacturers by establishing new stability limits.

Chapter 7

An experimental study will lead to a better understanding of the crystallographic anisotropy effects on surface quality and repeatability is proposed. Surface quality is found to be affected by phenomena such as chip formation, burr and ploughing. In the first part, the empirical study focuses on analysing the material deformation phenomena which lead to chip and burr formation. Chip morphologies will be identified based on Klufts' classification (Altintas, 2008) of desirable, acceptable and unacceptable chip morphologies. Main chip typologies will be investigated for different crystallographic directions. Burr and ploughing measurements will be analysed based on their dimensions and occurrence within a 360° workpiece rotation. Lastly, machined features dimensional accuracy will be investigated by acquiring measurements and determining main deformation patterns. Based on these analyses, dimensional accuracy and repeatability will be investigated by correlating the main chip typologies, burr formation patterns and channel dimension variation with the analytical results of the single crystal anisotropic model developed in Chapter 4 and with the experimental findings in Chapter 5.

Chapter 8

Chapter 8 presents the overview of the findings in the thesis and it formulates possible directions for future research.

CHAPTER 4

CRYSTALLOGRAPHIC ANISOTROPY INFLUENCE ON CUTTING FORCES

4.1. Introduction

In micro-cutting, precision is directly related to process repeatability. However, due to micro-level specific factors such as size effect and material anisotropy, micro-cutting parameters vary. A new, improved understanding of how these parameters vary and the level to which they affect precision is required in order to bridge classic multigrain models to micro-level specific ones.

By linking machining knowledge and material properties, it is possible to improve micro-cutting understanding and advance the calculation of micro-specific cutting parameters.

In the current chapter, material microstructure models applied to cutting operations are employed. These predictive methods are based on the fundamental knowledge that within single grain materials, material properties are anisotropic. Properties such as elastic recovery, tensile strength, Young's modulus and shear band formation are grain orientation-dependent.

By employing predictive models for shear band formation, and thus cutting force calculation, it is possible to determine the variation of micro-cutting parameters with material microstructure. While cutting force anisotropic models have been employed

in the past, their impact on cutting precision and micro-cutting parameters has not been studied before. Effectively, all the parameters that depend on the shear angle and cutting force will vary due to their relationship with crystallographic anisotropy. For this reason, it is imperative to determine the deviation of cutting parameters from known multigrain values.

Among all the cutting parameters that are known to affect cutting precision, tool deflection is at the forefront of cutting precision.

In the past, micro-cutting of face-centred cubic (f.c.c.) metals have been modelled by crystallographic anisotropy principles. These known analytical force models are now employed in a Matlab program that further improves knowledge by calculating material microstructure-specific tool deflection and slope.

This study serves to improving parametric prediction in micro-cutting, thus improving process repeatability, and ultimately micro-cutting precision. When an individual material grain is machined, the cutting force is calculated for an arbitrary position of the tool (Boothroyd and Knight, 2006). However, the tool path is not stable in one crystallographic plane due to changes caused by tool deflection. This chapter aims to determine the cutting force variation due to tool deflection in cutting a face-centred cubic metal.

4.2. Method

This study is based on cutting force calculation starting from the theoretical prediction of shear angles in a single crystal.

For this, the maximum work principle was employed. Initially strains and stresses in a single crystal have been defined according to Mendelson (1968). Then, the Bishop-Hill or the maximum work principle was used as described by Reid (1973).

The maximum work value thus identified is employed to predict shear angle formation. Kota's simplified orthogonal cutting model (2011) serves to set up a procedure which is also validated by developing a Matlab program for it.

Lastly, a tool deflection calculation and stability analysis are employed to improve the understanding of micro-cutting of materials, namely single-crystal f.c.c metals.

4.2.1. The maximum work principle

The maximum work principle (Hill, 1950) uses the shear strain to derive the stress state. Based on the yield criterion, out of all the possible stress states the right stress state is the one that maximises the external plastic work.

4.2.1.1.Shear stresses and strains (Mendelson, 1968)

In a coordinate system, the six components of stress of a point are considered. The stresses acting on any plane passing through this point can be calculated with the static equilibrium of an infinitesimal tetrahedron, as shown in Figure 4.1 (Mendelson, 1968, p. 30).

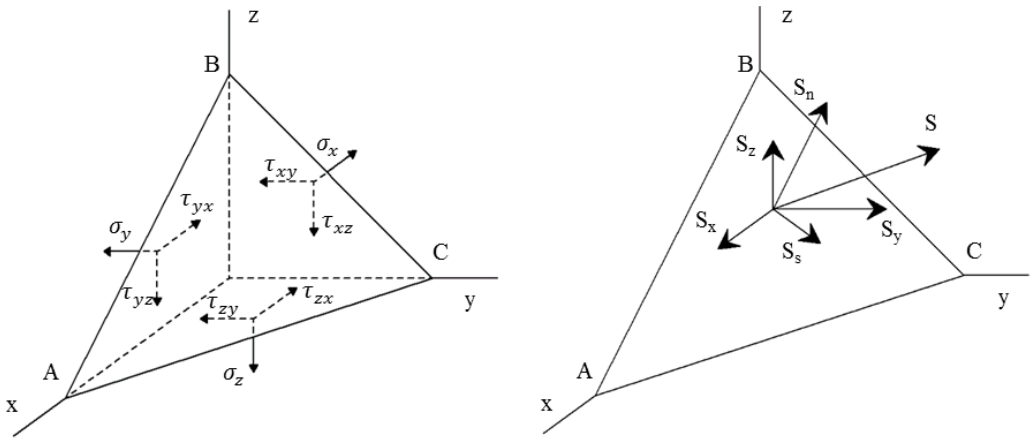


Figure 4.1. Forces on infinitesimal tetrahedron. After Mendelson, 1968

In order to determine the stresses acting on the *ABC* plane, for example, one can consider the direction cosines *l*, *m* and *n* of the normal *ON*.

The equilibrium condition generates

$$S_x = \sigma_x l + \tau_{yx} m + \tau_{zx} n \tag{4.1}$$

and, similarly, S_y and S_z.

The normal stress acting on a plane:

$$S_n = S_x l + S_y m + S_z n \tag{4.2}$$

By substituting the initial stresses in S_n, this becomes:

$$S_n = l^2\sigma_x + m^2\sigma_y + n^2\sigma_z + 2(lm\tau_{xy} + mn\tau_{yz} + nl\tau_{zx}) \quad (4.3)$$

In order to obtain the resultant shear stress S_s acting on this plane

$$S_s^2 = S^2 - S_n^2 = S_x^2 + S_y^2 + S_z^2 - S_n^2 \quad (4.4)$$

If the plane becomes a principal plane, its normal direction becomes the principal direction and the stress $S = S_n$ becomes the principal stress.

The components of S in the *x, y, z* directions are written as:

$$S_x = lS \quad (4.5)$$

$$S_y = mS \quad (4.6)$$

$$S_z = nS \quad (4.7)$$

and thus, the initial stress equations become:

$$l(\sigma_x - S) + m\tau_{yx} + n\tau_{zx} = 0 \quad (4.7)$$

$$l\tau_{xy} + m(\sigma_y - S) + n\tau_{zy} = 0 \quad (4.8)$$

$$l\tau_{xz} + m\tau_{yz} + n(\sigma_z - S) = 0 \quad (4.9)$$

which can be written in tensor notation as:

$$l_i(\sigma_{ij} - \delta_{ij}S) = 0 \quad (4.10)$$

Next, the coordinate axes in the principal directions are considered, which involve null shear stresses. This gives:

$$S_n = l^2\sigma_1 + m^2\sigma_2 + n^2\sigma_3 \quad (4.11)$$

$$S_s^2 = S_1^2 + S_2^2 + S_3^2 - S_n^2 \quad (4.12)$$

If the shear stresses are null, then:

$$S_1^2 = l^2\sigma_1^2 \quad (4.13)$$

$$S_2^2 = m^2\sigma_2^2 \quad (4.14)$$

$$S_3^2 = n^2\sigma_3^2 \quad (4.15)$$

This generates

$$S_s^2 = l^2\sigma_1^2 + m^2\sigma_2^2 + n^2\sigma_3^2 - (l^2\sigma_1 + m^2\sigma_2 + n^2\sigma_3)^2 \quad (4.16)$$

It is known that the shear stress is minimum (zero) on the principal planes.

The maximum shear stress intersects midway the angle between the largest and the smallest principal stresses, and is equivalent to half of the difference between them. The shearing stresses are written as:

$$\tau_1 = \pm\frac{(\sigma_2-\sigma_3)}{2} \tag{4.17}$$

$$\tau_2 = \pm\frac{(\sigma_1-\sigma_3)}{2} \tag{4.18}$$

$$\tau_3 = \pm\frac{(\sigma_1-\sigma_2)}{2} \tag{4.19}$$

The maximum shear strains corresponding are similarly obtained:

$$\gamma_1 = \pm\frac{(\varepsilon_2-\varepsilon_3)}{2} \tag{4.20}$$

$$\gamma_2 = \pm\frac{(\varepsilon_1-\varepsilon_3)}{2} \tag{4.21}$$

$$\gamma_3 = \pm\frac{(\varepsilon_1-\varepsilon_2)}{2} \tag{4.22}$$

4.2.1.2.Determination of plastic strain increments

In the plastic deformation of a monocrystalline material, the strain is based on multiple slip.

The condition for the material to change its shape is malleability, or ductility (Abbaschian, 2010; Honeycombe, 1968; Herzberg, 1996)). A crystal's ductility depends on its capacity of undertaking an arbitrary strain.

Compared to single or duplex slip, multiple slip looks at 3 x 3 systems of strains and stresses. The stress necessary to develop an increment $\delta\varepsilon'_{ij}$ in plastic strain can be written as:

$$\sigma_{ij} = \begin{bmatrix}\sigma_{11} & \sigma_{12} & \sigma_{13}\\ \sigma_{21} & \sigma_{22} & \sigma_{23}\\ \sigma_{31} & \sigma_{32} & \sigma_{33}\end{bmatrix} \tag{4.23}$$

The shear stress tensor τ_{ij} can be defined as a product between the σ_{ij} stress tensor and the direction cosines b_i and n_j:

$$\tau = b_i \cdot \sigma_{ij} \cdot n_j \tag{4.24}$$

Or, written in extended form:

$$\tau = b_1 \cdot \sigma_{11} \cdot n_1 + b_2 \cdot \sigma_{22} \cdot n_2 + b_3 \cdot \sigma_{33} \cdot n_3 + (b_2 \cdot n_3 + b_3 \cdot n_2) \cdot \sigma_{23} +$$

$$(b_1 \cdot n_3 + b_3 \cdot n_1) \cdot \sigma_{13} + (b_2 \cdot n_1 + b_1 \cdot n_2) \cdot \sigma_{12} \tag{4.25}$$

For a set of five independent systems in this matrix form, the notations are:

$$A = \sigma_{22} - \sigma_{33}$$

$$B = \sigma_{33} - \sigma_{11}$$

$$C = \sigma_{11} - \sigma_{22}$$

$$F = \sigma_{23}$$

$$G = \sigma_{13}$$

$$H = \sigma_{12}$$

Which are used in the definition of the five slip systems' shear stress matrix:

$$\begin{pmatrix} \tau^1 \\ \tau^2 \\ \tau^3 \\ \tau^4 \\ \tau^5 \end{pmatrix} = \begin{pmatrix} n_2^1 b_2^1 & n_3^1 b_3^1 & n_2^1 b_3^1 + n_3^1 b_2^1 & n_1^1 b_3^1 + n_3^1 b_1^1 & n_1^1 b_2^1 + n_2^1 b_1^1 \\ n_2^2 b_2^2 & n_3^2 b_3^2 & n_2^2 b_3^2 + n_3^2 b_2^2 & n_1^2 b_3^2 + n_3^2 b_1^2 & n_1^2 b_2^2 + n_2^2 b_1^2 \\ n_2^3 b_2^3 & n_3^3 b_3^3 & n_2^3 b_3^3 + n_3^3 b_2^3 & n_1^3 b_3^3 + n_3^3 b_1^3 & n_1^3 b_2^3 + n_2^3 b_1^3 \\ n_2^4 b_2^4 & n_3^4 b_3^4 & n_2^4 b_3^4 + n_3^4 b_2^4 & n_1^4 b_3^4 + n_3^4 b_1^4 & n_1^4 b_2^4 + n_2^4 b_1^4 \\ n_2^5 b_2^5 & n_3^5 b_3^5 & n_2^5 b_3^5 + n_3^5 b_2^5 & n_1^5 b_3^5 + n_3^5 b_1^5 & n_1^5 b_2^5 + n_2^5 b_1^5 \end{pmatrix} \begin{pmatrix} -C \\ B \\ F \\ G \\ H \end{pmatrix} \tag{4.26}$$

The longitudinal and shear strains ε_{ij} are based on six independent factors (3 on the main diagonal and 3 that are mirrored). In their matrix form, they appear as:

$$\varepsilon_{ij} = \begin{bmatrix} \varepsilon_{11} & \varepsilon_{12} & \varepsilon_{13} \\ \varepsilon_{21} & \varepsilon_{22} & \varepsilon_{23} \\ \varepsilon_{31} & \varepsilon_{32} & \varepsilon_{33} \end{bmatrix} \tag{4.27}$$

Due to the fact that plastic deformation contributes to a very low volume variation, below 0.2%, it can be assumed that the material is incompressible. Thus, the relationship between the longitudinal shear strains can be expressed as:

$$\varepsilon_{11} + \varepsilon_{22} + \varepsilon_{33} = 0 \tag{4.28}$$

This also contributes to the fact that only five out of six components need to be independent for slip to occur.

Moreover, the increment in strain $\delta\varepsilon'_{ij}$ can be written in its matrix form as:

$$\delta\varepsilon'_{ij} = \begin{bmatrix} \delta\varepsilon'_{11} & \delta\varepsilon'_{12} & \delta\varepsilon'_{13} \\ \delta\varepsilon'_{21} & \delta\varepsilon'_{22} & \delta\varepsilon'_{23} \\ \delta\varepsilon'_{31} & \delta\varepsilon'_{32} & \delta\varepsilon'_{33} \end{bmatrix} \tag{4.29}$$

The matrix is symmetrical on its principal diagonal, thus only the longitudinal increments in strain $\delta\varepsilon'_{11}, \delta\varepsilon'_{22}, \delta\varepsilon'_{33}$ and only three shear strains $\delta\varepsilon'_{12}, \delta\varepsilon'_{23}, \delta\varepsilon'_{13}$ are considered.

Since slip causes no volume change, then:

$$\delta\varepsilon'_{11} + \delta\varepsilon'_{22} + \delta\varepsilon'_{33} = 0 \tag{4.30}$$

The strain increment relative to the cube axes is obtained with the aid of the slip system cosines:

$$\delta\varepsilon_{ij} = a_{ki} \cdot a_{lj} \cdot \delta\varepsilon'_{kl} \tag{4.31}$$

4.2.1.3.Plastic work calculation

When the single crystal is loaded, it undergoes strain. The energy necessary to produce a certain amount of strain is indicated by the increment of work per unit volume (Mendelson, 1982):

$$dW = \tau_{ij} d\varepsilon_{ij} \tag{4.32}$$

In extended work, this is written as:

$$\delta W_p = \sigma_{11}\delta\varepsilon_{11} + \sigma_{22}\delta\varepsilon_{22} + \sigma_{33}\delta\varepsilon_{33} + 2\sigma_{12}\delta\varepsilon_{12} + 2\sigma_{13}\delta\varepsilon_{13} + 2\sigma_{23}\delta\varepsilon_{23} \tag{4.33}$$

The plastic work can also be written as a factor of the five independent systems:

$$W_p = -B\varepsilon_{11} + A\varepsilon_{22} + 2H\varepsilon_{12} + 2G\varepsilon_{13} + 2F\varepsilon_{23} \tag{4.34}$$

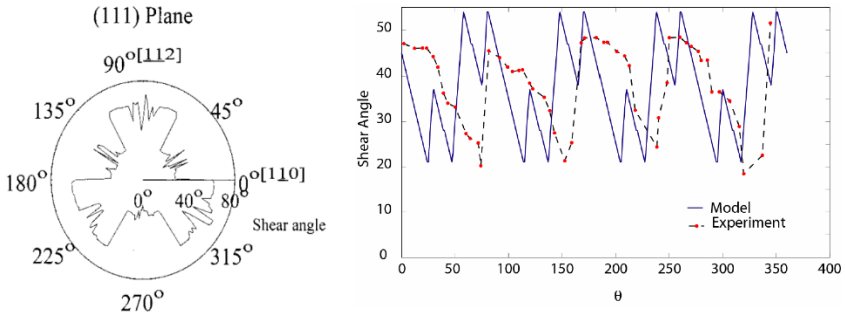
4.2.2. Shear angle calculation

The steps taken in order to calculate the shear angle depend on the methods used by various authors.

Generally, the shear angle ϕ is selected as the one that achieves the maximum work done.

In Kota's simplified orthogonal cutting procedure (2008), the possible 56 vertices achieved though the Bishop-Hill method are then implemented into a sum of plastic and friction work. The shear angle selected is the one that achieves the maximum total work done.

In Kota's further studies (2011), the shear angle procedure includes as well a lattice rotation and strain-rate dependency.



a. b.

Figure 4.2. Comparison between shear angle results for a 360° workpiece rotation, obtained by applying different methods: a. model with strain-rate plasticity, image from Figure 3b (Cheung et al., 2002); b. orthogonal cutting model, image from Figure 8 (Kota and Burak Ozdoganlar, 2008)

Other authors, such as Lee and Cheung (1993, 2002), only consider the plastic work. When obtaining the same work for more than one possible shear angle, they apply texture softening factors and consider the lattice rotation. This procedure is more complex and has an irregular profile, with big peak differences for neighbouring positions, when looking at a workpiece rotation.

However theoretically correct, experimental studies clearly disprove that such high peak differences between successive workpiece orientations can occur.

This is illustrated in the comparison between the shear angle evolution obtained by Lee (2002) and by Kota (2008) in Figure 4.2. In Figure 4.2a, one may see the profile irregularity in shear angle formation. In Figure 4.2b, the shear angle results are compared with an experimental study conducted by Cohen (1982). The red line indicates the empirically observed shear angles, and a less abrupt shear angle evolution.

For this reason, Kota's model will be preferred to other crystallographic anisotropy models from the specialty literature.

4.2.2.1. Shear angle calculation steps according to Kota's simplified orthogonal model

Orthogonal cutting assumptions (Saipaven, 2014):

- The tool is perfectly sharp and there is no contact along the clearance face.
- The cutting edge of the tool remains normal to the direction of tool feed or work feed.
- The direction of the chip flow velocity is normal to the cutting edge of the tool.
- The cutting edge is a straight line, extending perpendicular to the direction of motion and generates a plane surface as the work moves past it.
- The chip does not flow to either side.
- The depth of cut is constant.
- Width of the tool is greater than that of workpiece.
- The work moves relative to the tool with uniform velocity.
- A continuous chip is produced with no built-up edge.

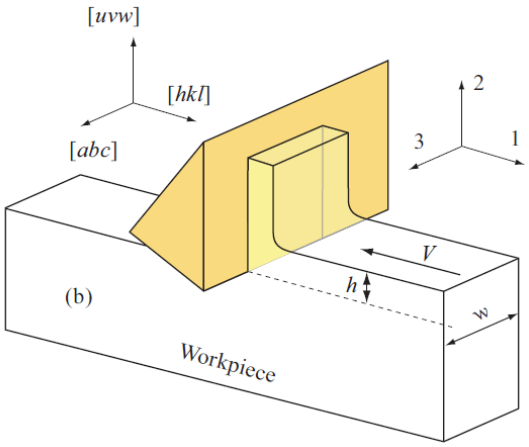


Figure 4.3. Orthogonal cutting processes coordinate system. From Kota (2011): Figure 2.1b, p.14

An orthogonal cutting process, for example planning, is illustrated in Figure 4.3. The three panes that are of interest are described according to: the direction of the cutting process, which is performed by the workpiece being pushed in the direction of the cutting tool, which is stationary; the plane normal to it in the vertical direction; and the last plane orthogonal to these two, which represents the plane from which the cutting process is analysed. As such, the three planes illustrated in Figure 4.3 are named below.

A cutting tool is moving in the cutting direction (*hkl*). The cutting plane is normal on the direction (*uvw*), and (*abc*) represents the observation direction.

In this orthogonal cutting system, the engineering shear strain γ is calculated based on the shear angle ϕ and on the rake angle α :

$$\gamma = \frac{\cos(\alpha)}{\sin(\phi)\cos(\phi-\alpha)} \tag{4.35}$$

The shear strain γ contributes to calculating the displacement gradient in the shear plane coordinates E_s:

$$E_s = d\gamma \begin{bmatrix} 0 & 1 & 0 \\ 0 & 0 & 0 \\ 0 & 0 & 0 \end{bmatrix} \tag{4.36}$$

Subsequently, the displacement gradient E_s and its transpose are used to determine the strain tensor ϵ_s:

$$\epsilon_s = \frac{E_s+E_s^T}{2} = \frac{d\gamma}{2} \begin{bmatrix} 0 & 1 & 0 \\ 1 & 0 & 0 \\ 0 & 0 & 0 \end{bmatrix} \tag{4.37}$$

According to Kota (2011), the symmetric part of the displacement gradient, namely the strain tensor ϵ_s, can be calculated by using a coordinate transformation matrix T_ϕ.

The shear angle ϕ, representing the shear band inclination against the cutting direction, is used to define the coordinate transformation matrix T_ϕ:

$$T_\phi = \begin{bmatrix} cos(\phi) & -sin(\phi) & 0 \\ sin(\phi) & cos(\phi) & 0 \\ 0 & 0 & 1 \end{bmatrix} \tag{4.38}$$

The strain tensor ϵ_w *in the workpiece coordinate system* is given by:

$$\epsilon_w = T_\phi \epsilon_s T_\phi^T = \frac{d\gamma}{2} \begin{bmatrix} -\sin(2\phi) & cos(2\phi) & 0 \\ cos(2\phi) & sin(2\phi) & 0 \\ 0 & 0 & 0 \end{bmatrix} \tag{4.39}$$

4.2.2.2. Shear angle calculation steps for turning operation

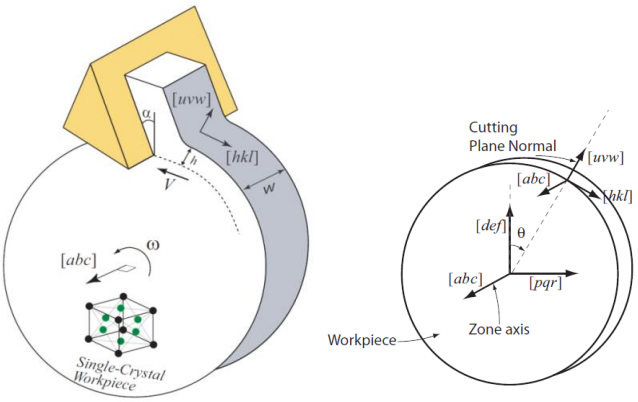


Figure 4.4. Turning cutting scheme. From Kota (2011): Figure 1.6a, p. 8 and Figure 2.2, p. 16

Oblique cutting assumptions:

- The cutting edge of the tool always remains inclined at an acute angle to the direction of tool feed or work feed.
- The direction of the chip flow velocity is at an angle β with the normal to the cutting edge of the tool. The angle is known as chip flow angle.
- The cutting edge of the tool is inclined at an angle *i* with the normal to the direction of work feed or tool feed i.e., the velocity *Vc*.
- Three mutually perpendicular components of cutting forces act at the cutting edge of the tool.
- The cutting edge may or may not be longer than the width of the cut.

Conventionally, turning cannot be assumed as an orthogonal cutting process.

However, the turning cutting scheme can be approximated as a succession of orthogonal 'cutting steps' taken as increments. Each 'cutting step' represents a rotation of the workpiece coordinate system against the workpiece rotation axis.

The cutting tool is placed on the outside of the cylindrical test piece, as in Figure 4.4. The cutting system coordinates (*uvw*), (*hkl*) and (*abc*) remain similar as in the orthogonal cutting process. The crystal coordinates (*abc*), (*pqr*) and (*def*) remain also the same.

To implement the workpiece rotation, the workpiece coordinates change with an angle increment for the orientation angle θ. The following steps show how the orientation angle θ is introduced in the system.

The elements of the strain tensor in the crystallographic coordinate system ϵ_{ij} can be calculated as a product between the workpiece coordinate system ϵ_w and the coordinate transformation matrix *P* corresponding to the workpiece rotation:

$$\epsilon = P\epsilon_w P^T \tag{4.40}$$

Here, the coordinate transformation matrix *P* is determined from the orientation of current coordinate system with respect to the crystal coordinates:

$$P = \begin{bmatrix} h & u & a \\ k & v & b \\ l & w & c \end{bmatrix} \tag{4.41}$$

where

$$P = RT_\phi \tag{4.42}$$

and

$$R = \begin{bmatrix} p & d & a \\ q & e & b \\ r & f & c \end{bmatrix} \tag{4.42}$$

The orientation angle θ represents the increment with which the test piece rotates during turning, and can take values from 0° (no rotation) to 360°. The coordinate transformation matrix for the orientation angles is:

$$T_\theta = \begin{bmatrix} cos(\theta) & sin(\theta) & 0 \\ -sin(\theta) & cos(\theta) & 0 \\ 0 & 0 & 1 \end{bmatrix} \tag{4.43}$$

A new strain tensor ϵ_{ij} including the test piece rotation can be written as:

$$\epsilon = RT\epsilon_s T^T R^T \tag{4.44}$$

The combination between the coordinate change matrices T_ϕ and T_θ gives:

$$T = T_\theta T_\phi = \begin{bmatrix} cos(\phi - \theta) & -sin(\phi - \theta) & 0 \\ sin(\phi - \theta) & cos(\phi - \theta) & 0 \\ 0 & 0 & 1 \end{bmatrix} \tag{4.45}$$

Next, the maximum work W_p is determined based on the Bishop-Hill principle. The values for all the 56 possible work values W_p are computed and the maximum value among the array is calculated:

$$W_p = \int dW_p = \int_0^{\gamma} g(\phi - \theta) d\gamma \tag{4.46}$$

where $g(\phi - \theta)$ is the function for maximising the 56 possible vertices.

The next step is applying the maximum work principle across a range of possible shear angle values.

The shear angle ϕ can take values from 0° to 90°, minus the friction and rake angles:

$$\phi = 90° - (\beta - \alpha) \tag{4.47}$$

A number of $90° - (\beta - \alpha)$ values are obtained for the work W_p.

Subsequent steps include summing the plastic work W_p with the friction work W_f.

The shear angle ϕ is selected as the one that achieves the maximum total work done.

4.2.3. Cutting force calculation in an orthogonal process

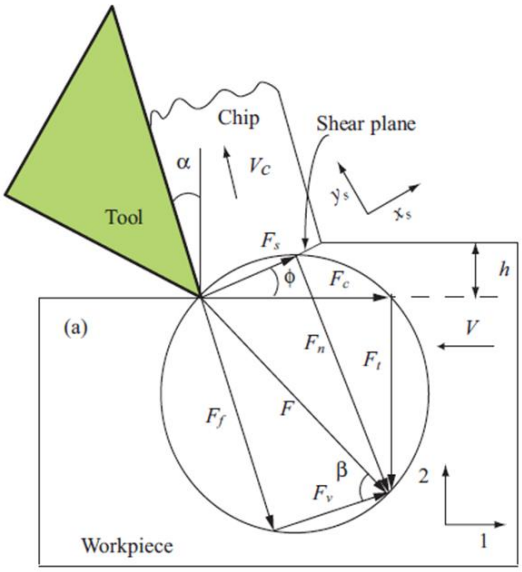


Figure 4.5. Cutting forces in an orthogonal cutting scheme. From Kota (2011): Figure 2.1a, p.14

The cutting forces are illustrated in Figure 4.5. The plastic power is calculated as:

$$\dot{W}_p = (hwV)W_p \tag{4.48}$$

The shearing power is then calculated as a product between the plastic work and the volumetric flow rate:

$$\dot{W}_p = F_s \cdot V_s \tag{4.49}$$

Then, the shear velocity V_s becomes:

$$V_s = \frac{V \cdot \cos(\alpha)}{\cos(\phi - \alpha)} \tag{4.50}$$

With which the shearing force F_s can be calculated:

$$F_s = \frac{\dot{W}_p}{V_s} \tag{4.51}$$

And also the thrust force F_f:

$$F_f = \frac{F_s \cdot \sin(\beta - \alpha)}{\cos(\phi + \beta - \alpha)} \tag{4.52}$$

And next the horizontal cutting force F_t can be determined:

$$F_t = \frac{F_s \cdot \cos(\beta - \alpha)}{\cos(\phi + \beta - \alpha)} \tag{4.53}$$

The friction force F_u is determined then based on the horizontal cutting force:

$$F_u = F_t \cdot \sin(\alpha) + F_f \cdot \cos(\alpha) \tag{4.54}$$

4.2.4. Matlab program procedure

The steps presented below are followed in Matlab to obtain shear angles, cutting forces and cutting energies.

1) Calculate the work necessary for plastic deformation
    a. Calculate crystal strain tensor ε_c based on crystal plane and crystal direction.
    b. Determine the orientation modification matrix based on the shear angle ϕ.
    c. Calculate workpiece strain tensor ε_w.

d. Calculate the plastic work W_p based on the workpiece strain tensorε_w and the maximum work principle (Bishop-Hill).

2) Calculate the shear angle
    a. Calculate the total work W_t as a sum of the plastic and friction work for the entire shear angles array.
    b. The angle which minimises the total work is the shear angle ϕ.
3) Calculate the cutting force
    a. Calculate the thrust force based on the set of shear angles identified.
    b. Calculate the friction force based on the set of shear angles identified.
4) Calculate the horizontal cutting force based on the set of shear angles identified
5) The next steps in the program will correspond to the changes analysed in the cutting force models; the influence of tool deflection, slope and stability analysis are investigated in the next section.

4.3. Results & discussion

The cutting force models reveal how different the cutting force evolution is during one single crystal workpiece rotation. This has been verified by previous studies (Kota 2008, 2011; Lee and Cheung 1993, 2002).

What is different in this study is looking at how precision is affected by the cutting force variation due to crystallographic anisotropy. Moreover, looking at how single crystal cutting can be integrated in a cutting stability analysis. Also, a tool deflection model based on cutting force variation is developed.

4.3.1. Cutting forces in turning

Kota (2011) has investigated the cutting forces necessary to cut single crystals at different orientations. He focused on the stereographic triangle (001) – (111) – (101) and has analysed 8 different crystallographic planes as workpiece orientations.
These are as follows: (001), (101), (102), (212), (213), (216), (111) and (112). Their projection on the stereographic map is presented in Figure 4.6.:

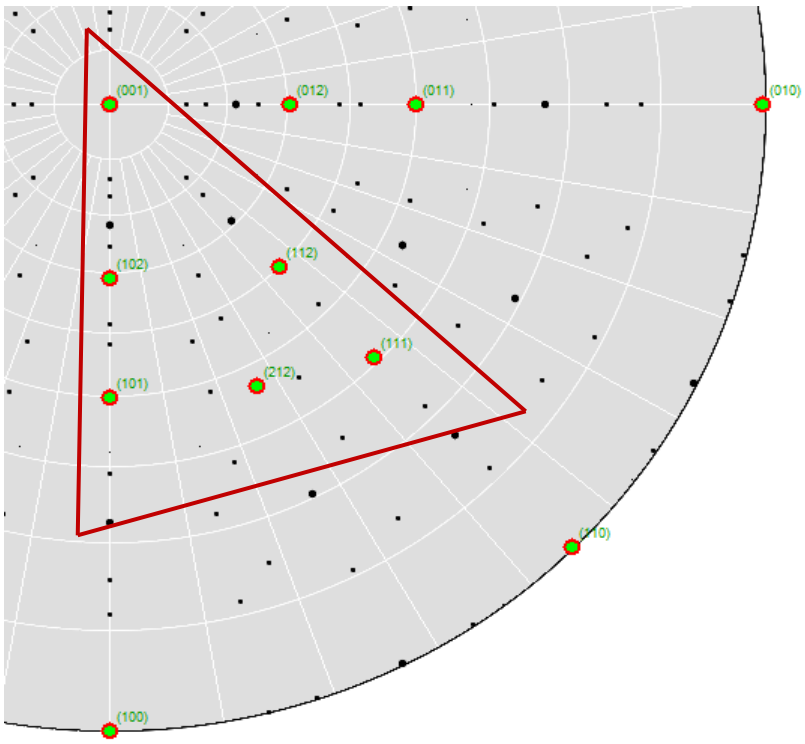


Figure 4.6. Stereographic map of crystallographic orientation with (001) as principal axis

Kota proposed a simplified orthogonal cutting model to calculate the cutting forces, shear angles and cutting energies in the 8 directions considered.

The following cutting parameters have been used by Kota and are also adopted in the current calculation: cutting velocity of 0.44 mm/s, uncut chip thickness of 0.11 mm, tool rake angle of 40°, tool friction angle of 50°, and a width of workpiece (in this case, chip width) of 1.46 mm.

In Chapter 2, micro-cutting was defined based on machined geometrical features as cutting dimensions varying between 1 and 100 μm. The depth of cut adopted by Kota, 0.11 mm, falls just over that threshold. However, since the author focused his studies on crystallographic anisotropy investigations of mechanical micro-machining, and the difference represents only 10%, his depth of cut is adopted throughout this chapter. This enables the application of any subsequent force, slope and deflection considerations to the cutting system assumed by both Kota and Cohen. Most importantly, Kota's analysis considered the cutting energies in the first phase, and the cutting energy represents the cutting force divided by the width and thickness of the

chip. This makes the following cutting energy consideration independent of the size of the chip.

Moreover, the focus of this chapter is the difference introduced by crystallographic effects in a single grain machined material. It can be observed that the same observations can be assumed for a general single crystal cutting force model, as the cutting force evolution is independent on the 100 µm micro-cutting threshold. As such, it can be stated that the focus of the study in the current chapter is the difference in cutting forces introduced by the size effects.

By using the previously-described Matlab program, the evolution of the cutting energies is calculated in the following section.

Observation

It was found, while calculating the cutting forces, that 1 out the 8 directions considered did not match Kota's results. The graph for (216) had a phase difference of 32°when compared to Kota's plot. The exact vector combinations specified by Kota were $[14\bar{1}]$ as cutting direction and $[216]$ as a zone axis. However, multiple iterations have identified that Kota's plot matched the combination between the $[216]$ zone axis and the $[\bar{1}\bar{4}1]$ cutting directions. This crystallographic direction is geometrically opposite on the central rotation axis$[001]$. The angles between $[14\bar{1}]$ and$[001]$, and between $[\bar{1}\bar{4}1]$ and$[001]$ are 16° each. This sums as the 32° difference observed in the plots obtain by the Matlab program and Kota's graph for cutting on the $[216]$ zone axis.

4.3.1.1. Cutting energies

Data was measured on Kota's graphs with the WebPlotDigitizer software. This data is represented with an orange line in the plots below. The data obtain with the Matlab program is represented with a blue line.

With the modification mentioned for the $[216]$ zone axis, all 8 graphs match Kota's results (Figure 4.7.).

This validates the Matlab program for cutting forces.

From this point on, the program serves to improve the understanding of cutting forces modification in order to improve micro-cutting precision.

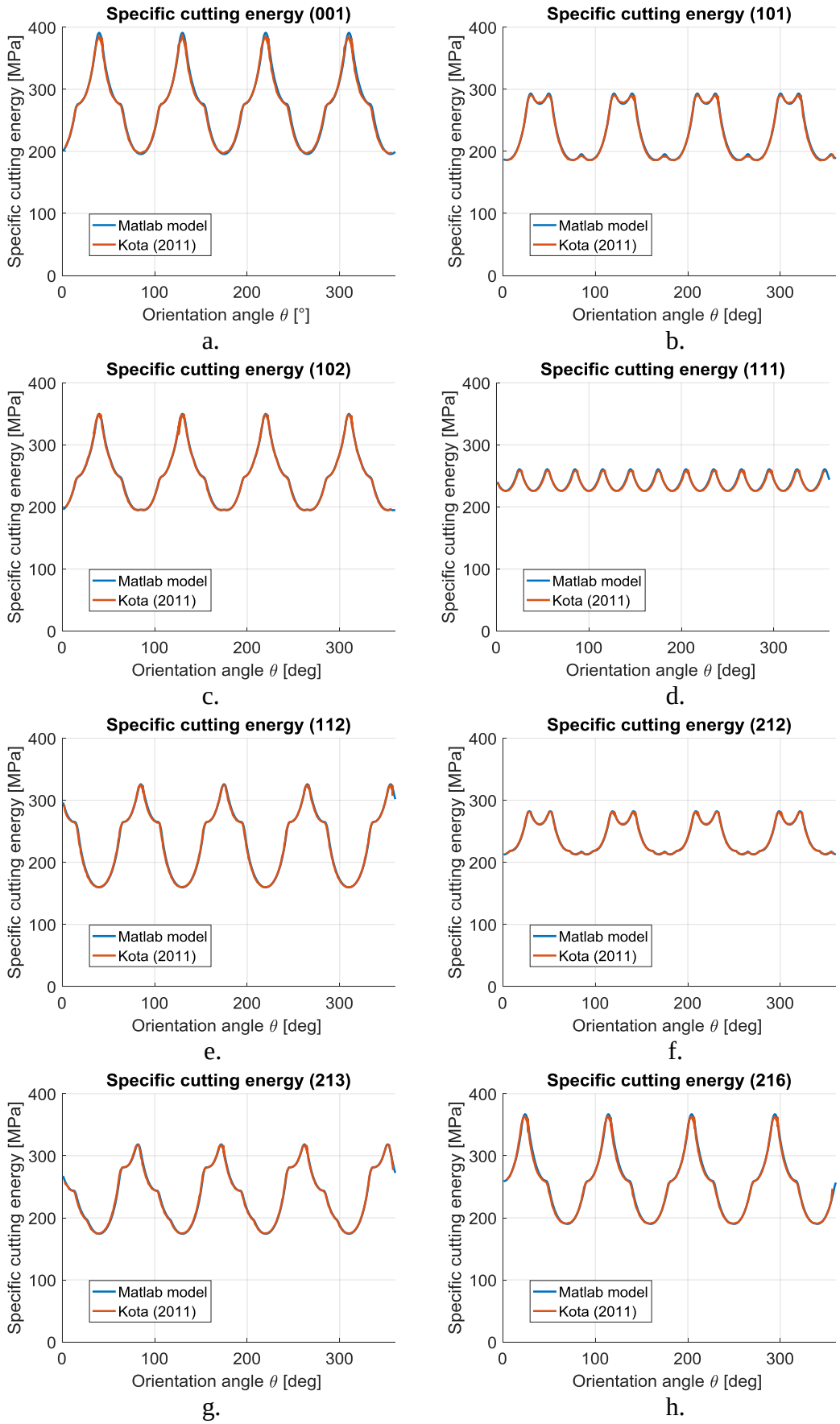


Figure 4.7. Matlab program validation of Kota's results for different crystallographic orientations: a. (001); b. (101); c. (102); d. (111); e. (112); f. (212); g. (213); h. (216)

Unlike the specific cutting energy, however, the magnitude of the cutting forces does depend on the uncut chip thickness and the chip width. Below, the cutting force profiles for the (001) and the (101) planes are computed in Figure 4.8.

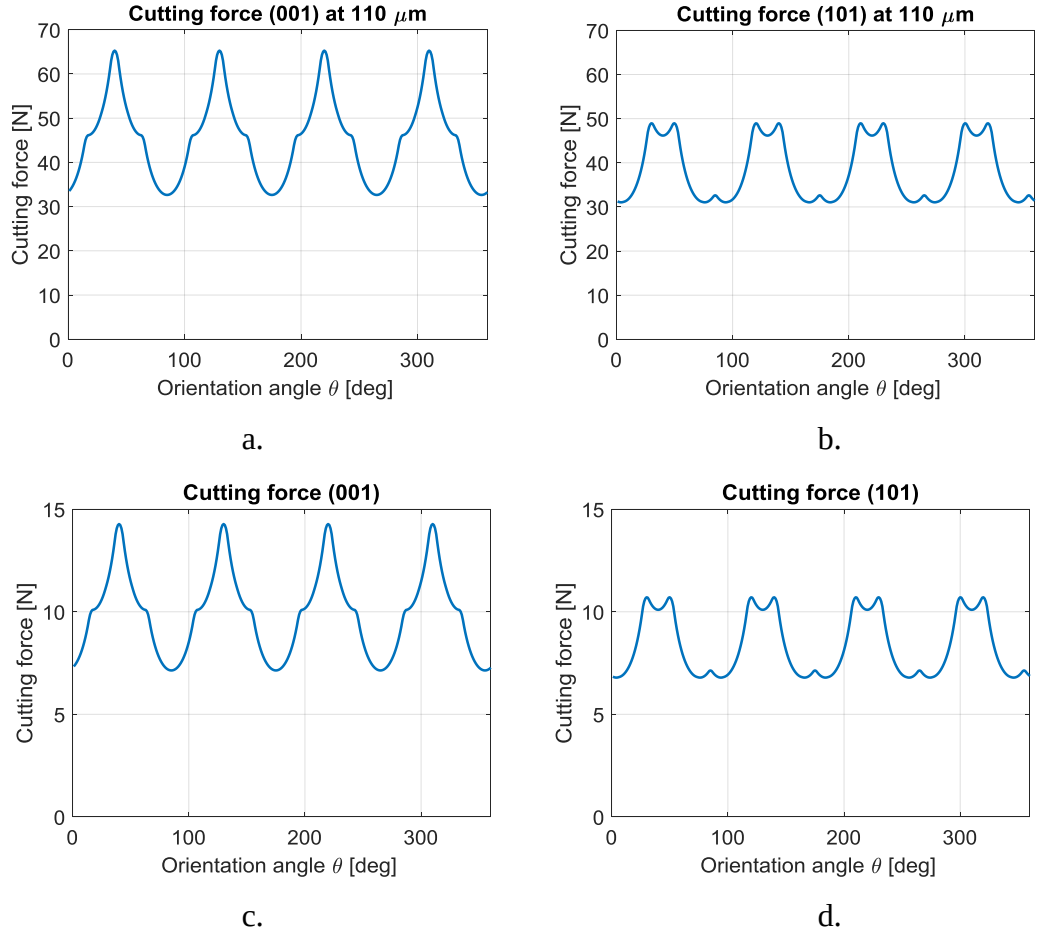


Figure 4.8. Cutting force profiles: a. (001) plane and Kota's 110 µm depth of cut; b. (101) plane and Kota's 110 µm depth of cut; c. (001) plane and 25 µm depth of cut; d. (101) plane and 25 µm depth of cut

By using Kota's cutting parameters, the results are illustrated in Figure 4.8.a. and b. Results for 25 µm depth of cut are plotted in Figure 4.8.c. and d.

4.3.1.2. Cutting force model contributions

Effects such as tool deflection affect the crystallographic plane that the tool path interacts with. More so, tool deflection causes a chip thickness difference that alters the cutting force values.

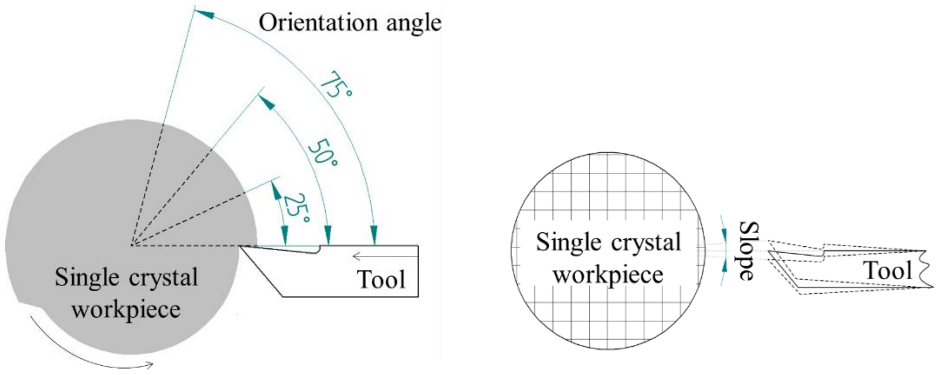
Secondly, tool deflection amplitudes may offer more information in the overall cutting force evolution when faced with the extremes of tool positions (constant chip thickness difference). This is the first step in assessing the linear model. The next step will be to move from the linear model to dynamic one, when chip thickness varies with each workpiece rotation and the uncut chip thickness is strictly dependent on the previous uncut chip thickness.

Thirdly, tool deflection causes a slope in tool positioning. This can be represented as an angular difference between the tool positioned on a horizontal orientation and the effects on cutting forces can be predicted.

The effects on a 360° workpiece rotation are considered in a linear model. Dynamic effects have to be considered, such as the cutting force evolution for more than one rotation. These results will contribute to new cutting stability models for single grain cutting.

4.3.2. Slope in turning

The single crystal cutting scheme is presented below:



a. b.

Figure 4.9. Single crystal cutting scheme: a. turning, indication the orientation angle; b. slope effect in turning

One workpiece rotation is considered for this step of the analysis. The effects of tool deflection and slope on the crystallographic orientation with respect to the initial crystallographic position are considered. The model is based on a succession of steps according to the incremental angle modification.

The next step will be to make the model more realistic and look at the dynamic effects on the slope and tool deflection.

The slope is based on a cantilever being subjected to a concentrated load at the end of the tool. The tool geometry is simplified to represent a prismatic section bar. The load corresponds to the cutting force obtained from the crystallographic anisotropy model.

$$\Theta = tan^{-1}\left(\frac{F_c \cdot length^2}{2 \cdot E \cdot I}\right) \tag{4.55}$$

where Θ is the slope, F_c represents the variable force, $length$ is the length of the tool, E is Young's modulus and I represents the second moment of area.

4.3.2.1. Linear model

Slope was calculated for the cutting forces obtained by Kota, with his study's cutting parameters. Additionally, the tool considered had an 8 mm x 8 mm square section, 80 mm length, with 60 mm in console and 20 mm overhang. Initial results indicate that the slope evolution corresponds to the cutting force evolution, as expected. The calculated values indicate small angular differences.

The largest amplitude between slope angles is determined for the (001) zone axis, between 1.371e^{-3}° and 2.739e^{-3}°.

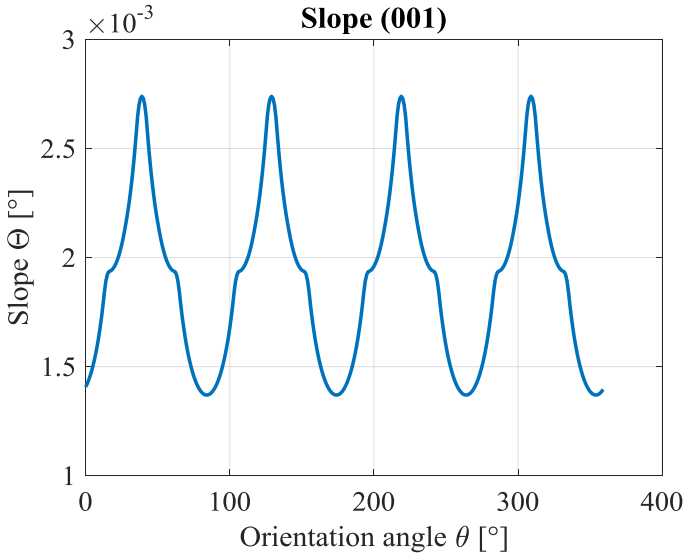


Figure 4.10. Slope for the (001) zone axis

The smallest amplitude between slope angles is determined for the (111) zone axis, between 1.582e^{-3}° and 1.826e^{-3}°. The results are presented in Figure 4.10 and Figure 4.11.

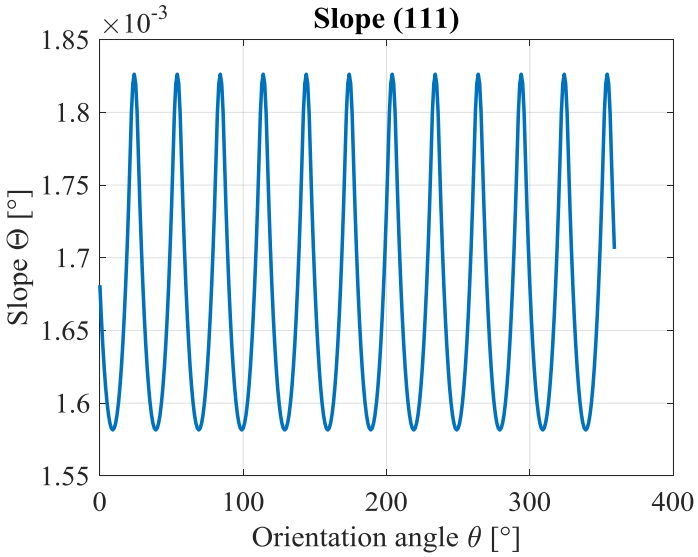


Figure 4.11. Slope for the (111) zone axis

The slopes calculated indicate very small angles. These are expected to show almost no difference in the cutting force model.

4.3.2.2. Slope effect on cutting forces evolution

After calculating the slope, the orientation angle θ is re-calculated by subtracting the slope value:

$$\theta_f = \theta_i - \Theta \tag{4.56}$$

where θ_f represents the re-calculated orientation angle and θ_i the initial orientation angle.

The results for the (001) and (111) zone axes are plotted in Figure 4.12.

As anticipated, the slope introduces a very low difference in the cutting force value, between 0.002° and 0.003°. This section justifies the decision to exclude slope considerations in situations which include cutting force models based on crystallographic anisotropy formulation. This is useful when understanding which parameters can affect the cutting force calculation, and which can be overlooked due to small values.

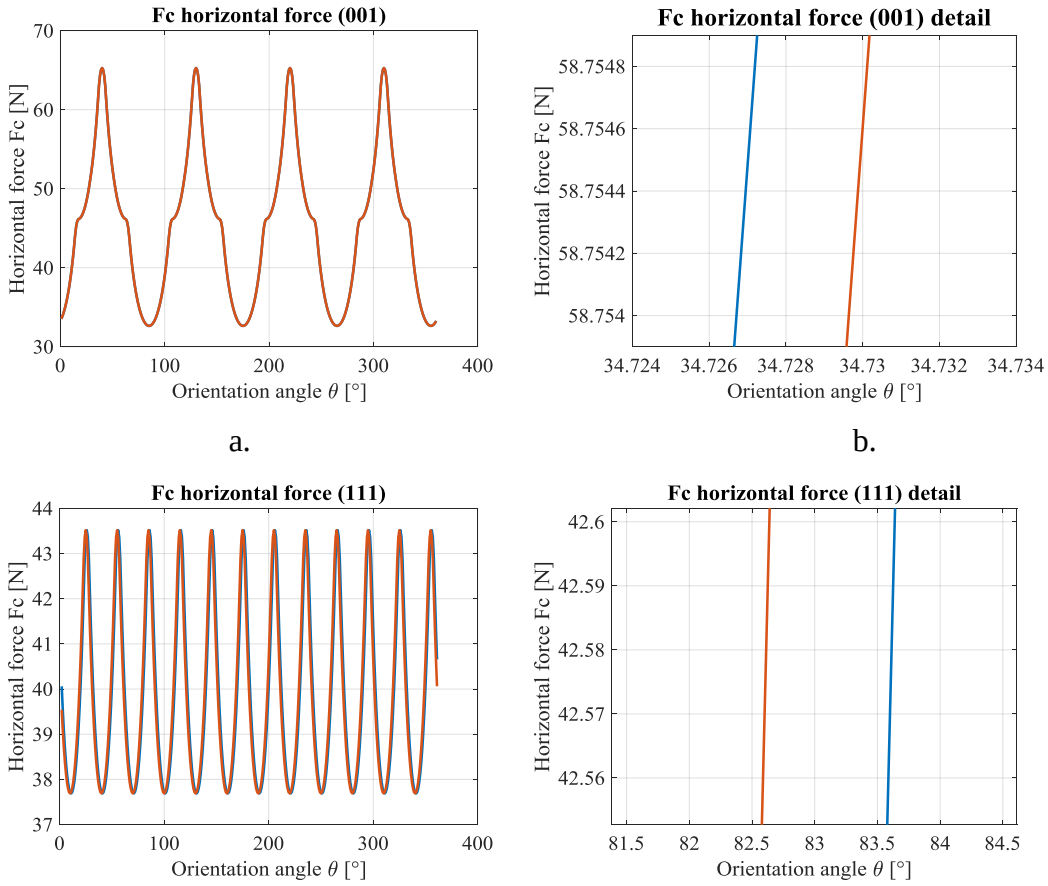


Figure 4.12. Cutting force calculated considering the slope difference. a. (001); b. (001) detail; c. (111); d. (111) detail

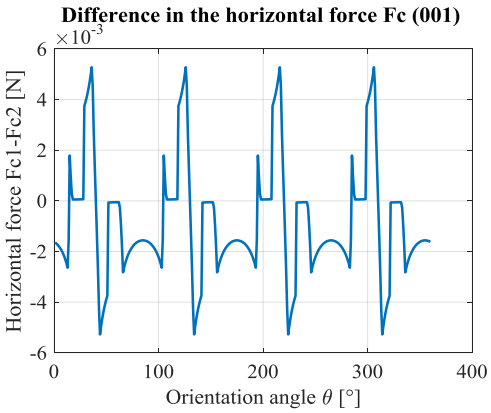
4.3.2.3. Cutting force differences analysis

The difference in the horizontal cutting forces is investigated further on. Despite small slope values, it is of interest to understand how the cutting force difference evolves. The results are shown in Figure 4.13.

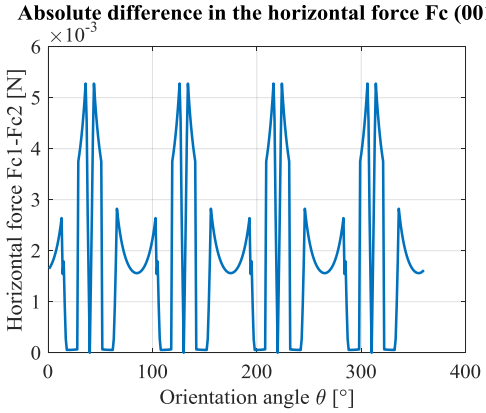
However, a better understanding of the physical model may be necessary. The calculated slope cannot directly affect the current orientation angle θ_i, but the next orientation θ_{i+1}.

For this reason, the orientation angle θ_f is further investigated based on the equation:

$$\theta_f = \theta_{i-1} - \Theta \tag{4.57}$$



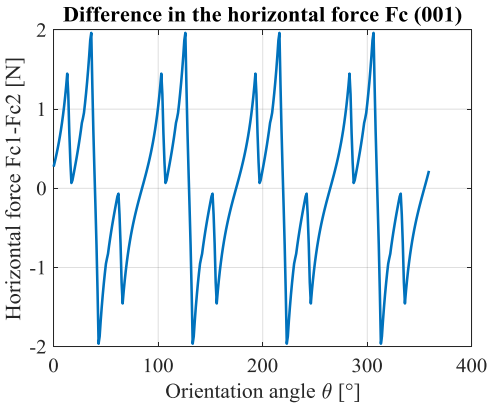
a.



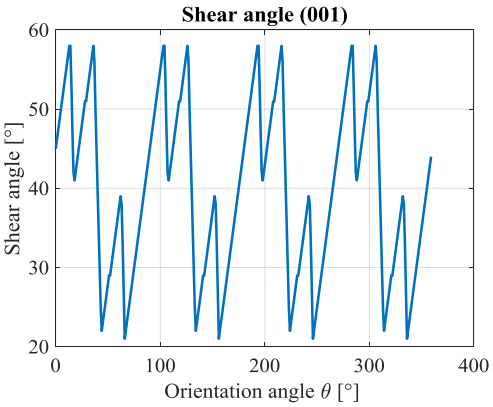
b.

Figure 4.13. Difference in absolute values for the cutting forces obtained on (001) zone axis. a. real values; b. absolute values

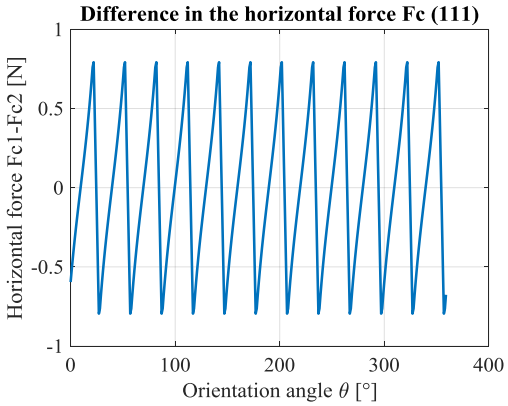
This new formula gives a difference of approximately 1° in the results. The new plot for the cutting force difference presents an evolution similar to that of the calculated shear angles (Figure 4.14).



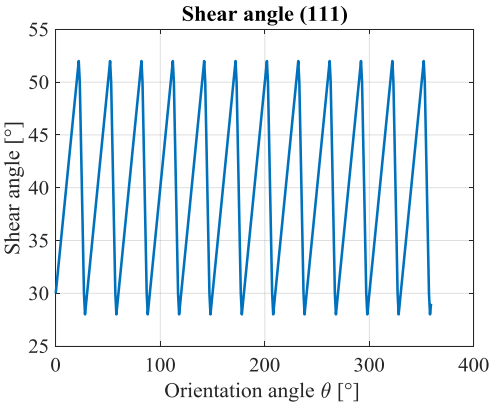
a.



b.



c.



d.

Figure 4.14. Horizontal cutting forces differences and shear angle profile association: a. Difference in the horizontal cutting forces (001); b. Shear angles (001); c. Difference in the horizontal cutting forces (111); d. Shear angles (111)

These results feed more into the step of going from a static to a dynamic approach, rather than on the influence of the slope.
This effect between the current cutting force and the one necessary to cut the previous crystal orientation will be further investigated in section 4.3.3.

4.3.3. Tool deflection in turning

The tool deflection model is based on a cantilever being subjected to a concentrated load at the end of the tool. The tool geometry is simplified to represent a prismatic section bar, just as in the previous slope analysis. The load corresponds to the cutting force obtained from the crystallographic anisotropy model, with the same cutting parameters as in the slope calculation.

The δ deflection at the tip of the tool is calculated based on the equation:

$$\delta = \delta_{max} = \frac{F_c \cdot length^3}{3 \cdot E \cdot I} \tag{4.58}$$

and according to the following turning scheme:

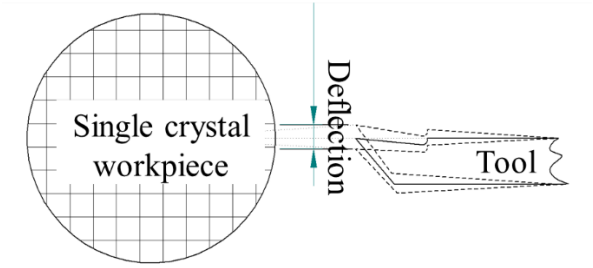


Figure 4.15. Tool deflection effect in turning

4.3.3.1. Linear model

The analysis follows the same steps as the slope analysis. Tool deflection is calculated for the entire rotation of the workpiece. Then, it is plotted for all the 8 crystallographic orientations considered (Figure 4.16). Two depths of cut are plotted: the first two graphs (Figure 4.16.a. and b.) illustrate the analytical results using Kota's cutting

parameters, and the latter (Figure 4.16.c. and d.) are the tool deflections at a 25 µm chip thickness.

The values obtained indicate the same evolution as the cutting forces, as expected.

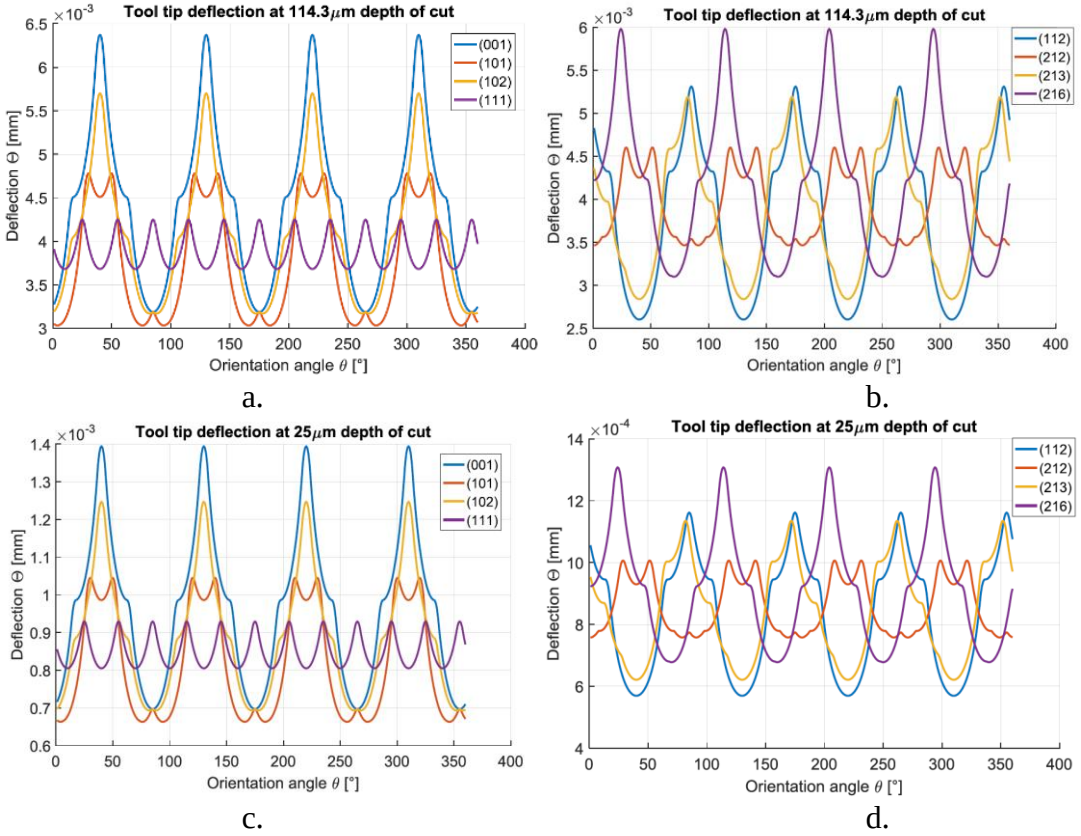


Figure 4.16. Tool deflections calculated for different crystallographic orientations: a. (001) - (111) at 114.3 µm depth of cut; b. (112) - (216) at 114.3 µm depth of cut; c. (001) - (111) at 25 µm depth of cut; d. (112) - (216) at 25 µm depth of cut.

The tool tip deflection is important in determining the tool path. As shown in Figure 4.17, this leads to different results and can affect the workpiece profile in a turning operation.

For a chip thickness of 114.3 µm, the tool deflections vary between 3.187 and 6.375 µm. For a chip thickness of 25 µm, they vary between 0.7 µm and 1.4 µm.

Once again, the highest amplitude is found on the (001) crystallographic plane, and the smallest on the (111) plane.

The minimum and maximum indicate change in chip thickness of 2.78% and 5.57%, respectively.

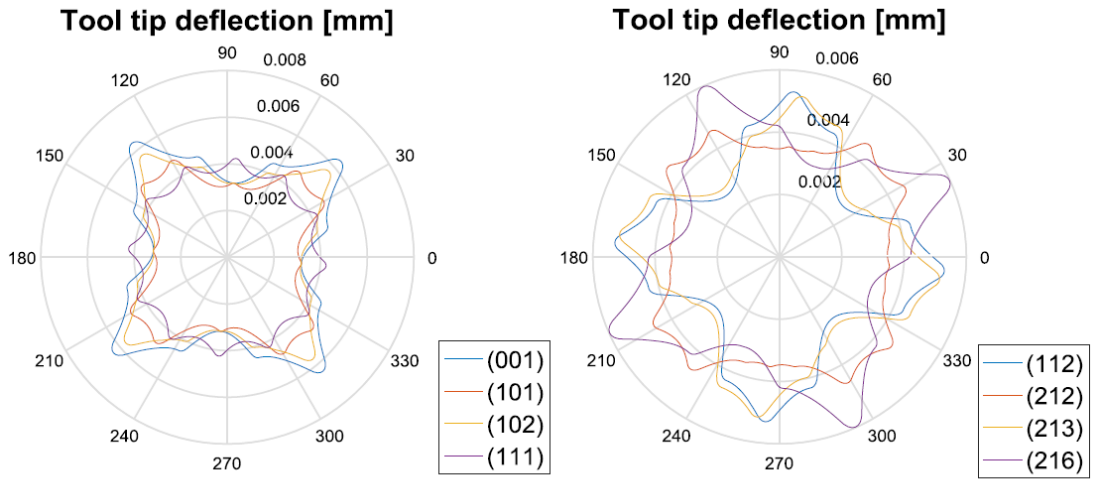


Figure 4.17. Comparison of tool tip deflections

4.3.3.2. Tool deflection effect on turning cutting forces

The tool deflection is calculated for each incremental step of orientation angles of the single crystal workpiece.

The difference is made by subtracting the δ tool deflection from the nominal chip thickness. This gives an insight into the areas (orientations) more affected by deflection.

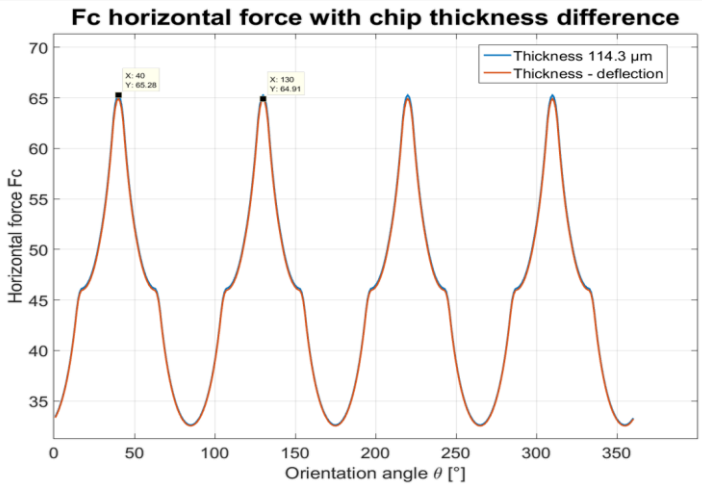


Figure 4.18. Implementing the tool deflection subtraction in the uncut chip thickness value

However, this is only a linear approach and has the main disadvantage that it calculates each tool deflection from an assumed orientation of 0° compared to the horizontal position of the tool. In practical terms, this is not possible, as the tool gets deflected and is affected by each previous tool deflection step, different than 0°.
In Figure 4.18, the tool deflection subtraction in the uncut chip thickness value can be observed. Such a plot aids in assessing the orientations more prone to tool deflection. However, the model must yet be improved.

The results confirm that micro-cutting precision is affected by the material crystallography through the significant, two-fold variation of tool deflection and of tool position throughout a complete workpiece revolution.

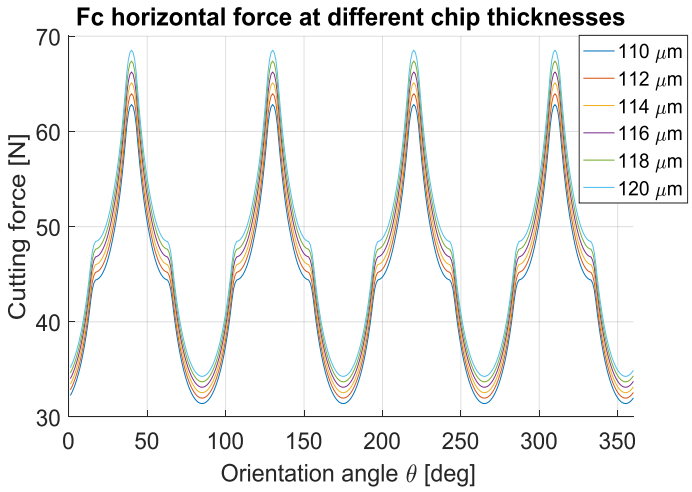
A better understanding of how chip thickness is affected by tool deflected during cutting can be seen when the amplitude of the observed tool deflection is considered, rather than calculating the deflection for each orientation angle.

When a dynamic cutting model is considered, the waviness of the chip formation surface is given through the lowest and highest values of chip height, as presented in Figure 4.19. For this reason, the next step is to look at incremental steps of 2 μm difference in the chip thickness (in turning, the depth of cut) between the observed tool deflection amplitude (from Figure 4.16).

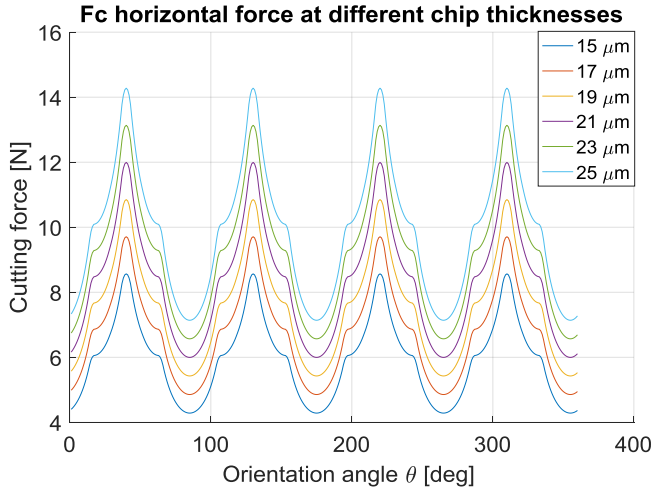
The chip thickness value is increased from 110 μm to 120 μm to observe if the cutting force values change (Figure 4.19).

4.3.3.3. Cutting force differences analysis

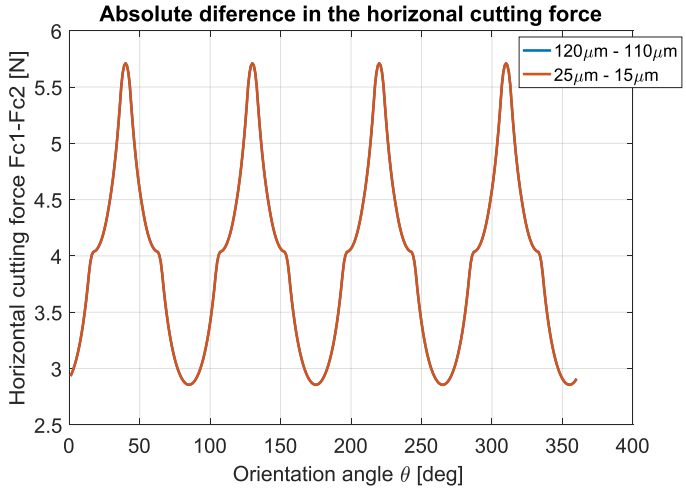
A difference between the extremes considered in Figure 4.19.a, between a chip thickness of 110 μm and one of 120 μm, close to Kota's cutting conditions, are considered. The same incremental steps are investigation for a micro-cutting specific dimension, between 15 μm and 25 μm. The plot reveals that both differences between cutting forces correspond to the profile of their respective crystallographic orientation (Figure 4.19.c).



a.



b.



c.

Figure 4.19. Analysing the effect of amplitude in tool deflection: a. incremental steps for different chip thicknesses between 110 µm and 120 µm; b. incremental steps for different chip thicknesses between 25 µm and 15 µm; c. the absolute difference between cutting force values

This represented the first step in assessing the cutting force variation within one rotation that contributes to the waviness of the dynamic cutting model surface (Figure 4.20).

4.3.4. Cutting stability lobes

4.3.4.1. Linear cutting force influence

As previously described, the cutting force varies with chip thickness. This is considered as a nominal value in cutting stability lobes. However, its variation, just as any variation in the cutting force value, introduces differences in a turning stability model. Figure 4.20 illustrates how chatter (machining vibrations) represent the damaging effect of the relative movement between the workpiece and the cutting tool.

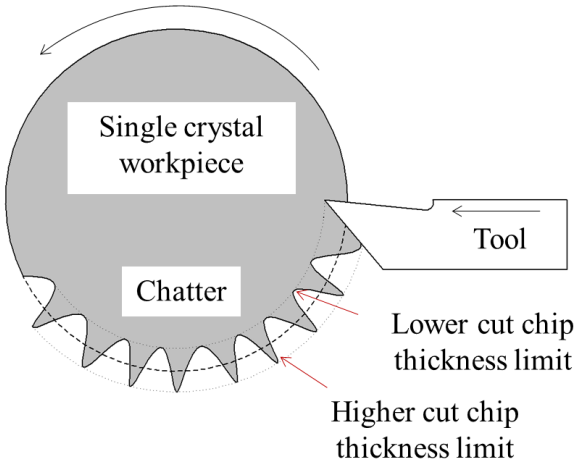


Figure 4.20. Schematic representation of chatter formation in an orthogonal turning process

4.3.4.2. Normalised cutting force model

The first step in assessing the difference between the cutting forces used in cutting stability models is to observe the calculation of the shear angle.
Theoretical prediction can be used by considering the maximum shear stress principle and the minimum energy principle.

The maximum shear stress principle proposed by Krystof (Altintas 2012) states that the shear angle ϕ can be obtained as:

$$\phi = \frac{\pi}{4} - (\beta - \alpha) \tag{4.59}$$

where β is the friction angle and α the rake angle used in the analysis.

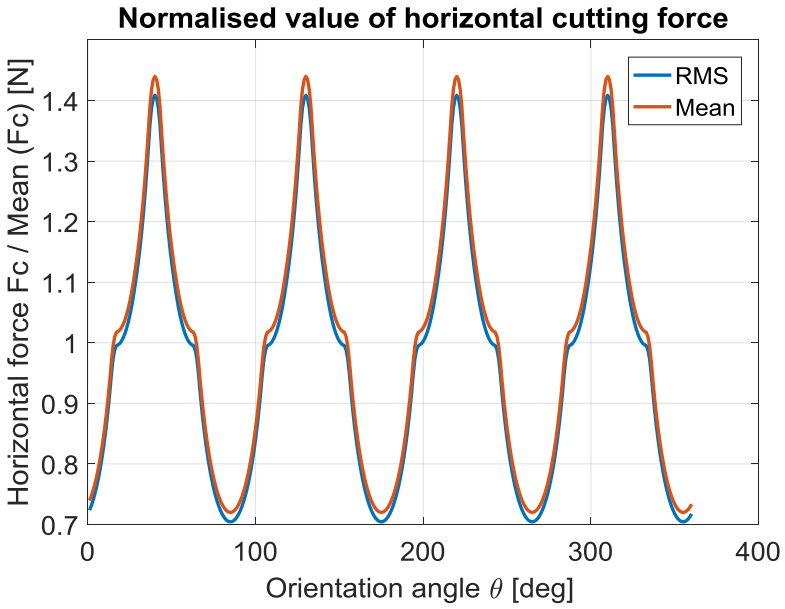


Figure 4.21. Normalised value of horizontal cutting force (001)

Merchant proposes a different equation for the shear angle based on the minimum energy principle:

$$\phi = \frac{\pi}{4} - \frac{(\beta - \alpha)}{2} \tag{4.60}$$

For Kota's parameters, the shear angles calculated with these two principles are 35° and, respectively, 40°.

Looking at the crystallographic orientation model, a multi-grain material can be assumed by considering that the material has all possible orientations at the same time – thus, by averaging the shear angles obtained for each orientation. This assumption would result in a 40° shear angle when the mean average is calculated, and of 41.44° when the root mean square is considered.

It is seen that Merchant's minimum energy principle results in the same shear angle result for a multi-grain material as the Matlab program.

Cutting stability is calculated using Schmitz and Smith's (2009) cutting parameters values for a shaping (slipping) system: a cutting coefficient K_f of 1,500 MPa, flexibilities θ_1 and θ_2 of 70°, stiffness's k_1 of 20 MN/m and k_2 of 22 MN/m, damping ratios ζ_1 and ζ_2 of 5%, natural frequencies ω_{n1} of 400 Hz and ω_{n2} of 700 Hz.
The change in the shear angle is considered. Cutting stability lobes are plotted below for the change between 40° and 41.44° shear angles (Figure 4.22):

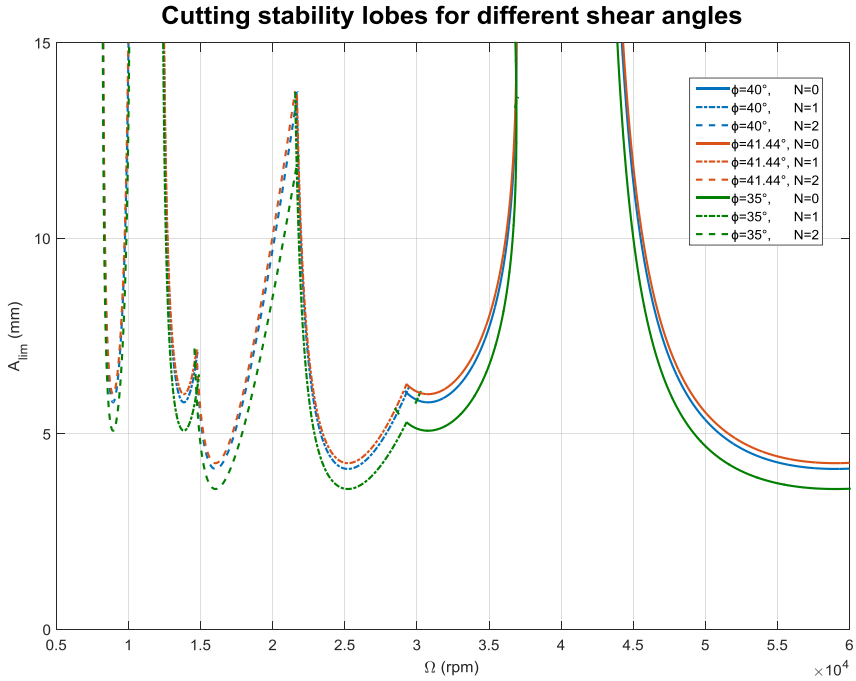


Figure 4.22. Assessing the difference of shear angles' influence on stability lobes

For a spindle speed of 31,160 rpm, the calculated stability limit varies from 5.823 mm in the initial stability model, corresponding to a shear angle of 40°, to 6.032 mm and, respectively, to 5.095 mm (corresponding to 41.44° and 35° values).

The next steps will be to assess the dynamic cutting feed force coefficient for all crystallographic orientations and to apply stability analysis for Kota's model.

The main aim is to identify the extent to which vibration affects cutting precision, and to look at the relationship between anisotropic cutting forces and tool deflection, respectively, regenerative chatter. This will serve to determine not only the change in cutting forces, but also on the tool path, as shown in Figure 4.23.

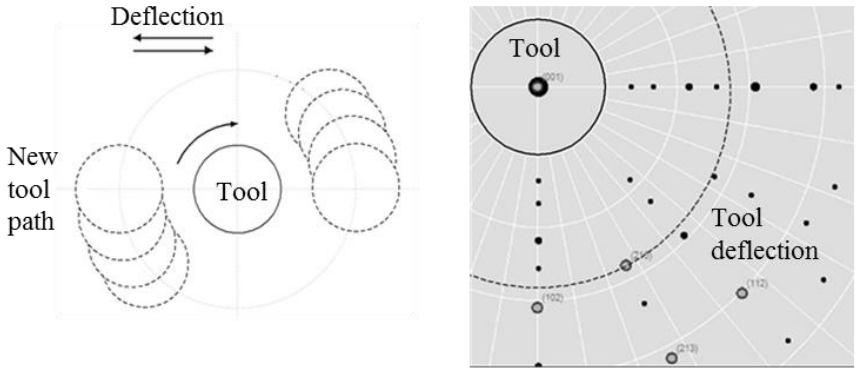


Figure 4.23. Tool deflection effect on tool path

4.4. Conclusions

An orthogonal cutting model for single crystal machining is used to determine the variation in cutting forces. The cutting forces are determined for one workpiece rotation, completed in a turning operation, by, using a Matlab program. The initial workpiece orientation is calculated based on the crystallographic strain tensor.
Eight crystallographic orientations are considered in the study: (001), (101), (102), (111), (112), (212), (213) and (216). Each cutting plane is shown to indicate a different force profile, in Figure 4.7.

The cutting force on the (001) cutting plane is shown to vary by twofold for a workpiece orientation of 85°, compared to that of 40°. This is the highest amplitude between force values obtained on a nominal cutting plane.
The smallest values and variations are obtained for the (111) cutting plane. This is explained by the fact that this plane has the highest number of slip systems; thus it is also the most facile to break (shear).

Slope values and tool deflection are calculated in a linear study, for the 8 crystallographic orientations. The same evolution profile as the force is shown to occur. Slope values are shown to be insignificant (due to being a third decimal of a degree), thus not influencing cutting force formation.

Tool deflection is calculated for each angle increment in the 360° rotation. The results indicate values ranging from 3.187 μm to 6.375 μm. Two approaches are taken when looking at the tool deflection influence: the first is where all the tool deflections are plotted in a sequence. This shows little influence on the effective cutting force model. However, when the amplitude between the lowest and highest deflection levels is considered, it is observed that the cutting forces vary by up to 6 N in value.

The dissimilarities between the initial cutting force models and the ones including slope, tool deflection and deflection amplitudes are considered. Tool deflection as illustrated in Figure 4.16 indicates pattern similar to cutting forces;, slope induced difference behaves in a different manner and is yet to be investigated.

At this stage, it has been established that tool deflection, but not slope, is a factor that affects micro-cutting precision in a repeatable manner, due to variation of cutting forces. This new understanding is important for process repeatability. The impact of tool deflection and the deviation from classic cutting values have also been investigated. While these considerations have been applied to static models, and the incremental angle change in workpiece orientation, future modelling studies should consider the dynamic evaluation of tool deflection in single crystal cutting.

This chapter also developed insights into the effect of slope for the first time. This new understanding indicates that it is not necessary for modelling and experimental studies to consider slope under single crystal micro-cutting conditions. However, under different circumstances, such as using long tools (which leads to an increase in both tool deflection and in slope values, to beam bending formulation), the slope could play a more important role and may be considered in future studies.

In future studies, the steps will include extending the model to a more realistic turning operation, and looking at the regenerative effects of vibration and how the cutting force is affected after more than one rotation of the single grain workpiece.

Another research question to answer is if this orthogonal cutting model would be appropriate to predict micro-milling cutting force; the main problem is that the tool tip

is not in continuous contact with the workpiece material and that it goes through multiple grain orientations at the same time.

This chapter concludes the first step in assessing cutting parameter variation in correlation with crystallography-dependent cutting force models. The next step is to apply this understanding to cutting precision methods, such as cutting stability, and to understand whether functions can be established for parametric variation, thus providing a new, improved model and broadened understanding of cutting stability. Moreover, in the next chapters crystallography-dependent cutting force models can give a better understanding of micro-machined surface quality and material phenomena, which at present is lacking.

The current limitation of the assumption of cutting force variation is that it is based on analytical models. Previous researches have validated the model against other experimental studies. However, in order to further material phenomena understanding and apply this knowledge to new stability models, the sufficient and necessary step is to experimentally analyse cutting force variation. Cutting force values must be empirically determined before any other steps are taken in this research, as they represent the most important parameter upon which current research is based. If the cutting force does not vary as predicted by these models, then new models cannot be developed, and a correlation with machined single grain phenomena cannot be established. As such, the next chapter deals with experimental analysis and validation of cutting forces measured in single crystal cutting of f.c.c. workpiece material.

CHAPTER 5

MICRO-CUTTING FORCES EXPERIMENTAL INVESTIGATION

5.1. Introduction

The main goal of the research in this chapter is improving micro-cutting precision. Various researchers have found that micro-cutting models, unlike those of traditional cutting processes, have to include the effect of material microstructure (Simoneau and Elbestawi, 2006; Zhou et al., 2001; Mian et al., 2010).

In Chapter 4, by studying the influence of crystallographic anisotropy on cutting forces, it has been established that micro-cutting results are correlated with material micro-structure. In general, the cutting force varies with the grain orientation. This has been shown by various analytical models and experimental studies, especially at low-speeds in microtomy processes (Cohen, 1982; Kota, 2008; Lee et al., 2002).

Proving that the cutting force varies with a four-fold symmetry in an arbitrarily selected (001) cutting plane (as exemplified by Figure 4.12.a) is an essential intermediary step to correlate the material microstructure influence with micro-cutting precision. This can support validating micro-cutting precision considerations on tool deflection, and new and improved cutting stability diagrams.

For this purpose, the current chapter deals with the empirical determination of the cutting forces developed in micro-cutting single crystal copper.

Cutting forces in the X and Y directions with respect to the tool orientation will be determined during a slipping/scratching process. Slipping is the cutting process that falls within most orthogonal cutting assumptions; thus, it is closer to Merchant's orthogonal cutting model (Altintas, 2012).

Although cutting forces have been determined for single crystal cutting in previous research, it is imperative to perform an intermediary step of cutting force measurement in order to validate whether the cutting force does vary according to models in the literature. Only then it is possible to make correlations with micro-cutting precision analysis techniques, such as cutting stability analysis.

It is also necessary to measure cutting forces in order to correlate them with post-processing material investigations, such as single crystal specific burr and chip formation mechanisms.

5.2. Data acquisition equipment and procedures

The following section deals with description of the equipment used in the experiments.

- Hurco VMX42SRTi machining centre

The Hurco machining centre can perform cutting operations up to 6,000 rpm. It can also be used for slipping experiments when the spindle rotation is locked on the main Z axis. The advantage in using this milling machine is that is has a large machine-tool bed, thus ample space for setting up different equipment such as a dynamometer, rotary table etc.

The Hurco was used in micro-cutting trials in parallel with the Kern in order to compare results coming from different machining centres. The Hurco is not a precision machine, thus it could develop higher vibrations. However, easy access to experimental set-up made it a good choice in initial testing phase.

- Kern Evo 5-axis machining centre

The Kern Evo is a precision micro-machining centre that can perform processes with tolerances as low as ± 0.5 μm. Its spindle rotation capability runs at 50,000 rpm, making it perfect for using small diameter tools, such as mills lower than 1 mm in diameter. The machining centre also benefits from having a polymer concrete bed that

absorbs vibration generated during processing. This is key in studying the tool-workpiece interaction, as most vibration occurring from the environment or the machine tool itself are dampened by the reinforced bed. This precision machine is used for scratching experiments, alongside Hurco, by locking its spindle and running the tool in one direction.

- Hermle C800U 5-axis machining centre

The Hermle C800U is a precision, micro-machining specialised machining centre. It benefits from having a reinforced machine-tool bed with a large operating surface that can rotate around its axis. It also benefits by having a rotating head, with a surface area much larger than Kern's. The machine has built-in sensors that measure the level of vibration experienced during cutting, and it signals warning messages when values exceed safe cutting operations. By having this, it has added vibration management. However, due to the built-in sensors and its programming, it is difficult to observe the level of vibration experienced during some operating conditions, which is a necessary step in the current research.

Due to its large surface area on the rotating head, this machining centre is very useful in calibrating the analysis equipment, such as dynamometers.

- PCB Piezotronics accelerometers

Two accelerometers, type 352C65 and 352C22, can be used simultaneously in order to capture synchronous signals from the vibrations occurring at different locations on the machine tool. Due to small tools used in micro-cutting, one of the accelerometers should be of a relatively small size and have a high sensitivity. The accelerometers are used with individual signal controllers and male BNC to male BNC coaxial cable type connections.

- Kistler 9129AA dynamometer

The Type 9129AA mini dynamometer has a height of 32 mm, a cover plate of 95 x 105 mm and a large measuring range, of up to ±10 kN. The design of the dynamometer minimises temperature error, while its threshold falls below 0.01 N. The dynamometer is used for measuring the three components of the resultant force vector with almost no displacement due to its piezoelectric sensor system.

- Kistler 5070A charge amplifier

The Kistler 5070A charge amplifier plays an important role in equipment calibration, in determining the sensitivity necessary for a specific process and for overall dynamometer functioning. Its measurement uncertainty is between 0.2% and 0.5% of the full scale output.

- DAQ National Instruments Compact DAQ chassis c9191 and 9216 data logger

A data logging equipment type 9216 is necessary to obtain experimental data. This equipment is a resistance temperature detector input module with 8 channels that can be configured for either a high sample rate (but with low resolution), either a high resolution one (with reduced sample rate). The c9191 chassis is used for the synchronization and data transfer between the input module modules and the external host.

5.3. Experimental program

The overall experimental goals are to measure micro-machining cutting forces, and in later chapters to analyse material deformations.

In the current chapter, a problem is represented by the low magnitude of micro-cutting forces. Generally, data acquisition equipment presents limitations when measuring Newton-level forces, as is the case in acquiring data from micro-cutting of 100 μm depth of cut or smaller.

Another problem is represented by the fact that in chapter 7, material phenomena occurring from this experiment will be investigated. Surface quality phenomena can be more easily observed at very low depths of cut. In chapter 7, the material phenomena are correlated with cutting forces and crystal planes material deformations.

A higher value for the depth of cut (200 μm) would enable accurate cutting force measurements, by increasing the effective volume of machined material and thus increasing cutting forces. However, a lower value in the depth of cut (50 μm), would enable a better analysis of material phenomena in single crystal samples. To achieve both goals, a series of experimental tests is performed at different depths of cut, to enable an accurate representation of single crystal micro-cutting phenomena.

The main goal of the current chapter is to measure cutting forces during single crystal copper micro-cutting by slipping (as a cutting method).

In order to clearly differentiate cutting force development aspects in multigrain versus single grain materials, as well as differences between higher versus lower depths of cut, three experimental phases are proposed.

It is important to specify that both depth of cut values are maintained at one order of magnitude lower than millimetre dimensions, to comply with micro-cutting dimension definitions.

5.3.1. Variables

The 3 experimental variables considered in this chapter are:

Workpiece material – 2 materials, multigrain and single grain copper, are used in order to highlight the intrinsic differences between regular-scale cutting and micro-cutting or cutting through individual grains of material. Material microstructure is the most relevant factor in this study. In order to develop new models and empirical findings in the following chapters, verifying the cutting forces development according single crystal properties (according to the analytical model in chapter 4) becomes a necessary and sufficient condition.

Depth of cut – 2 depths of cut, of 200 µm and 50 µm. The higher value depth of cut is necessary in order to ensure that the Kistler dynamometer is capable of measuring the cutting forces, while the second will enable surface phenomena analysis.

The uncut chip surface areas are calculated based on tool geometry (60° tip angle) and the 2 depths of cut considered (as seen in Figure 5.1). The two areas obtained for depths of cut of 50 µm and 200 µm are 1,433.5 μm^2 and 23,094 μm^2, respectively. This makes the uncut chip area at 50 µm depth of cut 16 times smaller than the uncut chip area at 200 µm depth of cut. Based on this difference, the cutting forces will also be 16 times smaller.

By performing a 50 µm deep channel, the limitations of the force acquisition equipment can be proven, as well as performing a better analysis of material deformations, which are easier observed at micro-cutting level.

Workpiece orientation – 24 orientations are proposed for the channels. While multigrain results should in theory indicate similar cutting force values, the single crystal material, oriented on the (001) crystallographic plane, having channels performed on 24 directions, should indicate a four-fold symmetry according to previous studies.

Considering these experimental variables, the three proposed phases are:

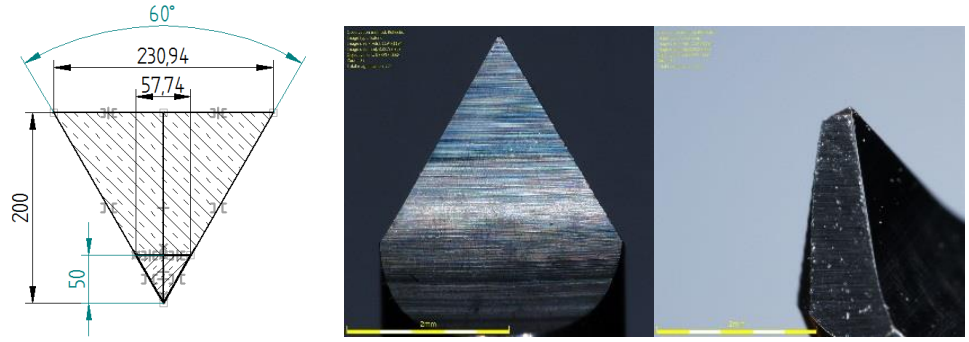
Determine cutting force variation in single crystal copper, comparing with multigrain sample.

- Phase 1. Perform 24 channels in multigrain copper at 200 µm depth of cut.
- Phase 2. Perform 24 channels in single crystal copper at 200 µm depth of cut.
- Phase 3. Perform 24 channels in multigrain copper at 50 µm depth of cut.

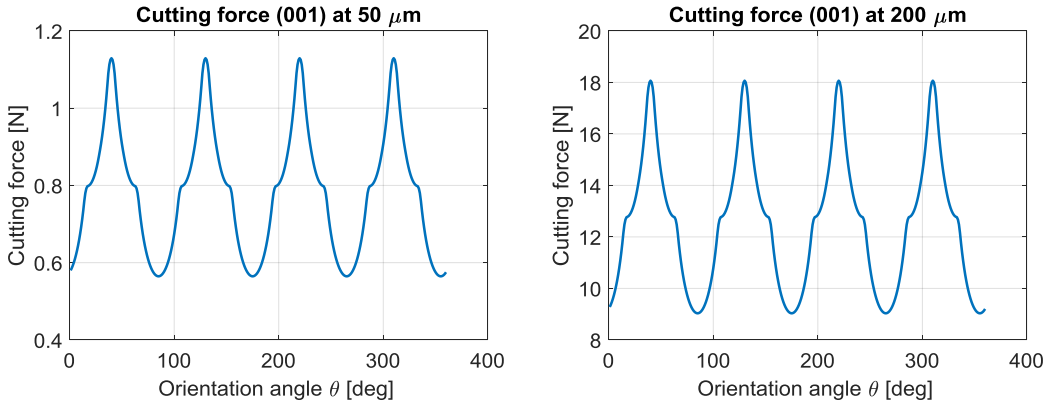
5.3.2. Design of experiments/ Program

Materials necessary for the experiment:

- Single grain copper disc of Ø12 mm x 2 mm;
- Scrapping tool x 1: commercially available (as shown in Figure 5.1), having a rake angle of 0.81° and a clearance angle of 12.58°; the tool had a stick-out of 25 µm, which was controlled by manually using gauges between tool clampings to limit the tool hangover;
- Aluminium support with 24 threaded screws for workpiece positioning;
- Clamps, screws, plate;
- Data acquition equipment, as presented in section 5.3.: Kern Evo, Hermle & Hurco machining centre; Kistler dynamometer & charge amplifier; 2 x accelerometers; DAQ National Instruments c9191 and 9216;
- Signal Express & Labview National Instruments software.



a.



b.

Figure 5.1. Cutting parameters: a. channel depth and slipping tools used in experiment, with a 60° tool angle; b. cutting force profiles estimated for a 50 µm and 200 µm depth of cut

Outcomes:

- Cutting force components on X, Y and Z directions, where: Z represents the tool plunge vertical component, X represents the radial and Y the tangential components of the cutting force.

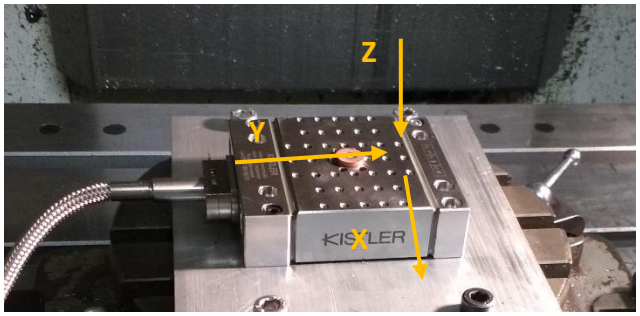


Figure 5.2. Cutting force components representation

Experimental set-up:

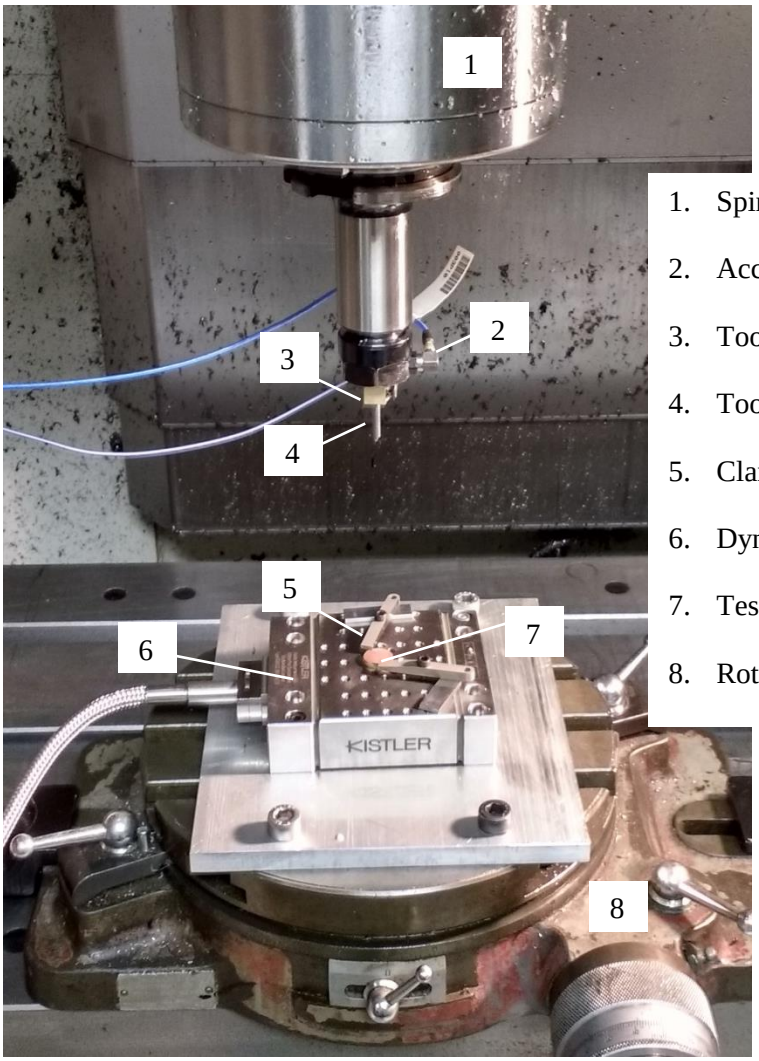


Figure 5.3. Experimental set-up used in preliminary test on Hurco machining centre.

A single crystal copper test piece is clamped on the dynamometer on top of the rotating table.

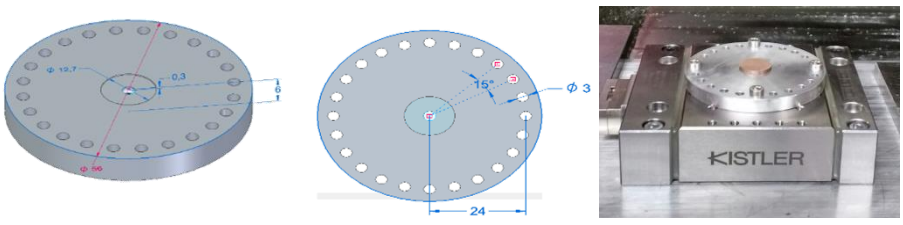


Figure 5.4. Aluminium support for enabling positioning of test piece in 24 orientations during micro-cutting. Dynamometer-aluminium support-test piece set-up, as in the experiment

Table 5.1. Experimental program

Trial no.	Channel number	Orientation angle [°]	Depth of cut [µm]	Phase
1	1	0	200	1
2	2	15	200	1
3	3	30	200	1
…	…	…	…	…
23	23	330	200	1
24	24	345	200	1
25	1	0	200	2
26	2	15	200	2
27	3	30	200	2
…	…	…	…	…
47	23	330	200	2
48	24	345	200	2
49	1	0	50	3
50	2	15	50	3
51	3	30	50	3
…	…	…	…	…
71	23	330	50	3
72	24	345	50	3

5.3.3. Experimental conditions

The machining method used in this experiment was slipping or scratching. Micro-channels were performed on copper test pieces.

Scratching or slipping is the method of cutting closest to orthogonal cutting principles. While milling and turning involve a feed motion and a tool or workpiece rotation, scratching only involves a feed-forward motion. Because of its strictly linear trajectory it is considered the first step in assessing if the cutting force varies with crystallographic orientation.

Channels were performed with commercially available slipping tools. The slipping tools have a triangular shape, with a sharp tip of approximately 5 µm and a 60° angle between cutting edges. The cutting tool profile resulted in channels with triangular section, with 15 µm at the bottom of the channels and dimensions up to 25 µm at the top, as shown in the figure below:

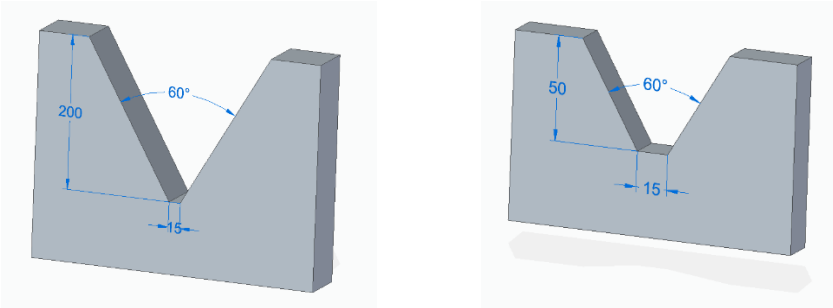


Figure 5.5. Section view of channel. The width of the cut varies, as the slipping tool has an angled tip.

5.4. Preliminary test

In the preliminary test, the changes of cutting forces, surface quality and cutting precision were observed for slipping tests done for 60 channels at 50 µm. Cutting was performed on two machines, on the KERN Evo 5-axis micro-machining centre and on the Hurco machining centre.

The spindle of both machines was locked to remove rotation. The tool was submerged 50 µm into the workpiece material, 1 mm away from the inner rim of the workpiece material, and then dragged towards the outer edge. The test piece was rotated 6° after each cut. This resulted in 60 channels and a complete workpiece rotation.

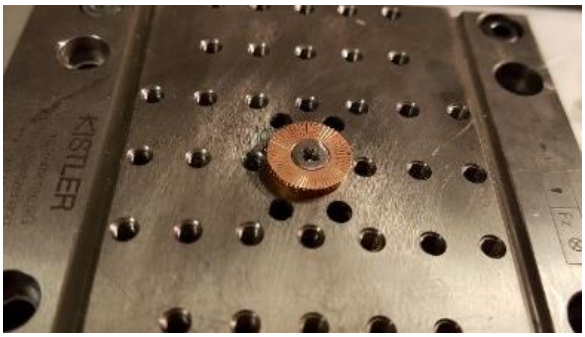


Figure 5.6. Test piece profile after machining.

Test piece manufacturing: discs of 12 mm in diameter and 2 mm width were cut from a single crystal copper bar, and from regular multigrain copper. The bar orientation was (001) on the cylinder symmetry axis.

The bar was wire-cut in a Sodick Electrical Discharge Machine. A 2 mm diameter counterbore hole was also machined in the centre of the test piece for use with the clamping method. EDM was the preferred method of manufacturing when preparing the test pieces to minimise the risk of breaking the single crystal and creating a multigrain material (as this may happen when using force in cutting). After cutting, the discs were manually polished to minimise the impact of the EDM-produced recast layer on experimental results.

Scanning electron microscopy investigation and comparison between the experiments showed that the recast layer was mostly removed, with only small ‘flakes’ of melted material remaining on the test piece surface. However, it was seen that manual polishing resulted in an uneven surface quality on top of the discs.

The test pieces were rigidly clamped by screwing them with a 2 mm bolt (no washer) on top of the dynamometer. This allowed an even distribution of the clamping forces across the test piece surface.

The preliminary tests indicate average values of cutting forces of 51.1 N and 32.3 N measured in single grain and multigrain copper cutting, respectively.

The cutting forces in multigrain material cutting are expected to have a linear behaviour, as material properties are isotropic. However, both test pieces indicate a double peak response.

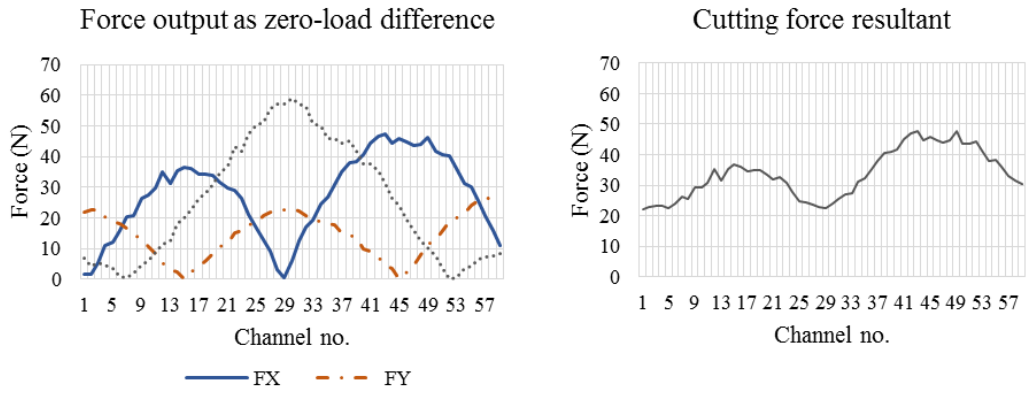


Figure 5.7. Individual force readings in multigrain copper cutting

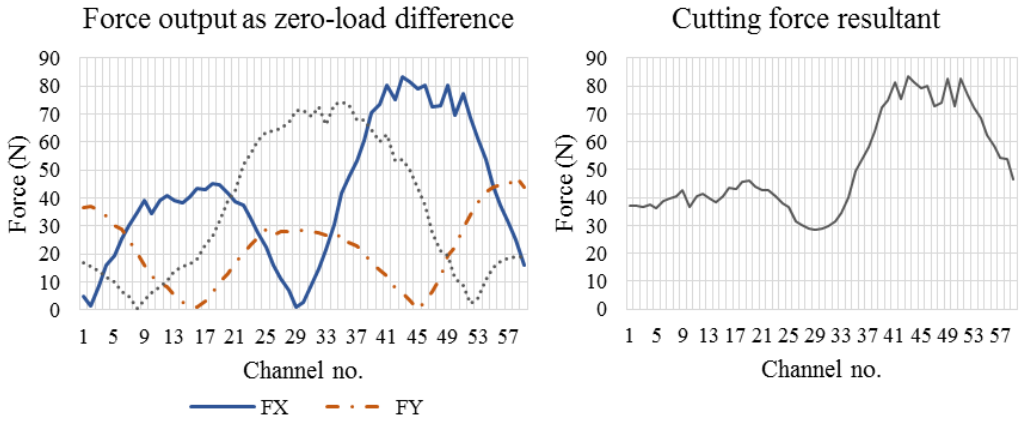


Figure 5.8. Individual force readings in single grain copper cutting

While the single crystal copper cutting results are uncertain, the nonlinear multigrain values clearly indicate that errors have been associated with the measurements.

For this reason, an accurate investigation of data acquisition equipment capabilities and limitations, and of individual equipment-introduced errors, is necessary. This was done in a subsequent step, in a detailed calibration of equipment testing phase.

5.5. Calibration of equipment

5.5.1. Cutting force calculation

The first step in calibrating the equipment is acquiring and interpreting the cutting forces registered by the Kistler dynamometer. For this, the following steps were undertaken.

The signals were acquired with the Kistler dynamometer with NI Signal Express software.

Sensitivity was set up as per dynamometer manual:

Table 5.2. Dynamometer recommendations

Direction	Sensitivity [pC/N]	Voltage to Newton conversion
X	25.22	100
Y	12.95	100
Z	25.81	100

Data points were input in Matlab as a function of voltage registered in time. The voltage signal was then converted to Newtons to calculate cutting forces. All force signals were seen to have a 'zero' level of registered forces along with an excitation, a 'cutting' or 'loading', level.

To determine the cutting forces, two ranges of points (intervals) were manually selected for the zero and cutting levels (as seen in Figure 5.9 below). The averages of the signal in these zero and cutting ranges was then calculated.

The acquired force was determined as the difference between zero level and cutting level averages:

$$\Delta F_x = F_{x_{loading}} - F_{x_{zero}} \tag{5.1}$$

$$\Delta F_y = F_{y_{loading}} - F_{y_{zero}} \tag{5.2}$$

$$\Delta F_z = F_{z_{loading}} - F_{z_{zero}} \tag{5.3}$$

With these values, the cutting force was calculated using:

$$F = \sqrt{\Delta F_x^2 + \Delta F_y^2} \tag{5.4}$$

$$F = \Delta F_x \cdot \cos(\theta) + \Delta F_y \cdot \sin(\theta) \tag{5.5}$$

where $F_{x_{loading}}$ represents the average of the signal obtained on loading

$F_{x_{zero}}$ represents the zero level of the signal (similar for y and z signals)

F is the cutting force that was determined

θ is the rotation angle of the test piece, values ranging 0° to 354°.

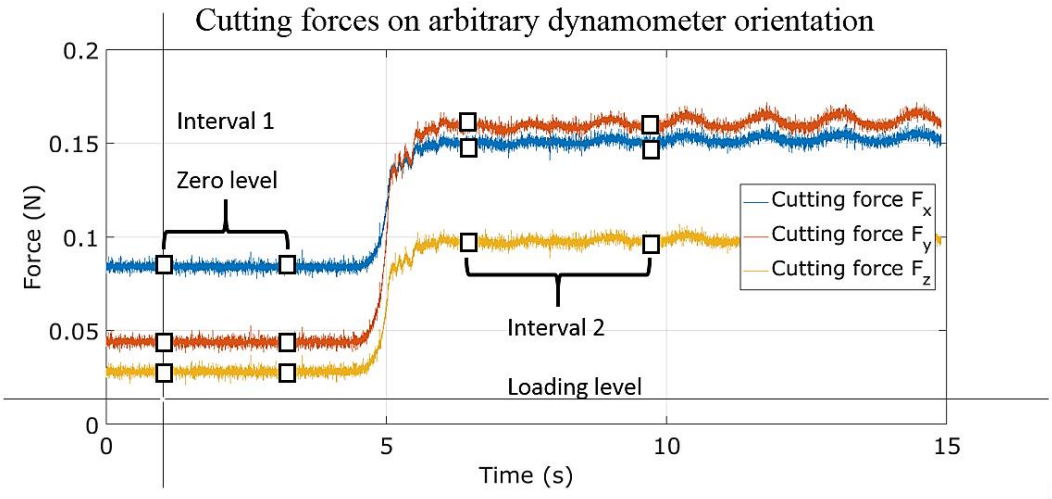


Figure 5.9. Selection of signal ranges for cutting force calculation

5.5.2. Dynamometer calibration

The objective was to calibrate the Kistler 9256C2 dynamometer for various loads and determine the implications for cutting force acquisition.

Initially, for dynamometer calibration, a series of objects with different masses were added onto the dynamometer to determine an initial calibration factor. The input load was calculated by converting mass into force. It was observed that the input load to output force ratio varied depending on the mass applied on the system.

When performing micro-cutting, the cutting forces developed often vary within Newtons or at sub-Newton level. The level of precision at which data is registered is limited by the capacity of the measurement system, the Kistler 9256C2 dynamometer.

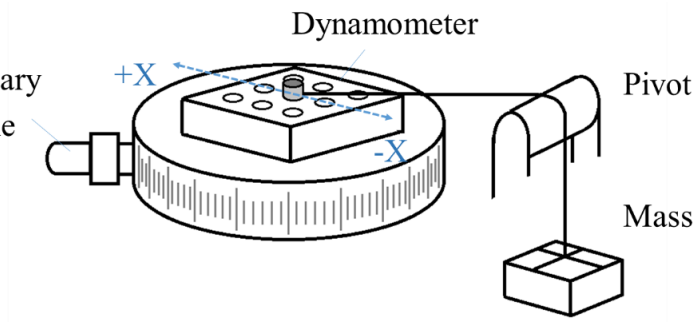
The cutting force acquisition equipment was tested for loads applied on ±X, ±Y and ±Z directions for loads of 0.108, 0.085, 0.071, 0.042, 0.0175 and 0.0085 kg. This phase was performed to determine the accuracy of the X, Y and Z sensors against each other.

Six masses have been attached, with a wire, against a pivot, to a screw positioned in the centre of the dynamometer, as illustrated in Figure 5.10a. The masses have been suspended against the 3 main dynamometer directions X, Y and Z, for both – and + values. A varying average ratio value was obtained for the small weights and then for the one of 3 kg:

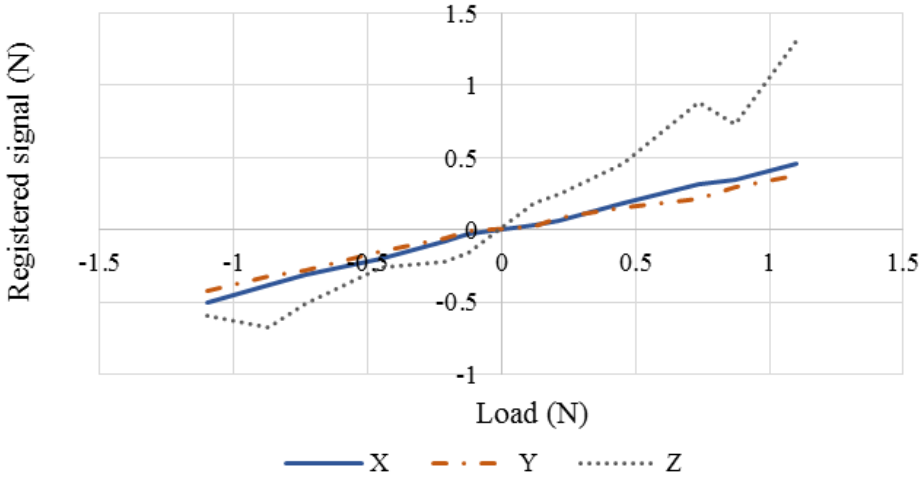
Table 5.3. Calibration of dynamometer: applied load vs. measured forces

Load (N)	Fx	Fy	Fz
-29.41	3.83	-11.97	98.47
-1.06	3.73	-13.24	-188.10
1.06	3.50	-17.62	221.80
29.41	3.76	-15.77	131.04
-29.41	-7.02	2.78	3.32
-1.06	-6.27	3.00	3.82
1.06	-7.38	3.18	3.74
29.41	-8.98	3.40	4.72
Average	3.70	3.09	

The results plotted in Figure 5.10b indicate that X and Y sensors give accurate results against each other, with the exception of the 0.12 N loads, which have been excluded from the table. However, the loads registered by the Z sensor raise a level of incertitude in such that the values recorded are half of X and Y. This is possibly the results of the different means of applying the loads (on Z: directly on the surface and then hanging from a vertical pivot, as opposed to a lateral one on X and Y). The calibration also resulted in a calibration factor of 2.8 between measured forces and applied loads.



a.



b.

Figure 5.10. Analysis of loads applied on different axes: a. calibration scheme; b. calibration results

After measuring the cutting force, and determining the calibration factor, the next step was to understand the best experimental set-up. Two solutions were available, in order to ensure a complete 360° workpiece rotation.

One was to clamp the test piece on the surface of the dynamometer, and to secure the dynamometer on an aluminium plate. The aluminium plate would then be mounted on the surface of a rotary table. This set-up was used in a preliminary test, which featured 50 μm depth of cut channels. This would also give the possibility of performing potentially more channels, for example 60 channels situated 6° apart. While this would be less relevant in determine the four-fold symmetry of cutting forces, it could give a better insight into subsequent studies of grain-specific material deformations.

The second set-up involved designing the afore-mentioned aluminium support. Its design was made based on the slots available for clamping workpieces on the dynamometer. The highest number of slots where the plate could be clamped on the dynamometer was determined to be 24. The test piece would be fixed rigidly in the centre of the aluminium support through a counterbore threaded hole, as shown in Figure 5.4. This set-up eliminated the need for a rotary table, which could potentially add errors due to misalignments of slides and affect experimental results.

To enable the first experimental set-up described, calibration was conducted by applying constant loads of 3 kg and 0.108 kg at 6° dynamometer rotation intervals. This phase was performed to determine if using a rotary table as means of rotating the dynamometer-workpiece system against a stationary tool position is a viable experimental set-up solution. Initially, an aluminium test piece support for 24 orientations was designed. However, using a rotary table would enable a higher speed in performing the tests and a wider array of orientations to be selected without clamping and unclamping the test piece after machining each channel.

The masses of 3 kg and 0.108 kg, respectively, were attached by a wire to the screw fixed on the centre of the dynamometer. The force values have been registered for 60 orientations spaced 6° apart from each other, starting with the +X direction, anticlockwise towards +Y, -X and then –Y.

Recordings in the X and Y directions are shown in Figure 5.11 below, and include the force output for individual X- and Y- directions and the resultant force as their vector sum.

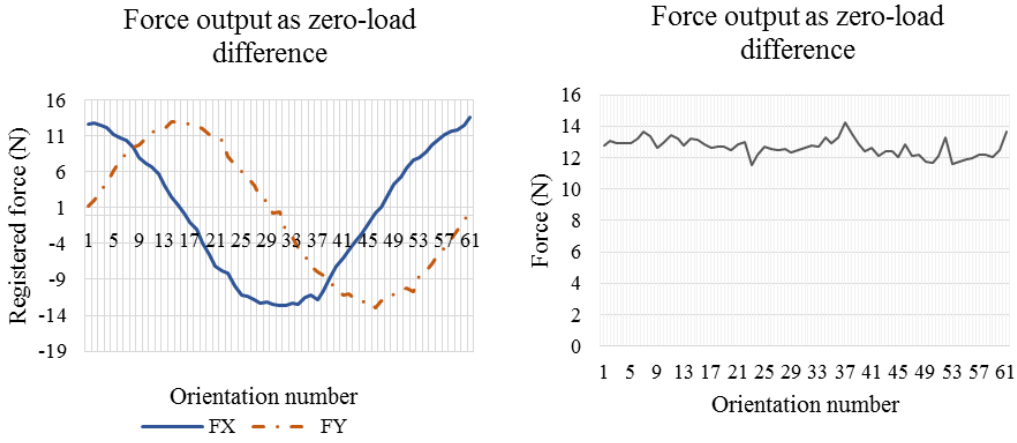


Figure 5.11. Measurements and calculation of X and Y readings for 3 kg applied load

The overall load chart indicates a good level of consistency of recorded forces. 80% of data is within ±5% of the average force value, while 20% of data varies between -10% and +12% of the average force value.

However, the forces measured in the X and Y directions are not the true components of the X and Y components of the force, not when taken individually. While their resultant, the overall force output, remains constant, the dynamometer undergoes a rotation that implies a coordinate change system.The general rotation matrix *R* in a 2-dimensional system for rotation in Euclidean space is given by the equation:

$$R(\theta) = \begin{bmatrix} cos\theta & -sin\theta \\ sin\theta & cos\theta \end{bmatrix} \tag{5.6}$$

The *R* matrix rotates column vectors by means of the matrix multiplication given below:

$$\begin{bmatrix} x' \\ y' \end{bmatrix} = \begin{bmatrix} cos\theta & -sin\theta \\ sin\theta & cos\theta \end{bmatrix} \begin{bmatrix} x \\ y \end{bmatrix} \tag{5.7}$$

Thus, resulting in (x', y') coordinates of the rotated pair of original points(x, y):

$$x' = x \cdot cos\theta - y \cdot sin\theta \tag{5.8}$$

$$y' = x \cdot sin\theta + y \cdot cos\theta \tag{5.9}$$

Considering this transformation of the Fx and Fy data (coordinate system of the rotary table), the forces in the original coordinate system of the dynamometer have been calculated as presented in the chart below. The graph indicates a concordance between X and Y data, with maximum and minimum values at 90° (15 orientations) apart.

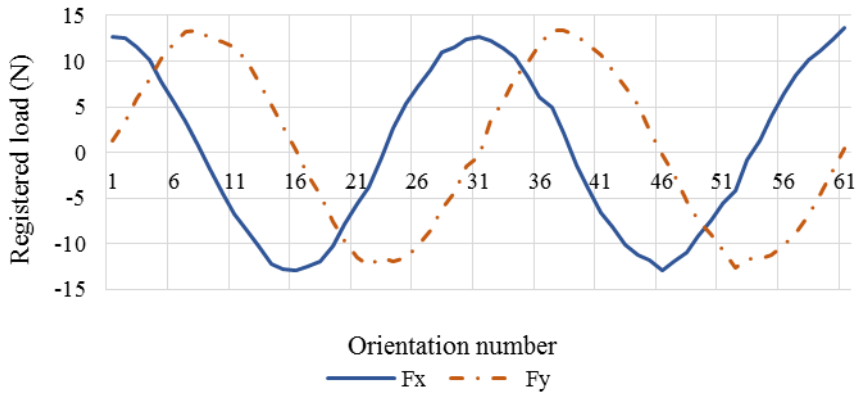


Figure 5.12. Force in dynamometer coordinate system at 3 kg applied load

The following step was to determine whether the agreement between X and Y registered loads hold up at low masses which would correspond more to the small cutting forces that are generally developed in micro-cutting.

The same calibration set-up having attached a mass of 0.108 kg was used, with results shown in Figure 5.13 (as voltage, instead of force; 1 V represents 100 N).

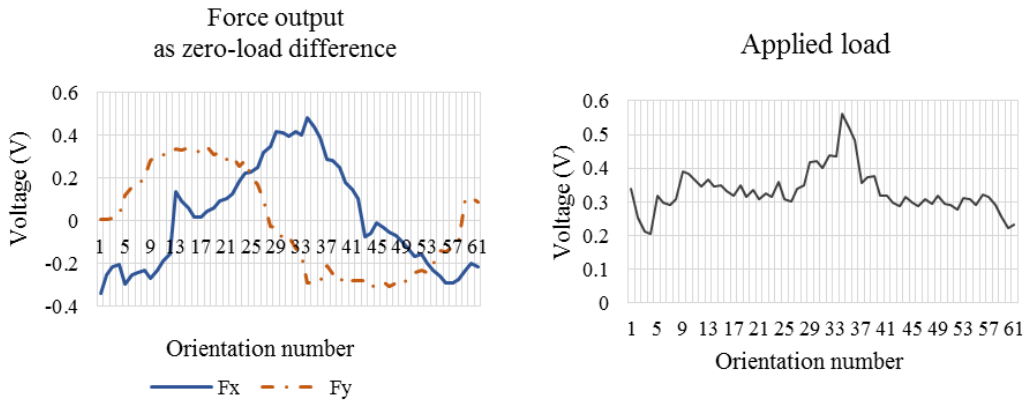


Figure 5.13. Measurements and calculation of X and Y readings for 0.108 kg applied load

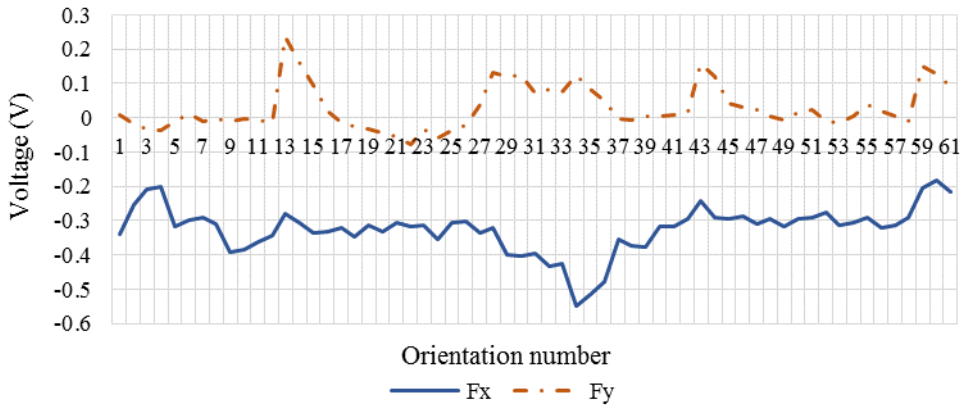


Figure 5.14. Force in dynamometer coordinate system at a 0.108 kg applied load

It has been observed that confidence levels in force readings have dropped significantly. From previous calibration results as shown in Figure 5.12, a minimum and maximum for X or Y appear at a 90° difference; the signal profiles have the shape of a sinewave. This signal behaviour would be expected in Figure 5.14 as well. However, the low levels in Figure 5.14 indicate that the dynamometer did not register the applied load value, as much as the rotation of the dynamometer itself.

For this reason, the depth of cut of 50 µm originally envisaged for the experiment has been reconsidered to be 200 µm, which would geometrically generate a volume of uncut chip material approximately 16 times higher than the original one. Likewise, the cutting forces registered would be in the same range of magnitude as the cutting force is directly related to the depth and width of cut. This would increase the level of confidence in registered values.

Furthermore, the zero levels (of no applied load) of all recorded testing have been investigated to observe whether they indicate the added sine waves corresponding to errors, or whether they have irregular profiles, as it would be expected in accurate experimentation.

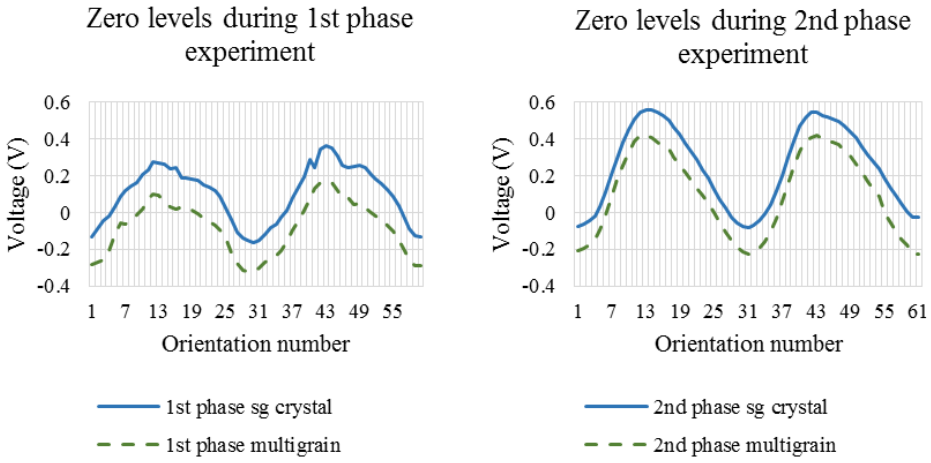


Figure 5.15. Zero Fx levels measurements in single crystal experiments

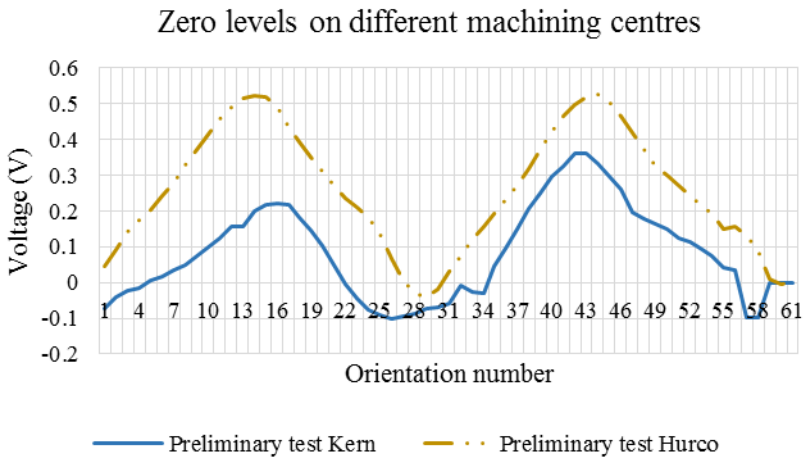


Figure 5.16. Force measurements in 100 N units of zero levels in various experiments

It has been shown that the rotary tables used in previous experiments introduced *errors* in the signal obtain from the dynamometer. As a result, it has been eliminated from this testing phase.
Additionally, the signal obtained while rotating the dynamometer (with no applied load) has been shown to correspond to voltages obtained in previous experiments. Thus, rotating the dynamometer resulted in further errors.

Considering these findings, the 24-holes aluminium support would enable rotating the test piece manually while clamping it against the dynamometer, and at the same time it would eliminate the errors generated by the rotary table and by the rotational movement of the dynamometer.

As the errors generated by the signal coming from the dynamometer have been found to be at the level of the predicted cutting forces, a higher depth of cut has been proposed, which would theoretically generate a cutting force 16 times higher than the previous depth of cut. By employing this operational update, the cutting force is expected to overcome the level of the error, thus producing more accurate results. This was also reflected in the 3kg versus 0.108 kg weights calibration operation.

As it has been observed that the dynamometer is influenced by rotating the equipment, in the following graphs an analysis of the errors introduced by each influential component of the experimental set-up is presented.
Initially, the rotary table having the dynamometer clamped has been rotated by hand and zero load levels have been measured.

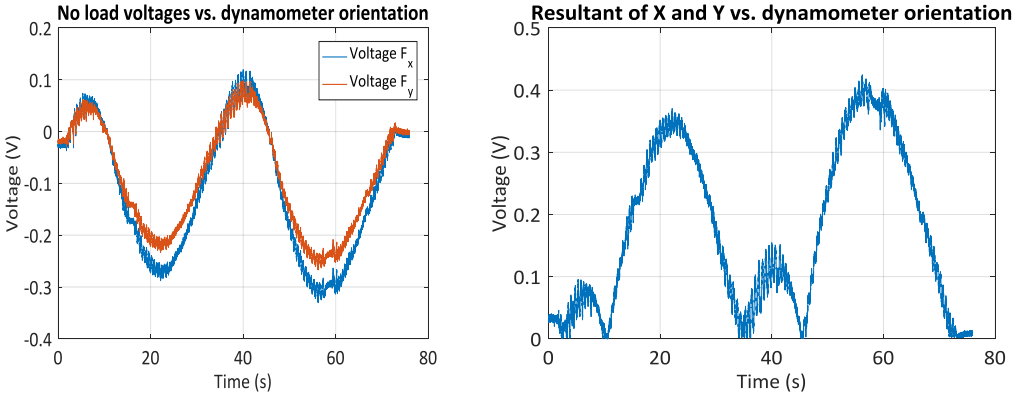


Figure 5.17. Zero load differences for manual rotation of table

Subsequently, the dynamometer without rotary table has been attached to the rotating head of the Hermle machining centre. There, it has been rotated on the machine command at the lowest, medium and highest rotation speed that can be manually selected. The dynamometer was tested both with and without an aluminium plate attached as support.

Results are shown in the plots below. Resultant forces in micro-cutting would be calculated from X and Y force readings. For this reason, the magnitude of the zero loads X and Y resultant was also calculated. The results indicate that zero levels are within cutting force magnitudes when 50 µm depths of cut are performed.

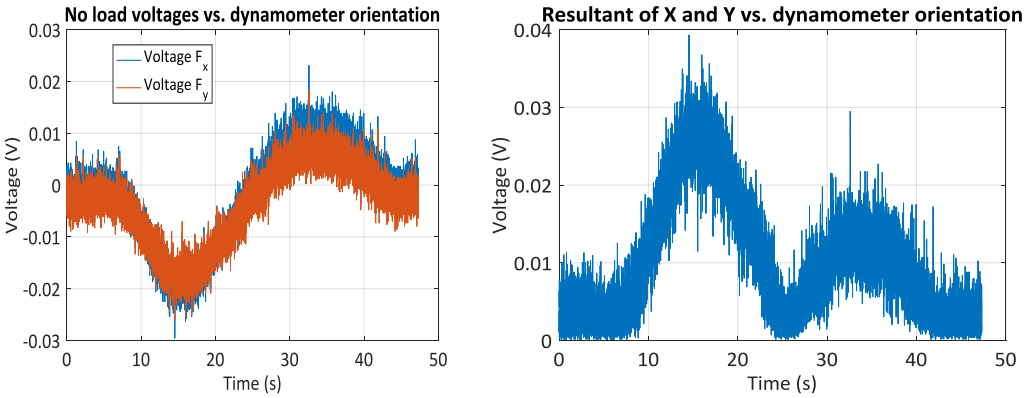


Figure 5.18. Measurements on Hermle, with aluminium plate. Medium speed. Direction of rotation C+

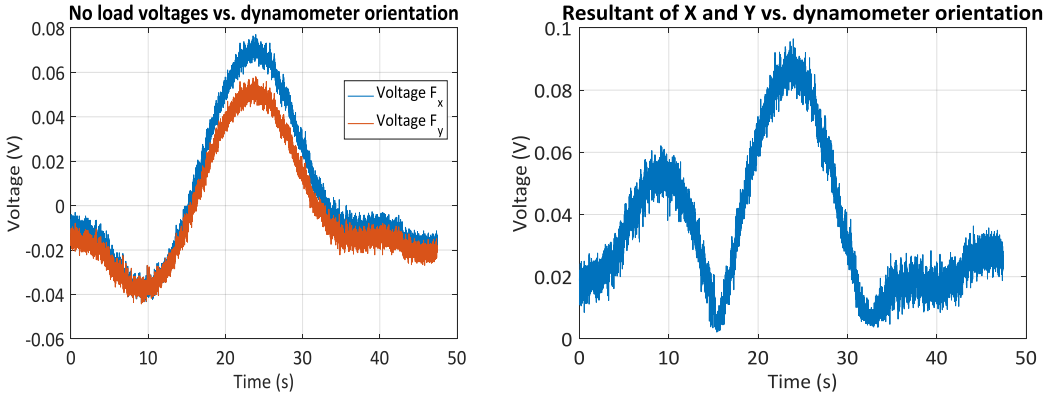


Figure 5.19. Measurements on Hermle, no aluminium plate. Medium speed. Direction of rotation C-

The values above indicate measurements of voltages rather than their conversion to Newtons. However, they are well within the same range of magnitudes as the cutting forces registered in the preliminary test. Also, the resultants between X and Y reading indicate a two peak response, such as that observed in the preliminary test.

For this reason, utilisation of the rotary table and rotation of the dynamometer are experimental conditions to be avoided when the goal is measurement of the cutting forces. They may still prove useful for material investigation purposes or for forces of much higher magnitudes. However, they have been eliminated from the experimental set-up necessary in this chapter. In the following section, results of copper cutting using solely a 24-channel aluminium support as means of test piece rotation are presented.

5.6. Experimental results of orthogonal cutting of copper

Two test pieces, multigrain and single grain copper, have been machined according to the 3-step designed experimental program. The depths of cut of 200 µm and 50 µm have been machined in 24 radial channels, and individual cutting force measurements in the X, Y and Z axes have been recorded with a Signal Express program.

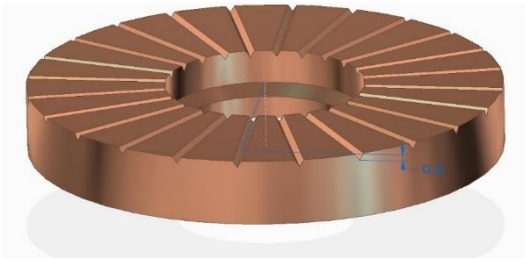


Figure 5.20. Test piece after cutting of 24 channels.

The first test piece analysed is the multigrain copper machined at 50 µm depth of cut. This step is necessary in order to understand if the errors previously analysed have been eliminated, and also to observe if a linear behaviour is exhibited by the X and Y force readings, which is anticipated in multigrain material cutting. This not being the case would be an indication that dynamometer cannot record data of forces developed at this the depth of cut, and it would prove the equipment limitation.

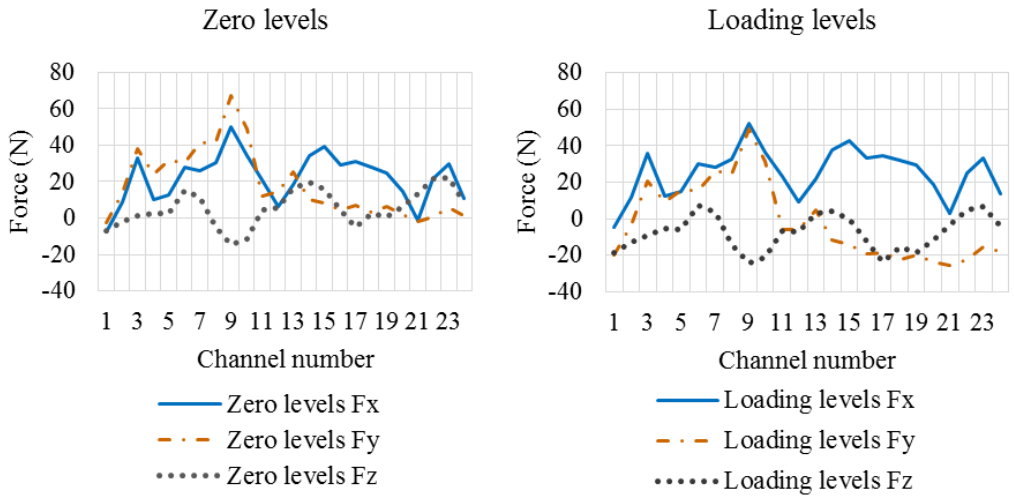


Figure 5.21. Zero and loading levels during multigrain copper cutting of 50 µm depth of cut

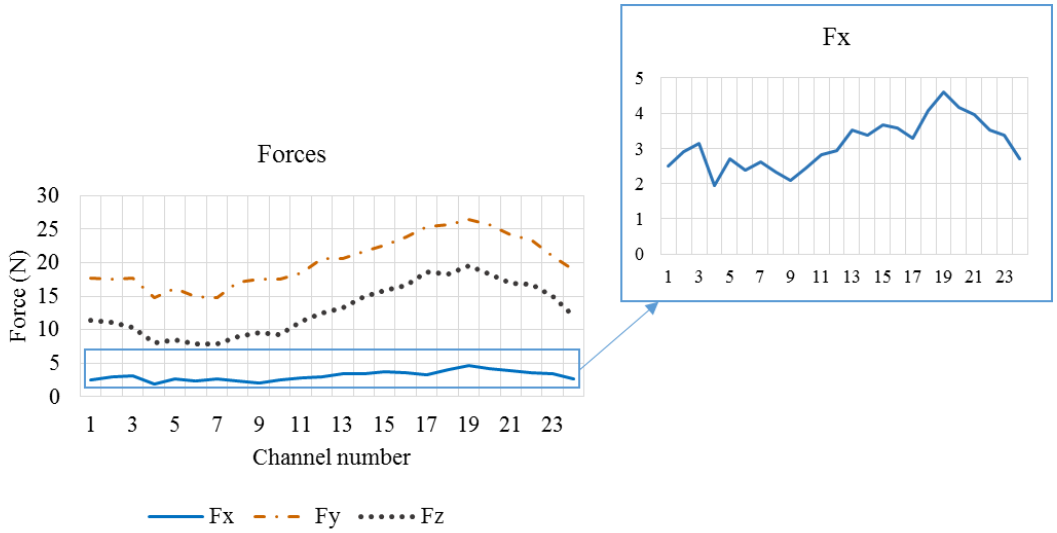


Figure 5.22. Individual force readings in multigrain copper cutting at 50 µm

The second step was machining a multigrain copper test piece at 200 µm depth of cut. This last adjustment of the experimental program was introduced to increase the cutting force magnitude to a level above dynamometer limitations.

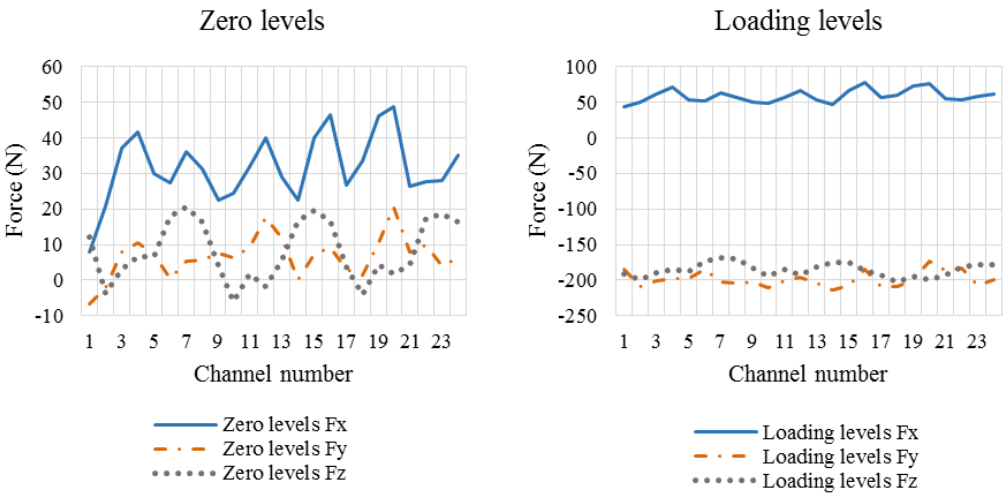


Figure 5.23. Zero and loading levels during multigrain copper cutting of 200 µm depth of cut

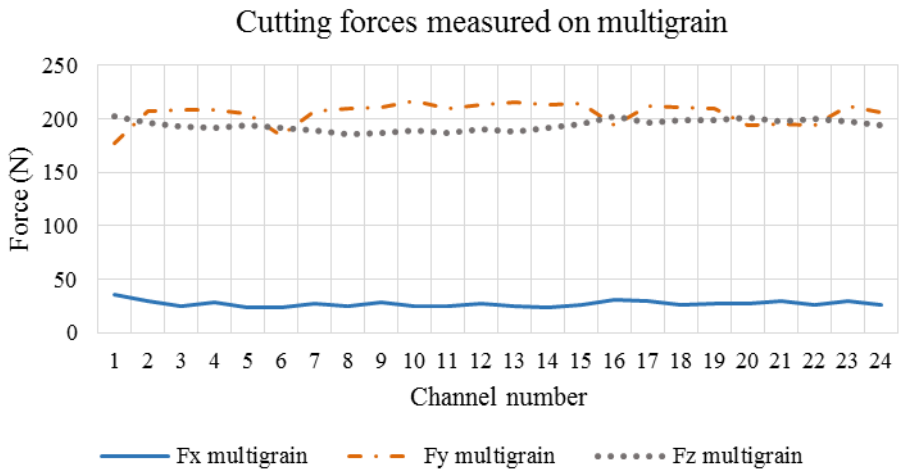


Figure 5.24. Individual voltage readings in multigrain copper cutting at 200 µm

The third and final step of the experimental trials was cutting the single crystal test piece at 200 µm depth of cut.

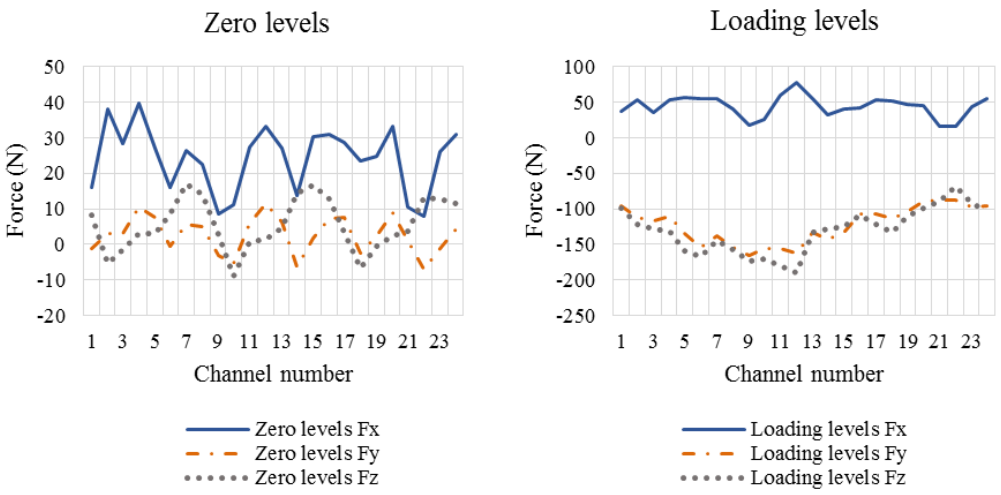


Figure 5.25. Zero and loading levels during single grain copper cutting of 200 µm depth of cut

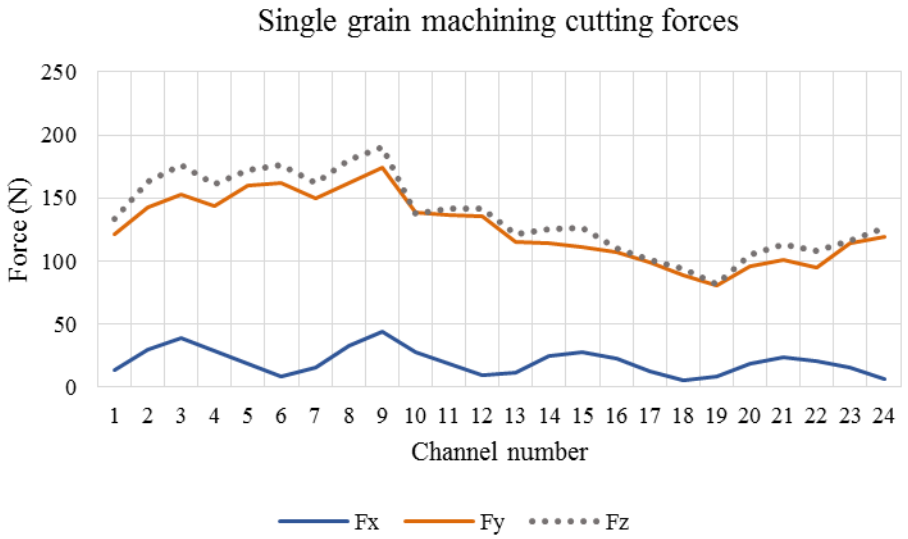


Figure 5.26. Individual cutting measurements in single crystal copper cutting at 200 µm

Furthermore, Figure 5.27 and Figure 5.28 show the differences registered in Fx and Fy, respectively, between multigrain and single grain copper.

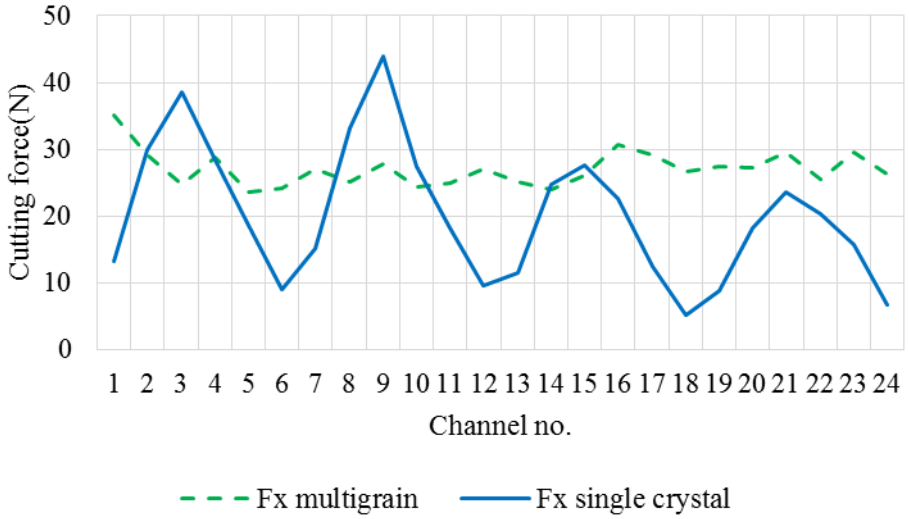


Figure 5.27. Cutting forces comparison for 200 µm depth of cut

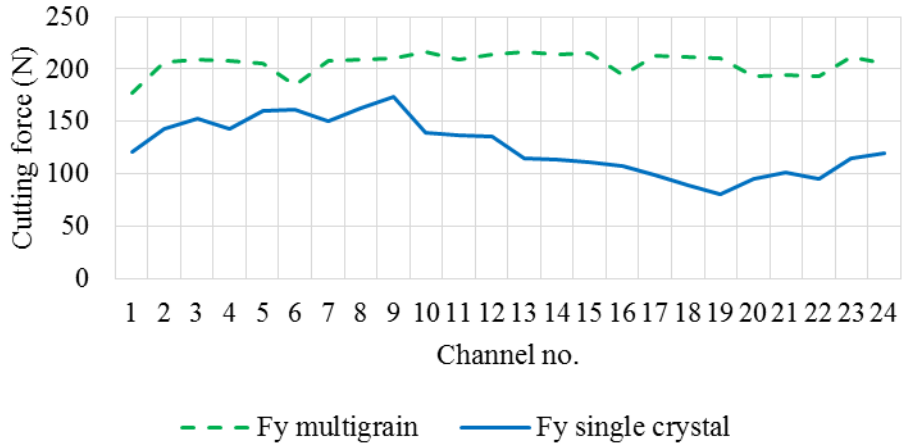


Figure 5.28. Cutting forces obtained at 200 µm depth of cut

Table 5.4. Average values of the cutting forces

	Fx (N)	Fy (N)	Fz (N)
Single crystal	20.10	125.77	136.05
Multigrain	27.05	205.45	194.16

Beside the overall cutting force value, which was calculated as the difference between zero and loading level averages, see Section 5.6.1, a more in-depth investigation of cutting force development in individual channels is necessary. In isotopic materials, a linear profile of the loading levels is expected to be seen. However, there is no known

comparison with single crystal profiles. Below, a selection of cutting forces measured in channels 13-18 of the two test pieces machined at 200 µm depth of cut is provided.

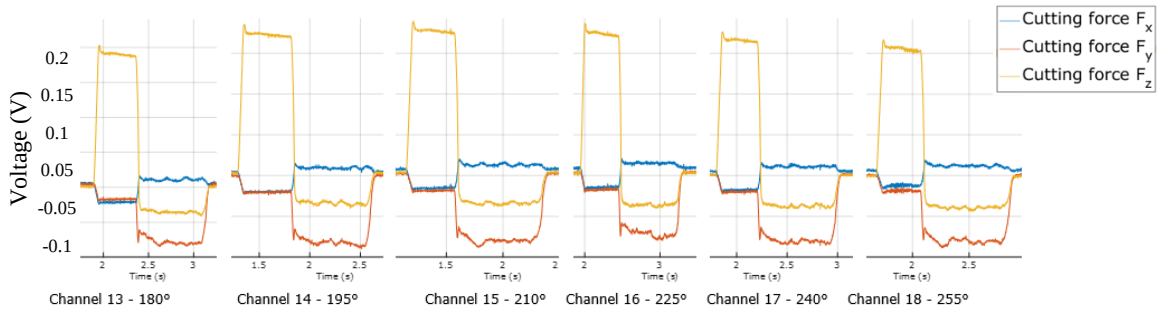


Figure 5.29. Multigrain copper cutting forces

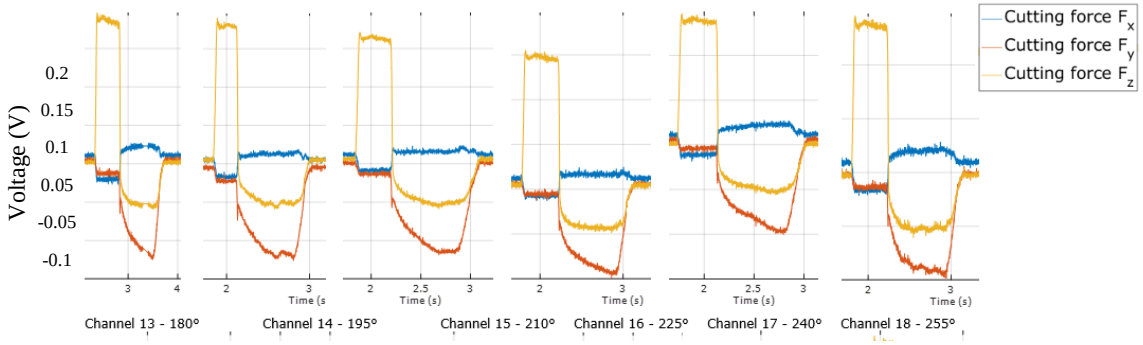


Figure 5.30. Single grain copper cutting forces

In Figures 5.29 and 5.30, the yellow data represents Z readings, the blue data X readings, and the red data Y readings. The initial spike in Z readings is conform to the tool plunge motion, before shearing in the XY plane begins. This is also suggested by the similar values developed by X and Y in the initial stage, where the stress would be equally distributed on X and Y when the tool plunges into material.

Different types of cutting forces were identified in the multigrain and single crystal cutting forces, as shown above. In the multigrain cutting forces, the force profiles appear as cutting forces type I, with steady cutting indicating single slip or constant multi-slip behaviour, as in normal shearing processes. Small disturbances appeared in the stable zone of cutting, but none representing type III behaviour such as in Lawson et al. (2008). In the single grain copper force profiles, the outlook of the forces varies. Cutting forces in the X direction are type I forces. Most cutting forces in the Y direction are also type I, with some presenting a slower development in the cutting force, which may be due to strain build-up up to the point of achieving the depth of cut. Cutting forces on the Y direction present a steadily increasing force, ending in a relatively

stable zone of stable cutting. In practice, this could occur when the tool is not entirely submerged in the workpiece material for most of the channel, resulting in a 'plunge' movement throughout the machined feature. However, in Chapter 7, the depth of cut at the beginning, centre and end of the channels has been measured. No relevant differences have been observed that could correspond to the Y component of the cutting force. Also, no large, cyclic fluctuations of the cutting forces have been observed. This eliminates the assumption that Y cutting forces variation is generated by operating parameters, and points to material microstructure causes.

Based on these profiles, two phases in cutting data have been identified, namely the tool plunge and channel cutting phases. While previous cutting force data has been the difference between zero levels and channel cutting, the difference between multigrain and single grain plunge and cutting time presents interest. With this scope, the time for these two phases has been calculated (based on time data such as the one available in Figures 5.29 and 5.30) and is shown in Figure 5.31 below. Average values for the tool plunge time are 0.9272 s for single crystal and 0.8312 s for multigrain, while for channel cutting time, they are 0.4119 s and 0.4614 s.

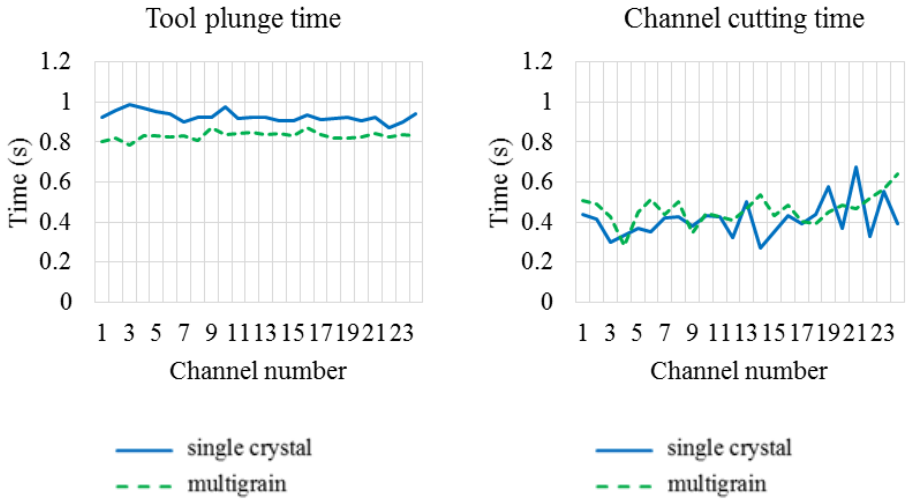


Figure 5.31. Duration of tool plunge and channel cutting phases

5.7. Discussion

In the multigrain copper test piece machined at 50 µm depth of cut, the initial investigation of zero and loading levels indicate that they do develop in the same manner, but not according to a sine wave. The absence of a sine wave is a good indicator of an improved measurement, meaning that the applied load has a higher magnitude than the variation in voltage due to dynamometer rotation; however zero and loading levels should differ. Also, the zero levels for individual X, Y and Z readings differ significantly and do not exhibit a two peak response, as in calibration and the preliminary test. This is further confirmation of eliminating errors associated with dynamometer rotation.

However, analysing the overall cutting forces, the dynamometer is introducing some errors itself, as the evolution of the X, Y and Z readings follows a similar pathway of a convex then concave shape. For this reason, it has been established that cutting forces cannot be accurately measured at 50 µm depth of cut due to equipment limitations.

In the second test piece, multigrain copper test pieced machined at 200 µm depth of cut, the results indicate significant difference between X, Y and Z readings, as well as between zero and loading levels, confirming an accurate representation of the cutting forces developed in multigrain copper cutting.

The profiles of Fx, Fy and Fz exhibit a linear development, confirming an experimental set-up with high confidence levels. These measurements are taken as a standard for the comparison between average cutting force values displayed in isotropic materials, and all the ensuing single crystal anisotropic implications.

In the third test piece made of single crystal copper, Fx, Fy and Fz exhibit a highly different development. Fy and Fz display similar profiles of a convex, followed by a concave shape.

However, the most relevant finding is the development of the four peaks in the Fx profile (Figure 5.27). As these peaks are repeatable every 6 channels (90°), this is confirmation of a four-peak repeatability in cutting forces developed on the radial direction of cutting through a (001) cutting plane. This result validates the analytical model behaviour observed in Chapter 4, namely the fact that single crystals have an anisotropic behaviour and a specific cutting force development, dependant on the grain

orientation. This impacts micro-cutting processes by a great degree, and endorses a new, in-depth analysis of single crystal cutting. This new required analysis is supported by the force profiles shown in Figure 5.27, due to the difference between multigrain material and single grain material cutting.

Previously, other authors (Moriwaki and Okuda, 1989; Lee, To and Cheung, 2000 and 2007) have studied results of single crystal cutting, but the correlation between specific cutting force profiles and single grain vs. multigrain materials is largely unexplored. The large amplitude between minimum and maximum single crystal Fx forces requires a deep analysis of material phenomena, and correlating this to the analytical model in Chapter 4, as well as the experimental results in the current chapter. Previous authors have reported a change in chip thickness, but they haven't established a clear correlation with known single crystal cutting force models. However, this can potentially lead to a new, improved understanding of single grain micro-cutting, by correlating cutting force variation with important micro-cutting precision and quality aspects. This correlation can be established by investigating burr and chip formation (to study quality), or process repeatability (to investigate cutting precision).

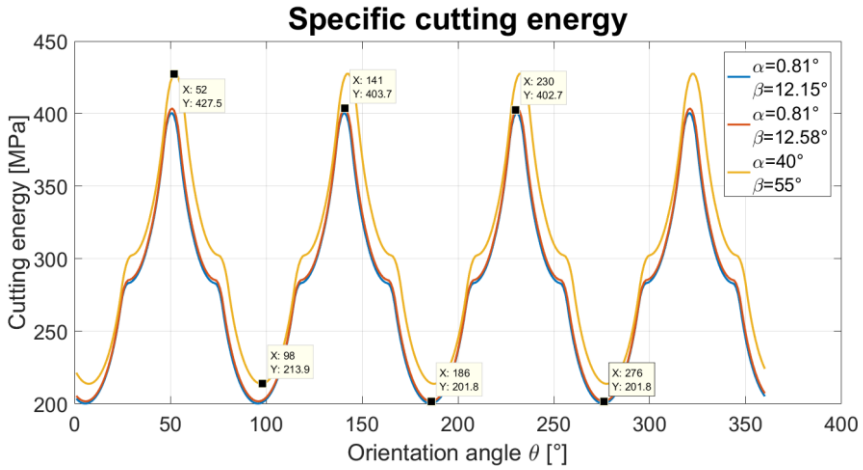


Figure 5.32. Comparison between the specific cutting energies obtained with Kota's tool geometry, and the tool used in the current study

One aspect that is not fully understood is the large amplitude between minimum and maximum Fx cutting forces. The analytical model in Chapter 4 predicted a ratio between these values of approximately 2. In Figure 5.32., it can be observed that the tool used in this research produces similar specific cutting energies as Kota's model, while the difference between maximum and minimum points of magnitudes have a ratio of 2, exactly as Kota's model.

However, the values obtained experimentally indicate a ratio of approximately 4. This cannot be explained by differences in the cutting tool parameters which were considered for the two analyses. In the analytical model used to generate Figure 5.32, the cutter is a turning tool with a rake angle α of 0.81° and a friction angle $\beta$of 12.58°. However, the cutter used in the present chapter has a more complex geometry, as illustrated in Figure 5.1. It may be that the mere analysis of the volume of the uncut chip thickness is not enough to surmise all the effects of the tool-workpiece interaction. The tool has a complex 3D geometry, which may interfere with the cutting plane illustrated in the model. This would, in effect, mean that there is an added level of complexity to the cutting force model, which hasn't thus far considered complex tools, but rather simple ones. In future studies, such geometries must be more in-depth investigated to the extent that more proficient analytical models could be computed. As such, a further analysis of the effects introduced by variation of cutting tool geometries should be explored. This will be further considered in Chapter 6.

Looking at material average, it is observed that single crystal Fx values are within 20 N averages, while multigrain values in 27 N. The average value of single crystal Fx forces is expected to be the same as that of multigrain. However, the 26% difference can be explained by looking at material purity. The multigrain copper material was scrap material, mixed with other elements, while the single crystal had a purity of 99.998%. The single crystal is thus much softer, and is expected to show a lower cutting force value.

Associated with the purity, what is unexpected is the tool plunge time. The tool plunge time is almost 0.1 seconds lower for multigrain, indicating a softer material. However, complex crystallographic phenomena associated with differences observed on the Z cutting direction can explain this. The slipping tool had a triangular shape, however it also had a complex lateral geometry necessary to detach chips on a forward motion with no rotation. This lack of symmetry from the side of the tool corresponds to the shearing planes being formed on different directions alongside the tool edges when the tool plunges into material. More insight is necessary in order to understand the tool plunge phenomena in single crystal cutting.

The channel cutting time respects, however, material purity assumptions, as the single crystal material was machined with 0.05 seconds faster than the multigrain.

Significant differences between single crystal and multigrain are observed in the channel cutting force profiles. Fx force readings indicate a steady, linear force development, corresponding to the main assumption that the channel is being machined along an arbitrary crystallographic direction. The linearity matches the assumption that the cutting direction is kept constant throughout shearing.

The surprising finding is the constant change of Fy profiles. Some channels exhibit a more linear profile, some a spiked profile, and some have a small wave formation. Due to a lack of in-depth knowledge of complex crystallographic phenomena associated with cutting force on the Y direction, this cannot be explained at the moment and causes motive for further investigation.

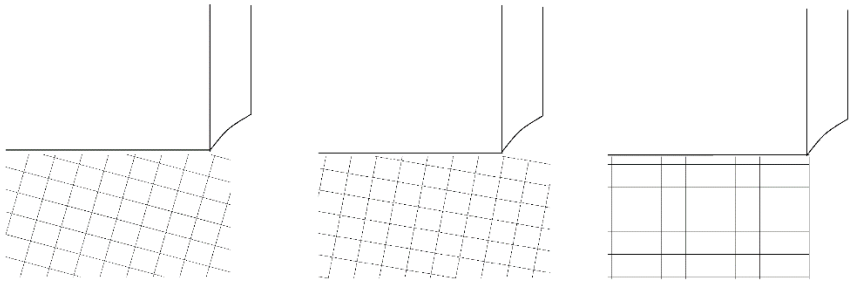


Figure 5.33. Scheme of slipping on a (001) crystal plane inclined at 15°, 10° and 0°

One possible reason is the interference of the measurement equipment. Especially considering the shape of Fy and Fz, which is similar to that of the dynamometer introduced error, one could assume the measurement is not accurate in these directions. To remove this doubt, a comparison has been established between the profile obtained for Fy in single grain and the profile obtained in multigrain cutting. The multigrain profile presents a linear shape, as theoretical assumptions indicate for multigrain cutting. This eliminates the doubt of equipment-induced errors, and signals towards material induced considerations.

The concave-convex combination profile indicated by the single grain results in Figure 5.28 corresponds more to an inclined crystallographic orientation, not to that of a (001) direction. As Y is perpendicular to X, it was anticipated to find a similar four-fold profile. However, perhaps due to the complex tool geometry, Fy is acting on a more complex crystallographic configuration than the radial force Fx.

This raises the need for further investigation to an even higher level: the complex shape and tool motion present in milling will have strong implications on the profile of the cutting forces associated with single crystal copper cutting.

5.8. Conclusion

Experimental set-ups have been proposed to enable orthogonal cutting through slipping of copper test pieces at 360° workpiece rotation. One experimental set-up was proven to induce errors, and based on complex calibration steps, the errors introduced by each equipment configuration have been analysed and mitigated.

Experimental trials have been conducted for multigrain and single crystal copper cutting at a 50 µm and 200 µm depth of cut. Cutting forces have been recorded for cutting 24 channels in arbitrary workpiece orientations.

Cutting forces vary significantly between multigrain and single grain cutting, and between the different depths of cut.

At a 50 µm depth of cut, the cutting forces are within the dynamometer limits of measurement and exhibit similar profiles, as shown in Figure 5.15. At a 200 µm depth of cut, the cutting forces increased above error levels.

An important finding is that in multigrain cutting, Fx, Fy and Fz forces displayed a linear profile, corresponding to material isotropic phenomena.

The main finding is that Fx, the radially-measured cutting force, presents a four-fold peak formation with a 90° repeatability, corresponding to the theoretical assumptions of four-fold symmetry in cutting force development on a (001) crystallographic plane.

Fy values indicate complex material and cutting direction phenomena which are the subject of further investigation.

This chapter proves that Fx forces differ significantly between multigrain and single crystal copper cutting. This justifies the need for more complex theoretical models for micro-cutting precision and for an updated stability analysis that includes material microstructure.

Due to empirical evidence of cutting force variation, cutting precision methods based on cutting force calculation in multigrain materials needs to be updated to include

material anisotropic properties for micro-scale specific procedures. For this reason, in the next chapter, cutting stability analysis will be advanced by including cutting force variation. Moreover, a comparison between analytical cutting forces and the one determined in the current chapter is necessary. This will help in understanding the limitations of material anisotropy assumptions and also allow for investigating their impact on cutting stability analysis.

Other than solely modelling work, this chapter proves the need for in-depth material consideration analysis. Complex phenomena on Fy and Fz profiles indicate the need for further investigation on material deformation. The symmetry and four-peak Fx force development drive this study towards analysing the symmetry in material deformation experienced when micro-cutting single crystal test pieces.

For these purposes, further chapters deal with the in-depth analysis of surface quality, burr formation, channel dimensional accuracy, plastic deformation, overall workpiece symmetry and chip formation, which are encompassed in a detailed material deformation study.

CHAPTER 6

CUTTING STABILITY ANALYSIS

6.1. Introduction

In stability analysis, critical depths of cut based on tool or workpiece rotations (in milling, respectively, in turning) can be established (Schmitz and Smith, 2009). These are used to determine which operating parameters can guarantee safe cutting processes, by avoiding chatter. Self-generated vibrations are produced at some spindle speeds, corresponding to a certain depth of cut. So far, no micro-cutting specific stability analysis has been developed, particularly one that considers the influence of the material microstructure. The first step in developing a new, micro-specific stability model is to establish whether the variation of cutting force in single grain materials can affect the classic, multigrain-specific stability lobes.

In this chapter, the effects of crystallographic anisotropy on a cutting process are investigated. In this respect, the cutting parameters values are not micro-cutting specific; rather, the investigation focuses on the differences introduced in a known cutting stability model by the variation of the cutting force. This is necessary as a first step in investigating whether instabilities can occur due to the effect of crystallographic anisotropy. As such, it can be stated that 'size effects', as a consequence of the relative differences introduced by a single grain cutting process, are hereby investigated.

In previous chapters, cutting force and shear angle variations have been theoretically modelled in order to demonstrate that they vary with crystallographic anisotropy when single crystal cutting is considered. Furthermore, cutting force variation within a 360° rotation of a single crystal copper workpiece has been demonstrated. This justifies the need to improve regular-scale cutting models and make them micro-level specific.

In this chapter, classic cutting stability analysis is applied to micro-cutting by incorporating single-crystal cutting principles. Cutting stability lobes generated by previous researchers (Schmitz and Smith, 2009) are employed in the new stability assessment. The effects of cutting force, shear angle and rake angle variations with crystallographic anisotropy are the input in the new stability models, as previously investigated in Chapter 4.

Differences between the classic multi-grain cutting force model and the new, improved stability model, based on single crystal formulation, are explored in order to determine whether at micro-level machining the classic model suffices or new stability analysis based on crystallography must be employed in order to obtain a better estimation of safe levels of chatter-free cutting. The evolution of the cutting force within one workpiece rotation is considered from the points of view of a multigrain, respectively a single grain material, and from analytical, as well as experimental results obtained in Chapter 4, respectively in Chapter 5.

In order to propose new stability models, the classic cutting model and the calculation of stability areas are described in the following section.

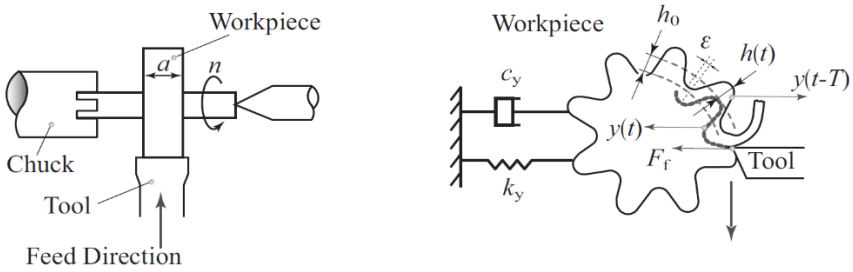
6.2. Regenerative chatter study in turning

6.2.1. Self-generated vibration in micro-cutting

The selected machining operation is turning, as it can easily be adapted to Kota's findings (2008) in orthogonal cutting based on a turning process.

In terms of the machining technique, the cutting tool employed in the process has the feed motion normal to the axis of a cylindrical test piece. The test piece is flexible in

the direction of feed, and the feed cutting force (F_f) causes it to vibrate, as illustrated in Figure 6.1.



Orthogonal plunge turning

Figure 6.1. Regenerative chatter vibrations in orthogonal cutting, from Figure 4.1. in Altintas (2012) p.126

The surface of the shaft pre-processing is smooth and no waves are produced during the first workpiece revolution. The second rotation produces a wavy machined surface due to the bending vibrations of the shaft in the feed direction Y.

The dynamic chip thickness is not constant, but it varies as a function of vibration frequency and the speed of the workpiece.

The general dynamic chip thickness can be expressed as follows:

$$h(t) = h_0 - [y(t) - y(t-T)] \tag{6.1}$$

where

h_0 is the intended chip thickness, which is equal to the feed rate of the machine, and

$[y(t) - y(t-T)]$ is the dynamic chip thickness produced owing to vibrations at the present time *t* and one spindle revolution period (*T*) before.

The dynamic chip thickness produces a cutting force of

$$F_f(t) = K_f a h(t) \tag{6.2}$$

where K_f represents the cutting force coefficient in the feed direction, and a is the depth of cut.

In stable cutting, the vibrations diminish from revolution to revolution. In unstable cutting, the vibrations grow from revolution to revolution until the tool loses contact with the workpiece.

The central relationship for this behaviour is:

$$a_{lim} = \frac{-1}{2K_f G(\omega_c)} \tag{6.3}$$

a_{lim} represents the maximum axial depth of cut for chatter vibration–free machining

$G(\omega_c)$ is the real part of the transfer function

and ω_c is calculated as

$$\omega_c T = 3\pi + 2\psi \tag{6.4}$$

Where ψ = phase shift of the structure's transfer function. The transfer function can be partitioned into real and imaginary parts:

$$\Phi(j\omega_c) = G + jH \tag{6.5}$$

The maximum axial depth of cut a_{lim} is plotted against the spindle speed. This graph represents the cutting stability diagram.

Any spindle speed and critical depth of cut pair (ω_c and a_{lim}) that appears above the plot line indicates *unstable* behaviour, while any pair below the boundary is assumed to be stable.

The cutting force variation with crystallographic orientation based on the feed cutting constant K_f depends on the fundamental value of the critical depth of cut.

Here, K_f is a function of the critical resolved shear stress τ_c , of the rake angle α , of the friction angle between the tool and the chip material β , and of the shear angle ϕ that was calculated based on the crystallographic procedure.

$$K_f = \tau_c \frac{\sin(\beta-\alpha)}{sin\phi \cos(\phi+\beta-\alpha)} \tag{6.6}$$

To the best knowledge of the author, no cutting stability analysis has been developed for micro-cutting specific models. By enabling K_f to include material microstructure effects, micro-cutting stability analysis would be possible.

6.3. Micro-cutting stability analysis proposed procedures

The fundamental difference between classic and micro-cutting can be reflected in the cutting coefficient K_f, which is a function of the critical resolved shear stress τ_c, of the

rake angle α , of the friction angle between the tool and the chip material β, and of the shear angle ϕ that was calculated based on the maximum work principle used in the crystallographic procedure.

In this chapter, the aim is to better understand the *fundamental differences* that may be reflect in cutting stability lobes designated for multigrain and single crystal materials, as it would occur in regular scale versus micro-level machining.

The key research question is: can classic cutting stability lobes be successfully used in single grain cutting to determine chatter-free operating parameters with the same level of accuracy as in multigrain cutting?

In the following four sections, fundamental differences occurring between multigrain and single grain cutting are explored and employed in generating new cutting stability lobes and evaluating their effectiveness in predicting chatter-free depths of cut.

These four approaches have not been studied before in the field of cutting stability analysis, and are the stepping stone in developing new models. The first stages are to define new procedures in which cutting stability incorporates material microstructure factors. In future studies, it could be possible to validate such procedures by performing experimental trials that can endorse the models. At this stage, some material microstructure-related factors are analysed and their effect on cutting stability lobes is evaluated as follows.

6.3.1. Calculation of new cutting stability factor based on tool cutting edge radius-generated process instability

In the first instance, the idea stemming from Chapter 4 is more largely investigated. When machining a single grain material, the tool is not perfectly sharp and will thus cut through several crystallographic directions, as illustrated in the Figure below. A portion of the machined material will undergo processing. Proposing using the root mean square of the cutting forces and, respectively, the cutting coefficients on those crystallographic directions can lead to a more accurate value for the cutting coefficient.

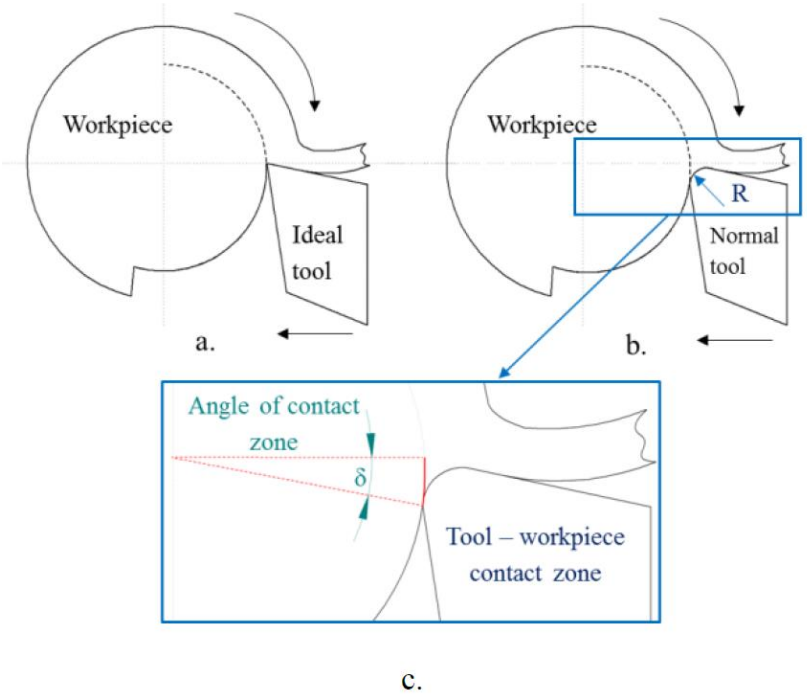


Figure 6.2. Cutting scheme: a. turning model assumes a perfectly sharp tool; b. regular tool, with a cutting tool edge radius *R;* c. detail of tool-workpiece contact zone

Generally, the feed force coefficient K_f is obtained for an entire rotation. For example, for Kota's copper cutting model, K_f would take the values illustrated in the plot in Figure 6.3.

The next step is to determine the angle measured from the centre of the cylindrical test piece to the limits of the workpiece – tool contact zone.

This angle δ represents a part of the orientation angle θ, and is a function of the tool cutting edge radius.

It is assumed that

$$\delta = R \tag{6.7}$$

where *R* is the cutting tool edge radius and is to be measured before experimental work.

Based on relative position between the tool and the workpiece, and based on the cutting tool edge radius *R*, the feed force coefficient K_{rms} is calculated as the root mean square of the values obtained for the selected orientation δ.

$$K_{rms} = K_f(\delta) \tag{6.8}$$

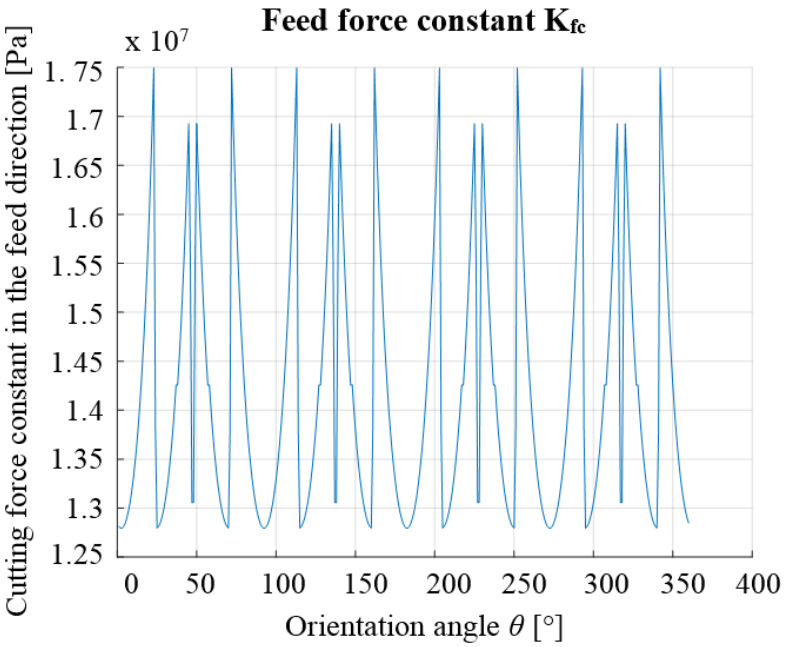


Figure 6.3. Feed force constant evolution in a 360° workpiece rotation

The feed force coefficient K_{rms} is then introduced in the critical depth of cut equation to general the new cutting stability lobes:

$$A_{lim} = \frac{-1}{2K_{rms}G(\omega_c)} \tag{6.9}$$

Based on this last equation, A_{lim} or the critical depth of cut is generated. Plotting this value against the spindle speed Ω results in regular cutting stability lobes, as previously illustrated in Figure 4.22 at the end of Chapter 4. However, this small step only provides the difference that tool sharpness and the roundness of the cutting tool edge introduce. The scale of crystallographic-influenced factors is larger, and can affect all the parameters that are used in the calculation of K_f.

The next three sections of the chapter illustrate more significant changes, at the level of the entire single crystal.

6.2.2. Instability generated by the variation in the cutting force

In this section, cutting stability lobes present the limitations of adopting a single-force value when cutting is done within a single grain of material. In order to validate this aspect, analytical force models developed in Chapter 4 are employed in order to better understand their effect on stability analysis. Consequently, the single grain and later

the multigrain force variation obtained in the experimental work done in Chapter 5 is applied in the procedure. Lastly, a comparison is drawn between the levels of critical depth of cut obtained with these three steps and their impact on adopting new procedures in stability analysis.

6.3.1.1. Cutting stability analysis based on theoretical cutting force within a single crystal material 45° rotation

In Chapter 4, several crystallographic planes have been investigated in order to identify the changes occurring in cutting forces during a 360° single crystal workpiece rotation.

For the rest of the sections, only cutting forces determined for the (001) crystallographic plane and their respective input parameters are considered.

Figure 4.12.a in Chapter 4 illustrates a four-fold evolution of the cutting force. Additionally to the 90° pattern repetition, cutting forces appeared mirrored at the 45° mark. For this reason, cutting force variation will be considered for a section of a 0° to 45° workpiece rotation, as this would suffice in illustrating changes in cutting stability analyses, and the rest of the crystallographic orientations can be extrapolated from these results.

In order to eliminate the need for operation-specific parameters (such as depth of cut, necessary in both crystallographic anisotropy evaluation as well as in cutting stability), only the ratio between cutting force evolution and mean of all possible crystal orientations on the (001) is considered.

In classic stability lobes, the cutting force is generated based on a shear angle corresponding to all possible crystallographic orientations, or a multigrain isotropic material. The examples below are based on Schmitz and Smith's (2009) models for turning stability analysis, and the factors proposed in their calculation.

The shear angle φ was obtained based on Merchant's cutting principles, and has a value of 45°, which corresponds to multigrain materials.

Looking at the minimum and maximum cutting forces in a single crystal material, two-times increase between the values is calculated. The maximum (according to Figure 4.12a in Chapter 4) also belongs to a workpiece orientation of 45°. An initial

comparison is drawn in the graph below, in order to get a preliminary image of the differences between multigrain, minimum and maximum cutting forces.

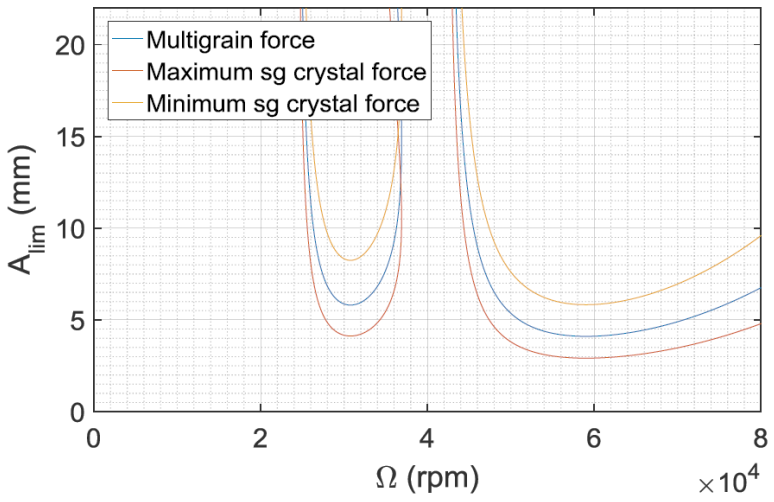


Figure 6.4. Investigation of the cutting stability lobes values for minimum, maximum and average (multigrain) cutting forces developed on the (001) plane

A 2 mm difference on the vertical direction between multigrain, minimum and maximum single crystal forces can be observed in the points furthest apart on the three generated lobes. The multigrain cutting force accounts for a safer area of cutting, as it establishes safe areas of cutting well under the zones indicated by minimum single crystal forces. However, this also implies that a higher depth of cut was achievable with the same operating parameters. A difference of 2 mm can be reflected in a higher productivity, lesser tool wear (due to reduced tool passes), and lesser time necessary to machine a certain product.

This chart was generated only for the first iteration of cutting stability analysis. In the next Figure, two additional sets of cutting stability lobes are generated.

The differences generated by ratios of cutting forces obtained between 0° to 20° workpiece rotation are plotted. This is done to comply with 5° increments and analyse whether differences between cutting stability lobes are constant, or whether they change.

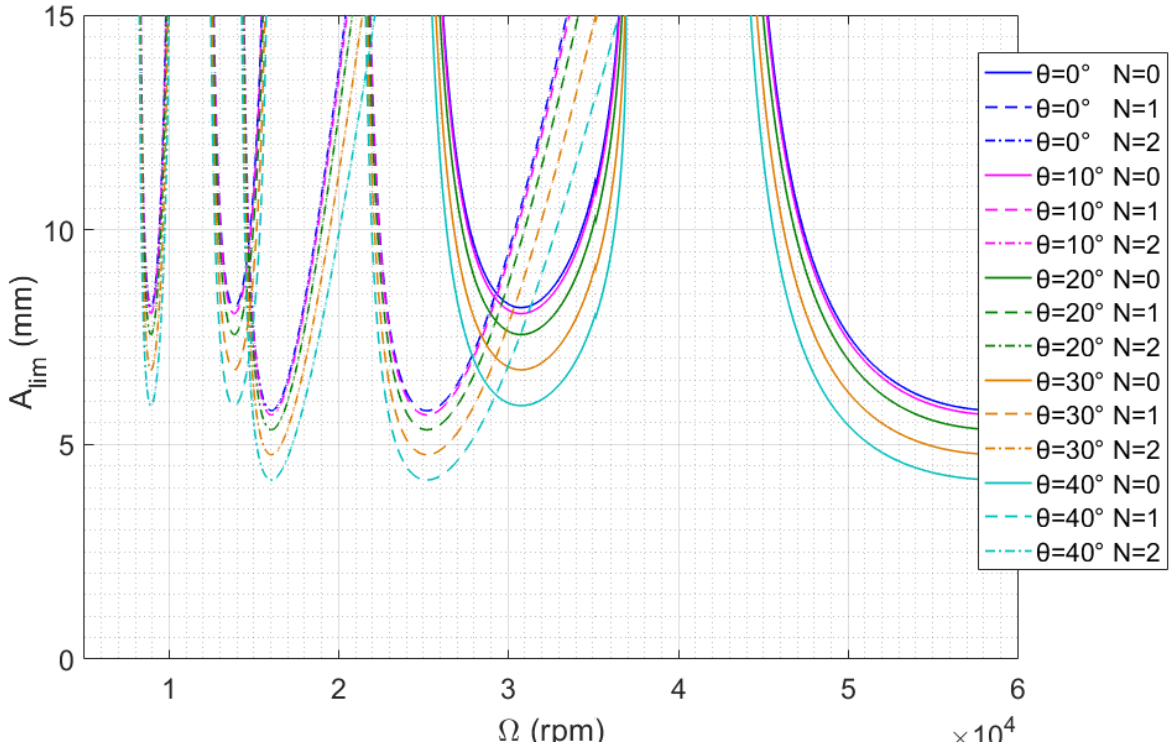


Figure 6.5. Cutting stability lobes generated for a 0° to 20° workpiece rotation generating an incremental cutting force variation

In the image above, it is possible to see a relatively constant change in the critical depth of cut between the 20° and 10° segment. However, the difference severely decreases in the interval 5° to 0°. This denotes that the cutting forces corresponding to a 0° to 5°, respectively 85° to 90°, workpiece rotation and their homologues positions on the (001) plane vary to a little extent, at about 5% of the possible difference. The rest of the increments correspond to more evenly distributed changes, and it can be recognised that for the 10° to 20° sector the change is incremental as well. The minimum and maximum values remain between the 6 mm and 8 mm bounds.

To obtain a complete image on the apparent incremental changes of cutting stability lobes due to cutting force increase, only the first set of lobes is generated for the entire 0° to 45° increments in Figure 6.6.

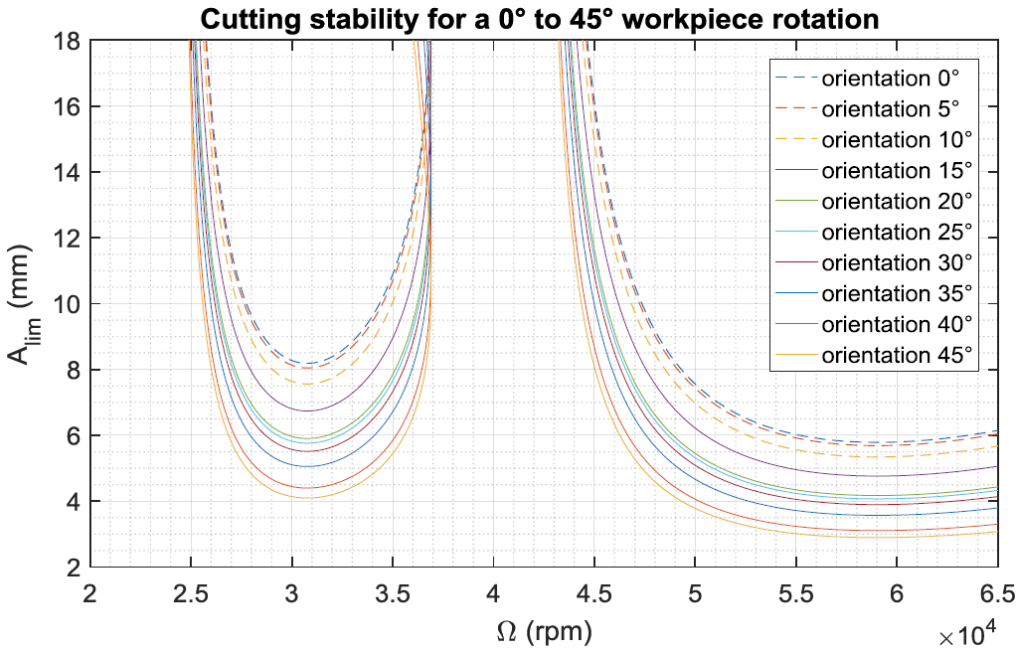


Figure 6.6. Cutting stability lobes generated for a 0° to 45° workpiece rotation with 5° increments

The lowest point found on the first cutting stability lobes corresponds to a value of 4.097 mm, while the highest on the same position to 8.1988 mm. This tallies well with cutting force evolution between minimum and maximum values.

However, this also indicates that cutting stability lobes are insufficient in estimating the entire area of safe regions that can be processed. At 8.1988 mm, the discrepancy in estimating the capability of critical depth of cut is 41.16%.

Also, the cutting stability lobes cannot estimate the variance generated by the higher cutting forces, at ratios above 1. The maximum ratio plotted in Figure 6.6 was 1, with low values for the first lobe at 5.808 mm. However, all the cutting forces with ratios above that generate lower stability lobes, down to minimums of 4.097 mm. The difference between amplitudes is 1.711 mm, and it enforces the need to determine the crystallographic direction and adjust the cutting stability lobes. Another alternative would be to adopt the lowest level of cutting stability lobes, which corresponds to the highest values obtained in the cutting force.

6.3.1.2. Cutting stability analysis based on experimental cutting force within a single crystal material 360° rotation

The next step is to investigate the amplitude of the cutting forces determined experimentally in Chapter 5, Figure 5.27. Again, ratios are calculated based on individual readings of the 24 values of the cutting force and their average. The results are divided into 'sectors', or 90° workpiece segments corresponding to 6 channels each, as shown in Table 6.1.

Table 6.1. Ratios between radial cutting force Fx measured on single crystal copper cutting at 200 μm depth of cut and average of the force

Channel no.	1	2	3	4	5	6
Sector 1	0.65	1.49	1.91	1.41	0.9	0.44
Sector 2	0.75	1.64	2.18	1.36	0.90	0.47
Sector 3	0.56	1.22	1.37	1.12	0.61	0.25
Sector 4	0.44	0.90	1.17	1.01	0.78	0.33

Next, the same procedure is applied in obtaining new cutting stability lobes. Only the first iteration of the cutting stability lobes proposed by Schmitz and Smith (2009) is considered. The cutting coefficient K_f is multiplied by a value of 1 (corresponding to an isotropic material), and indicated in the figures below with a dark blue line, for comparison purposes.

The rest of the lines are obtained by multiplying the cutting coefficient with the cutting force ratios, as in the previous section. The graphs have been separated in 4 plots to analyse the differences occurring in the four distinct test piece 90° segments.

On the newly generated graphs, the lowest points on the first stability lobe, corresponding to each channel, have been measured. Consequently, the ratio between the amplitude (maximum and minimum points) has been calculated. Moreover, the ratios been the maximum or minimum point and the average value corresponding to multigrain (5.808 mm) have been calculated for each sector. This would give an insight of the general amplitude, as well as maximum-average and minimum-average distribution points. Results are indicated in Table 6.2.

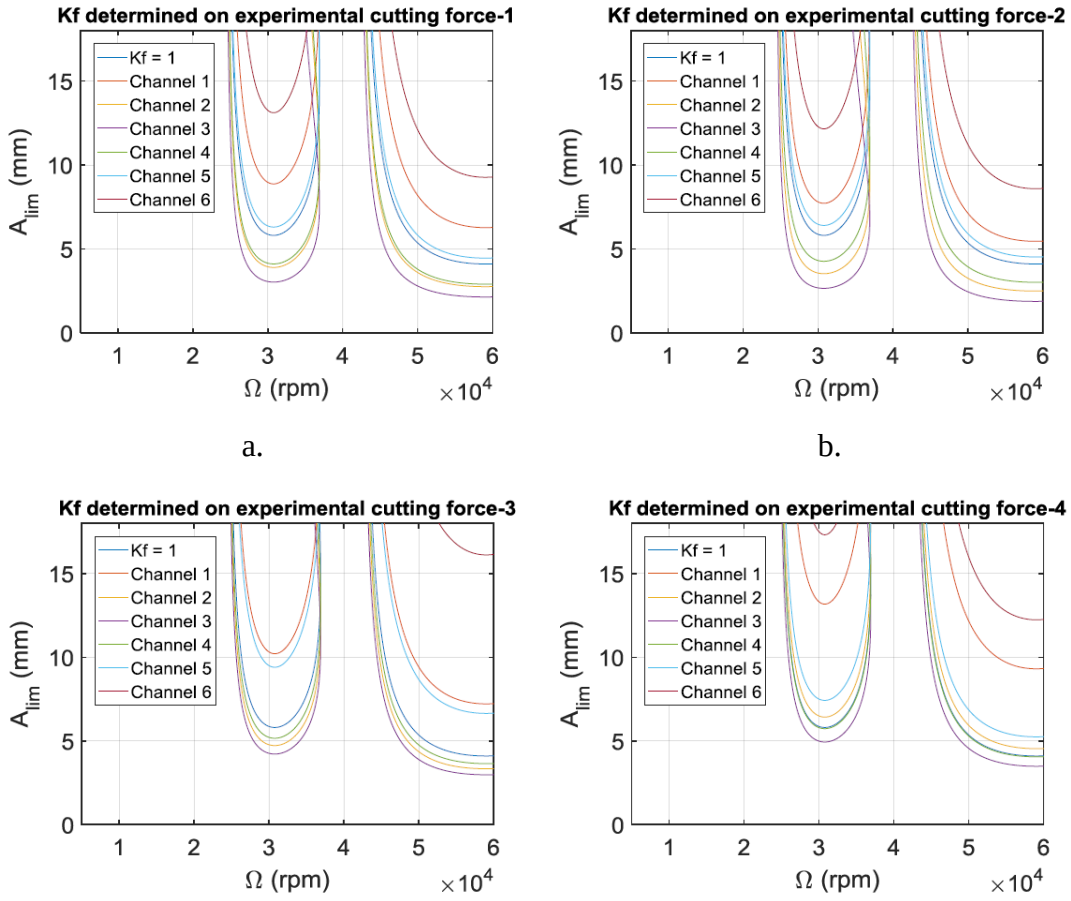


Figure 6.7. Cutting stability lobes generated with cutting forces measured in single grain copper cutting: a. Sector 1; b. Sector 2; c. Sector 3; d. Sector 4.

Table 6.2. Amplitudes between the maximum, minimum and multigrain values measured on the first cutting stability lobe generated with experimental single grain force

	Ratio between max/min	Ratio max/average	Ratio min/average
Sector 1	4.33	2.25	0.52
Sector 2	4.58	2.09	0.45
Sector 3	5.40	3.92	0.72
Sector 4	3.50	2.98	0.85
Average	**4.45**	**2.81**	**0.63**

Averages are generated for the ratios between maximum and minimum points and between maximum or minimum points and regular cutting coefficients, as shown in Table.

These measurements indicate a very high variation between extreme amplitude points. The ratio between maximum and minimum generated on the stability lobes is 4.45, compared to a ratio of 2 in the analytical model. The ratio generated for single crystals in the previous section was 2.0011.

The absolute lowest point was measured in Sector 2, Channel 3, with a value of 2.65 mm. The highest point was in Sector 3, Channel 6, with a value of 22.81 mm.

By using cutting forces measured for single grain micro-cutting in Chapter 5, a +181.51% and -36.13% discrepancy is generated in the classic cutting stability values. In the previous analytical section, the discrepancy was found to be +41.16% and -29.45%.

However, the lowest value is the one of interest, as that signifies the maximum acceptable level of depth of cut which leads to a stable cutting process. Anything higher than the lowest value would generate chatter for unknown crystallographic directions.

6.3.1.3. Cutting stability analysis based on experimental cutting force within a multigrain material 360° rotation and comparison with single crystal results

The same procedure as in section 6.2.2.2. is applied in determining the influence of multigrain force variation on cutting stability lobes. Based on the force values presented in Figure 5.27 in Chapter 5, ratios are obtained between the 24-force point values and their average, as indicated in the Table 6.3.

Based on these coefficients, new cutting coefficients are calculated and new stability lobes are generated for the four 90 °sectors of workpiece material, as shown in Figure 6.8.

The absolute lowest point has been measured in Channel 1, Sector1, with a value of 4.48 mm. The highest absolute point has been measured on Channel 6, Sector 1, with a critical depth of cut of 6.63 mm.

Table 6.3. Ratios between radial cutting force Fx measured on multigrain copper cutting at 200 µm depth of cut and average of the force

Channel no	1	2	3	4	5	6
Sector 1	1.29	1.07	0.91	1.06	0.87	0.89
Sector 2	1.00	0.93	1.03	0.89	0.91	0.99
Sector 3	0.92	0.88	0.96	1.13	1.08	0.98
Sector 4	1.01	1.00	1.09	0.94	1.09	0.97

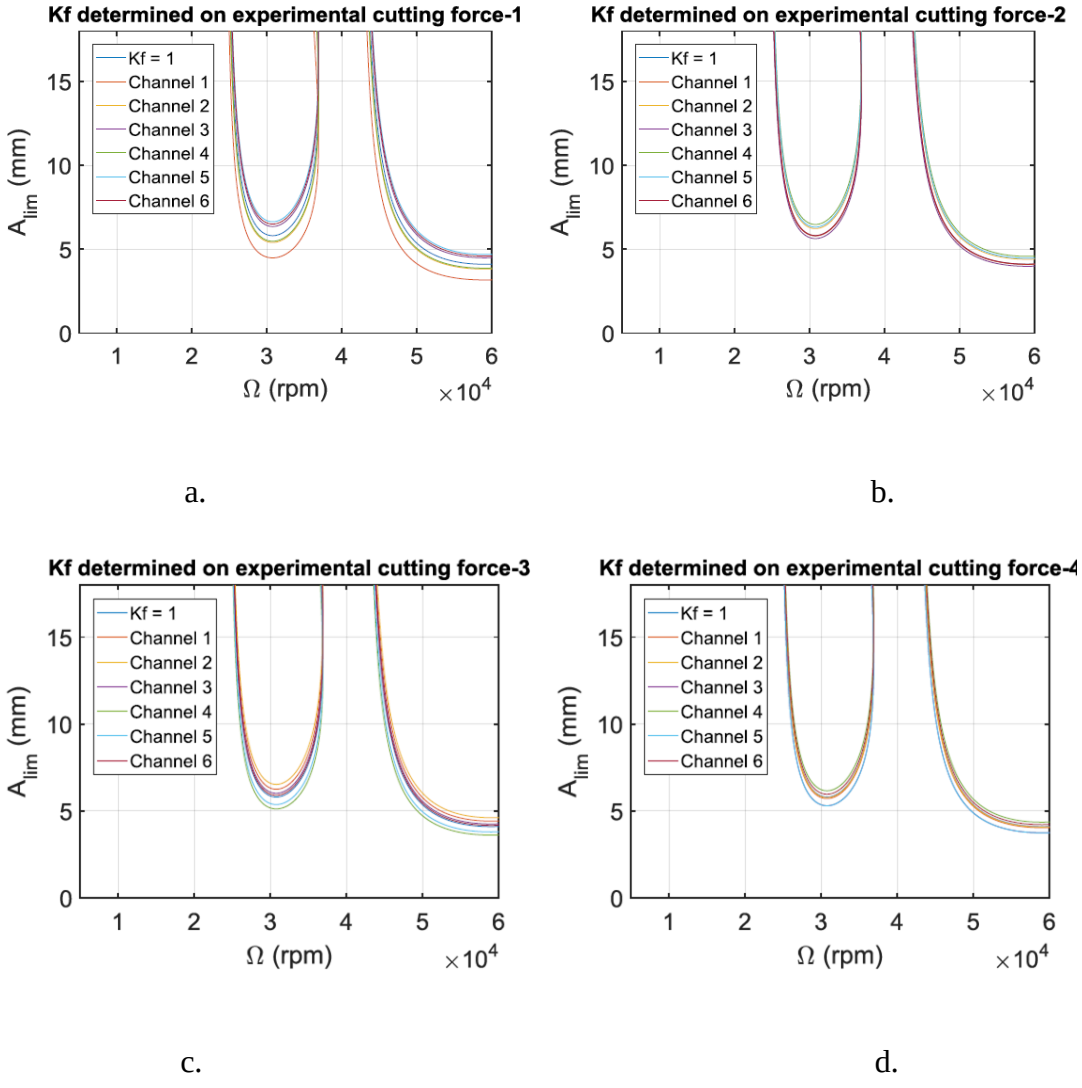


Figure 6.8. Cutting stability lobes generated with cutting forces measured in multigrain copper cutting: a. Sector 1; b. Sector 2; c. Sector 3; d. Sector 4.

Table 6.4. Amplitudes between the maximum, minimum and multigrain values measured on the first cutting stability lobe generated with experimental multigrain force

	Ratio between max/min	Ratio max/average	Ratio min/average
Sector 1	1.47	1.14	0.77
Sector 2	1.14	1.11	0.97
Sector 3	1.27	1.12	0.88
Sector 4	1.162	1.06	0.91
Average	**1.26**	**1.11**	**0.88**

From the lowest point measured on the first cutting stability lobe, averages of the ratios between maximum and minimum points and between extreme points and regular multigrain theoretical cutting coefficients are determined as shown in Table.

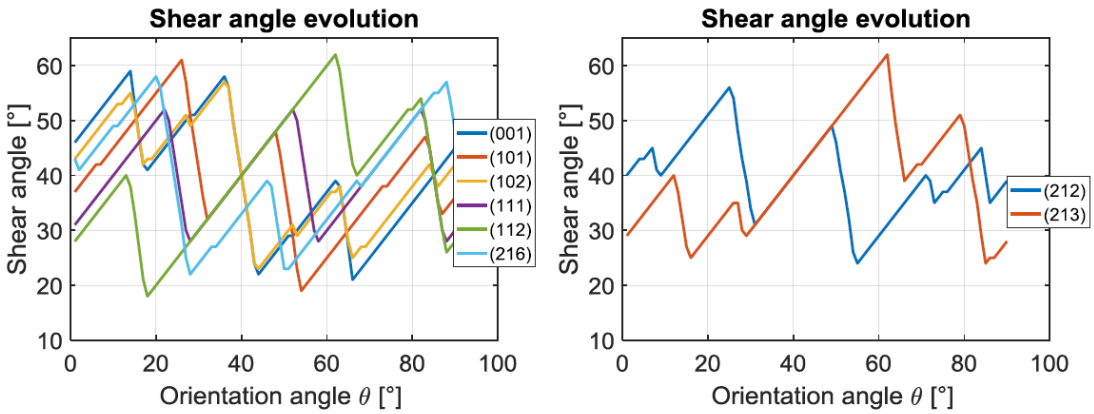
The conclusion of these measurements is that cutting forces measured for multigrain micro-cutting in Chapter 5 generate a +11% and -12% discrepancy in the cutting stability values. The amplitude between the maximum and minimum points measured is 1.266, much lower than the amplitudes obtained in analytical and experimental single grains. The current discrepancy can be attributed to cutting force measurement errors. As such, a ±12% error could be accepted for multigrain micro-cutting stability lobes.

However, the cutting force is not the only parameter that varies with crystallographic orientation. As such, two more factors are investigated from an analytical point of view, to explore which is the lowest acceptable limit at which cutting stability lobes in a single crystal could be generated.

6.2.3. Instability generated by the variation in the shear angle within a single crystal material 90° rotation

In a similar approach as in previous sections in this chapter, the differences introduced by shear angles are explored.

The relevance of shear angle variation is illustrated in Figure 6.9. In the first image, six crystallographic planes present highly different values of shear angles. In the second image, it can be seen that the position of different maximum and minimum points on the shear angle orientation graph with respect to crystallographic orientation introduces parametric variabilities.



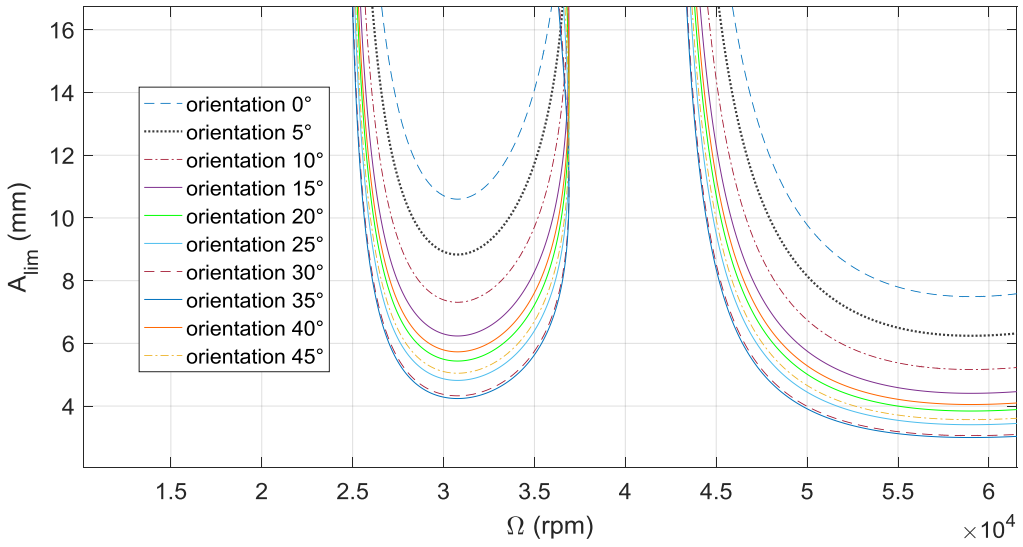
a. b.

Figure 6.9. Shear angle evolution in a 90° segment based on the analytical model described in Chapter 4: a. on the crystallographic planes (001), (111), (101), (112), (216) and (102); b. comparison of evolution and change of phase on planes (212) and (213)

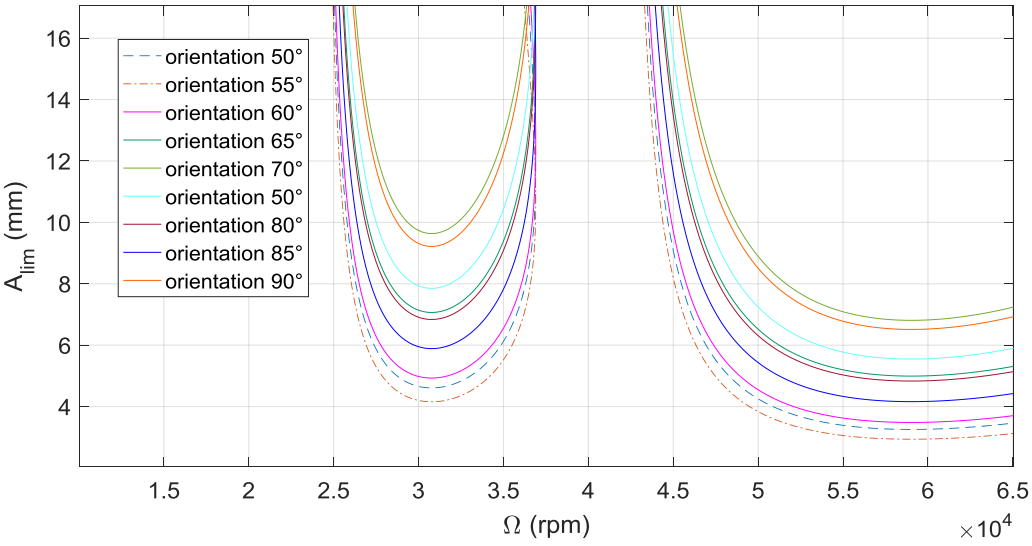
Previously, the cutting force impact has been estimated, due to the dependence of the cutting coefficient K_f on the cutting force.

However, the factor K_f is based in its calculation on the shear angle value. Thus, if the shear angle evolution is considered as a ratio between shear angle values obtained in Chapter 4, and the mean shear value, then it would be possible to establish new cutting stability lobes that include the shear angle variation.

The minimum and maximum critical depths of cut obtained in Figure 6.10.a on the first stability lobe are 4.241mm and 10.6 mm. The minimum and maximum critical depths of cut obtained in Figure 6.10b on the first stability lobe are 4.16 mm and 9.638 mm. These give extreme values of 4.16, respectively 10.6 mm according to shear angle variation on the (001) plane. The ratio between the extremes is 2.548. The multigrain value lies close to the 20° workpiece orientation, in Figure 6.10.a, at 5.808 mm. The classic cutting stability lobes prove ineffective by 1.648 mm difference on the critical depth of cut scale.



a.



b.

Figure 6.10 Cutting stability analysis based on 5° increments of the shear angle obtain on a 90° workpiece rotation of a (001) oriented single crystal: a. orientations 0° - 50°; orientations 50° - 90°

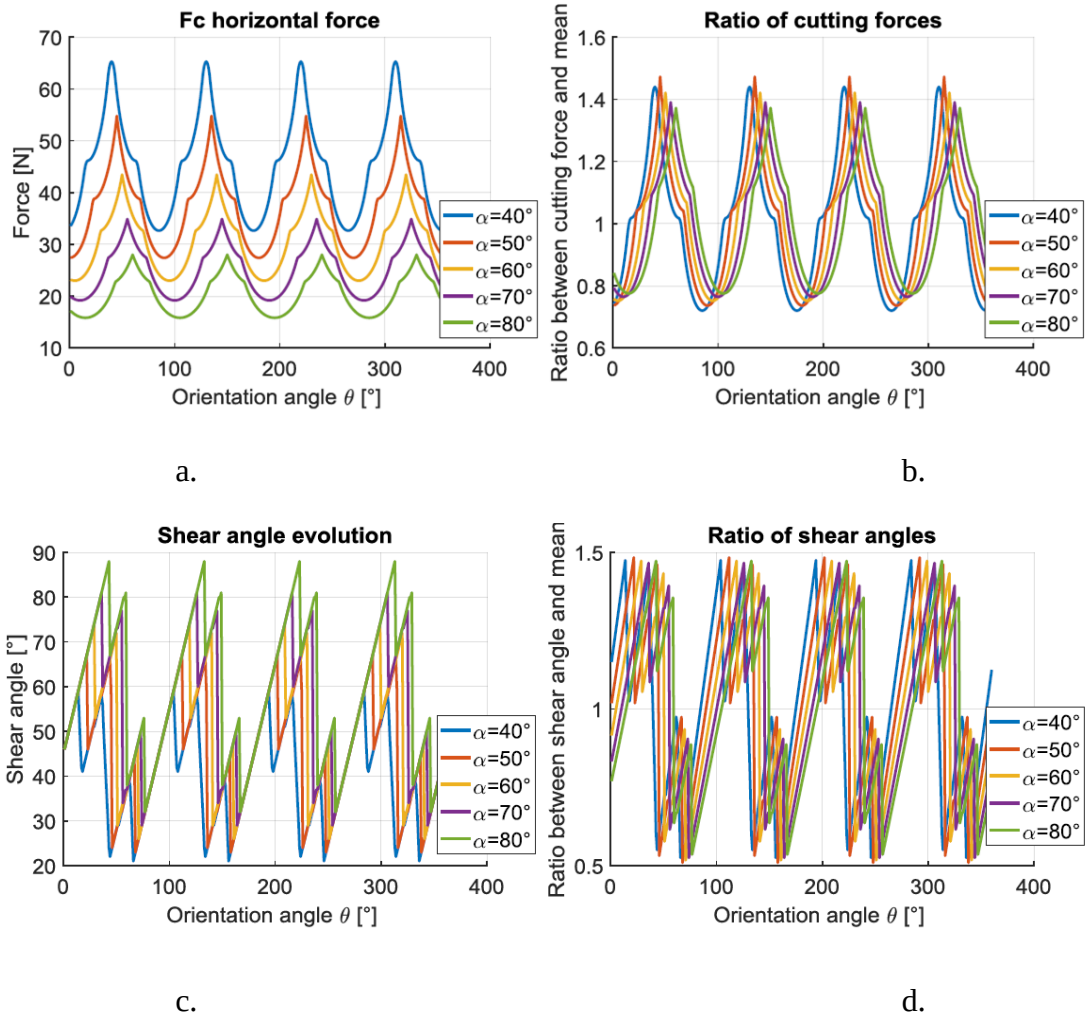
Compared to the results obtained in section 6.2.1, the lowest cutting stability lobes (and thus the safest irregardless of single crystal orientation) are obtained by cutting force estimation. However, they are both in the region of 4.1 mm. The shear angle provides a much ampler area of cutting stability capability, with highest values over

10 mm. This signifies that classic stability lobes are 54.7% ineffective when estimating the capability of critical depths of cut.

6.2.4. Instability generated by the differences in the rake angles

As seen in the previous section, shear angles are the ones that introduce the highest variability in cutting stability lobes. However, there are operational factors that influence shear angles, cutting forces and cutting coefficients when altered.

One such factor is the rake angle of the tool.



a. b.

c. d.

Figure 6.11. Instability generated by the differences in the rake angles: a. differences at the level of Fc horizontal force estimations; b. differences at the level of ratios of Fc horizontal force; c. differences at the level of shear angle estimations; d. differences at the level of ratios shear angles.

While the rake angle α has a constant value due to its physical generation on the cutting tool, the relative difference due to size effects (such as described in section 6.2.1.) can make the rake change value. It is known that rake angles with negative values (at over the 90° of the tool) generate ploughing.

Rake angle incremental changes are applied to a similar linear model in estimating the differences between cutting forces and shear angle ratios. The results are shown in the images below, with a highlight on the rake angle α variation between 40° (Kota's model) and 80°. The influence of the negative rake angle value is yet to be investigated.

From the charts, it is possible to note that rake angles introduce a variation on both force and shear angle evolutions. Their profile remains similar, however their position with respect to workpiece orientation changes with up to 20° for cutting force ratios, and with up to 30° for shear angle ratios. Maximum and minimum magnitude, however, remain similar, particularly for shear angle ratios. These results for minimum, maximum values and change in positions are illustrated in the Tables below:

Table 6.5. Cutting force variation introduced by rake angle differences

Point type	Orientation position [°]	Force [N]	Difference between positions	Force ratio max/min
Min	102	125.74		
Max	57	224.19	45	1.78
Min	97	151.11		
Max	52	278.45	45	1.84
Min	92	180.28		
Max	47	348.24	45	1.93
Min	87	214.74		
Max	42	428.87	45	1.99
Min	82	256.76		
Max	37	513.17	45	1.99

Table 6.6. Shear angle variation introduced by rake angle differences

	Shear angle ratio between shear value and mean for each iteration					
Rake angle value	Maximum	Minimum	Ratio max/min	Position max	Position min	Difference between positions
40°	1.45	0.54	2.65	7	65	58
50°	1.46	0.53	2.77	15	67	52
60°	1.48	0.51	2.87	24	69	45
70°	1.47	0.52	2.81	31	72	41
80°	1.46	0.53	2.76	38	75	37

From the previous sections, it has been established that a variation of 20° or 30° on the workpiece orientation can generate differences in the cutting stability analysis of more than 6 mm (e.g. shear angle variation between 0° and 30°, Figure 6.11.d.

This is proof that rake angles have to be monitored and investigated in relation to the crystallographic plane and workpiece orientation, as there is potential of affecting the results by up to 30° in workpiece positioning.

6.3. Conclusion

In this chapter, differences introduced by the material microstructure have been considered when generating cutting stability lobes.

Shear angles, cutting forces and tool rake angles have all been found to influence maximum and minimum levels of critical depths of cut. The highest disparity has been observed in stability analysis based on single crystal cutting forces and shear angle variation, where the ratios between extreme values have been respectively 4.45 and 2.548.

Classic cutting stability lobes have been employed in order to calculate ‘safe’, stable cutting regions for a wide range of workpiece orientations. However, the multigrain low level on the first stability lobe is estimated at 5.808 mm, while cutting force and shear angle-based new cutting stability lobes have generated minimum values of approximately 4.1 mm in analytical estimations and 2.65 mm in empirical estimations. This means that the classic cutting stability lobes could be unsuccessful in estimating 1.7 mm and 3.15 mm of dangerous areas of cutting depths, while also being ineffective in generating higher safe regions of depths of cut for other crystallographic orientations.

In terms of applicability of this new findings, both newly established limits shed light on the potential importance of some factors in reducing processing cost and also improve productivity. The lower stable limits of depth of cut indicate that the overall stability limit is much lower for single crystals. Chatter can occur at a lower limit of 70% or 45% of the classic cutting value, affecting the workpiece material surface quality. Deburring operations would significantly affect the cost of the operations. In terms of the higher stability limits established for some crystallographic orientations, these would affect the process productivity; if higher stable depths of cut can be achieved, then the process would take less steps and the time necessary to machine a feature would decrease.

Based on this new understanding, it is established that if cutting stability lobes are kept at the lowest level of the single grain results (corresponding to the highest values of cutting forces and shear angles), the area of cutting would be chatter free. However, it has been revealed that the cutting stability lobes do vary with crystallographic anisotropy, particularly in relation to single grain-specific cutting forces, and to shear angles. These new cutting stability models can lead to increased productivity due to models providing an ampler safe-to-process area of cutting. Future research is now better informed because of these new novel findings, and it has opened up many research questions that should be answered.

This chapter has established correlations between crystallographic anisotropy models and parameters, and new micro-cutting specific stability lobes. Previous research done by Afazov et al. (2013) has investigated operating and process parameters effects on micro-milling cutting stability lobes. One of the main parameters found to influence stability limits was the tool rake angle, as illustrated in Figure 6.12. At arbitrary points,

the stability limits were 10 µm for the 0° rake angle, respectively 25 µm for 8°. This research supports the new findings identified in the current chapter, particularly in section 6.2.4.

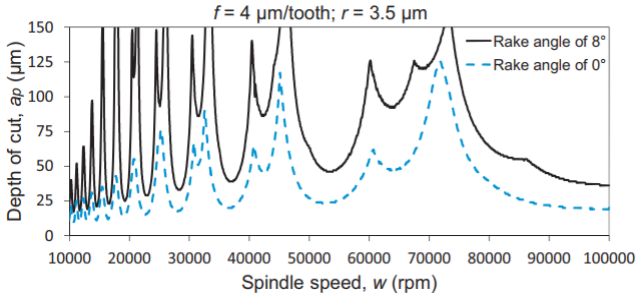


Figure 6.12. Stability lobes variation with rake angle. From Afazov et al. (2013): Figure 16.a, p. 682

An interesting direction for future research would be to demonstrate these correlations experimentally, and determine which factor out of cutting forces and shear angles is more influential in estimating stable, chatter-free zones of cutting. Some difficulties are anticipated in providing a definitive stability analysis model for single crystal materials in turning or milling operations at this stage, due to complex tool geometries, and tool or workpiece motions. The intermediary stage that is necessary before experimental validation in milling or turning is understanding the micro-cutting process that employs the simplest tool motion, tool geometry and constant operating parameters. It is only after this is fully understood that cutting stability assumptions can be tested in the micro-cutting of single crystals. As a means of understanding micro-cutting stability, orthogonal cutting while employing a straight feed-forward tool path, no rotations and constant operating parameters (constant speed and depth of cut) is proposed, with no rotations. The variable is single crystal orientation, while the parameters that need to be fully assessed are machined surface phenomena that affect cutting precision, stability and repeatability.

CHAPTER 7

CONTRIBUTIONS TO MATERIAL PHENOMENA UNDERSTANDING BY CONSIDERING EXPERIMENTAL INVESTIGATION OF SINGLE CRYSTAL COPPER ORTHOGONAL CUTTING

7.1. Introduction

The purpose of this chapter is producing a comprehensive study of material phenomena in micro-cutting. The research question is whether machined surface accuracy, at constant operating parameters (such as constant cutting speed and depth of cut), can be determined based on single crystal properties during micro-cutting. By answering this question, it would be possible to effectively predict chip and burr formation in single crystal cutting, positively impacting product quality and the cost of production.

A programme for material investigation is proposed in the schematic in Figure 7.1, which highlights the motivation for each experimental investigation, and the correlation between different methodology steps.

The three main parameters that are identified to produce a new and improved understanding of micro-machined material phenomena are:

- Chip formation
- Burr formation

- Material phenomena repeatability.

As such, this chapter is constructed around the analysis of these three main parameters.

One of the main differences that needs to be addressed is the one between the results of:

- Single crystal material cutting and
- Multigrain material cutting.

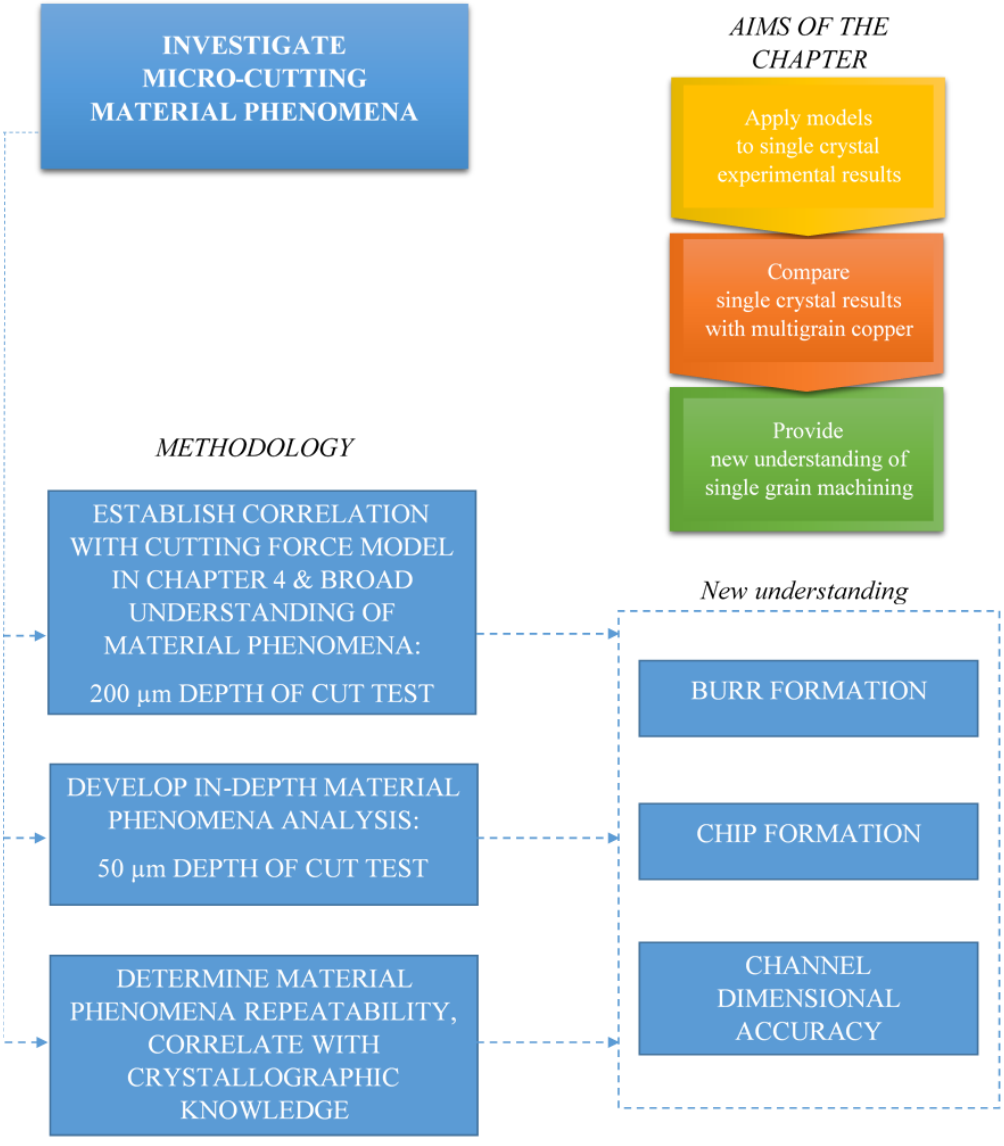


Figure 7.1. Chapter outline

This has been analytically studied in Chapters 4 and 6. Moreover, the cutting force variation between the two different materials has been validated in Chapter 5.

Those past findings lay the groundwork for the four experimental steps necessary in the analysis of micro-machined material phenomena.

7.2. Method of experimental analysis

Previous studies, including these given examples, have aimed at explaining material deformation mechanisms in single crystal cutting. However, the main knowledge gap remains the correlation between observed material behaviour and analytical models according to crystallographic anisotropy. This becomes the main goal of the current chapter: to observe material phenomena in single crystal micro-cutting and to establish a relationship with anisotropic findings, such as cutting force and shear angle models.

In cutting, the most difficult step is to isolate one investigated parameter from the influence of others involved in the process: machine tool vibration, tool motion, tool geometry, tool path, workpiece clamping system etc. It is of utmost importance, when investigating material phenomena, to try and keep these parameters constant. When this is not possible, it is important to understand which of those parameters have produced certain results: which can be attributed to process parameters, and which to material behaviour. Only by minimising the influence of cutting tools, cutting tool geometries, operating parameters and other process-induced parameters it is possible to observe and measure the influence of the material microstructure.

The current chapter describes the experimental procedures followed for all the experimental steps, from workpiece surface preparation and measurement, to the acquisition and analysis of experimental results. Tests have been carried out and repeated in order to ensure the accuracy and repeatability of data.

The experimental procedure is the one followed in Chapter 5. Micro-cutting experiments have been carried out on single and multigrain copper discs, by scratching the surface with a slipping tool at a cutting speed of 900 m/min. Previously, in Chapter 5, the measurements of cutting forces have been determined. In the current chapter, the analysis focuses on material phenomena.

Other resolutions after the initial set of experiments have been to characterise material phenomena based on: exit burr formation, lateral (Poisson) burr formation, ploughing and plastic deformation on the channel walls and channel dimensional accuracy. Exit burr formation is correlated with the exit chip, as it allows chip twist (helix)

observation and it builds on chip formation phenomena. Lateral burr formation and wall ploughing can be correlated with chip bending (on the XY plane of cutting). Channel dimensional accuracy enables surface quality characterisation of a micro-machined feature. Data resulting from the first two phases of experimental trials are included in material microstructure considerations for micro-cutting of single crystal copper.

Due to the large volume of data, tables containing images and measurements for the 24 or 60 channel samples are included in Appendix A. However, the data is found in graphs and plots presented in each subsection, and Appendix A can be consulted for a more detailed analysis.

7.3. Equipment and procedures

The equipment, procedures and materials used in micro-cutting, presented in chapter 5, remain the same. However, the material is undergoing several steps of post-processing characterisation, which include measurement and imaging with SEM and white-light interferometry, followed by processing the data in Excel statistical and Matlab programs.

A brief description of the equipment used is given in the section below.

7.3.1. Equipment

- Hitachi S-2600N Variable Pressure Scanning Electron Microscope (VPSEM)

The Hitachi Scanning Electron Microscope allows imaging of either secondary electrons (SE mode) or backscattered electrons (VP mode). The equipment benefits from integration of an X-ray detector coupled to Quartz Imaging Systems XOne software, which allows collection and processing of data used in full spectrum Energy Dispersive X-ray analysis (EDX). The pressure range of the equipment varies between 1 Pa and 270 Pa, while the resolution in VP mode comes at 5.0 nm. Topographical or compositional images are produced by using a four-quadrant backscatter detector. The data collected comes in digital imaging format of 8 bit and EDX spectra. The data is registered at the BioImaging Facility server and recovered with Quartz PCI.

- VEECO NP Flex White-light Interferometry

Flexible, non-contact 3D surface characterization is enable by using the NP Flex white light interferometre. The device has been used in industry in the study of large parts, such as orthopaedic medical implants and parts from aerospace, automotive and precision cutting industries. The equipment provides data in terms of density, resolution, and repeatability, exceeding limitation of contact instrumentation. The NPFLEX is used in precision manufacturing metrology due to its flexibility, accuracy, and throughput, as acquiring data with it improves tolerance estimation, efficient processes, and better finite products.

Both equipment benefit from having handling (rotating) facilities for the workpiece, a feature that enables channel observation without the need for manual handling and eventual misorientation of the workpiece.

7.3.2. Procedure

Prior to each experiment, the workpiece material was machined by EDM and its recast layer was manually removed by polishing down to 0.1 µm surface roughness. This was done in order to prevent surface roughness-induced phenomena, such as vibration, due to instability of the tool position at the tool-workpiece contact. The recast layer presents different chemical and physical properties which may affect micro-cutting results for the top 5-8 µm. Polishing has been done manually as mechanical systems would introduce loads generated by acting forces, and would be in danger of breaking the single crystal into multi-grains. Manually polishing the material has introduced, however, irregularities between different parts of the top surface; for this reason, measurements of the top surface roughness values have been taken between machined channels, not only inside of the channel. This also allows calculation of the inclination of the test piece top surface.

Acquisition of data has been made on several different equipment. Zeiss Optical microscopes have been used to determine channel integrity and to monitor exit burr attached to the surface of the test piece. The NP Flex White-Light Interferometer was used to acquire values of: depth of channel (in three points along each channel), highest point of burr formation, surface roughness 2D and 3D parameters, differences in the

height of the top surface (to estimate surface misalignment induced by the polishing operation). The Hitachi Scanning Electron Microscope has been used to obtain SEM images of: 2 positions along the channel, entrance of tool in material, exit of tool from material, exit burr formation, details of micro-cracking.

The initial evaluation of chip and burr formation for each channel has been done qualitatively, to get an initial estimate about the level of correspondence between ploughing and irregularity on the lateral walls of the channels.

The next step was to use an image analysis software Web Plot Digitizer to measure the points between ploughs (plastic deformation folds), to measure the length and width of burr formation, as well as measurements between each edge of the channel and the bottom of the channel. These coordinates served in the calculation of distances and estimation of irregularities in a statistic designed program for estimating channel irregularities and repeatability of results.

Lastly, channel measurements and calculations have been associated with the cutting force four-peak evolution.

7.3.3. Method of analysis

In order to establish an empirical relationship between the plastic deformation, ploughing, burr formation, channel dimensional accuracy and the cutting forces measured in Chapter 5, detailed measurements have been acquired of these parameters from channel images captured by SEM.

A lack of existing methods in defining these material deformation factors has determined setting up an experimental program and method to achieve such parameters, described in the following section.

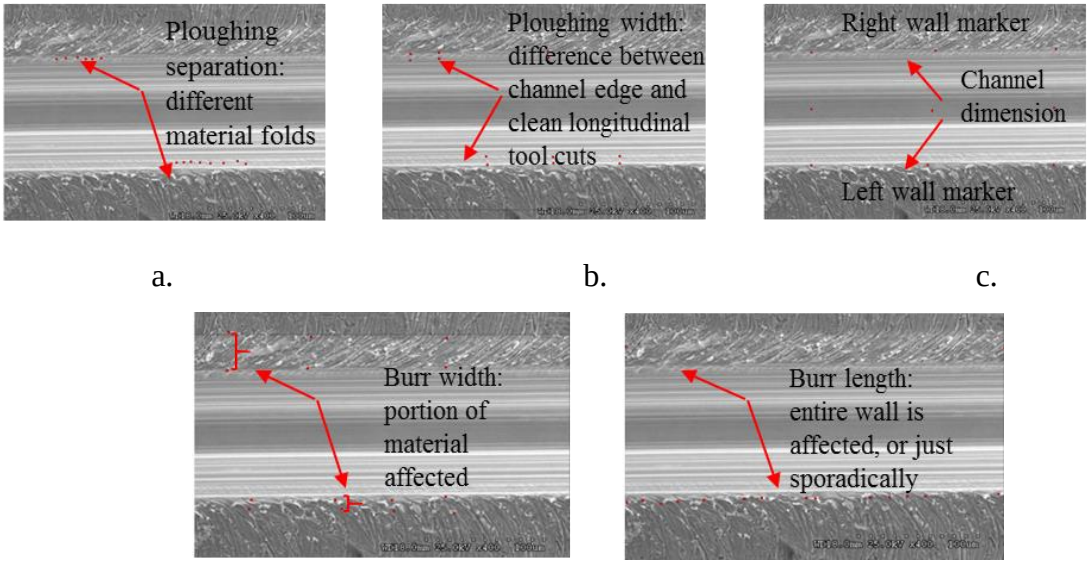
In the first instance, SEM images of the micro-machined channels were acquired with the Hitachi SEM. The images went under image analysis with the software WebPlotDigitizer, which allows measurement of different coordinates based on a scale.

Distances between coordinate points were calculated with the formula

$$d = \sqrt{(x_i - x_{i-1})^2 + (y_j - y_{j-i})^2} \quad (7.1)$$

where x_i and $y_j$represents the number of points selected for each side of channel measurements (left and right). The number of points is arbitrarily chosen and varies based on channel features, which can indicate more or less obvious evolution of ploughing, burr formation or other material phenomena.

For one image obtained with SEM (Figure 7.2), examples are given for the selection of points that can serve to estimating the different material phenomena.

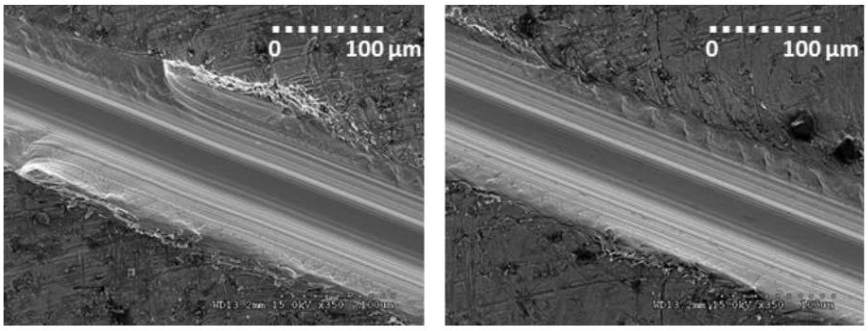


a. b. c.

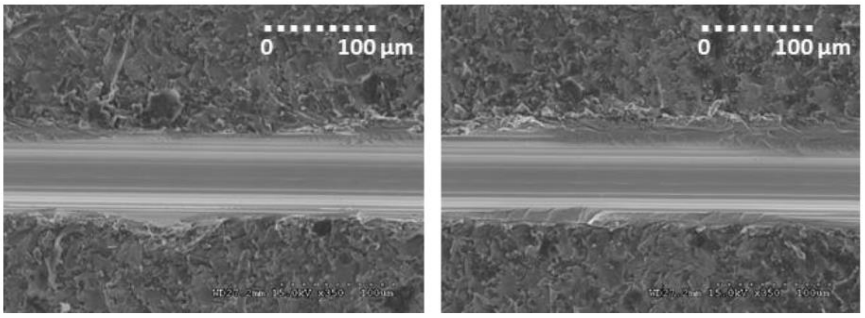
d. e.

Figure 7.2. Selection of points representing material deformation on SEM images: Ploughing or lateral plastic deformation; b. Ploughing width; c. Channel dimensional accuracy; d. Burr width; e. Burr length

Although a better interpretation for ploughing separation or channel wall plastic deformation was expected after this analysis, it proved difficult to assess the regularity or irregularity of plastic deformation found on the walls of the machined single crystal channels. One problem arose from the variation of the behaviour along the channel: plastic deformation or ploughing folds could disappear, appear regular or irregular sometimes on the same channel wall. Another difference arose from the position of the measurement, where differences have been observed between an image taken at about 1/3 channel length towards the entrance tool mark, and a second taken at 2/3 length (Figure 7.3).



a.



b.

Figure 7.3. Differences between images taken at different points along the channel:
a. channel 57, single crystal copper sample machined at 50 µm depth of cut;
b. multigrain copper with a surface machined by EDM.

To counteract this obstacle, image comparison was established for photos taken at similar positions on the channel length, at 2/3 channel length towards the entrance tool mark.

7.4. Experimental program

The experimental trials took place as described in Chapter 5.

Material phenomena have been studied by using specialist imagining techniques, namely scanning electron microscopy and white-light interferometry. Image analysing software, WebPlotDigitzer, has been used to determine the coordinates of various selected points which are used in calculating distances and estimating the various material phenomena.

7.5. Experimental results and analysis

7.5.1. Analysis of exit chip formation in single crystal cutting

The purpose of this chapter is to investigate chip formation phenomena occurring in multigrain and single grain materials, as identified in the schematic presented in the chapter outline. By correlating chip formation phenomena with cutting force analytical models, a better understanding of material cutting phenomena in single crystals is sought.

This is one of three main results sections. The results analysis is made on SEM images of chip formation. Qualitative factors, determined by visual inspection of the SEM images, are proposed in order to define chips geometrical features, such as bend or helix angle. A selection of the images obtained for the four samples types is given in each subsection. Comments on chip morphologies accompany the SEM images and qualitative data, in order to explain machined material features. Lastly, a discussion section follows after results, and aims at explaining chip morphology phenomena and their correlation to cutting force and shear angle variation.

7.5.1.1. Multigrain copper machined at 50 µm depth of cut

Initially, a 50 µm deep channel has been performed in multigrain copper. This is done to gain a basic understanding of classic copper chip morphologies, as shown in Figure 7.4.

It is known that for an arbitrarily chosen workpiece material, the main factor contributing to chip morphology is the tool geometry. When using the same tool at micro-cutting of a multigrain copper test piece, highly similar chip formation phenomena, or exit burr formation with the same morphology, is expected.

This can be easily verified by performing straight channels on a multigrain copper test piece that has been prepared by using EDM on its top surface. With the same operating parameters as the cutting force study described in Chapter 5, several cuts are performed in the workpiece material. In Figure 7.4, it is possible to observe the same direction of the chip helix and bend, as well as a similar length of the formed chips. Highly serrated

edges display properties of ductile material cutting, as well as indicating the presence of high burr formation.

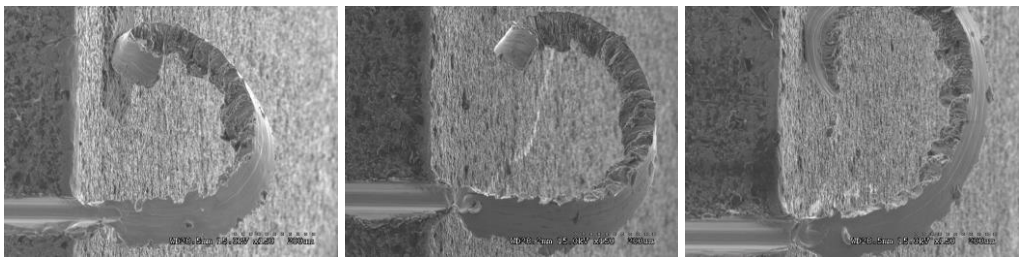


Figure 7.4. Chip adjacent to channels 1, 2 and 5 on the copper multigrain sample

7.5.1.2. Multigrain copper chip and burr formation at 200 µm depth of cut

Next, multigrain copper is machined at 200 µm depth of cut. In Figure 7.5, it is possible to see a selection of 4 out of the 24 chips. All chips are twisted towards the left, are much longer than generally observed in single crystal cutting, and have highly serrated edges. The chips serration and twist is repeatable across all 24 workpiece orientations.

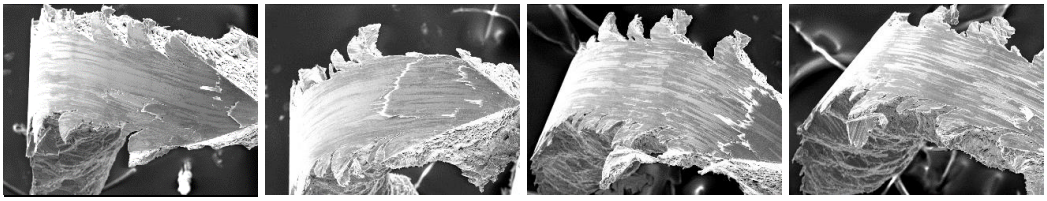


Figure 7.5. Chips 1-4 formation in multigrain sample machined at 200 µm depth of cut

In order to determine whether tool positioning has interfered with chip formation, the tool entrance area and tool positioning is evaluated based on images such as the ones in Figure 7.6.

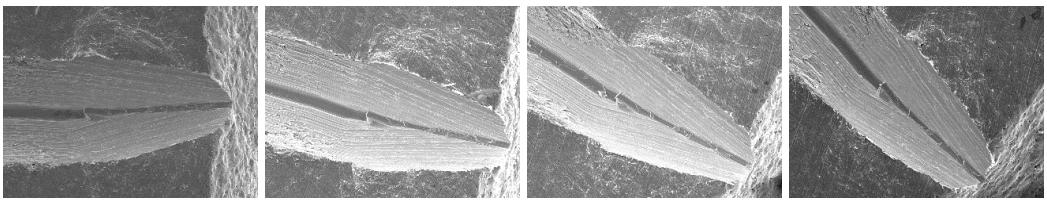


Figure 7.6. Tool entrance for channels 1-4 in multigrain sample machined at 200 µm depth of cut

7.5.1.3. Single crystal copper machined at 200 µm depth of cut

In the next sections of this chapter, chip morphologies of single crystal samples are studied based on SEM imaging of each machined channel. The four-fold periodicity found in (001) plane is expected to be obtained in the types of the chips obtained. More importantly, differences between favourable and unfavourable morphologies are researched, in order to validate the fact that through chip formation, a micro-cutting process can be established as precise, repeatable, or poor. Strict chip periodicity must be established in order to ensure empirical assumptions, as the grain orientation is the limiting critical factor in prediction of surface quality. For this reason, the 24 chips have been grouped in 4-channel sets situated 90° apart. With a red line, the direction of cutting is represented, so that the position of the chip with respect to the workpiece can be better estimated. Results are presented and explained in the following paragraphs.

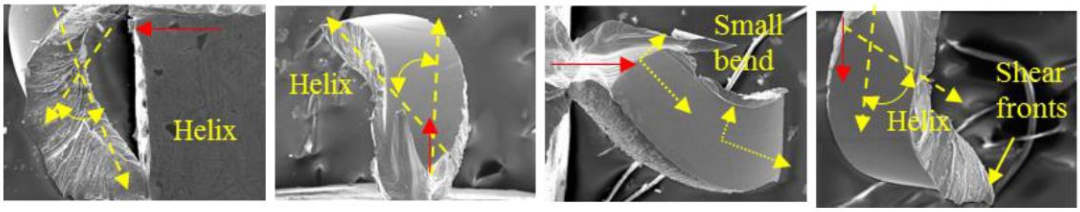


Figure 7.7. Group 1 – Chips for channel 1 (0°), 7 (90°), 13 (180°), 19 (270°)

In Group 1, the chip edges are mostly clean, with little serration at the ‘root’ of the chip. A chip twist or helix is present, most notable in chip 1, 7 and 19 (indicated with arrows on the figure). It is probable chip 13 presents a helix as well. However, the shear fronts on its right side are more prominent, and this shows that the chip was dislocated at its connection with the workpiece material more than the rest of the chips in this group, and the chip was rotated towards its left side. Further analysis is necessary, where the chips are removed from the part, mounted in resin with a constant arbitrary orientation and analysed individually, for better positioning under SEM or the microscope.

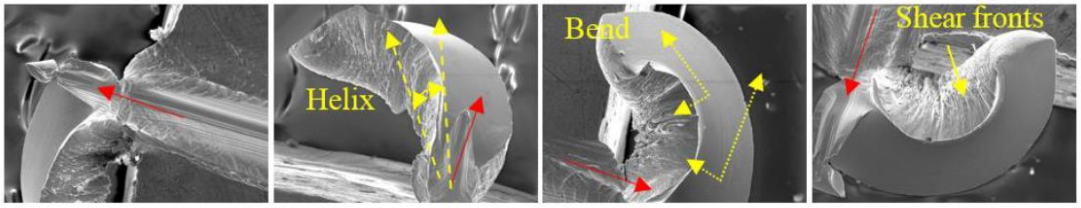


Figure 7.8. Group 2 – Chips for channel 2 (15°), 8 (105°), 14 (195°), 20 (285°)

Group 2 presents a mix of small helix and bend characteristics. This combination produces a piling up of the shear fronts in an almost accordion-like shape, on the back of the chips. The shear fronts are noticeable on the left side, with a small portion on the right at the chip 8 'root'. The edges of the chips are clean cut, indicating shear formation. The chip tip differs, with chip 14 and 20 being alike.

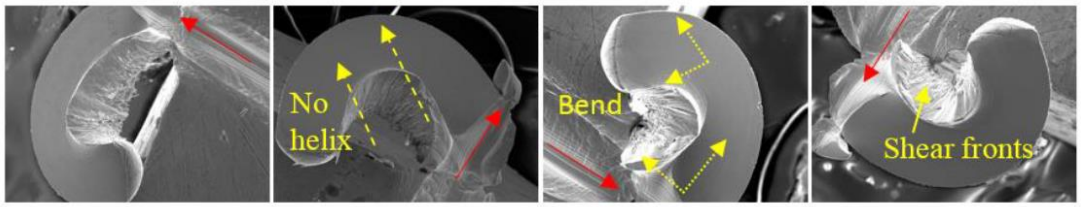


Figure 7.9. Group 3 – Chips for channel 3 (30°), 9 (120°), 15 (210°), 21 (300°)

The most similar chip morphology is observed in Group 3. All the chips present a high bend towards the left side, in a dome shape. The surface resulting from contact with the tool remains in the same plane, indicating no helix, and all of the chips have clean-cut edges, without raggedness. These characteristics allow observation of the oval chip tip.

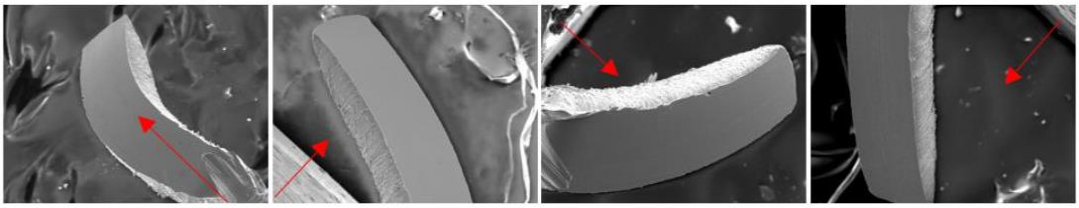


Figure 7.10. Group 4 – Chips for channel 4 (45°), 10 (135°), 16 (225°), 22 (315°)

The chip morphology drastically changes in Group 4: the chip remains in the same plane, presenting no helix, but it has a straight, linear shape. The edges are relatively smooth, with little serration in chips 4 and 16.

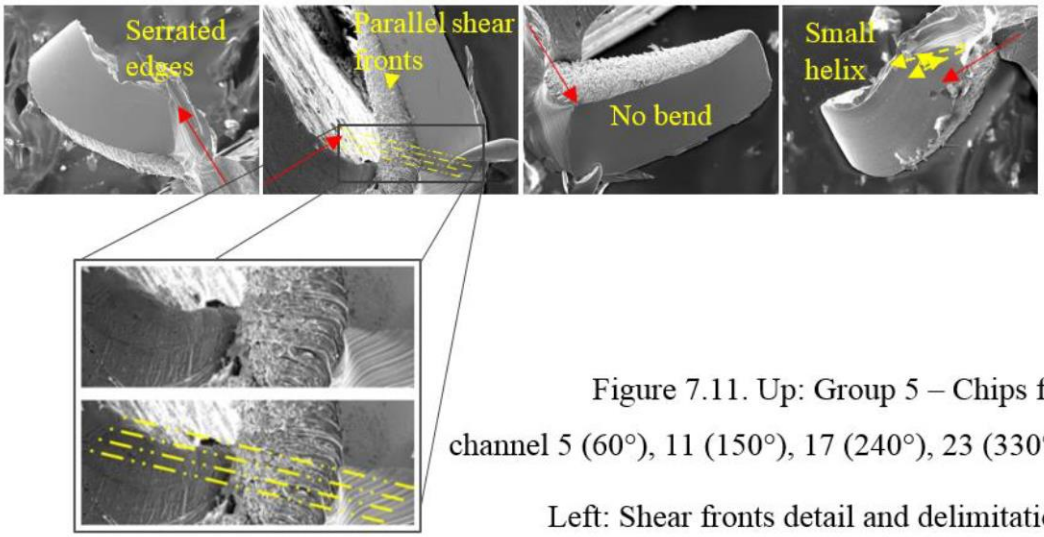


Figure 7.11. Up: Group 5 – Chips for channel 5 (60°), 11 (150°), 17 (240°), 23 (330°). Left: Shear fronts detail and delimitation

Group 5 present highly serrated edges, with ripped and pulled material (more notable in chips 5 and 23) and burr specks clumped on the chip. The chips appear to have a small helix angle and no bend characteristics. Due to the chip not having bend and twist, it is possible to observe lamellae formation on the back of the chip. Magnifying the image, it is possible to observe the lamellae pilling up in parallel shear fronts, as opposed to the converging ones in Group 3.

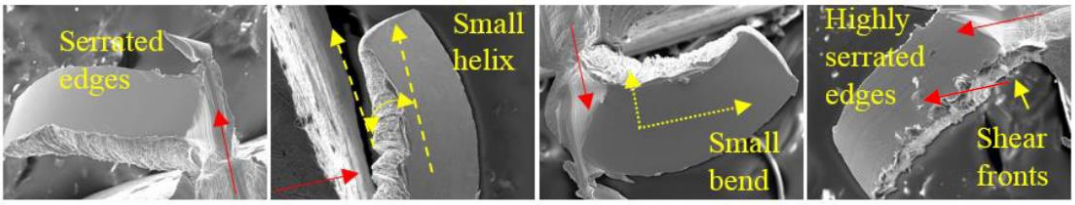


Figure 7.12. Group 6 – Chips for channel 6 (75°), 12 (165°), 18 (255°), 24 (345°)

Small helix and small bend are observed in Group 6 of chips. These present the highest observed serration of edges. Serration is complemented by irregular shear front behaviour. On the left side of chip 12, it is possible to see prismatic shapes formed out of shear fronts pilling up and gathering of lamellae, which correspond with edge roughness.

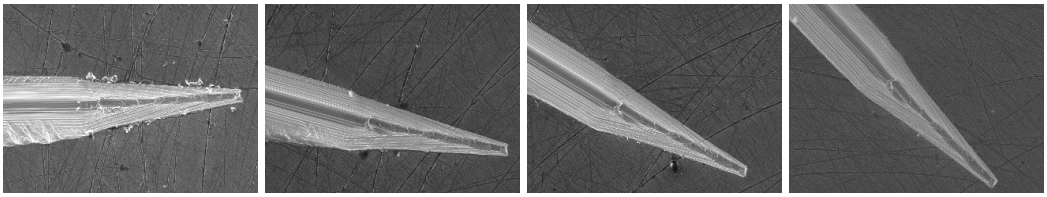


Figure 7.13. Tool entrance areas for channels 1 – 4 at 200 µm depth of cut

Due to chips being partially detached from the edge of the workpiece, as well as them being rotated at different angles with respect to the plane of observation, it was difficult to assess quantitatively the twist and bend values of the chips.

However, looking at similar chips in their group, it was possible to differentiate between dominating characteristics, and these were annotated with a magnitude factor on a 1 to 3 scale, where 1 indicated no presence of that characteristic (e.g. no twist), 2 represents a small occurrence and 3 a moderate or high occurrence. This is based on visual observation of the SEM images, thus is a qualitative assessment of the magnitude of a certain morphology.

Table 7.1. Qualitative assessment of the magnitude of morphologies in single crystal 24-channels micro-machined chips

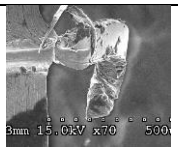
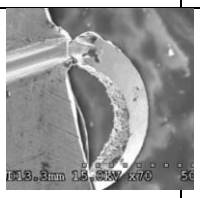
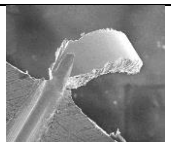
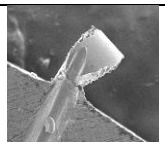
Group	Bend description	Bend factor	Helix description	Helix factor
1	Small	2	High	3
2	High	3	High	3
3	High	3	None	1
4	None	1	None	1
5	None	1	Small	2
6	Small	2	Small	2

7.5.1.4. Single crystal copper machined at 50 μm depth of cut

Chip investigation continues with SEM images of the exit chips obtained for 60 channels performed at 50 μm depth of cut in single grain copper. Three main behaviours are considered: the helix and bend aspects of the chip, as well as the orientation of the chip. The morphology of the chip is visually evaluated, with marks awarded for different chip behaviours: if the behaviour is lacking, the mark would be 1; for a reduced, small behaviour, the mark would be 2; for a pronounced material behaviour, the mark is 3. Additionally, chip orientation (left to right) and the change in direction is considered. Results are shown in Table 7.2, containing a few examples

of SEM photos of the chip and behaviour marks. The complete results are presented in Table for all 60 channels in Appendix A.

Table 7.2. Qualitative assessment of exit chip form and orientation

Channel no	Chip morphology	Helix None=1 Small=2 High=3	Bend None=1 Small=2 High=3	Refe-rence	Orien-tation	Orien-tation change
2		3	1		R	1
3		1	3	1	R	1
4		1	3		R	1
11		3	1	2	0	2-3
12		3	1	2	0	2-3

The chip helix and chip bend indicators are plotted in Figure 7.14.

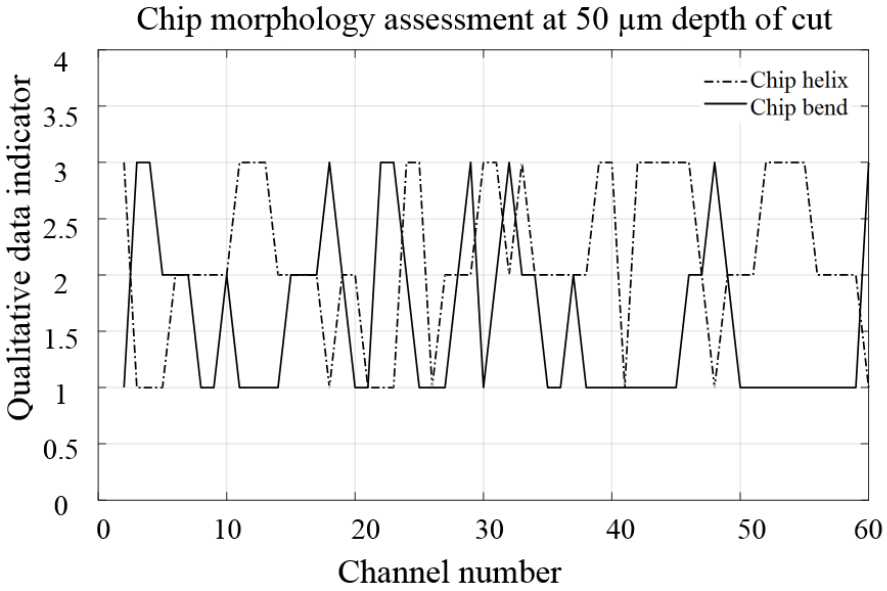


Figure 7.14. Chip morphology assessment at 50 µm depth of cut

Complex behaviour leads this research in the direction of investigation by correlating the chip morphologies not only with cutting force evolution, but also with shear angle formation. It is known that chip formation depends on shear angles. As such, the findings in Chapter 4 referring to shear formation on the (001) cutting plane are approached. In Chapter 4, Figure 4.14.b and 4.14.d, shear angles occurring in the (001) and (111) have been calculated based on Kota's orthogonal cutting model. A correlation between 90° workpiece sectors is sought, and in the following paragraphs shear angle values are calculated for increments corresponding to the channels orientation. This entails calculating the shear angle values at arbitrary positions.

For the (001) cutting plane, a four times repetition of the shear angle pattern is observed. While the shear angles feed into the calculation of cutting forces (which have a repeatable pattern at every 90°, and symmetry at every 45°), it is seen that the shear angle profiles do not exhibit the same profile evolution as cutting forces. Most notably, no symmetry appears at 45°, and there are several peak and minimum values between which the shear angle varies within a 90° sector. Thus, a workpiece segment representing 90° is considered; within it, two zones of higher and lower shear angles can be identified.

To understand how chip behaviour is influenced by the shear angle, the 90° segment is divided into equal sections representing the two experimental procedures followed

in cutting: one 90° sector with 6, and one 90° sector with 15 channels, respectively. The points generated for these are given in the Tables 7.3 and 7.4 (presented in Appendix A), and plots are generated in Figure 7.15.

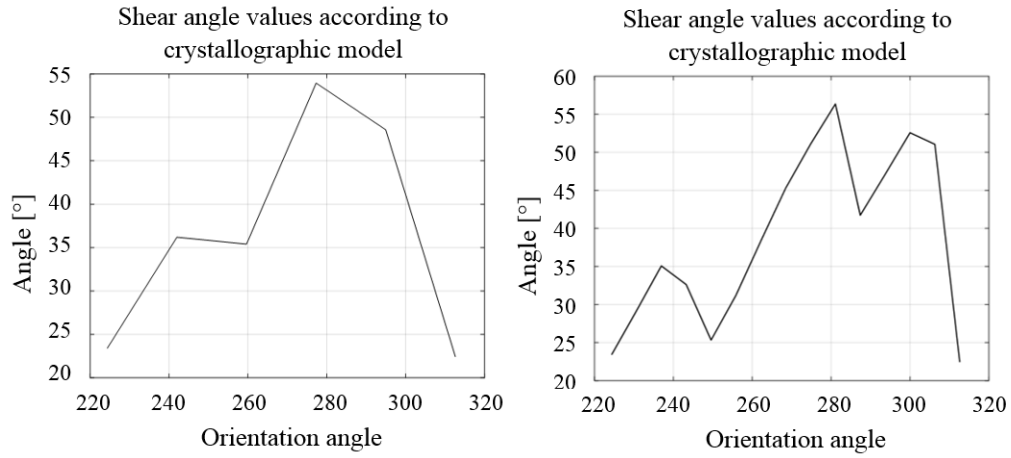


Figure 7.15. Shear angle increments on the (001) plane for 6, respectively 15 increments on a 90° workpiece segment

In the discussion section, correlation between these points and qualitative data available for both 24 and 60-channel samples is established.

7.5.1.5. Repeatability of chip formation in single crystal copper machined at 50 µm depth of cut

Chip formation assumptions can be established as certain, predictable material behaviour only if they prove repeatable. The periodicity of chip bend, twist, or straight chips in correlation with an arbitrary crystallographic plane leads to a better understanding and can potentially lead to new models in future research and established experimental practices when cutting at micro-level and going through a single material grain with several tool steps.

For this reason, a quick estimation of a second experiment following the same steps as the 60-channels at 50 µm depth of cut is made. The monitored factor is chip periodicity for high bend and straight chips every 15 channels (or 90°), as described in the table above.

A selection of 26 chips is shown in Figure 7.16, with the entire set of images presented in Appendix B.

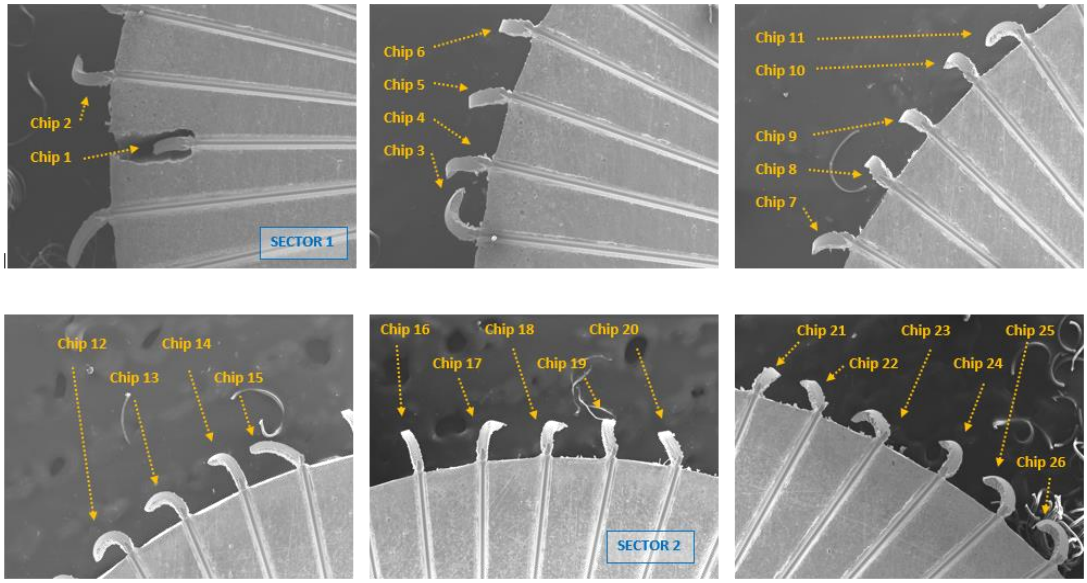


Figure 7.16. Second experiment with 50 µm depth of cut

Upon first observation, chips 11, 12 and 13 are found to present high bend, with chip 12 indicating a pure bend, with no helix angle morphology. The same bend behaviour is found in chips 26, 27, and 28, then 41, 42, 43, respectively 56, 57 and 58. The middle chips in every group, 27, 42 and 57, present high bend.

Straight chips have been clearly identified at the end of channels number 1, 16, 31 and 46.

7.5.1.6. Discussion

In micro-cutting, chip formation has been the aim of many studies over the past decades.

Many studies have focused on understanding the minimum chip thickness values (Liu et al., 2005; Özel et al., 2007; Dhanorker and Özel, 2007) which would ensure chip formation. Chip formation is essential in cutting; the negative case is when the chip is not able to separate from the workpiece material, as it occurs in processes with high ploughing and elastic recovery phenomena. A major drawback of the studies is the fact that while they have been done for micron-levels of depth of cut, they have considered the material to be perfectly isotropic. However, it is widely known that at micron-level depths of cut, grain dimensions and orientation affect chip formation, as grain size is much larger than the depth of cut. For this reason, the current study focuses on cutting

of single grain materials. To establish the clear difference between chip formation in multigrain materials, and chip formation as driven my material microstructure-specific phenomena, a comparative analysis is proposed. This is based on micro-cutting of multigrain copper at the same levels of depth of cut; for these channels, chip investigation should reveal that similar chips are formed when operating parameters are kept constant. This is done to validate the assumption that chip morphologies are driven by single crystal specific deformation processes, and not by operating parameters, which are kept constant.

Furthermore, the main factors that have been investigated in specialty literature in terms of chip formation are chip thickness (Moriwaki and Okuda, 1989; Lee et al. 2000 and 2007) and lamellae formation (Turkovich and Black, 1970; Black, 1972; Ramalingam and Black, 1973).

No single grain specific chip morphology has been investigated, and no correlation with single grain material analytical models have been established. These are knowledge gaps that need to be fulfilled in order to mitigate against poor chip formation, which negatively affects process and product quality.

- Multigrain copper machined at 200 µm depth of cut

The chip serration has the potential to interfere with chip separation from the tool – the more serrated a chip is, the more likely it is to stick to the tool and form a built-up edge. One chip morphology is identified throughout the entire workpiece, and that is categorised as ‘acceptable’ in Kluft’s classification, as illustrated in Figure 7.17.

In order to verify tool positioning, the tool entrance area is evaluated. The material appears as if the tool used in micro-cutting was very blunt. The tool entrance area is wide and indicates a soft, ductile material. In contrast, in the following Section 7.5.2, tool entrance areas in single crystal exhibit sharp edges indicating a more resilient material.

The general finding is that copper chips have a constant morphology in multigrain copper samples cut at 50 µm depth of cut, with a high bend towards the left and constant orientation throughout different channels. This validates expectations that chip morphology in multigrain materials is repeatable, due to material isotropy.

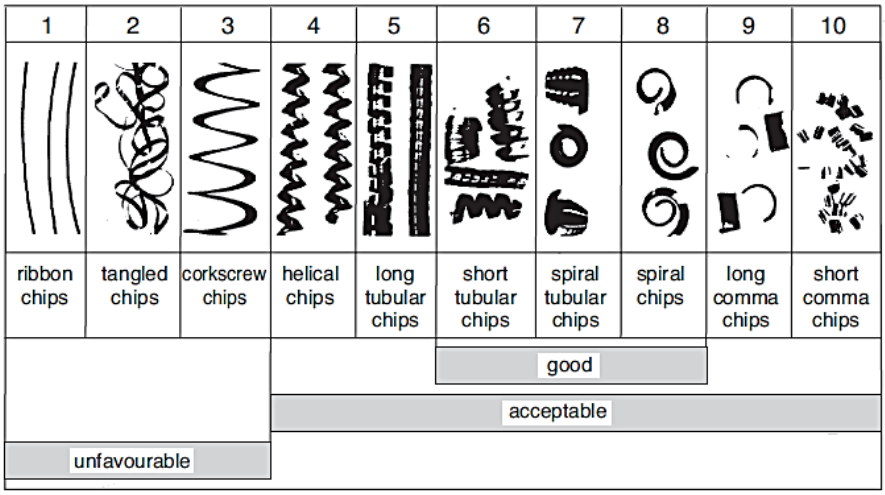


Figure 2.14: Classification of chip forms. Source: Kluft et al. CIRP [60].

Figure 7.17. Classification of chip forms. Kluft et al. (1979) from: Altintas (2012) Figure 2.14, p. 34

- Multigrain copper machined at 50 µm depth of cut

It is known from literature, as well as industrial studies, that copper tends to form long, disorderly chips that are sometimes difficult to remove during cutting (Grzesik, 2017). There is a high probability of the chips becoming attached to the tool, blocking the cutting edge, or spiralling around the tool and prevent the forward feed. Technical staff compensate by adjusting the speed and feed in order to create shorter swarf, and sometimes manually remove accumulated chips while processing takes place. As typology, copper chips can form as helical or tangled chips. One is an acceptable form of chip, while the other is classified as unfavourable. This chip typology is found in the initial test done on the multigrain copper in both Section 7.5.1.1 and 7.5.1.2.

- Single crystal copper machined at 200 µm depth of cut

The general cutting assumption is that the chips will form based on the geometry of the tool. However, in Chapter 5, the change in the cutting force variation was identified as a result of crystallographic anisotropy in single crystal cutting. The cutting force variation is based on the changes of the shear angle necessary to create shear through a certain orientation of single crystal f.c.c. material, as calculated by Kota (2008). Since the shear angle varies, it is expected that the single crystal chips will have different morphology Kota (2011).

One driving factor in chip formation is represented by the cutting forces occurring on the left and right sides of the channel, whose behaviour is reflected in the differences between the edges of the same chip. An interfering factor in this case was tool positioning, as shown in Figure 7.13. As the tool was inclined, most of the chips formed or bent towards the left side. This is reinforced by the chip exit path observed at the 'root' of the chip, which is always on the right side. This has to be factored in when analysing results and remedied in future experiments by better tool positioning prior to experimental trials.

It was expected to observe a four-fold symmetry, according to the four-fold radial cutting force measured in Chapter 5. This was a successful pursuit, as six groups of chips were observed having the same repeatable morphologies, situated 90° apart.

It was also expected to discern symmetry across the 45° delimiter, within every 90° sector. However, this was not observed. The reason is the poor orientation of the tool, which tampered with results. In future experiments, the symmetry will again be investigated as it is possible to correlate cutting force data with growing or declining plastic deformation.

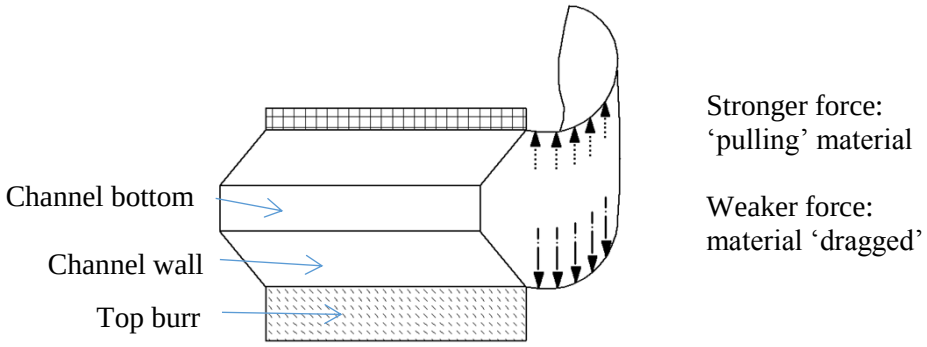


Figure 7.18. Schematic of effect of strain difference on the two channel walls

In Group 4, the symmetry of the straight chip can be correlated with a symmetrical cutting force on the left and right side of the channel, with no ploughing phenomena to 'pull' the chip on one side, as indicated in Figure 7.18. The strain on the right side appears to be weaker, and the strain on the left side, much stronger, resulting in a lateral chip bending process, as indicated in the figure. This would be expected if the tool was positioned perpendicular at the beginning of the channel; from tool entrance images it was observed that the tool has an initial orientation towards the left, thus it was not perfectly perpendicular.

The material behaviour illustrated in Figure 7.18 can potentially impact chip flow. One flank of the chip travels faster due to being easier to break; the other flank travels at a lower speed, due to high material hardness. This makes the chip travel at varying speed across its cross-section. The 'slower' flank of the chip can be caught under the material already displaced by the ‘faster’ flank. The sheared material is also pulled towards the area with a higher ‘stick’ behaviour. Instead of seeing perfectly sheared channel edges, this would generate ploughs, or material folds, as illustrated later in Section 7.5.2.

The existence of perfectly straight chips in Group 5 is explained by high levels of cutting forces and strains sustained on the left side of the chip, strong enough to counteract the effect of inclined tool positioning. Straight chip morphology is most representative for a [111] cutting direction, corresponding to the average 45° shear angle measured and calculated throughout literature. This morphology would reflect symmetrical cutting forces on both edges of chip, corresponding to both walls of the channel.

The prismatic morphologies in Group 6 indicate high ploughing phenomena, with prismatic tips appearing as broken up plastic deformation folds; this is seconded by the high edge roughness. Correlating this with the phenomena observed alongside channels, it is possible to describe the outlook of the channel by analysing the chip, or vice versa. The morphologies of the channel walls, burr formation and plastic deformation result from the same material failure phenomena and mechanical behaviours that affected the chip formation.

Similar behaviours are observed in neighbouring types of chips. An example: bend characteristics occur in every 2 neighbours – either no bend, or high bend. This is valid for the helix angle as well. Helix and bend are not paired with each other, however, seemingly one channel increment apart.

Previous studies have looked at shear front formation as a consequence of shear angle variation due to crystallographic orientation (Turkovich and Black, 1970; Black, 1972). However, the studies have not been advanced enough over the years in the direction of making recommendation on what crystallographic orientations generate good chip morphologies. Lamellae spacing has been the only factor investigate in earlier studies. Later, To et al. (1997) have found that chip thickness varies between 0.6 µm and 1.7 µm for various crystallographic orientations. However, none of studies

have investigated chip morphologies, or their impact on surface and process quality. Furthermore, none of them have established a correlation between chip formation and analytical models that have been developed for single crystal cutting. This makes the state of research in specialty literature at reporting level of various empirical chip investigations. This is a major drawback, which the current chapter was aimed at improving. By providing qualitative analysis of the 24, chip morphologies have been defined. Moreover, their strict variation with analytical models (developed for single crystal cutting) has been established.

As a general conclusion, chip morphologies have been established for 6 different chip morphologies. Four-time repeatability of results due to crystallographic anisotropy on the (001) plane is validated. However, tool positioning affected chip behaviour and in future studies perfect tool alignment must be ensured before experimental tests, which can be verified by symmetrical tool entrance areas.

This is the first time that chip behaviour repeatability in single crystal cutting, and their 90° periodicity within a (001) plane, has been reported. This is a landmark finding, as these aspects have not previously been established, but greatly affect cutting precision and the cost of manufacture.

- Single crystal copper machined at 50 µm depth of cut

A practical assessment of the helix and bend angles of the chips was found to be challenging. Measurements of 3D ribbon-like structures, such as chips, have been found difficult in specialty literature. Moreover, with the equipment available, only 2D images were possible to obtain. Based on the 2D images, the estimation of the chip twist was impossible, as the angle occurs in space, and not on a plane. As such, qualitative indicators have been given based on visual inspection of the chip SEM images, as shown in the Table 7.2.

The qualitative indicators have been plotted in Figure 7.14. High helix angles have been observed in 33% of chips, while moderate helical shapes in 48%, and no helices in 18% of analysed samples. Highly helical shapes are generally correlated with a twist and bend morphology of the chip, indicating two material plastic deformation phenomena occurring at the same time. The no-helix behaviour appears in either straight (ribbon-like) chips, or in highly bent chips, with a general appearance of long

comma chips (as defined by Kluft, with a slight spiralled tip towards the end of the chip, and with a top surface at the chip-tool interface that remains in the same plane).

A remark toward ribbon-like defined structures: the terms ‘ribbon’ is used in defining different chip morphologies in two ways: the first is used in the 3D assessment of helical bodies and helix angles. The second represents the long, straight chip morphology defined by Kluft. These two connotations are pointers of opposite material behaviours, however, as the first term is used in helical bodies or chips, which are acceptable forms of chips, while the second represents a denomination of unfavourable types of chips.

In Figure 7.14, a high bend appearance in chips is found in only 15% of samples, while no bend is estimated in 55% of chips. The overall graph indicates random areas of high chip twists, that can’t be directly associated with a four-fold crystallographic behaviour.

The problem comes from differentiating between helical and bend behaviours, and estimating when one occurs, rather than the other. For this reason, the qualitative estimation of all chips does not indicate an obvious evolution of the two material behaviours. One way to circumvent this issue is identifying clear areas of pure helix angles, pure bend, or no helix and no bend. Pure helical chips are difficult to identify, as there is an element of bend in most of them. For this purpose, a selection of straight, ribbon-like, unfavourable chips, as well as chips with a pure bend appearance was made.

Arbitrarily, chips number 3 (Reference 1 in Table 7.2), then 11 and 12 (Reference 2 in Table 7.2), have been chosen for their pure bend, or, respectively, straight appearance. In order to prove the correlation between chip formation and crystallographic anisotropy based on the cutting force and shear angle models, these two arbitrarily selected behaviours should repeat at every 15 channels (or 90°). Theoretically, purely bent chips should occur in chips 3, 18, 33 and 48; straight chips should occur in 11 and 12, 26 and 27, 41 and 42, and 56 and 57.

In Table 7.2, the 60 chips have been investigated and optically assessed in order to identify the chips with the most similar morphology as the initial selection. The chips that have been found to exhibit the most similar traits have been highlighted by using

a dotted line in Table 7.2. The rest of the chip images are shown in a full table presented in Appendix A.

The pure bend chips have been identified as 3, 18, 32 and 48. Straight chips have been identified in positions 11 and 12, 26 and 27, 41 and 42, 56 and 57.

There is a strong correlation between the crystallographic anisotropy cutting model developed by Kota in his orthogonal cutting study (2008), which indicates a four-fold cutting force evolution in the (001) crystallographic plane of a f.c.c. material, and chip formation findings in the current research. The straight chip morphology occurs precisely every 90°. With the exception of chip 32, which is misplaced by one position, the bend behaviour repetition proves the same principle.

A correlation between repeatability of material behaviour observed in chip morphology and material microstructure properties (as illustrated by the cutting force in Chapter 4) has been established. Chip morphology repetition and correlation with cutting forces highlights the need for a better understanding of the impact of material microstructure on micro-cutting processing. Chip formation affects the quality of the processes, resulting in a range of varying morphologiess, from favourable and acceptable shapes (as defined by Kluft in Figure 7.17), to unfavourable, as found in chips type 11 and 12 in the 50 μm deep channel study, or in Group 4 in the 200 μm deep channel test.

An initial confirmation of chip repeatability has been found in the study of the 24 channel test piece. Six groups of similar material behaviour have been recognised. A factor that has interfered with chip formation has been the initial tool position; the 24 channels' tool entry zones have all indicated that the tool was not positioned symmetrically with respect to the two limits of the channel. This initial inclination has accounted for all the chips having a straight to left bend behaviour, and none which have been inclined towards the right.

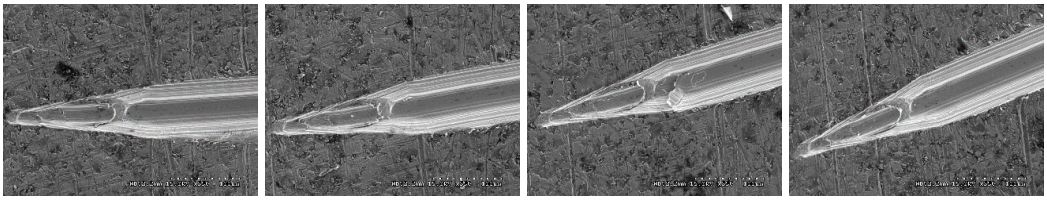


Figure 7.19. Tool entrance for channels 1-4 in the first phase single crystal 60-channels experimental trial

The experiments are later improved by ensuring a more accurate tool position at the beginning of the channel (as shown in Figure 7.19), and also by performing a higher number of channels. The higher number of increments performed at a lower depth of cut provide more intermediary steps of material deformation during a 360° workpiece rotation, which ultimately leads to obtaining a comprehensive understanding of chip behaviour. The morphologies of the chips has been found to be repeatable among 90° sectors, with arbitrarily selected straight and bent chips that were set for evaluation. The shape of intermediary twisted chips was more difficult to assess due to combined material deformation phenomena that is not yet fully understood. While the higher number of channels has increased the level of confidence in establishing chip behaviour, it has also provided more difficulties in obtaining chips that look exactly the same. Copper ductility, combined with the lower volume of cut chip (which makes the chip more prone to temperature deformations; Grzesik, 2017), have increased the chip deformation process, making individual helices and bend angles more difficult to estimate.

The first step in estimating the influence of the shear angle on chip generation is to understand the association between results obtained in Section 7.5.1.3 (single crystal copper machined at 200 μm depth of cut) and shear profiles as generated analytically in Chapter 4.

According to the shear angle values determined for the first 6-points distributed within 90° (Figure 7.15), there would be two channels resulting from shear angles with values lower than 25°, two from shear angles of approximately 35°, and two above 45°. Drawing a parallel with the six types of chips found in the 24-channel sample experiment, these delimitations represent well the material behaviour. Group 2 and 3 indicate chips with a high bend and twist behaviour; Group 4 and 5 indicate almost straight chips; Group 6 and 1 indicate chips with a small twist or bend. The delimitation of the shear angles is reflected well in the behaviour of every two neighbouring groups of chips.

The reason why shear angle values are a reason for concern is that higher shear plane angles indicate smaller shear planes (as illustrated in Figure 7.20). Smaller shear planes are representative for lower cutting and shear forces, as well as lower temperature generated at the tool-chip interface. Thus, in manufacturing, higher shear angles are associated with better results. Lower shear angles lead to thick chips that are difficult

to remove, generate high cutting forces, and can lead to instabilities of the tool. Based on this principle, recommendations can be made for manufacturers to improve micro-cutting precision.

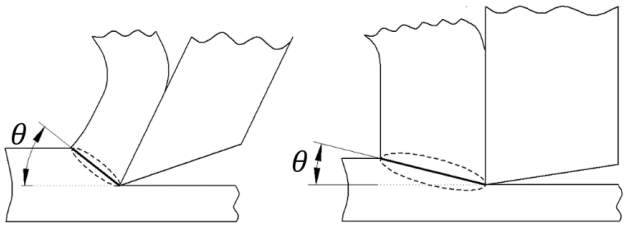


Figure 7.20. Differences in chip thickness due to shear angle formation

As an additional example, in milling, it is known that surface roughness can be improved by selecting cutters with high helix angle values. The high helix angle produces helical or tubular chips, which are the desired shape in chip formation. Chatelain and Zaghbini (2012) studied large helix angles and concluded they result in smooth surface generation, compared to small helix angles. A high helix can artificially introduce high shear angles.

In this study, the shape of the tool remains the same, but the material microstructural properties change with grain orientation. Some orientations have been observed to generate twisted chips, e.g. chips 14-17 on the 60 channel workpiece, or Group 2 and 3 on the 24 channel workpiece. These are acceptable morphologies, according to Kluft's classification of chip forms (Altintas, 2012).

These good chip morphologies can be associated with higher shear angle values, while the straight chips, which are classified as unfavourable, can be associated with lower shear angles. This is supported by the milling investigation of helical cutters (Chatelain and Zaghbini, 2012), which sought to introduce higher shear angles, in order to generate lower cutting forces, lower shear planes, lower work, and achieve a good surface quality.

The next step is understanding the association between shear angles and their effect on chip formation, based on the 15-increments analysis. In order to achieve this, higher and lower limits are established for shear, while chip orientation is also investigated.

In Figure 7.15, a limit can be identified around the 35° shear angle mark. In the second graph, featuring 15 increments, the shear angle limits are evident. There are 9 values

above the mark, and 6 under, representing a 1.5 ratio of high to low shear angles found on a 90° single crystal workpiece rotation. This can be extrapolated to the entire 360° workpiece.

By summing the orientations (left vs. right) of the chips in Table 7.2, it is found that right oriented chips account to 35 channels, while left-oriented chips, to 25. The straight chips, with no left-right orientation, were equally divided between the two. The left to right ratio is thus 1.4.

While initial assumptions were that chip formation would be mostly dependent on the cutting force evolution, empirical analysis has proved that the shear angle is more important in generating chips with different morphologies. However, this is an initial observation and further steps need to be taken in order to study the relationship between chip morphology, tool geometry, chip flow, stresses and strains in single crystal material micro-cutting.

One limitation comes from the fact that the change in orientation, left vs. right, seems plausible when the cutting force is considered as the main chip deformation mechanism. Initial lower cutting forces generated highly twisted chips, while peak cutting forces account for straight chips. The shear angle's role in this is not well understood. While the 1.5 ratio of shear angles (higher versus lower) is similar to the 1.4 ratio of chip orientations (right versus left), it is not sufficient to explain the mechanism in which the chip becomes twisted at both ends of a 90° segment. That mechanism is better explained by a correlation with the cutting force. A succession of different cutting forces (with a channel exhibiting a higher and a smaller strain on the two channel walls) leads to chips as illustrated in Figure 7.16: for the first 0°- 45° workpiece orientation, cutting forces increase, leading to chips twisted towards the right; for the 45° - 90° workpiece orientation, cutting forces decrease, generating chips twisted towards the left. Thus, the change in chip orientation can be attributed by the small difference in cutting force and strains due to crystallographic anisotropy in single crystals. However, it was observed that the right-chip orientation dominated the behaviour of chip morphology; this behaviour can be attributed more to the occurrence of higher shear angles. The lower number of left-oriented chips correspond to the lower number of under 35° shear angles. As such, more investigation is necessary in order to understand the main material deformation mechanisms and which is the main phenomena which leads to chip twisting.

A different reason for the predominant right chip twist can be non-symmetrical tool positioning, which was the main chip formation factor in the experimental findings of the 24-channels single crystal workpiece in Section 7.5.1.3. An investigation of the tool traces left at the entry of the tool for all 60 channels does not indicate this behaviour, however, as the initial tool position was improved. A selection of tool entries for channels 1-4 illustrated this in Figure 7.21.

- Repeatability of chip formation in single crystal copper machined at 50 µm depth of cut

The same experimental steps as the ones in Section 7.5.1.4 are repeated, in a 2nd testing phase. Chip investigation is also performed as done in in Section 7.5.1.4. As illustrated in Figure 7.16, the precise periodicity of straight chips and of bend chip groups at every 90° is confirmation of the anisotropic behaviour of chip formation in single crystal micro-cutting. It is also proof of repeatability of chip formation results based on empirical trials and estimations. Some differences are observed when looking at the two experimental phases: in the first trial, right-bent chips have been identified more clearly. In the second experiment, those positions of chips appear straighter. Similar numbers of left-bent chips are observed in both experiments.

The difference in right-bent chips can be explained by tool positioning and differences in surface preparation. The second experiment, upon investigation with the SEM, presents a surface with more EDM recast layer at the surface of the workpiece. This is observed due to a higher number of material 'flakes' at the top surface of the workpiece surrounding channels, and can interfere with results. The imprecision in obtaining the same level of EDM recast layer removal form the surface of the machined single crystal comes from the fact that polishing has been done manually, in small steps, in an attempt to not damage the crystallographic structure of the test piece, whilst trying to obtain a flat test piece surface. Polishing with a lapping equipment would give a recurrence of surface roughness between different test pieces. However, this is avoided due to the possibility that cutting forces involved in the process would damage the upper layer of workpiece and the crystallographic structure. Losing the single grain crystallographic structure was considered a too high risk, and thus surface preparation was a compromise by choosing manual polishing.

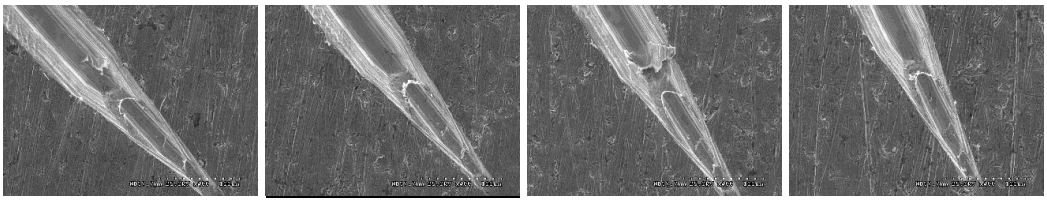


Figure 7.21. Tool entrance for channel 10, 11, 12 and 13 in the second phase single crystal 60-channels experimental trial

The second and most important factor affecting chip formation was identified as tool positioning. In Figure 7.21, it is possible to observe a similar tool position as obtained in the initial 200 µm depth of cut experiment. Tool was positioned towards the left, which resulted in mostly straight and left-bent chips. Despite this interfering with repeatability of results in the case of the two 50 µm depth of cut experimental trials, it shows a correlation between tool positioning and chip formation. Again, the strain on the left side of the channels was much higher, 'pulling' the chip towards the left side. Due to surface preparation and tool positioning interfering with experimental results, it was difficult to obtain the same left to right chip ratio between the two 60-channels trials. This also interfered with the relative position between monitored straight and bent chips.

Chip thickness has been previously investigated by Black (1972) and Lee et al. (2000 and 2007), but the main findings referred to chip thickness variation, lamellae formation, and no correlation of these aspects has been established with crystallographic anisotropy. There was a high need for chip morphology to be investigated, and this section proves the existence of specific chip morphologies that can lead to chip prediction based on crystallographic anisotropy.

Strict periodicity of chip formation in single crystal cutting has not been established before, but the current section proves this periodicity, which is a milestone for both current research and can potentially lead to new analytical models. This is the new understanding of material phenomena that has been sought, and with this new knowledge chip formation studies have been advanced. The newly established chip periodicity positively affects manufacturers, as it is possible now to mitigate against some chip morphologies that are undesirable in cutting, and this ultimately positively affects the cost of production.

7.5.2. Analysis of burr formation and plastic deformation in single crystal cutting

One of the main aims of this chapter is to investigate burr formation and plastic deformation phenomena (as shown in the schematic presented in the chapter outline). This section represents the second of the three main results subchapters.

Based on burr formation and plastic deformation phenomena it is possible to provide a new understanding of material mechanical deformation occurring in single grain versus multigrain materials. This new understanding can be then compared with cutting force analytical models in order to improve the specific understanding of material cutting phenomena in single crystal micro-cutting.

In the current section, SEM images of burr formation and ploughing along the channel walls are obtained, and images are analysed by different methods. A selection of the images obtained for the four test pieces generated by micro-cutting of single and multigrain copper, at 50 µm and 200 µm depth of cut, is given in each subsection.

Quantitative analysis is proposed for burr and ploughing measurements on the 24-channels single crystal samples, based on measurements obtained with a digital image analysing software, WebPloDigitizer.

Qualitative factors, based on visual inspection of the SEM images, are proposed for the 60-channel single crystal behaviour, in order to differentiate between a high or little occurrence of burr formation and ploughing behaviours. This is also performed for a later correlation with the similarly generated Table 7.2 for chip formation, to enable a comparison between the material phenomena. Comments on the SEM images accompany results, to enable a better understanding of material behaviour.

Following results, the section ends with discussion, which intends to correlate burr formation and plastic deformation phenomena with crystallographic anisotropy models.

7.5.2.1. Multigrain material machined at 200 µm depth of cut

In order to demonstrate that the material behaviour illustrated in this chapter regarding single crystal cutting is strictly related to crystallographic anisotropy and is not the result of the machining process, or the tool used, experiments must be performed on

multigrain samples. An exhaustive analysis is not necessary in this case, just a general observation of the state of the channels.

The first sample analysed is multigrain copper machined at 200 µm depth of cut. A selection of four channels is presented in Figure 7.22.

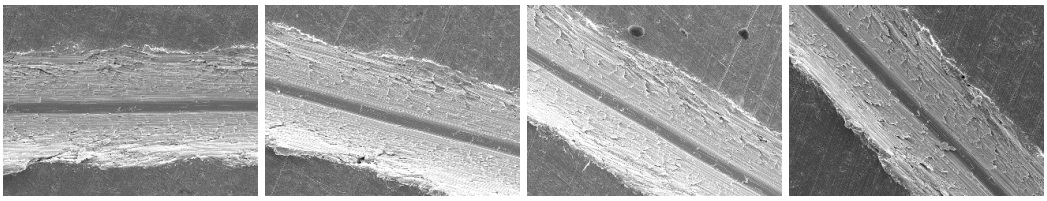


Figure 7.22. Channels 1-4 in multigrain sample machined at 200 µm depth of cut

This serves as a norm for standard burr formation and ploughing inside the channel walls.

7.5.2.2. Multigrain copper machined at 50 µm depth of cut

Next, the experimental investigation focuses on material behaviour occurring in a copper test piece machined at 50 µm depth of cut. The results are shown in Figure 7.23.

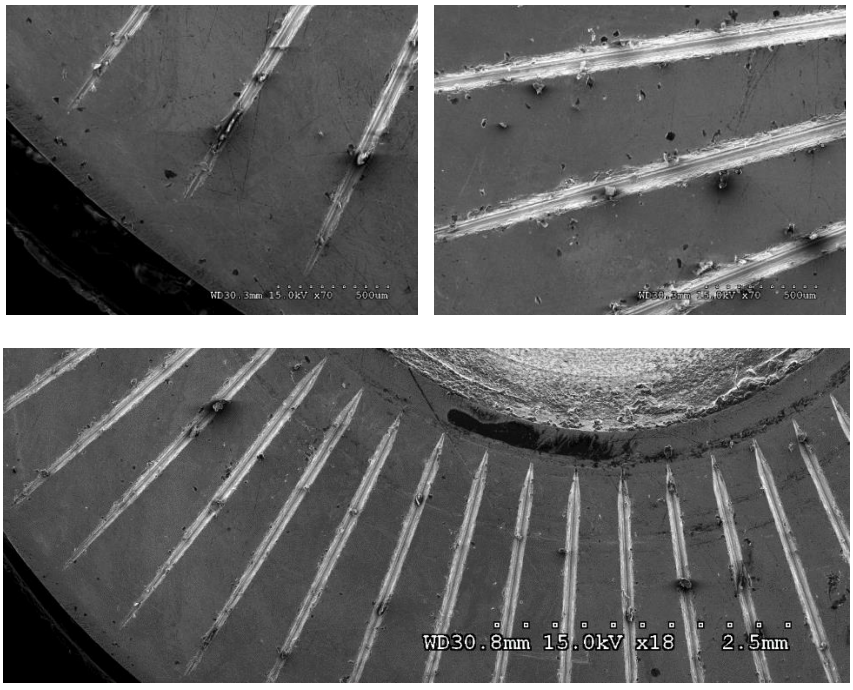


Figure 7.23. Multigrain copper disc machined at 50 µm depth of cut.

Is possible to observe the lack of exit chip formation, which was previously described in Section 7.5.1.1 and 7.5.1.2. The reason is that the channels were not cut up to the margin of the workpiece, such as in the previous sections, which led to chips detaching from the material.

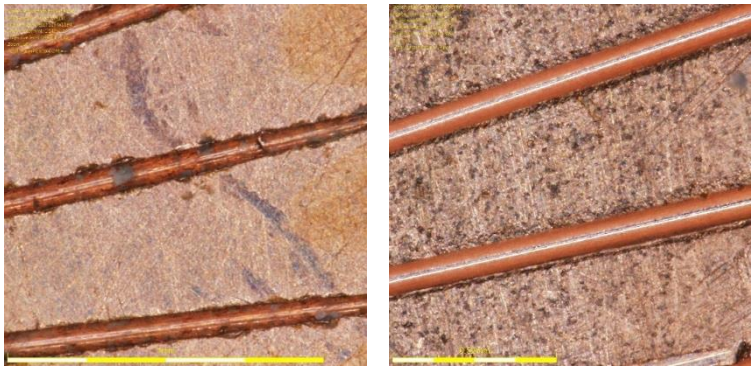


Figure 7.24. Microscope photos of multigrain, respectively single grain channels

A brief comparison between multigrain and single grain channels is provided in Figure 7.24, based on images acquired with the Zeiss microscope.

7.5.2.3. Single crystal copper machined at 200 µm depth of cut

The next subsection deals with the only quantitative analysis that was possible to acquire with the current equipment and methods of image analysis. Ploughing and burr formation measurements are done with an image analysis software, WebPlotDigitizer, as described in Section 7.3.3., method of analysis. This assessment has been attempted for all material phenomena studied, from plastic folds width, to plastic folds separation, and more. However, a more precise mathematical model is still needed to differentiate between plastic deformation regularity and irregularity along the same channel wall inside an arbitrarily chosen channel. In a similar manner, it has been difficult to establish the burr length, as sometimes this spreads along the entire channel, but burr specs appear sporadically. And, for other channels, burr is interrupted but has a much higher volume. At this moment, it was impossible to assess the burr volume as it was difficult to measure both burr length, as well as burr height.

For this reason, this section focuses on ploughing width and burr width parameters, which are shown in Table 7.5 in Appendix A.

Based on these experimental measurements, ploughing and burr formations patterns are investigated in Figure 7.25.

Strictly for comparison purposes, the pattern of ploughing and burr on the left wall are plotted against each other. In order to facilitate a pattern comparison, 10 µm are subtracted from ploughing values.

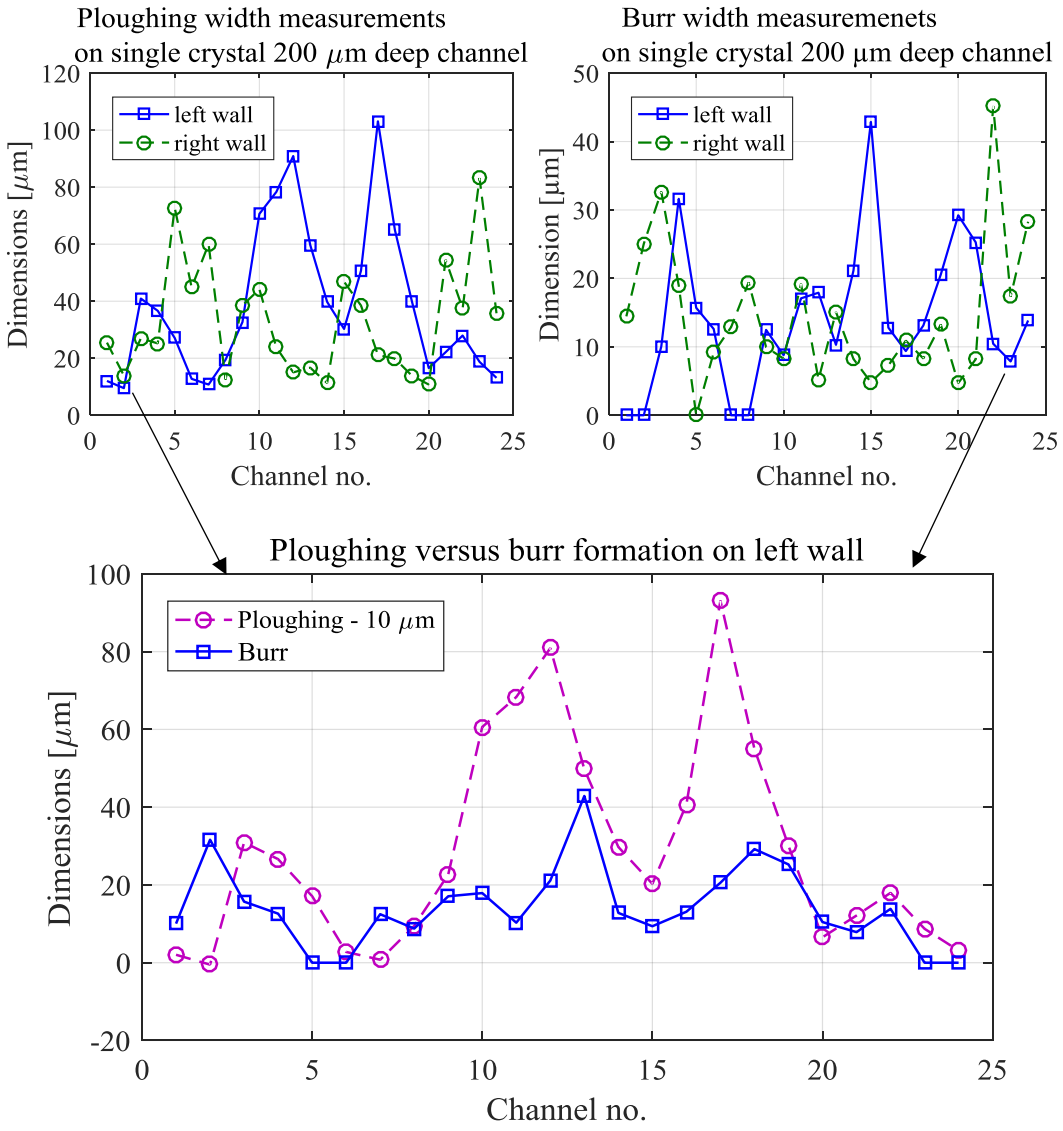


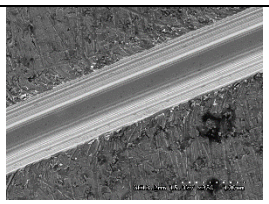
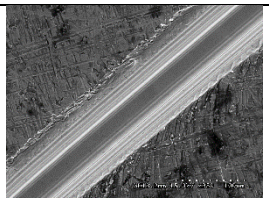
Figure 7.25. Comparison between ploughing and burr formation

7.5.2.4. Single crystal copper machined at 50 µm depth of cut

Lastly, single crystal copper samples are machined at a 50 µm depth of cut.

Similar to the chip estimation in Section 7.5.1, burr and ploughing phenomena are given marks for the observed material behaviour. SEM images for a selection of channels are provided in Table 7.6, with the images and indicators of channels 1-60 being presented in a complete table in Appendix A. Results are presented in Figure 7.26.

Table 7.6. Qualitative assessment of burr and ploughing phenomena

Channel no	Channel shape	Ploughing left None=1 Small=2 High=3	Ploughing right None=1 Small=2 High=3	Burr left None=1 Small=2 High=3	Burr right None=1 Small=2 High=3
1		1	3	1	3
5		1	1	2	2
8		2	1	3	1
13		2	2	1	1

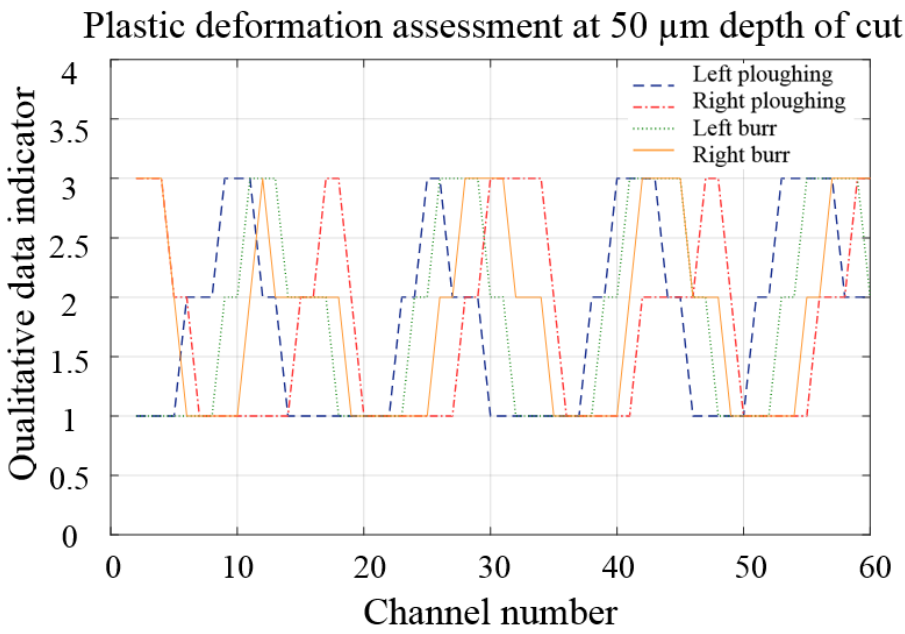


Figure 7.26. Plastic deformation assessment of single grain material phenomena in 50 µm deep channels

- Correlation between chip and burr formation

Chip orientation has been estimated to change 8 times within the 360° workpiece rotation in Section 7.5.1.

As there is an apparent correlation between burr formation and chip morphology, the 60 channels are looked into based on a comparison established between Table 7.2 and Table 7.5. This is based on the assumption that main material deformation phenomena that affect chip morphology are the ones that drive burr formation as well, as illustrated schematically in Figure 7.27. A qualitative approach is proposed, in order to enable the comparison.

The first objective of the qualitative assessment is chip form quality. Straight chips are considered undesired. Straight chips are thus chosen as the marker between the chip orientation change (left to right and vice versa). This marker is followed in the Table 7.2.

The second objective is the qualitative assessment of burr formation. Again, the change between surfaces with no burr formation, and how they change from the left to the right side of the channels, is being studied. This marker is investigated in the Table 7.5

images. A correlation is sought between material behaviour occurring on the two walls of the channel. As such, material behaviour with similar burr qualitative markers are investigated.

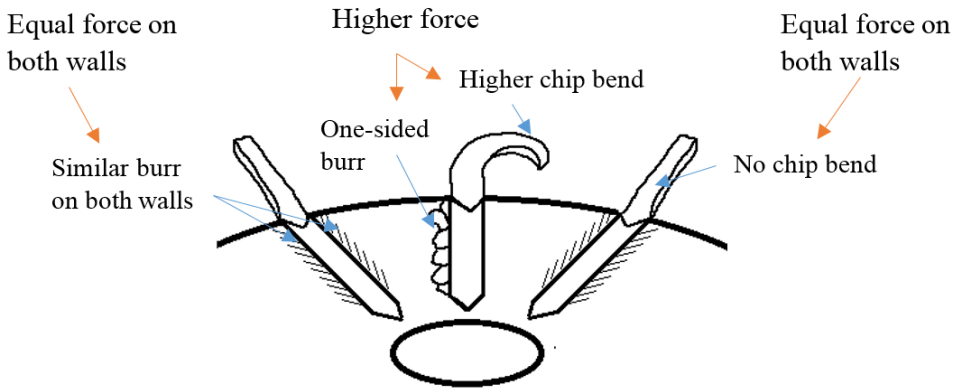


Figure 7.27. Correlation between burr formation and chip morphology

An example: the '1' indicators are followed in Table 7.5. The position when '1 indicators seize to occur on a certain channel wall is selected. Then, the '1' indicators are followed on the opposite wall of the channel. This represents the marker of change of burr mechanisms.

Next, chip orientation is sought in Table 7.2. Where the chip changes orientation, or the chip is straight, the channel becomes the marker of change of chip formation.

These two markers are then compared against each other. When they coincide, this indicates similar material deformation mechanisms, which affect both burr and chip formation.

When the markers differ, the material phenomena also differs, or there are other process parameters which interfere with the correlation.

For correlation between the behaviours, the marker is 'positive'. For dissimilarity, the marker is 'negative'. An example of this qualitative approach is presented in Table 7.7.

There are still some cases which needs to be accounted for. For channels where a '1' indicator is present in both columns, but the chip orientation occurs on a different channel, the occurrence is given 'negative' mark. For channels where a '1' indicator is present in both columns, as this coincides with chip orientation change, the occurrence is given 'positive' mark.

Table 7.7. Example of indicator calculation

Burr left None=1 Small=2 High=3	Burr right None=1 Small=2 High=3	Chip orientation	Mark
1	2	Right	Positive
1	**1**	Right	Negative
2	**1**	Right	Negative
2	**1**	Left	Positive

Lastly, the overall number of positive markers, out of 60 possible markers, is calculated to obtain the level of correlation between chip and burr formation.

- Burr formation

Top burr formation is the next step in investigating material deformations affecting surface quality. A microscope comparison between channels corresponding to different crystallographic orientations is provided in Figure 7.28. Bur formation mechanisms are explained in the Discussion section.

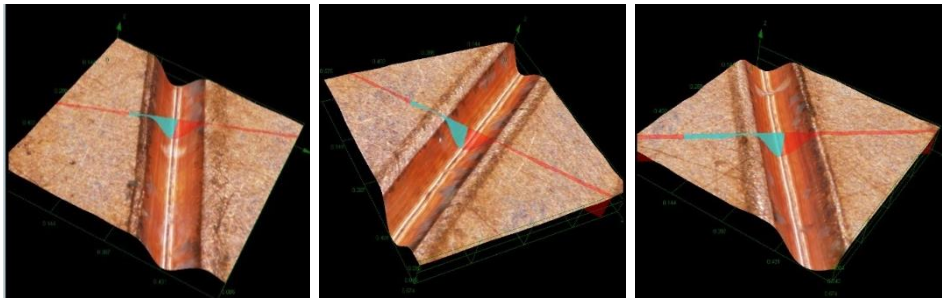


Figure 7.28. Microscope observation of top burr formation in 50 µm depth of cut single crystal cutting

- Ploughing formation

Alongside qualitative analysis, a quantitative estimation of the burr and ploughing has been attempted. No numerical, theoretical or empirical models that could serve to calculating these behaviours have been found in literature. Moreover, no clear way of

defining the ploughing folds formations or the burr specs at the top of the machined surface has been identified. For this reason, an attempt at measuring the distance between plastic folds and that of burr width was made, with an image analysis software. The results are found in Table 7.8., and plotted in Figure 7.29.

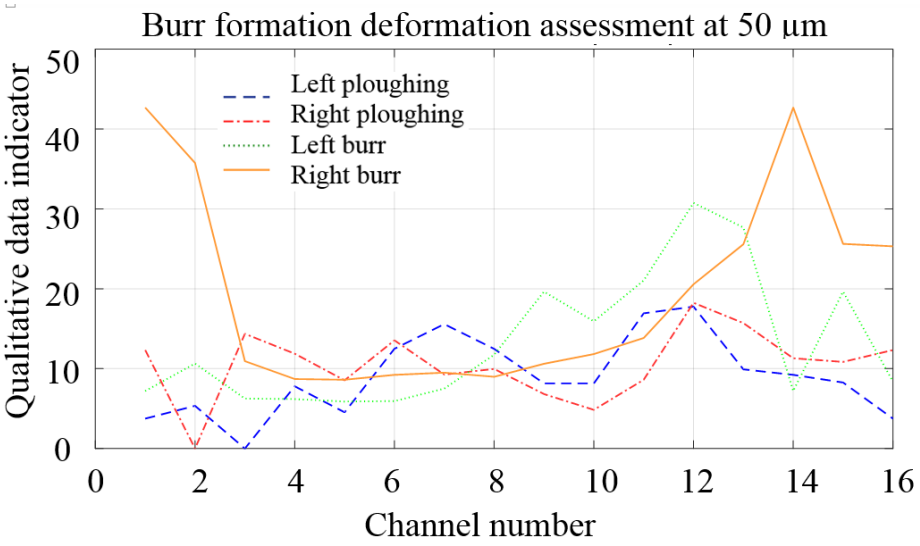


Figure 7.28. Burr assessment of single grain material phenomena in 50 µm deep channels

7.5.2.5. Discussion

In cutting, the lack of burr formation reflects the quality of a machined material surface. Furthermore, burr removing operations can also increase the cost of production (Oliveira et al., 2015).

In micro-cutting, it is imperative that burr formation is predicted as deburring operations become impossible at small depths of cut in the range of under 50 µm. Due to the scale of the product, surface quality is a major concern in micro-cutting. As such, material deformation phenomena become significant to understand and to predict (Liu et al., 2005).

One of the material phenomena investigated in this research is shearing. Shearing is the material fracture behaviour desirable in cutting operations; this is correlated with optimal surface quality and a general absence of burr. However, in micro-cutting, plastic and elastic phenomena also occur; it has been observed that these affect single crystal cutting to a larger extent than observed in multigrain materials.

Shearing has not been amply studied in correlation with crystallographic models; this represents a drawback in literature specialty. Some crystallographic planes and directions are known to generate good surface quality. However, no clear recommendation as to which these directions are exists. Thus, it is imperative to develop recommendations for obtaining shearing (associated with burr-free machined surfaces) on clearly identified crystallographic directions.

Another material deformation phenomena is plastic deformation, and in terms of surface quality it represents an undesirable effect (Wan et al., 2014). Plastic deformation appears in the form of ploughing folds, which can have a higher or lesser regularity along a channel, and are correlated with poor surface finish. Ploughing has previously been investigated as a parameter depending on the minimum chip thickness (Malekian et al., 2012; Oliveira et al., 2012). However, ploughing has not been studied in single grain cutting, thus no models for ploughing formation during cutting of differently oriented grains exist. This is a major drawback; as minimum chip thickness is a function of free surface energy, this is expected to vary due to material anisotropy.

Other material parameters include specific material strains, elastic recovery, tensile strength, etc. All the material-specific parameters are known to vary in single grains, due to anisotropy (Zhou et al., 2014).

Some important aspects that have been studied in this respect are reporting surface quality for single grain material cutting. One study done by Lee et al. (2007) has indicated burr formation in patterns that could be attributed to cutting forces determined by crystallographic plane models. For the (111) crystallographic plane, which indicated three patterns, three zones of burr were identified; for the (001) plane, four patterns were associated with four zones of burr. While this study represented a good step in the direction of burr formation analysis, mechanical deformation processes that occur within each ‘pattern’, or within each 90° sector, have not been analysed. Moreover, burr has not been characterised; it was only reported to occur over large surfaces of the workpiece material. Lee’s study (2007) indicates that there is a correlation in burr formation and pattern repeatability due to crystallographic anisotropy. However, without material investigation to clearly define the material phenomena (shearing, ploughing, elastic recovery), recommendations cannot be done for micro-cutting purposes. No clear levels of surface quality indicators have been

correlated with crystal-specific cutting forces; this is a big limitation, as researchers and manufacturers alike need this information in order to diminish burr formation.

Thus, the current chapter has focused on an in-depth analysis of ploughing and burr formation patterns, and their correlation with crystallographic anisotropy models developed in Chapter 4.

In the following subsections, experimental results in Section 7.5.2 are discussed. Based on these findings, recommendations for improving surface quality and thus micro-cutting precision are provided.

- Multigrain material machined at 200 µm depth of cut

The first step is identifying the behaviour of the multigrain material on the channel walls. In Figure 7.22, the walls of channels 1 through 4 indicate a very soft material, with irregular behaviour, but repeatable across the 24 channels. Burr formation is present throughout the length of the channel, with no shearing marks at the top surface of the workpiece. The irregularity of the material makes it difficult to assess the main material deformation phenomenon, between ploughing and shearing. However, the flat surface of the exit chip, at the chip-tool interface, indicates normal cutting behaviour. This is expected in ductile materials, and copper is known to produce difficult surface roughness.

The main conclusion is that copper behaviour is ductile material-specific, and it is repeatable across all 24 analysed channels. High burr formation and high ploughing is prevalent.

- Multigrain copper machined at 50 µm depth of cut

In Figure 7.23, it is possible to observe the general outlook of channels formed in the 50 µm depth of cut experimental trial. Initially, it is easy to notice the repeatability of the shape and relative surface roughness, across all channels observed. It has been observed that in multigrain samples, chips break easily from the surface of the test piece, thus it is much more difficult to assess them. That can be explained by the presence of multigrain – where the grain boundary occurs, it is much easier for chips to break, rather than form exit chips as in single crystal. The channels present high burr

formation, but without ploughing or plastic deformation folds. Chips and burr tend to stick to the inside of the machined channel, which is a stark contrast with what was observed in single crystal cutting, where the channel walls were clean throughout and burr formation was reserved to the levels of top burr alongside the edges (as illustrated in Figure 7.24, where a microscope photo shows the difference between multi and single grain burr formation). Channels also present a similar width, with no noticeable differences.

- Single crystal copper machined at 200 µm depth of cut

A general image on ploughing and burr formation is sought by quantitative analysis of burr width and ploughing width measurements, with results indicated in Figure 7.25.

Ploughing is seen to occur on both left and right walls, with an approximate 6 channels peak formation. The magnitude of the peaks and the valleys differs significantly, however. Peaks are found to form at 18.72 µm, 40.93 µm, 90.91 µm and 103.1 µm for the left side of the channel. For the right side of the channel, 72.77 µm, 44.18 µm, 46.83 µm and 54.51 µm. The averages of the left versus right wall ploughing differ by 5.65 µm (which represents 17% of the ploughing value), with the higher average for the left wall ploughing. This is considered to be a direct results of the tool misorientation towards the right side, as it introduced additional strains on the left side of the channel which caused an increase in material deformation on the wall of the machined surface.

One main aspect of interest is that ploughing evolution on the left and right sides appears as consecutive steps among channels situated at 15° apart. This finding requires further investigation, which endorses the level of analysis established in the later 60-channel study.

Burr width has also been measured on the two top surfaces of the machined walls. Averages for the left and right side are similar, at 14.29 µm and 14.45 µm. On the left wall, it is possible to observe a clearer four peak pattern, with maximum values within each machined sector of 31. 62 µm, 17.08 µm, 42.87 µm and 29.22 µm. On the right side of the channel, it is not possible to observe a peak formation.

This finding indicates that there is a higher difficulty in estimating burr occurrence, rather than ploughing. Furthermore, ploughing and burr formation on the left channel

wall are compared against each other in Figure 7.25. It becomes obvious that peaks and minimum values occur on the same channels, indicating the same main material deformation driving mechanism. This is to be further investigated in more detail in the study of 60-channel single grain results.

- Single crystal copper machined at 50 μm depth of cut

Several aspects of burr and ploughing formation have been investigated. Furthermore, the correlation between burr formation and previously identified chip formation (in Section 7.5.1) are analysed.

- Correlation between chip and burr formation

A qualitative approach is undertaken, in order to identify whether chip orientation and burr formation take place on the same crystallographic directions (on the same channels).

When a chip is being machined and material is removed from within the channel, the material behaves in two different ways. The chip is being compressed and pushed, while shear occurs at the channel edges (attaining plastic yield), being directed by the cutting edges of the tool. On the inside of the channel, chip material is, thus, being 'compressed'. On the outside of the channel, material is being 'pulled'. Accounting for this tensile behaviour, many channels exhibit pulls of the top material, looking like whiskers, as it can be observed in Table 7.5 on channel 5, 6 and on all the channels that have a '1' indicator for burr on both left and right sides of the channel.

From the point of view of chip formation, twisted chips have one edge that underwent compression, while the outer edge has been stretched, due to the difference between the forces developed on sides of the tool cutting edge. On the workpiece material surface, a high top burr would be theoretically expected to occur for material with higher tensile strength. If material strength is resisting shear deformation on the tool cutting edge, this would cause higher pulls to be formed, thus higher burr. Higher burr is associated with a decrease in precision and stability in cutting processes.

A second cause for the decrease in precision is the correlation between channels with high top burr surfaces and the morphology of the chips formed. In chips 26 and 27,

and 41 and 42, the chip morphology is straight, which is characterised as one of the most unfavourable chip morphologies. Examining the level of burr associated with them, the channels exhibit '3'indicators for both edges of the chip, thus there is a direct correlation between the high burr and adverse chip morphology. This chip type, marked undesired in industry, is another cause of decreased precision.

This has led to the procedure aimed at assessing positive correlation between burr formation and chip orientation. When summing the negative and positive marks in the qualitative approach, it is found that negative correlation is established for 20.339% of all analysed channels, while 79.661% are found to be positive. This initial analysis reveals that there is a strong correlation between chip and burr formation. The method of analysing this correlation can be, nevertheless, improved. An apparatus for a better estimation and measurement of the burr is necessary in future studies. At this moment, this method is based on qualitative analysis and thus is error-prone. However, it represents a good first step in the direction of estimating the correlation between chip morphology and top burr formation.

- Burr formation

Analysing the graph in Figure 7.26, the most important finding is that on either side of the channel, top burr formation has an evolution that follows the cutting force pattern, and presents a four peak evolution. This is a direct correspondence and it indicates that in order to estimate burr formation mechanisms and thus plan for burr-free operations in a micro-cutting process, grain orientation must be accounted for, as it depends on the specific cutting forces as determined by the crystallographic anisotropy model.

More interestingly, burr evolution on the left and right sides of the channels appears to be 45° out-of-phase, with very few intercalating points. This validates the fact that burr changes sides, just as the cutting force changes with a 45° symmetry (as indicated in the microscope photos in Figure 7.28). It also proves that (under the current experimental conditions) burr is a direct consequence of the material response under a certain cutting force, rather than a certain angle, and it can be predicted in single crystal cutting.

One interesting aspect is a comparison of these findings with those of Lee et al. (2007). Based on their study of burr formation in turning, wide areas of 'cloudy' burr

formations appear on the frontal surface of the workpiece material, which appears to be a direct effect of crystallographic cutting force patterns. However, this would indicate that for a certain number of consecutive crystallographic directions, burr formation is at its highest, while for a large number of other consecutive crystallographic directions, burr does not occur. In the current research, this would signify that there is a number of consecutive channels with the same behaviour- high or no burr formation mechanisms. Furthermore, both walls of the channels should exhibit the same behaviour, as they belong to the same large zone of cutting. At most, one channel could exhibit opposite burr behaviour as the two channel walls belong to different 'zones' of burr formation. This behaviour is contradicted by the findings in Table 7.5. Burr formation is a much more complex material deformation mechanism, and burr-prone areas are not just a function of the larger four-peak patterns, but of the mechanisms occurring on individual crystallographic directions. This is supported by the high number channels which exhibit different behaviour of their channel walls. Micro-cutting occurs differently on different crystallographic directions, more than just considering the wider four-pattern cutting models.

This shows that the current study takes burr characterisation to a deeper analysis than previous studies in specialty literature, and it constitutes a new material phenomena understanding, which expands the level of knowledge in single grain micro-cutting.

- Ploughing formation

In a similar manner as chip formation, plastic deformation on the walls of channels appears as having a four peak evolution throughout a 360° workpiece rotation. This is shown in Table 7.6 in Appendix A.

Dissimilarly though, the left end right sides of the channels undergo a much lower out-of-phase process, as they appear located only 1 or 2 positions apart (6° or 12°). This indicates the fact that the channel sides undergo very similar ploughing phenomena.

This finding validates the fact that the edges of the channel are undergoing different cutting forces, but even more – the fact that the cutting forces on the two sides of each channel correspond to a small crystallographic change due to which they are formed by neighbouring, consecutive points on the cutting force 360° evolution. This also

confirms the fact that one side of the channel exhibits a stronger ‘pull’, while the other undergoes elongation and is dragged towards the stronger one.

From this theoretical point of view, the expectation was that ploughing would have a symmetrical behaviour at the 45° mark. However, the 6°-12° phase difference appears constant throughout the workpiece rotation.

In this case, each side of the channel behaves as being formed by the normal distribution of cutting forces, without having the interference of the opposite side of the cutting tool. Initial assumptions were that one of the side was ‘weaker’ and thus being dragged towards the other. However, the behaviour of the machined workpiece material must be distinguished from that of the chip. While chip undergoes compression, the edge of channel undergoes tension. So, it is possible that the chip, being a relatively small volume of material, has been under the influence of the consecutive points of cutting forces, being twisted as a result of this difference in force (this accounts for the chip orientation change from left to right within each 90° sector). The main volume of workpiece material, despite being machined, remains a relatively large body, which is not as easily affected by small crystallographic changes in strain, and behaves as the normal evolution of the cutting force dictates.

Compared to previous studies, this new understanding represents a step forward in understanding ploughing mechanisms. These have been developed for micro-cutting of multigrain materials and have almost exclusively considered the minimum chip thickness as the main driving factor in ploughing formation (Oliveira et al., 2012; Malekian et al., 2012). In the current research, the depth of cut has been a constant operating parameter (this is supported by analysis of depth of cut as indicated in Appendix C). Furthermore, the depth of cut has been selected at a much higher level than the cutting edge radius (which is approximately 5 μm), to overcome the minimum chip thickness effect. However, despite these approaches, ploughing is still seen on many of the 60 channels.

The evolution of burr and chip formation, and their correlation with cutting forces in micro-cutting of single crystal copper has not been studied in this manner before. Considering multiple material phenomena, as well as understanding the correlation between chip morphology, ploughing, and surface quality, accounts towards an

improved understanding of material behaviour in single crystal cutting and thus towards improving precision during micro-cutting.

Further steps need to be taken in appreciating the relationship between uncut chip sizes, chip mass, and to what extent the process is affected by crystallographic changes, such as grain rotation. If the mass of the chip is large enough, it is necessary to investigate whether it exhibits a helical and bent shape, such as in the current empirical study. Also, the extent to which the crystallographic influence can overcome that of the operating parameters (e.g. feed or depth of cut) must be better understood. The initial 24-channels study has shown that the chip still changes orientation; however, tool misorientation prevents the same analysis on a larger scale chip (200 µm).

In Figure 7.29, no obvious correlation appears between workpiece rotation and the material phenomena. This is largely due to the mathematical apparatus that has served to estimate the ploughing and burr formation values. Although the points measured and distances calculated are done on the same images that have undergone qualitative analysis, no correlation can be made with those results, or with expected crystallographic effects. The selection of points could not accurately represent what an average ‘ploughing’ or ‘burr’ looks like, just like it could not account for the severity of ploughing. These are not just geometrical measurements, but aspects related to material behaviour and classification of the different types of burr or ploughing is necessary in the future in order to obtain quantitative results for material deformation in single crystal cutting.

7.5.3. Analysis of channel dimensional accuracy in single crystal cutting

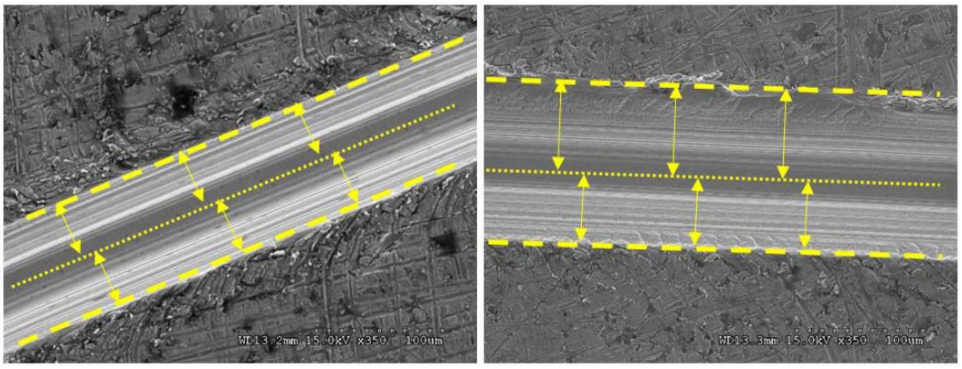
The last aim of this chapter (in investigating the material microstructure influence on micro-cutting precision) was to identify the changes introduced at the level of geometrical features, namely channel width and dimensional accuracy (as shown in the schematic presented in the chapter outline). This section represents the last of the three main results subchapters.

One aspect that has not been investigated in specialty literature focusing on micro-cutting and on single grain material cutting is the effective dimension of a machined feature. Some studies have looked at the relationship between cutting forces in single crystal cutting and the depth of cut (Zhou et al., 2001), but this has been done as a function of the uncut chip thickness and the measured cutting force. Different studies have considered single grain-specific material properties, such as elastic recovery, which can be interpreted as the depth of cut variation due to elastic recovery obtained for an arbitrary uncut chip thickness (Lee et al., 2000 and 2007).

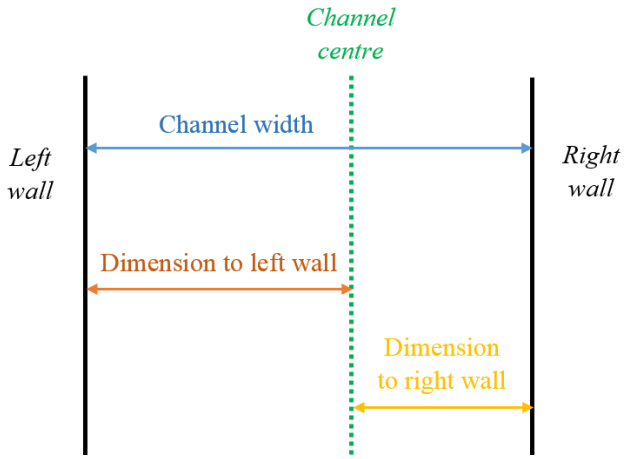
It becomes imperative that channel dimension variation with crystallographic anisotropy needs to be established, due to the importance it has on micro-cutting precision and product quality. A channel that will have varying geometrical features will negatively affect production. As such, a study is proposed for channel width estimation, and association, if possible, with known anisotropic models. Based on these, recommendations for manufacturers can be proposed, in order to compensate for any variation that might affect the desired feature size.

One example of channel width variation is given in Figure 7.30. The images are obtained at the same magnifying scale. It is obvious that not only channel width is affected by single grain specific phenomena, but also channel dimensional accuracy, which ultimately reflects a product quality.

Material mechanical deformation in single crystal cutting has been previously investigated in Sections 7.5.1 and 7.5.2. A correlation between microstructure changes and experimental results has been observed and analysed at the level of chip, burr and ploughing formation. As ploughing has been identified to vary with a four-peak formation in the previous section, it reflects a different surface quality on the machined feature. Not only does this affect precision, but also it introduces differences in the geometrical features of channels machined with constant process parameters.



a.



b.

Figure 7.30. Channel dimensions: a. comparison between a symmetrical channel width and one with a high variation due to ploughing phenomena occurring on one of the channel walls; b. method of measuring the channel width, and the left and the right dimensions from the centre of the channel

In the current section, an assessment of channel dimension variation due to material microstructure properties is sought. Qualitative analysis is employed by obtaining measurements of channel width and channel dimensional accuracy with the aid of an image analysis software.

7.5.3.1. Single crystal copper machined at 200 µm depth of cut

In the current section, channel width and channel dimensional accuracy (relative to the two dimensions given by the distance from the centre from each wall) are measured

for a 24-channel sample. Dimensions are plotted in the graph presented in Figure 7.31, while detailed results are presented in Appendix A.

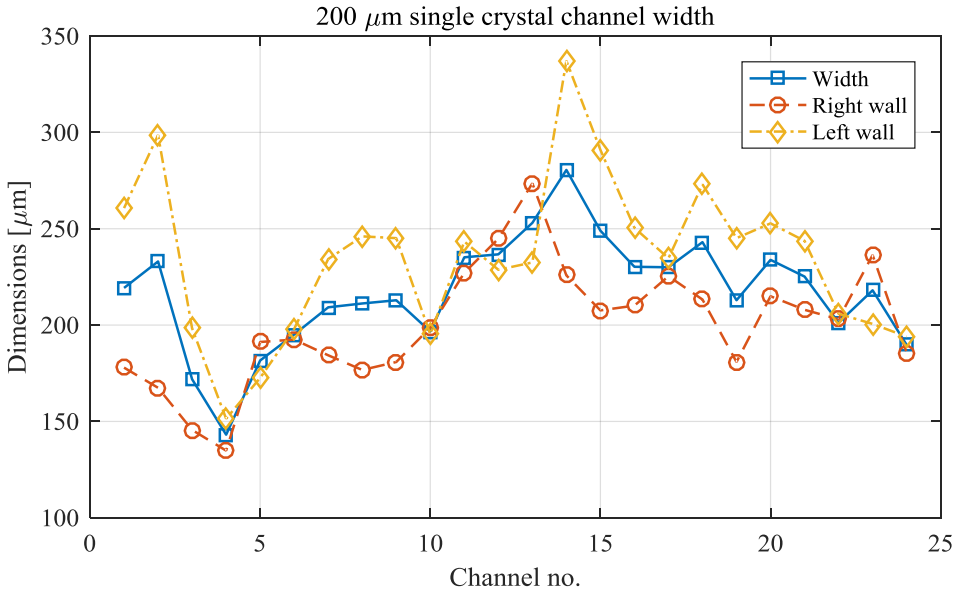


Figure 7.31. Channel dimensional accuracy measurements in 200 µm deep channels

7.5.3.2. Single crystal copper machined at 50 µm depth of cut

In the current section, channel width and channel dimensional accuracy are determined in a similar manner as the previous section, with image analysis software that enabled dimension measurement.

One problem during measurements has been identified as the small variation of the magnifying scale appearing in images, compared to certain known features on the workpiece material. This topic is approached in the discussion. To compensate for the small variation in dimensions, averages have been determined for each 90° sector of the sample. Then, ratios have been calculated between the measurements in their respective sector and the sector average.

Results are shown in the plot in Figure 7.32, while detailed measurements are included in Appendix A.

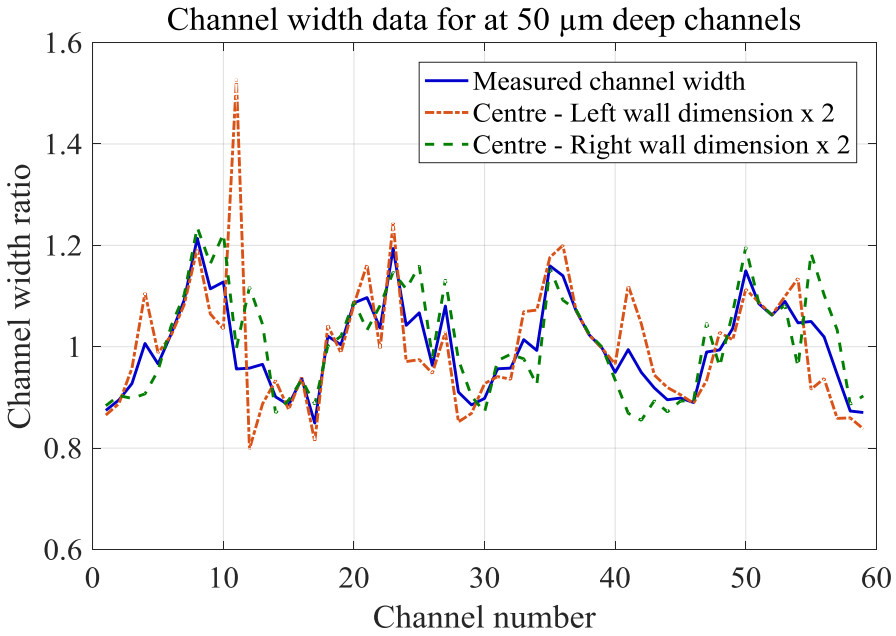


Figure 7.32. Channel width data for single grain material channels machined at 50 µm depth of cut

7.5.3.3. Discussion

In specialty literature, Zhou et al. (2001) have found that surface roughness varies between 0.01 µm and 0.04 µm for four crystallographic directions. More, they have found that the difference between the four results corresponds with the variation of the shear angle, as indicated in Figure 7.33. This represented an important finding, as it proves the direct relationship between dimensional changes (in this case, surface roughness) and crystallographic properties. However, the study was restricted to a very limited number of crystallographic orientations, which do not give the full ensemble of results necessary to characterise an entire workpiece rotation.

Chae, Park and Freiheit (2006) have found that when the uncut chip thickness is lower than the tool edge radius, elastic recovery has higher values (as illustrated previously in Figure 2.6). Their study was based on multigrain material microcutting. While variations in elastic recovery (and thus changes in the effective dimension of a machined feature) are important at micron-level depth of cut, this was mostly associated with the minimum chip thickness effect.

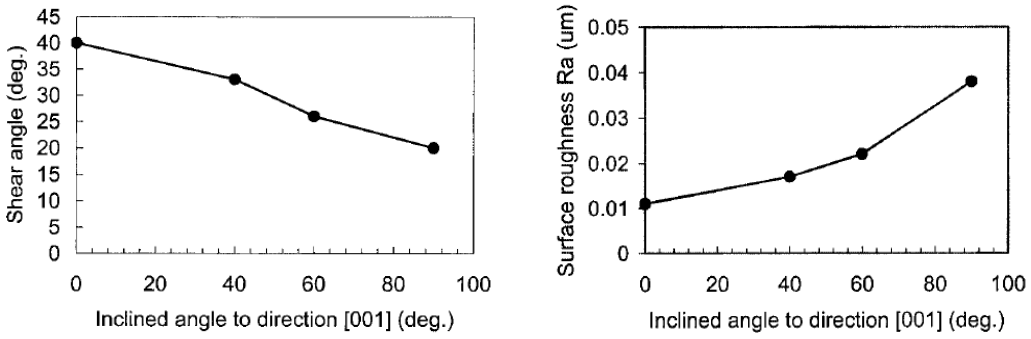


Figure 7.33. Variation of shear angle and surface roughness with crystallographic cutting directions. From Zhou et al. (2001) Figure 7, p. 821; Figure 9, p. 822.

Some correspondence has been established between surface texture (Bunge, 1982), depth of cut, surface roughness and crystal orientation. However, dissimilarities between physical dimensions of differently oriented channels have not been sufficiently explored.

This is a highly important topic of study, as it reflects the quality and precision of a process from many points of view: different volumes of removed material lead to different machinability indicators for each grain orientation; effective differences between nominal and measured dimensions affect precision, accuracy, part quality and repeatability of results.

- Single crystal copper machined at 200 µm depth of cut

Thus, in the current section, channel width has been measured for 24 and 60-channel single grain samples.

The bottom of the channel has also been identified in the SEM images, and a central line going parallel with the machined edges has been selected. On this line, points have been set on the intersection with the transversal line that determines channel width. The distance between the central points and the left, respectively the right points, has served to understand if a channel is unbalanced or more symmetrical. The half-distance to the centre point has been calculated, then doubled to obtain a theoretical value of the channel width in the case of a symmetrical channel. This results in channel width values based on doubling the distance from the centre of the channel to the left, respectively right measured coordinates (as illustrated in Figure 7.30b).

The 24 channel sample has indicated no obvious pattern or repeatability of channel width results. However, this factor can be attributed to the tool misorientation at the beginning of the channel, which introduced supplementary strains on the left walls. This inaccuracy has tampered with results, in terms of both burr formation and channel dimensional accuracy.

The maximum value for channel width has been obtained at 280.51 μm, while the minimum at 143.13 μm. The average of all 24 channels has been calculated at 217.19 μm.

An important observation is the nominal channel width which has been calculated for multigrain materials, as indicated in Figure 5.1. At a 200 μm depth of cut, the channel width was estimated at 230.94 μm. This represents a -6% error between nominal and measured width of cut.

Looking into channel dimensional accuracy, is becomes obvious that due to the additional strains introduced by tool orientation towards the left, left and right walls would be imbalanced. The average for the left wall calculated dimensions (doubling the distance between points on the left wall and points on the centre of the channel) is 200.27 μm, while for the right wall it is 234.71 μm. These represent an -17.8% and +8% variation from the measured average. In an ideal setting, the two averages should match.

The depth of cut of each channel has also been investigated, but no relevant findings have been established. The results of the depth of cut analysis with white-light interferometry is provided in Appendix C.

- Single crystal copper machined at 50 μm depth of cut

To provide a better understanding of channel dimensional accuracy in single grain copper cutting, the width of the 60 channels machined at 50 μm has been measured with an image analysis software.

Based on results and observation in Section 7.5.2, channel walls are found to exhibit different plastic deformation behaviour. Some ploughing has the aspect of very regular plastic deformation, while other appears irregular. A different level of ploughing indicates wider or steeper channel walls, which can be observed in Figure 7.31.

While initially performing the measurement of channel width, a difference was found in the 90° sectors which indicated a drift in the plotted values. More investigation into the quality of SEM photos has revealed that the scale bar of 100 μm did not change despite small variations in the dimensions monitored. This can be due to the imaging software ineffectiveness when the magnifying power varies little, e.g. between x180 and x200. It can also be the cause of electron backscattering at a small inclination angle, which indicates that the surface of the workpiece has a small rotation in the vertical plane. The second situation is more likely, as the SEM sample holding table has the possibility of rotating the sample in the vertical plane, and it might be slightly misaligned from previous measurements.

However, since the drift observed has a small value, the values can be normalised by obtaining an average value for each 90° sector, and then obtaining the ratios between the average and all the preceding dimension measurements: channel width, channel dimensions resulting from the left coordinate, and then channel dimensions given by the right coordinate. The results is in non-dimensional ratios, and this removes the degree of incertitude introduced by the sample rotation. As a results, the results plotted in Figure 7.32 indicate similar values for the lower areas of the lines, signifying removal of drift.

The graph shows three lines corresponding to the measurement and two dimensional accuracy estimations. It is clear that all three lines indicate a four-fold evolution, exactly 15 channels apart. As such, there is an obvious correlation between channel width measurements and their variation when a single grain material is rotated in in the (001) plane. This aspect has not been explored before in literature, but it has a direct relevance to surface quality.

Maximum values of channel width for the four 90° workpiece sectors have been 127.76 μm, 146.65 μm, 146.345 μm and 128.74 μm. Minimum values have been 91.6 μm, 104.34 μm, 111.7 μm and 99.64 μm.

Average values of the four workpiece sectors have been calculated as 105.25 μm, 122.84 μm, 126.84 μm and 111.96 μm.

Interestingly, the average values of left and right channel dimensional estimations follow the same four-peak evolution as the main channel width results, and they appear

to be in the same 90° phase. Due to previous observations that ploughing varied by 1 or 2 positions, and the difference in the width of the channel was in effect given by ploughing, the expectation was to observe a difference between left and right estimations. However, they follow the same pattern. This indicates that despite the lower or higher left and right estimations, they are determined by the same crystallographic direction.

The deviation from an average width value is high. The plot in Figure 7.32 indicates minimums of 0.85, with most maximums reaching 1.2. The exceptions are channels 17 and 18, which reach 1.52, respectively 0.8. These channels appear abnormal, and can be due to errors in measurements or tampering with the channels while the test piece was being handled. In terms of the majority of channels, however, the variation between the average goes from -15% to +20%. The difference between maximum and minimums can be as high as 42 µm.

This is a relevant finding in modelling the material behaviour, if pre-processing mapping of a multigrain surface is possible, in order to determine grain orientations and adjust cutting parameters to compensate for the 35% possible dissimilarity.

The most notable difference is between that of the nominal channel width, of 57.74 µm (Figure 5.1), and the overall measured channel width average, 116.56 µm. The measured average is with 101.87% higher than the prescribed channel width.

However, a few measurements of multigrain samples in Section 7.5.2 has revealed that the multigrain channel width average is 99.34 µm (72.04% higher than the nominal channel width values), and it varies very little between different channels, by only ±2%. This indicates that there is a material formation mechanism that occurs at 50 µm depth of cut for both multigrain and single grain samples.

One possible explanation for the increased channel width is a high occurrence of elastic recovery and ploughing on the channel walls, where material cannot successfully be removed. Using a triangular tip tool makes the chip flow process more complex (a section view of the channel is illustrated in Figure 5.1). Firstly, on the edges of the channel, where there is a shallow depth of cut, elastic phenomena takes place (which varies with crystallographic orientation, as shown by Zhou et al., 2001). As the tool advances at higher depths of cut in the channel, ploughing becomes the main material deformation mechanism. Lastly, fracture takes place in the centre of the

channel, where the bulk of the material is. Due to the low depth of cut of 50 µm, a larger portion of the machined material undergoes phenomena that can be attributed to elastic recovery and ploughing due to the minimum chip thickness effect (Dhanorker and Özel, 2007; Filiz et al., 2007; Malekian et al., 2012). The minimum chip thickness appears to affect both types of microstructures, isotropic and anisotropic. The channel width is seen as constant in the multigrain samples, but it varies significantly in the single grain channels. This is the first time that the minimum chip thickness has been considered in single crystal materials. Due to anisotropic material properties, the minimum chip thickness is also expected to vary with grain orientation.

However, the minimum chip thickness does not explain the difference in channel width variation between single grain and multigrain averages. In the single grain sample, the average is 116.56 µm, compared to 99.34 µm in the multigrain material. In future research, it would be important to establish whether single grain materials are more affected by elastic and plastic phenomena than multigrain samples.

Another interesting observed phenomena is represented by the occurrence of slip dislocations, as presented in Appendix D. They appear to form according to pattern of the experimentally-measured Fy force in Chapter 5.

Channel dimensional accuracy is a parameter that indicates cutting precision. When material behaviour cannot be accurately predicted, micro-cutting precision is affected. Regular multigrain models found in literature do not account for material microstructure when operating parameters are selected.

In future studies, the connection between variations of cutting speed and channel width must be established. It is expected that channel width will behave in a four-peak pattern during a 360° workpiece orientation. It will be important to establish whether minimum and maximum values remain constant at -15% and +20% of the average channel width. It will also be important to determine at which uncut chip thickness the single grain samples generate average dimensions closer to the nominal values.

7.6. Recommendations for improving precision in single crystal micro-cutting

According to the results in this chapter, material phenomena findings can be employed by manufacturers in improving micro-cutting precision, as presented in the following section.

One pre-requirement is to 'map' the surface of the selected workpiece material. By using X-ray diffraction or laser ultrasound techniques, it is possible to determine the material grain size and orientation. This leads to a good characterisation of the material microstructure, usually in the form of a workpiece surface 'map'. This can be used, in analytical or numerical investigations, in order to generate the best micro-cutting precision and surface accuracy.

The first study, of chip formation, has led to establishing different chip morphologies for a single grain material cutting process. In both 24 and 60 channel samples, straight chips have been identified to occur for approximately a third of the machined channels. However, it is known that chip formation is also influenced by operating parameters. By using the workpiece surface 'map', it is possible to determine which grains have crystallographic directions that can generate high cutting forces and straight chips. If such grains are observed in the material microstructure, a small tool inclination (as indicated in Section 7.5.1.3) can serve to create helical chips, thus avoiding poor chip generation. Alternatively, feeds and speeds can be selected such that the chip formation process is accelerated and good chip morphologies, found in neighbouring grains, are used as chip-breakers for the grained with undesirable chip morphologies.

The second study has focused on understanding burr and ploughing formation due to crystallographic anisotropy. One way to overcome this is to investigate the highest burr formation level that can be generated on the machined channel edges, and to use this information as the norm for cutting, instead of that of multigrain. In this manner, the process is regulated by adopting the worst-outcome principle. Thus, operating parameters can be selected to achieve a certain finish, not of a multigrain, but of a material with microstructural properties corresponding to the most difficult grain orientation.

The last study has focused on dimensional accuracy, which has been found to vary with single crystal orientation. Manufacturers can use the 'mapped' image of the

multigrain surface, and a step-by-step cutting process is suggested. A series of grains is grouped together, and channel dimensional accuracy is estimated for the group; this provides a value in between that of a single and a multi-grain. Then, operating parameters are selected for individual groups, and machining is performed in successive steps which lead to good dimensional accuracy.

7.7. Conclusions and future work

In the current chapter, material phenomena investigation for micro-cutting of single and multigrain copper has been performed. The analysed material deformation mechanisms are chip, burr and ploughing formation, and their effect on machined feature dimensional accuracy.

Chip formation, burr formation and ploughing have been found to vary closely with crystallographic anisotropy, and trends have been established based on observed empirical values.

Five copper samples have been machined at a 50 µm and 200 µm depth of cut, with constant operating parameters; two samples were made of multigrain copper, while the other three, of single crystal copper. The multigrain copper test pieces have served as reference for regular material behaviour in cutting, and to prove that material phenomena is repeatable despite changes in the workpiece orientation.

Initially, chip morphology has been investigated and a correlation with crystallographic anisotropy has been sought. Chip morphology has not been previously characterised in specialty literature in relationship with single crystal material properties.

The first multigrain analyses, at a 50 µm and 200 µm depth of cut, have revealed that copper chips have a high bend and helix angle, very serrated edges, and a long shape. On Kluft's chip classification scale (Altintas, 2012), they are found to be acceptable forms of chip. Most importantly, chip morphology is established as constant (illustrated in Figures 7.4 and 7.5). This is an indicator of chip repeatability, which suggests linear stability in the micro-cutting process of a multigrain workpiece material.

The following three steps have been made for single crystal cutting, with one sample having 50 μm deep channels, and two others 200 μm deep channels.

The first and most important finding has been that chip morphology varies with crystallographic orientation (Figures 7.7-7.12). This newly-established variation in chip morphology due to material microstructure endorses the use of cutting force models (as presented in Chapter 4) in the prediction of the chip type that is generated for a certain crystallographic orientation.

The next step has been assessing the chip formation process for a lower depth of cut, of 50 μm, and 60 channels. Qualitative analysis has indicated three main characteristics of chips: bend angle, helix angle and straight shapes. Some chips have exhibited a combination of these characteristics.

The correlation between chip morphology and material microstructure is further confirmed by the observation of straight or bent chips which were positioned 90° apart. However, more chip morphologies have been identified, and a clear classification of all typologies was not possible. This has been attributed to material being more prone to thermal deformation due to the smaller volume of chip material. Again, some chip types have been found to be unfavourable for cutting, as illustrated by chips 11 and 12.

In future research, a numerical model of a single crystal workpiece could be used in generating chip formation mechanisms for more materials and for more crystallographic orientations. If a material surface is ‘mapped’ and grain distribution and grain orientations are determined, then the numerical approach would make it possible to generate the best cutting process due to incorporating the material microstructure influence.

The second step in assessing material phenomena that can help improve micro-cutting precision has been the investigation of ploughing and burr formation.

In the multigrain samples, the material’s high ductility has led to channels which exhibit a high burr formation, and poor surface finish.

For the 200 μm deep channels, in the single grain sample, ploughing and burr measurements have been made for both left and right walls of the channel. Burr and

ploughing formation on the left channel wall have been shown to display similar profiles (Figure 7.32). The absence of a similar pattern correspondence between burr and ploughing on the right wall has been attributed to tool misorientation. The highest ploughing width is estimated at 103.1 µm for the left wall, and at 72.77 µm for the right wall. Since the channel nominal width has been estimated at 230.94 µm, these represent very high values of irregular material behaviour, estimated at 53.79% of the channel width. However, other workpiece orientations have generated ploughing values as low as 9.5 µm on the left wall and 10.77 µm on the right wall. These represented 10.1% of the channel width. Burr width has also been analysed; left and right edges of the channels indicate similar burr averages, of 14.29 µm and 14.45 µm.

The 60-channel single grain sample has been qualitatively assessed and four major burr and ploughing formation patterns have been observed on both machined channel walls. A qualitative estimation of chip and burr positions has been proposed; chip orientation has been found to change on the same channels as when burr formation changes between channel sides for 79.661% cases. This analysis indicates that changes both burr and chip typologies are led by the same material deformations mechanisms.

The third analysis has focused on dimensional accuracy of machined single grain features.

A 24 channel sample investigation in channel dimensional accuracy has indicated no patterns in channel width results. This has been attributed to the initial tool misorientation, which introduced large variations in the strains developed on the right side of the channel. The average of all 24 channel widths has been estimated at 217.19 µm, representing a -6% deviation from the 230.94 µm nominal value.

The most important finding of this experimental study has been gained through investigation of the 50 µm deep single crystal channels. The experimental results of the 60-channel test piece have indicated a clear four-peak formation in channel width, and in the left and right calculations of channel dimensional accuracy. Channel width has been found to form regularly between 91.6 µm and 146.65 µm, in a 15-channel distribution of values which mirrors the cutting force anisotropic behaviour. This is the first time that channel width has been found to vary according to crystallographic properties. This new finding and improved understanding of dimensional accuracy in

machined single grain features has a large impact on micro-cutting precision and quality. Large deviations from the average, of -15% and +20%, recommend that multigrain knowledge would not be applicable in industrial processes where cutting is done through individual grains.

The measured channel width average has been estimated at 116.56 μm in the single grain sample, and at 99.34 μm in the multigrain sample. Both represent a big dissimilarity compared to the nominal channel width, of 57.74 μm. The additional lateral material deformation has been attributed to the minimum chip thickness effect which took place at the 50 μm depth of cut, but was not found at the 200 μm depth of cut. Moreover, single grain channels appeared to be more affected by the elastic recovery and ploughing phenomena than the multigrain channels.

However, channel width repeatability on the (001) plane in single crystal has been established in every 90° sector. This is an important finding, which affects many process parameters. Machinability indicators (such as volume of machined material) are highly influenced by the dimensional accuracy of a prescribed feature; when channel width varies by 35% difference, productivity and surface accuracy can vary by 35%. This effect is highly undesirable for manufacturers.

In future research, a better mathematical approach can be employed in burr estimations. Moreover, material deformation mechanisms (such as individual strains and stresses) which lead to different burr types should be further investigated.

Future studies could also investigate the effect of uncut chip thickness (on dimensional accuracy of single crystal materials) by considering the cumulative influence of elastic recovery and minimum chip thickness.

Based on crystallographic modelling, new predictive models could be developed to analyse both lower and higher depths of cut. The lower depths of cut would provide a more accurate understanding of elastic and plastic deformation in single crystals, while higher depths of cut would highlight the influence of crystallographic properties on dimensional accuracy by eliminating the minimum chip thickness effect.

In conclusion, material phenomena such as shearing, ploughing and elasticity depend on crystallographic anisotropy principles, which lead to different material deformation mechanisms. These mechanisms have been experimentally investigated in the current chapter, and a new understanding has been established for chip, burr and ploughing formation mechanisms, as well as their effect in dimensional accuracy. By providing correlations between these parameters and crystallographic properties, linear stability and repeatability have been better understood and can be implemented in manufacturing processes. Further work is needed to understand the dependency on some operating factors in achieving different levels of burr and chip formation.

CHAPTER 8

CONCLUSIONS AND FUTURE WORK

This section provides an overview of the work undertaken in the thesis. Key findings are reported as follows.

One important phenomenon that takes place in micro-cutting is the size effect. During regular scale cutting, cutting takes place at a depth of cut that is considerably larger than the average grain sizes. In micro-scale cutting, machining is often performed at depths of cut smaller than the average grain size. This makes the material removing process to go through individual grains and cause intra-granular fracture, rather than inter-granular fracture (which occurs at regular scale, as grain boundaries as easier to break than the grain itself). Hence, micro-cutting has to consider the influence on individual grain sizes, orientations and material properties as they vastly differ from multigrain materials. Moreover, multigrain materials have isotropic properties, while single crystal materials are anisotropic by nature.

Important studies cite the influence of the material microstructure as the main driving phenomenon in generating micro-cutting results. Chip formation in two-phase multigrain materials revealed different chip morphologies. These endorse the need for further material experimental investigations which can provide a better understanding in chip formation phenomena, due to its correlation with surface accuracy results. However, a gap in the knowledge is represented by the lack of chip formation analyses in single grain cutting.

Another surface accuracy investigation topic is analysed by several authors in correlation with the minimum chip thickness. In micro-cutting, the desired material deformation mechanism is shearing, as it leads to chip formation. However, it has been observed that ploughing and elastic recovery often occur and negatively affect dimensional accuracy, surface roughness and machined feature integrity. These phenomena have been attributed to the minimum chip thickness effect (MCT), which states that for small uncut chip thickness, lower than half of the cutting tool edge radius, chips seize to form and ploughing takes place instead. A gap in knowledge has been identified as the lack of minimum chip thickness studies that research the influence of the material microstructure, despite the fact that MCT occurs in micro-cutting.

A large body of work has focused on developing cutting force models based on crystallographic anisotropy principles. Other studies have investigated the experimental variation of cutting forces in single crystal cutting. However, a knowledge gap has been identified as the absence of analytical and experimental studies that investigate micro-cutting precision in correlation with material microstructure properties. As such, the analytical cutting force models can be employed in further analytical and experimental analyses that can lead to improving micro-cutting precision.

Based on these literature surveys and identified knowledge gaps, the following aim of this research has been formulated as improving precision by studying the effects of material microstructure and properties in micro-cutting.

Based on the main aim, four research objectives have been formulated. The first objective has been to provide a better understanding of linear stability based on parametric variation in single crystal analytical models. The second objective has been to experimentally validate the cutting force variation in single grain cutting, and to provide a comparative analysis with multigrain results. The third objective has been formulated as the development of new, single grain-specific cutting stability models. The final objective has been to improve the understanding of material deformation mechanisms, due to single crystal cutting effects on surface quality and repeatability of results.

In achieving these four main objectives, the following four chapters have contributed by providing new analytical models and empirical-based understanding of single crystal copper micro-cutting. Key findings and the contribution to research are presented in these four chapter summaries as follows.

Chapter 4

In light of addressing the first objective, precision has been studied based on parametric variation in single crystal analytical models. In this chapter, the precision parameter analysed is linear stability. Cutting force development in single crystal cutting is modelled using orthogonal cutting and crystallographic anisotropy principles. A Matlab program is developed in order to gain an overview of the cutting forces generated on 8 crystallographic planes - (001), (101), (102), (111), (112), (212), (213) and (216) - for a theoretical workpiece rotation of 0° to 360°.

Due to the variation of the cutting forces, linear stability is affected in single crystal cutting. New models are developed in order to study the variation of linear stability between single and multi-grain material cutting. In multigrain, tool deflection and slope have constant values, as they are proportional with the cutting forces. In single grain materials, the new models generate tool deflection profiles similar to those of the cutting forces. As tool deflection varies, the difference in cutting forces values due to geometrical instability introduced by the tool deflection is calculated. The same approach is undertaken in the new models provided for slope.

The new cutting force models, including the influence of linear instability, are compared to original ones. It is found that slope introduces insignificant differences between force profiles, between 0.002° and 0.003°. These values show that slope does not need to be further included in the analysis.

The new cutting force models indicate that tool deflection also introduces small differences, however they are estimated to be between 3.187 μm to 6.375 μm. By considering both minimum and maximum levels in new cutting force calculations, a difference of up to 6 N is observed. This finding recommends the use of new cutting force models that include the influence of tool position.

Chapter 5

The second objective of this thesis has been met by experimentally validating the cutting force variation in single crystal cutting according to the four-peak patterns identified in Chapter 4.

While single crystal cutting has been performed in other tuning and orthogonal studies, they did now investigate the radial and tangential components of the cutting forces developed during a 360° workpiece rotation.

Detailed calibration steps have been performed in order to ensure accuracy of results. Two experimental set ups that enabled workpiece rotation have been proposed. Furthermore, two levels of depth of cut, 50 µm and 200 µm, have been investigated. Based on calibration results, the best experimental set-up has been selected as the 200 µm depth of cut cutting process where the test piece is manually rotated and clamped around the dynamometer axes.

Orthogonal cutting has been performed by a slipping process, with a triangular tip commercially available tool, in single grain (oriented on the (001) crystallographic plane) and multigrain copper samples. This was necessary in order to establish the difference between isotropic and anisotropic material properties which generate different cutting forces.

In this respect, a relevant finding is that all three multigrain cutting forces displayed a linear profile, due to material isotropic phenomena.

The most important finding, however, has been that in single grain cutting at a 200 µm depth of cut, the radial component of the cutting force presents a four-peak formation. This indicates a 90° repeatability of values, corresponding to four-peak symmetry in cutting force development on a (001) crystallographic plane. However, the ratio between minimum and maximum values is 4, while in analytical estimations, it has been 2. The tangential component of the cutting force has not been found to correspond to the previously developed analytical models, and, thus, further investigations are necessary in order to understand its behaviour.

The variation of the cutting force with a four-peak profile justifies the need for new stability analysis, as well as new material understanding that include the effects of the material microstructure.

Chapter 6

Precision can be established based on nonlinear, dynamic stability analysis. However, current limitations in the field are that cutting stability lobes are generated for regular scale cutting, and no stability analysis that includes the effect of the material microstructure has been identified.

In Chapter 4, some parameters have been established as influencing micro-cutting results due to crystallographic anisotropy: shear angles, cutting forces and tool rake angles.

To address the third objective of this study, new cutting stability models are developed based on the variation of these parameters. As such, cutting stability analysis encompasses the effects of crystallographic anisotropy on stability limits for the depth of cut.

The new models have been compared against classic stability lobes. A significant difference has been estimated in results. Considering cutting force variation, the magnitude between maximum and minimum critical depths of cut was estimated at 4.45. Considering the shear angle variation, the ratios was estimated at 2.548. A comparison was also provided between the variations of the cutting forces in analytical (Chapter 4) and empirical (Chapter 5) findings. Multigrain limits fall between the newly identified minimum and maximum values. Also, multigrain cutting stability falls short in estimating the critical depth of cut by a difference of 1.7 mm (based on analytical cutting force) and 3.15 mm (based on empirical cutting force).

These new models and new understanding of the material microstructure influence on cutting stability can help establish improved stability limits which would generate stable, chatter-free areas in cutting. The manufacturing approach recommended is that cutting stability lobes should be kept at the lowest level of the single grain results (corresponding to the highest values of cutting forces and shear angles). This would mitigate against chatter for any single grain orientation.

Chapter 7

The final objective of this research is met by performing a study of the effect of material anisotropy on material main deformation mechanisms in orthogonal cutting of copper. These deformation mechanisms influence surface quality aspects, namely chip formation, burr and ploughing mechanisms, dimensional accuracy and repeatability of results.

By employing the same experimental set up as in Chapter 5, it is possible to correlate the effect of measured cutting forces variation and those of the machined material phenomena. By adopting constant operating parameters, in the form of constant speed and constant depth of cut in each machined sample, the influence of operating parameters has been mainly removed. The only identified error has been a small tool misorientation, as shown in the tool entrance area.

Experimental trials have been performed at a 900m/min feed, in single grain and multigrain samples. Two depths of cut have been suggested, of 50 μm and 200 μm. Experimental results have been investigated with scanning electron microscopy and white-light interferometry. SEM photos have served to measure dimension with an image analysis software. The output parameters that were considered have been chip morphology, burr and ploughing width, and channel width.

Different chip morphologies have been identified for different crystallographic orientations, with a four-pattern repeatability. Chip typologies have been assessed based on Kluft's classification of chip morphologies, and a third of all chips analysed have been found to exhibit straight shapes; this is undesirable in machining operations as it leads to poor surface finish. This represents a new finding and it improves the understanding of chip formation, as chips have not been previously characterised in specialty literature in relationship with single crystal material properties. Furthermore, similar chip morphologies are identified on crystallographic directions which generate similar cutting forces. This validates chip repeatability, and can be used an indicator of linear stability in the micro-cutting process.

Investigations of ploughing and burr formation are the second analysis that has been done in assessing material phenomena, with the objective of improving micro-cutting precision. Qualitative and quantitative estimations of burr and ploughing width have revealed a four-pattern repeatability. In the 200 μm deep channels, the highest

ploughing width is measured as 103.1 µm on the left wall, and as 72.77 µm on the right wall. These indicate very high values of irregular material behaviour, as they represent 53.79% of the channel width. However, the lowest ploughing values are calculated at only 10.1% of the channel width. This indicates a high variation of ploughing phenomena, and its four-peak repeatability can be attributed to crystallographic anisotropy models.

By comparing the chip and burr formation results in the 50 µm deep channels, chip orientation has been found to change on the same channels as burr formation for 79.661% cases. This is a new and significant finding, which indicates that material deformations mechanisms cause changes in both burr and chip typologies.

The final analysis has been done in the estimation of machined feature dimensional accuracy on a 360° single crystal workpiece rotation. Dimensional accuracy was identified by the value of the channel width. In the 50 µm deep channels, a clear four-peak pattern of channel dimensions has been observed. Channel dimensions have been found to vary between 91.6 µm and 146.65 µm. This represents the first time when a machined feature dimensional accuracy has been found to vary according to crystallographic properties.

These three material phenomena studies have provided a new and improved understanding of surface quality and repeatability in machined single grain features. By providing correlations between material phenomena and crystallographic properties, linear stability and repeatability have been better understood. This largely affects micro-cutting precision, and the new findings can be employed in micro-cutting processes in order to improve manufacturing results.

Future work

In this section, the recommendation of areas in which further work can be undertaken is presented.

The impact of tool deflection and the deviation from classic cutting values have also been investigated. These considerations can be expanded to include the dynamic evaluation of tool deflection in single crystal cutting, and this can be done by performing turning experiments of single crystal cutting where tool deflection is

measured with the help of sensors. This would validate the tool position variation due to crystallographic anisotropy.

Also by investigations of single crystal turning operations, it would be important to validate the micro-cutting specific stability lobes. It would also be important to establish the variation of the cutting force in a dynamic process, rather than the linear approach that was undertaken in this thesis.

In future research, a numerical modelling is suggested for single crystal cutting as it would the generation of chip formation for more materials and more crystallographic orientations. This can be done by defining the workpiece in small increments with different material properties, as calculated with analytical models.

In the final chapter, ploughing was identified to occur over large areas of the channel width. This has been correlated with the minimum chip thickness effect. However, future research could investigate the effect of uncut chip thickness by considering the cumulative influence of elastic recovery and ploughing in single crystal cutting. Initial steps have been taken in this direction by analysing the depths of cut between which ploughing has been observed to occur. These measurements can provide an indication on the channel wall inclination, and correlations with material microstructure can help predict the minimum chip thickness for individual crystallographic directions. One question to be answered is why the MCT affected the single grain material (by looking at its average) to a higher extent than the multigrain material.

Based on these findings, the contributions to knowledge are formulated below:

Contributions to knowledge

1. New values for tool deflection based on crystallographic anisotropy
2. New cutting stability lobes, based on crystallographic anisotropy, leading to new critical depth of cut limits
3. New, comprehensive analysis of material deformation mechanisms and repeatability in single crystal copper cutting
4. Recommendations for industry for cutting strategies that include single crystal considerations

Overall, the modelling and experimental investigations have been targeted at improving micro-cutting precision.

New machining strategies have been proposed based on the findings.

By using the new stability, repeatability and machining deformation phenomena knowledge, it is possible to reduce and even remove imprecision due to material microstructure.

These are the first steps necessary in eliminating the overarching influence of size effects on micro-cutting.

The large benefit of this is the possibility of developing, in the future, a micro-cutting process which can be undertaken with the same degree of confidence as a regular cutting process; a technology or set-up where micro-cutting and regular cutting have the same level of precision.

REFERENCES

1. ABBASCHIAN, R. (2010) *Physical Metallurgy Principles*. 4th edition. Stamford, Connecticut: Cengage Learning
2. AFAZOV, S.M., RATCHEV, S.M., SEGAL, J. (2010) Modelling and simulation of micro-milling cutting forces. *Journal of Materials Processing Technology*. 210. 2154–2162.
3. AFAZOV, S.M., RATCHEV, S.M., SEGAL, J., POPOV, A. (2012) Chatter modelling in micro-milling by considering process nonlinearities. *International Journal of Machine Tools & Manufacture*. 56. 28–38.
4. AFAZOV, S.M., ZDEBSKI, D., RATCHEV, S.M., SEGAL, J., LIU, S. (2013) Effects of micro-milling conditions on the cutting forces and process stability. *Journal of Materials Processing Technology*. 213. 671–684.
5. ALBRECHT, P. (1961) New development in the theory of the metal-cutting process part 2: the theory of chip formation. *ASME Journal of Engineering for Industry*. 83. 557–571.
6. ALBRECHT, P. (1962) Self-induced vibrations in metal cutting. *ASME Journal of Engineering for Industry*. 84. 405–417.
7. ALTINTAŞ, Y. (2012) *Manufacturing Automation. Metal cutting mechanics, machine tool vibrations, and CNC design*, 2nd edition. University Press: Cambridge.
8. ALTINTAŞ, Y. LEE, P. (1996) A General Mechanics and Dynamics Model for Helical End Mills. *CIRP Annals - Manufacturing Technology*. 45 (1) 59-64.
9. ALTINTAŞ, Y., JIN, X. (2011) Mechanics of micro-milling with round edge tools. *CIRP Annals - Manufacturing Technology*. 60. 77-80.

10. ALTINTAŞ, Y., LEE, P. (1995) Combined Mechanics and Dynamics of Ball End Milling. *ASME Publication MED.* 2 (1) 657-677.
11. ASTAKHOV, V. (2005) On the inadequacy of the single-shear plane model of chip formation. *International Journal of Mechanical Sciences*. 47 (11) 1649-1672.
12. ATKINS, A.G. (2003) Modelling metal cutting using modern ductile fracture mechanics: quantitative explanations for some longstanding problems. *International Journal of Mechanical Sciences*. 45. 373-396.
13. BACKER, W.R., MARSHALL, E.R., SHAW, M.C. (1952) The size effect in metal cutting. *Transactions of the ASME*. 74. 61-72.
14. BARRETT, C.S., MASSALSKI, T.B. (1980) *Structure of metals: crystallographic methods, principles and data*, 3rd revised edition. Pergamon international library. International series on materials science and technology; v. 35. Oxford : Pergamon
15. BISSACCO, G., HANSEN, H.N., DE CHIFFRE, L. (2006) Size Effects on Surface Generation in Micro Milling of Hardened Tool Steel. *CIRP Annals - Manufacturing Technology*. 1 (55) 593-596.
16. BLACK, JT. (1972) Shear Front-Lamella Structure in Large Strain Plastic Deformation Processes. *ASME. Journal of Engineering for Industry*. 94 (1) 307-313.
17. BOOTHROYD, G., KNIGHT, W.A. (2006) *Fundamentals of machining and machine tools*, 3rd edition. Series: Mechanical Engineering. Boca Raton, Florida: CRC/Taylor & Francis
18. BUNGE. H.-J. (1982) *Texture analysis in material science. Mathematical methods*. Butterworth-Heinemann
19. CALLADINE, C.R. (1985) *Plasticity for Engineers. Theory and Applications*. Woodhead Publishing Series in Civil and Structural Engineering. Chichester: Ellis Horwood
20. CAO, Y., ALTINTAS, Y. (2007) Modelling of spindle-bearing and machine tool systems for virtual simulation of milling operations. *International Journal of Machine Tools and Manufacture*. 47 (9) 1342–1350.
21. CÂMARA, M.A., CAMPOS RUBIO, J.C., ABRÃO, A.M, DAVIM, J. (2012) State of the Art on Micromilling of Materials, a Review. *Journal of Materials Science & Technology*. 28. 673-685.

22. CHAE, J., PARK, S.S., FREIHEIT, T. (2006) Investigation of micro-cutting operations. *International Journal of Machine Tools and Manufacture.* 46 (3–4) 313-332.
23. CHATELAIN, J., & ZAGHBANI, I. (2012). Effect of tool geometry special features on cutting forces of multilayered CFRP laminates. *Journal of Composite Materials*. 85-90
24. CHENG, K. AND HUO, D. (2013) *Micro-cutting. Fundamentals and Applications*, 1st edition, The Wiley Microsystem and Nanotechnology Series, Oxford: John Wiley & Sons.
25. COHEN, P. (1982). *The orthogonal in-situ machining of single and polycrystalline aluminum and copper*, volume 1. Doctoral thesis.
26. DEMIR, E. (2008) Taylor-based model for micro-machining of single crystal fcc materials including frictional effects—Application to micro-milling process. *International Journal of Machine Tools and Manufacture*. 48 (14) 1592–1598.
27. DEPARTMENT OF TRADE AND INDUSTRY (2003) Micro and Nanotechnology Manufacturing Initiative [Online]. Available at: http://webarchive.nationalarchives.gov.uk/ 20060214115915/http://www.dti.gov.uk/nanotechnology/ [30.09.2017]
28. DHANORKER, A., ÖZEL, T. (2008) Meso/micro scale milling for micro-manufacturing. *International Journal of Mechatronics and Manufacturing Systems*. 1 (1) 23-42.
29. DING, H., CHEN, S., CHENG, K. (2010) *Two dimensional vibration-assisted micro-milling: kinematics simulation, chip thickness computation and analysis*. Advanced Materials Research, 97-101. 2779-2784.
30. DONATUS, U., THOMPSON, G.E., ELABAR, D., HASHIMOTO, T., MORSCH, S. (2015) Features in aluminium alloy grains and their effects on anodizing and corrosion. *Surface & Coatings Technology*. 277. 91–98.
31. DORNFELD, D., LEE, D.-E. (2008) *Precision Manufacturing*, New York: Springer.
32. DUCOBU, F., RIVIÈRÈ-LORPHÈVRE, E., FILIPPI, E. (2012) Chip Formation in Micro-cutting. *9th National Congress on Theoretical and Applied Mechanics*, Brussels.

33. EGASHIRA, K., HOSONO, S., TAKEMOTO, S., MASAO, Y. (2011) Fabrication and cutting performance of cemented tungsten carbide micro-cutting tools. *Precision Engineering*. 35. 547-553.
34. ENDRES, W. J., DEVOR, R. E., KAPOOR, S. G. (1995) A Dual-Mechanism Approach to the Prediction of Machining Forces, Part 2: Calibration and Validation. *Journal of Manufacturing Science and Engineering*. 117 (4) 534-541.
35. ENGEL, P (1986) *Geometric crystallography: an axiomatic introduction to crystallography*. Dordrecht: D. Reidel
36. ERNST H., MERCHANT M.E. (1941) Chip formation, friction and high quality machined surfaces. *Surface treatment of metals*. American Society of Metals. 29. 299–378.
37. FILIZ, S., CONLEY, C., WASSERMAN, M., OZDOGANLAR, O. (2007) An experimental investigation of micro-machinability of copper 101 using tungsten carbide micro-end mills. *International Journal of Machine Tools and Manufacture.* 47. 1088-1100.
38. FU, Z., ZHANG, X., WANG, X., Yang, W. (2014) Analytical modelling of chatter vibration in orthogonal cutting using a predictive force model. *International Journal of Mechanical Sciences*. 88. 145–153.
39. GHERMAN L., GLEADALL A., BAKKER O., RATCHEV S. (2017) Manufacturing Technology: Micro-machining. In: Fassi I., Shipley D. (eds) *Micro-Manufacturing Technologies and Their Applications.* Springer Tracts in Mechanical Engineering. Springer, Cham. 97-127.
40. GILLESPIE, L. (1973) *The formation and properties of machining burrs*. PhD thesis. Utah State University.
41. GRZESIK, W. (2017) Chapter 7 - Chip Formation and Control. In: GRZESIK, W. (ed) *Advanced Machining Processes of Metallic Materials. Theory, Modelling, and Applications.* 2nd edition. Amsterdam: Elsevier. 113–146.
42. HARDER, E.E. (2013) *12 Industry Trends that Are Shaping Contract Manufacturing*, [Online], Available: http://blog.metalcutting.com/blog/bid/ 318891/12- Industry-Trends -that-Are-Shaping-Contract-Manufacturing [25.09.2013].
43. HERTZBERG, R. (1996) *Deformation and fracture mechanics of engineering materials*, 4th edition. New York : J. Wiley

44. HESKETH, J., JU, C., GOWDA, S., ZANORIA, E., DANYLUK, S. (1993) Surface Free Energy Model of Silicon Anisotropic Etching. *Journal of the Electrochemical Society*. 140 (4) 1080-1085.
45. HONEYCOMBE, R.W.K. (1968) *The Plastic Deformation Of Metals*. London: Edward Arnold.
46. HUO, D.H., CHENG, K. (2006) A dynamics-driven approach to precision machines design for micro-manufacturing and its implementation perspectives. *Special issue paper. Proceedings of the Institution of Mechanical Engineers. Part B: Journal of Engineering Manufacture*. 222 (1) p. 1-8.
47. JIN, X., ALTINTAS, Y. (2011) Slip-line field model of micro-cutting process with round tool edge effect. *Journal of Materials Processing Technology*. 211. 339-355.
48. JIN, X., ALTINTAS, Y. (2013) Chatter stability model of micro-milling with process damping. *Journal of Manufacturing Science and Engineering*. 135. 1-9.
49. JUNZ WANG, J.-J., ZHENG, C.M. (2002) An analytical force model with shearing and ploughing mechanisms for end milling. *International Journal of Machine Tools & Manufacture*. 42. 761-771.
50. KANG, Y.-H., ZHENG, C.M. (2012) Fourier analysis for micro-end-milling mechanics. *International Journal of Mechanical Sciences*. 65. 105-114.
51. KARPAT, Y., ÖZEL, T. (2006) Predictive Analytical and Thermal Modelling of Orthogonal Cutting Process—Part II: Effect of Tool Flank Wear on Tool Forces, Stresses, and Temperature Distributions. *Journal of Manufacturing Science and Engineering*. 128. 445-453.
52. KAWASAKI, Y. (1974) Cell structures in deformed copper single crystals. *Journal of the Physical Society of Japan.* 36. 142-148.
53. KELLY, A., KNOWLES, K. (2012) *Crystallography and crystal defects*. Chichester: Wiley
54. KOTA, N. (2011) *Mechanical Micromachining-Effect of Crystallographic Anisotropy on Machining Forces*, Ph.D. Thesis, Carnegie Mellon University.
55. KOTA, N., OZDOGANLAR, O.B. (2008) A simplified model for orthogonal micromachining of fcc single-crystal materials. *Transaction of NAMRI/SME*. 36. 193-200.

56. KLUFT, W., KONIG, W., LUTTERWELT, C.A., NAGAYAMA, K. PEKELHARING, A.J. (1979) Present knowledge of chip form. CIRP Annals. 28 (2) 441–455.
57. LAWSON, B.L., KOTA, N., OZDOGANLAR, O.B. (2008) Effects of crystallographic anisotropy on orthogonal micromachining of single-crystal aluminium. *Journal of Manufacturing Science and Engineering, Transactions of the ASME*. 130 (3) 031116-1 – 031116-11.
58. LEE, P., ALTINTAS, Y. (1996) Prediction of ball-end milling forces from orthogonal cutting data. International Journal of Machine Tools and Manufacture. 36 (9) 1059-1072.
59. LEE, W.B., CHEUNG, C.F, TO, S. (1999) Materials induced vibration in ultra-precision machining. *Journal of Materials Processing Technology*, 89–90 318–325.
60. LEE, W.B., CHEUNG, C.F, TO, S. (2002) A microplasticity analysis of micro-cutting force variation in ultra-precision diamond turning. *Transactions of the ASME.* 124. 170-178.
61. LEE, W.B., CHEUNG, C.F, TO, S. (2003) Friction-induced fluctuation of cutting forces in the diamond turning of aluminium single crystals. *Proceedings of the Institution of Mechanical Engineers.* 217 (B) 615-631.
62. LEE, W.B., CHEUNG, C.F, TO, S. (2007) Multi-scale modelling of surface topography in single-point diamond turning. *Journal of Achievements in Materials and Manufacturing Engineering.* 24 (1) 260-267.
63. LEE, W.B., TO, S., CHEUNG, C.F. (2000) Effect of crystallographic orientation in diamond turning of copper single crystals. *Scripta Materialia*. 42. 937–945.
64. LEE, W.B., ZHOU, M. (1993) A theoretical analysis of the effect of crystallographic orientation on chip formation in micromachining. *International Journal of Machine Tools and Manufacture.* 33. 439–477.
65. LEKKALA, R., BAJPAI, V., SINGH, R.K., JOSHI, S.S. (2011) Characterization and modelling of burr formation in micro-end milling. *Precision Engineering*. 35. 625-637.
66. LIU, X., DEVOR, R. E., KAPOOR, S. G., EHMANN, K. F. (2005) The Mechanics of Machining at the Microscale: Assessment of the Current State of

the Science. *Journal of Manufacturing Science and Engineering.* 126 (4) 666-678.

67. LUTTERVELT, C.A., CHILDS, T.H.C., JAWAHIR, I.S., KLOCKE, F., VENUVINOD, K., ALTINTAS, Y., ARMAREGO, E., DORNFELD, D., GRABEC, I., LEOPOLD, J., LINDSTROM, B., LUCCA, D., OBIKAWA, T., SHIRAKASHI, SATO, H. (1998) Present Situation and Future Trends in Modelling of Machining Operations Progress Report of the CIRP Working Group 'Modelling of Machining Operations'. *CIRP Annals - Manufacturing Technology*. 47 (2) 587-626.
68. MALEKIAN, M. MOSTOFA, M.G. PARK, S.S. JUN, M.B.G. (2012) Modelling of minimum uncut chip thickness in micro machining of aluminium. *Journal of Materials Processing Technology*. 212. 553-559.
69. MASUZAWA, T. (2000) State of the Art of Micromachining. *CIRP Annals - Manufacturing Technology*. 49 (2) 473-488.
70. MASUZAWA, T., TÖNSHOFF, H.K. (1997) Three-dimensional micromachining by machine tools. *Annals of the CIRP*. 46 (2) 621–628.
71. MATUSZAK, M., KOCHMAŃSKI, P., POWAŁKA, B. (2014) *Workpiece Grain Size Influence on the Vibration in Micro-milling*, in Ševĉik, L., Lepšík, P., Petrů, M., Mašín, I., Martonka, R. (eds), Modern Methods of Construction Design: Proceedings of ICMD 2013 (Lecture Notes in Mechanical Engineering), Springer International Publishing 583-588.
72. MENDELSON, A. (1968) *Plasticity: theory and application*. Macmillan series in applied mechanics. New York: Macmillan
73. MENDELSON, A. (1968) *Plasticity: Theory and Application*. The Macmillan Company: New York
74. MERRIT, H.E. (1965) Theory of self-excited machine tool chatter. *ASME Journal of Engineering for Industry,* 87 447–454.
75. MORCOM (2013) *Micromachining involves a lot more than using scaled-down tools*, [Online], Available: http://www.micromanufacturing.com/content/micromachining-involves-lot-more-using-scaled-down-tools [25.02.2014].
76. MORIWAKI, T., OKUDA, K. (1989) Machinability of Copper in Ultra-Precision Micro Diamond Cutting. *Annals of the CIRP*. 38. 115-118.

77. NAMAZI, M., ALTINTAS, Y., ABE, T., RAJAPAKSE, N. (2007) Modelling and identification of tool holder–spindle interface dynamics. *International Journal of Machine Tools & Manufacture*. 47. 1333–1341.
78. OLIVEIRA, F.B., RODRIGUES, A.R., COELHO, R.T., FAGALI DE SOUZA, A. (2015) Size effect and minimum chip thickness in micromilling. International Journal of Machine Tools & Manufacture, 89. 39–54.
79. ÖZEL, T., LIU, X., DHANORKER, A. (2007) Modelling and Simulation of Micro-Milling Process. *4th International Conference and Exhibition on Design and Production of Machines and Dies/Molds,* Cesme, Turkey, 21-23.
80. ÖZEL, T., THEPSONTHI, T., ULUTAN, D., KAFTANOĞLU, B. (2011) Experiments and finite element simulations on micro-milling of Ti–6Al–4V alloy with uncoated and cBN coated micro-tools. *CIRP Annals - Manufacturing Technology*. 60. 85-88.
81. PARMAR, H. (2013) *Performance evaluation of cutting tool materials*, [Online], Available: https://harshparmar.files.wordpress.com [16.04.2014].
82. PHAM, D.T., DIMOV, S.S., POPOV, K.B., ELKASEER, A.M.A. (2008) Effects of microstructure on surface roughness and burr formation in micromilling: A review. *Proceedings of the 3rd Virtual International Conference on Innovative Production Machines and Systems (IPROMS*). 270-275.
83. PIOTROWSKA-KURCZEWSKI, I., VEHMEYER, J. (2011) Simulation Model for Micro-milling Operations and Surface Generation. *Advanced Materials Research*. 223. 849-858.
84. QIN, Y., BROCKETT, A., MA, Y., RAZALI, A., ZHAO, J., HARRISON, C., PAN, W., DAI, X., LOZIAK, D. (2010) Micro-manufacturing: research, technology outcomes and development issues. International Journal of Advanced Manufacturing Technology. 47. 821–837.
85. QUINTANA, G., CIURANA, J. (2011) Chatter in machining processes: A review. *International Journal of Machine Tools & Manufacture.* 51 363-376.
86. RAO, S. (2011) *Mechanical vibrations. 5th edition*. Singapore; London: Prentice Hall
87. RAMALINGAM, S., BLACK, J.T. (1973) An electron microscopy study of chip formation. Metallurgical Transactions. 4. 1103-1112.

88. REID, C. N., OWEN, W. S. (1973) *Deformation Geometry for Materials Scientists*. Pergamon Press: Oxford
89. SAIPAVEN (2014) *Orthogonal and oblique cutting*, Available: http://mechanicalbuzz.com/orthogonal-and-oblique-cutting.html [15.04.2016].
90. SCHMID, E., BOAS, W. (1968) *Plasticity of crystals: with special reference to metals*. London: Chapman and Hall
91. SCHMITZ, T., SMITH, K. (2009) *Machining dynamics: frequency response to improved productivity*. New York; London: Springer.
92. SCHMITZ, T., SMITH, K. (2011) *Mechanical vibrations: modeling and measurement*. New York; London: Springer
93. SHANAHAN, J. (2013) *Trends in micro machining technologies*, [Online], Available: http://www.makino.com/about/news/trends-in-micro-machining-technologies/315/ [27.09.2013].
94. SHAW, M. (1984) *Metal Cutting Principles*. Oxford on Advanced Manufacturing. Oxford University Press, USA
95. SIMONEAU, A., ELBESTAWI, M.A. (2006) Chip formation during microscale cutting of medium carbon steel. *International Journal of Machine Tool and Manufacture*. 46. 467-481.
96. SIMONEAU, A., ELBESTAWI, M.A. (2006) Surface defects during microcutting. *International Journal of Machine Tools & Manufacture*. 46. 1378-1387.
97. SIMONEAU, A., ELBESTAWI, M.A. (2006) The effect of microstructure on chip formation and surface defects in micro-scale, mesoscale and macroscale cutting of steel. *Annals of the CIRP*. 555. 97-102.
98. STEPAN, G., SZALAI, R., INSPERGER, T. (2003) *Nonlinear dynamics of high-speed milling subjected to regenerative effect*, in G. Radons (ed), Nonlinear Dynamics of Production Systems, New York: Wiley-VCH. 1-18.
99. SUH, C. S., LIU, M.-K., (2013) *Control of Cutting Vibration and Machining Instability : A Time-Frequency Approach for Precision, Micro and Nano Machining* [Online], John Wiley & Sons, Available: http://site.ebrary.com/lib/uon/reader.action?docID=10748724&ppg=179 [18.03.2015]

100. SZALAI, R., STEPAN, G., HOGAN, S.J. (2004) *Global dynamics of low immersion high-speed milling*. Chaos. 14 (4) 1069-1077.

101. THOMSON, W.T., DILLON DAHLEH, M. (2014) *Theory of vibrations with applications*. Essex: Pearson Education.

102. TO, S., LEE, W.B, CHAN, C.Y. (1997) Ultraprecision Diamond Turning of Aluminium Single Crystals. *Journal of Materials Processing Technology*. 63. 157-162.

103. TOBIAS, S.A. (1965) *Machine-tool vibration*. London: Blackie and Sons Limited.

104. TRENT, E.M. (1991) *Metal cutting*, 3rd ed. Oxford : Butterworth Heinemann

105. TLUSTY, J., POLACEK, M. (1963) The stability of machine tools against self-excited vibrations in machining. *International Research in Production Engineering, ASME*, 1 465–474.

106. TURKOVICH, B.F., BLACK, J.T. (1970) Micro-machining of aluminium and copper crystals. *Journal of Engineering for Industry*. 92. 130-134.

107. VAN LUTTERVELT, C.A., CHILDS, T.H.C., JAWAHIR, I.S., KLOCKE, F., VENUVINOD, K., ALTINTAŞ, Y., ARMAREGO, E., DORNFELD, D., GRABEC, I., LEOPOLD, J., LINDSTROM, B., LUCCA, D., OBIKAWA, T., SHIRAKASHI, SATO, H. (1998) Present Situation and Future Trends in Modelling of Machining Operations Progress Report of the CIRP Working Group 'Modelling of Machining Operations'. *CIRP Annals - Manufacturing Technology*. 47 (2) 587-626.

108. VENKATACHALAM, S., FERGANI, O., LI, X., YANG, J.G., CHIANG, K.-N., LIANG, S.Y. (2015) Microstructure effects on cutting forces and flow stress in ultra-precision machining of polycrystalline brittle materials. *Journal of Manufacturing Science and Engineering*, 137 (2) 1-8.

109. VOLLERTSEN, F., BIERMANN, D., HANSEN, H.N., JAWAHIR, I.S., KUZMANE, K. (2009) Size effects in manufacturing of metallic components. *CIRP Annals - Manufacturing Technology*. 58 (2) 566–587.

110. VORONOV, S.A., KISELEV, I.A. (2011) Dynamics of flexible detail milling. *Proceedings of the Institution of Mechanical Engineers, Part K: Journal of Multi-body Dynamics*. 225-299.

111. WALDORF, D.J. (2006) A Simplified Model for Ploughing Forces in Turning. *Journal of Manufacturing Processes.* 8 (2) 76-82.

112. Wan, Z., Li, Y., Tang, H., Deng, W., Tang, Y. (2014) Characteristics and mechanism of top burr formation in slotting microchannels using arrayed thin slotting cutters. Precision Engineering. 38 (1) 28-35.

113. WEULE, H. HUNTRUP, V., TRISCHLER, H. (2001) Micro-cutting of steel to meet new requirements in miniaturization. *Annals of the CIRP*. 50. 61-64.

114. WU, J.-S. (2013) *Analytical and Numerical Methods for Vibration Analyses*. Singapore: Wiley.

115. ZHANG, S.J., TO, S., WANG, S.J., ZHU, Z.W. (2015) A review of surface roughness generation in ultra-precision machining. *International Journal of Machine Tools and Manufacture.* 91. 76–95.

116. ZHOU, M & W.B., LEE. (1993). A microplasticity analysis of shear zone formation in single crystal cutting. *Advances in Engineering Plasticity and Its Applications*. 875-880.

117. ZHOU, M., LEE, W.B. (1999) Materials induced vibration in ultra-precision machining. *Journal of Materials Processing Technology,* 89–90 318–325.

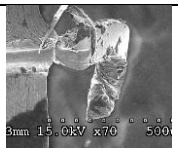
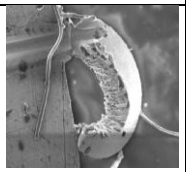
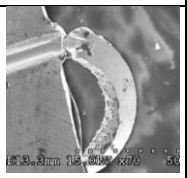
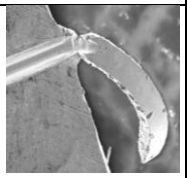
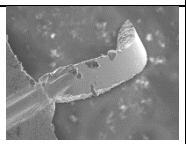
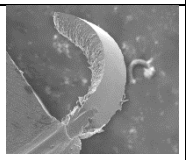
118. ZHOU, M., NHOI, B.K.A., ZHONG, Z.W., WANG, X.J. (2001) The effect of material microstructure on microcutting processes. Materials and Manufacturing Processes, 16 (6) 815–828.

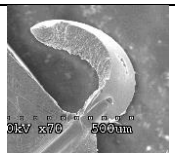
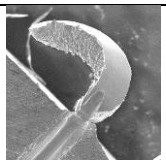
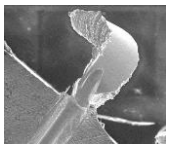
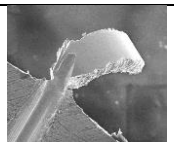
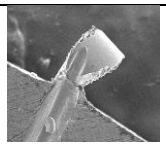
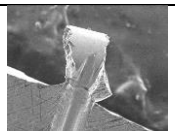
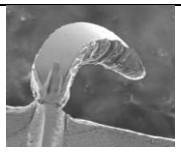
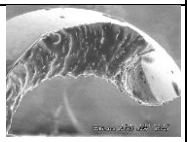
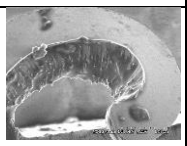
119. ZHOU, Y., YANG, L., HUANG, Y. (2014) *Micro- and macromechanical properties of materials*. Boca Raton, Florida; London: CRC Press

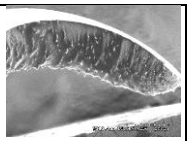
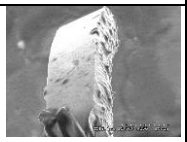
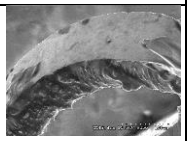
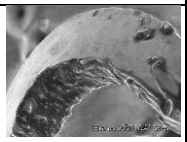
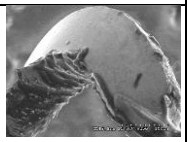
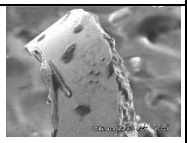
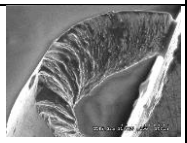
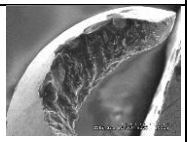
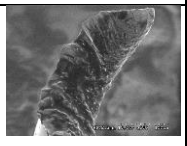
120. ZOREV, N.N. (1966) *Metal Cutting Mechanics,* 1st English edition. Oxford : Pergamon Press

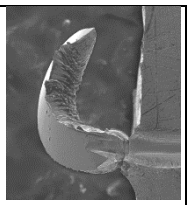
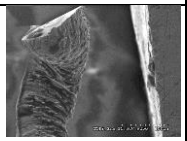
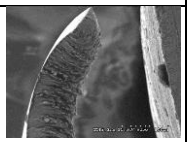
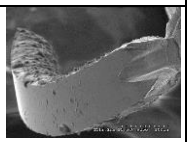
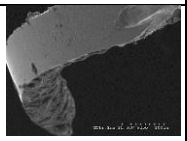
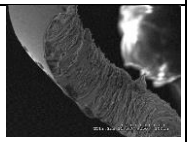
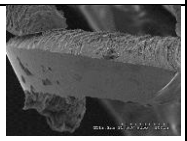
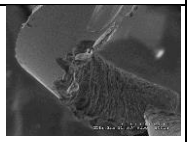
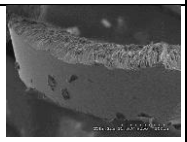
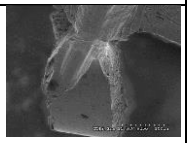
APPENDIX A. TABLES FOR DATA POINTS ANALYSED IN SINGLE CRYSTAL MICRO-CUTTING

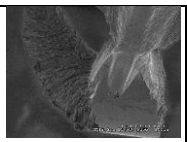
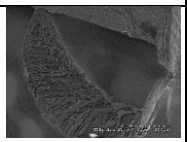
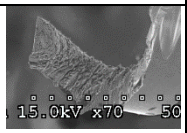
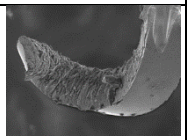
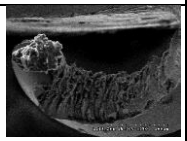
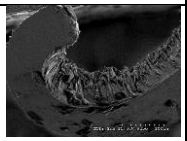
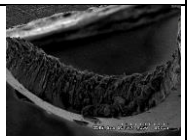
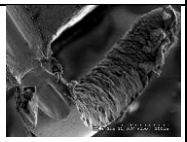
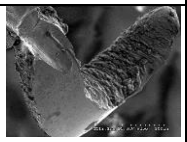
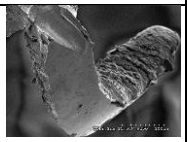
Table 7.2. Qualitative assessment of exit chip form and orientation

Channel no	Chip morphology	Helix None=1 Small=2 High=3	Bend None=1 Small=2 High=3	Refe-rence	Orienta-tion	Orienta-tion change
2		3	1		R	1
3		1	3	1	R	1
4		1	3		R	1
5		1	2		0	1-2
6		2	2		L	2
7		2	2		L	2

8		2	1		L	2
9		2	1		L	2
10		2	2		L	2
11		3	1	2	0	2-3
12		3	1	2	0	2-3
13		3	1		0	2-3
14		2	1		R	3
15		2	2		R	3
16		2	2		R	3
17		2	2		R	3
18		1	3	1	R	3

19		2	2		R	3
20		2	1		R	3
21		1	1		0	3-4
22		1	3		L	4
23		1	3		L	4
24		3	2		L	4
25		3	1		0	4-5
26		1	1	2	0	4-5
27		2	1	2	0	4-5
28		2	2		R	5
29		2	3		R	5
30		3	1		R	5

31		3	2		R	5
32		2	3	1	R	5
33		3	2		R	5
34		2	2		R	5
35		2	1		R	5
36		2	1		L	6
37		2	2		L	6
38		2	1		L	6
39		3	1		L	6
40		3	1		L	6
41		1	1	2	0	6-7
42		3	1	2	0	6-7

43		3	1		R	7
44		3	1		R	7
45		3	1		R	7
46		3	2		R	7
47		2	2		R	7
48		1	3	1	R	7
49		2	2		R	7
50		2	1		R	7
51		2	1		L	8
52		3	1		L	8
53		3	1		L	8
54		3	1		L	8

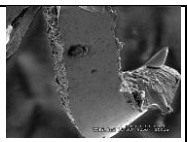
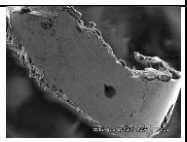
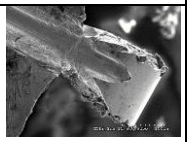
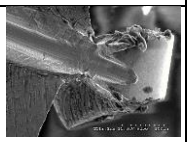
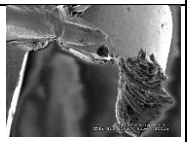
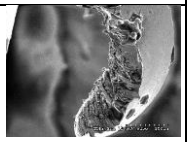
55		3	1		L	8
56		2	1	2	0	8-1
57		2	1	2	0	8-1
58		2	1		R	1
59		2	1		R	1
60		1	3		R	1
1		N/A	N/A		N/A	N/A

Table 7.3. Shear angle values calculated for 6 channels in a 90° segment of workpiece

Point no	Orientation angle [°]	Shear angle value [°]
1	224.35	23.40
2	242.00	36.19
3	259.65	35.40
4	277.30	53.96
5	294.95	48.58
6	312.60	22.43

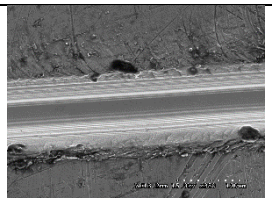
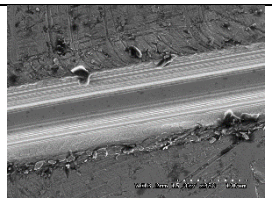
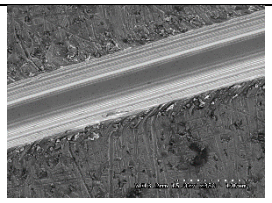
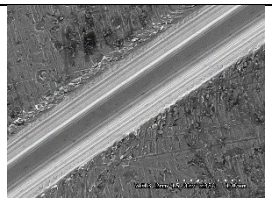
Table 7.4. Shear angle values calculated for 15 channels in a 90° segment of workpiece

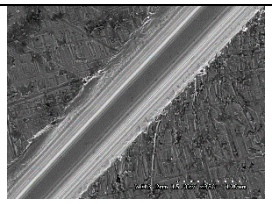
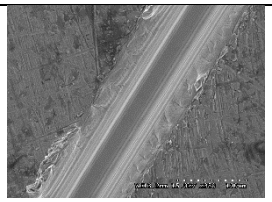
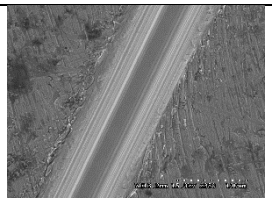
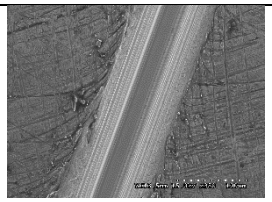
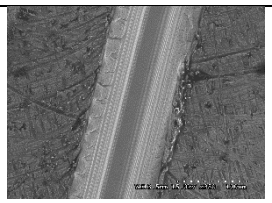
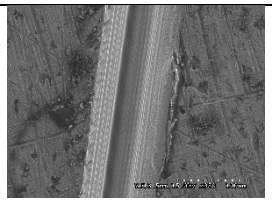
Point no	Orientation angle [°]	Shear angle value [°]
1	224.35	23.40
2	230.65	29.18
3	236.96	35.08
4	243.26	32.63
5	249.56	25.33
6	255.87	31.21
7	262.17	38.33
8	268.48	45.28
9	274.78	51.07
10	281.08	56.35
11	287.39	41.73
12	293.69	47.10
13	300.00	52.57
14	306.30	51.06
15	312.60	22.43

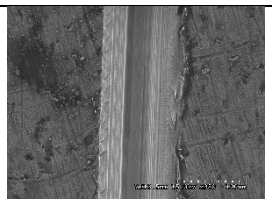
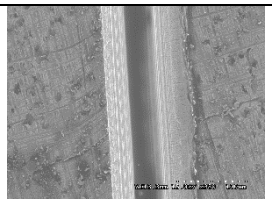
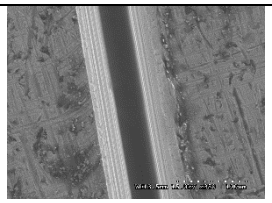
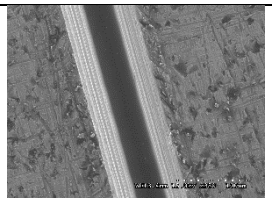
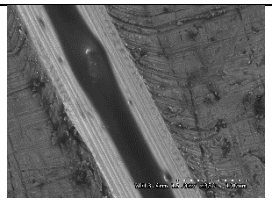
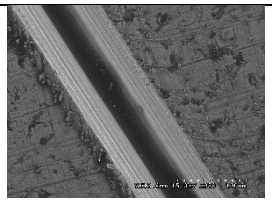
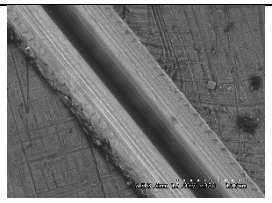
Table 7.5. Quantitative assessment of ploughing and burr formation

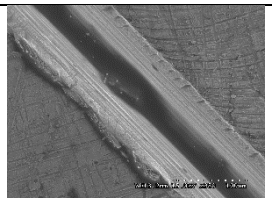
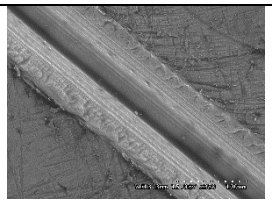
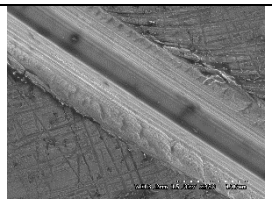
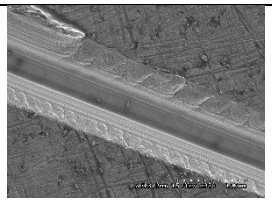
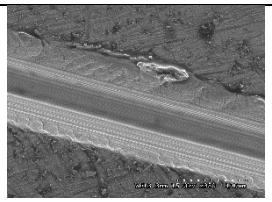
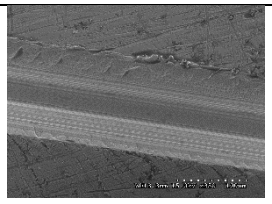
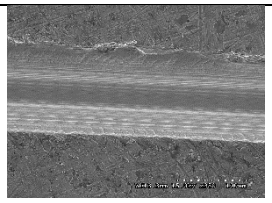
Channel	Ploughing width left [µm]	Ploughing width right [µm]	Burr width left [µm]	Burr width right [µm]
1	18.72	83.19	0.00	14.45
2	13.12	35.77	0.00	25.06
3	12.04	25.47	10.05	32.67
4	9.51	13.92	31.63	18.95
5	40.94	26.96	15.71	0.00
6	36.63	25.20	12.61	9.15
7	27.11	72.77	0.00	12.89
8	12.77	44.83	0.00	19.41
9	10.77	60.01	12.48	9.96
10	19.46	12.56	8.78	8.28
11	32.68	38.55	17.09	19.21
12	70.63	44.19	17.91	5.22
13	78.32	23.82	10.29	15.09
14	90.91	15.04	21.12	8.24
15	59.76	16.69	42.88	4.82
16	39.77	11.30	12.81	7.29
17	30.28	46.84	9.38	10.91
18	50.70	38.48	13.11	8.30
19	103.11	21.12	20.56	13.26
20	65.00	19.88	29.22	4.69
21	40.08	13.91	25.27	8.19
22	16.54	10.77	10.45	45.19
23	22.14	54.52	7.86	17.34
24	27.97	37.46	13.85	28.28

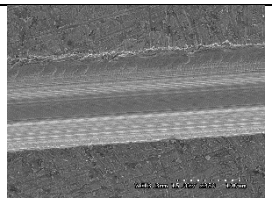
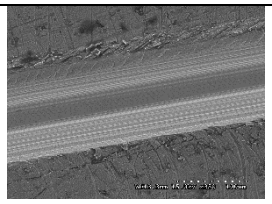
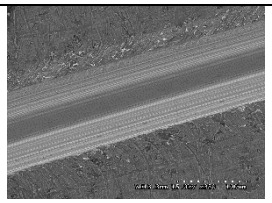
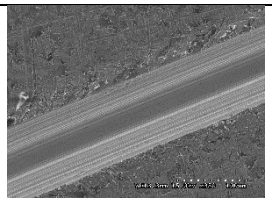
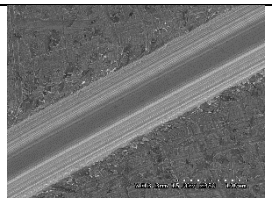
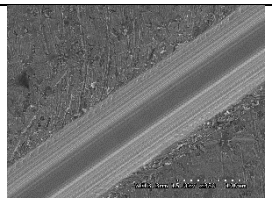
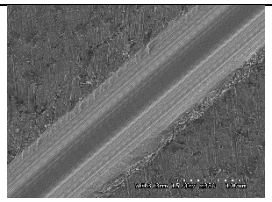
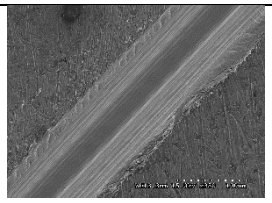
Table 7.6. Qualitative assessment of burr and ploughing phenomena

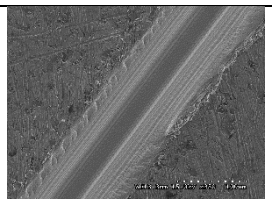
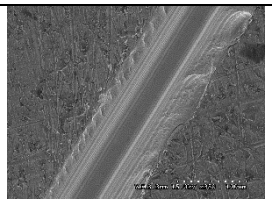
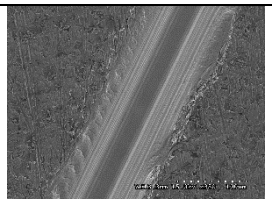
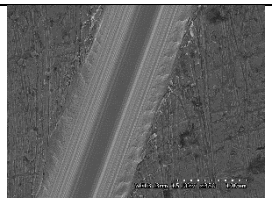
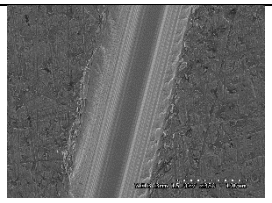
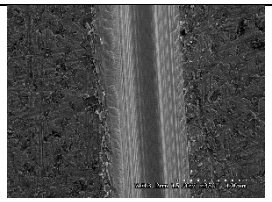
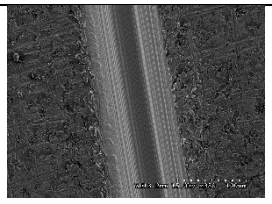
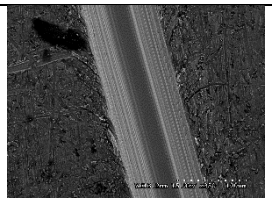
Channel no	Channel shape	Ploughing left None=1 Small=2 High=3	Ploughing right None=1 Small=2 High=3	Burr left None=1 Small=2 High=3	Burr right None=1 Small=2 High=3
1		1	3	1	3
2		1	3	1	3
3		1	3	1	3
4		1	2	1	2
5		1	1	2	2
6		1	1	2	1
7		1	1	2	1

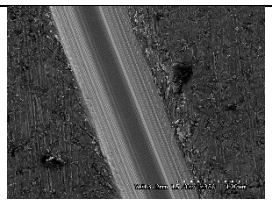
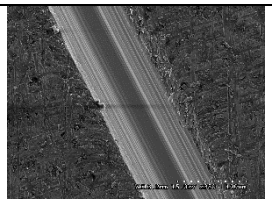
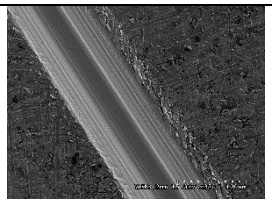
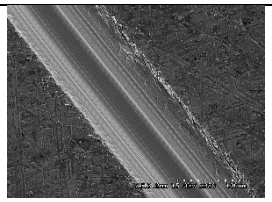
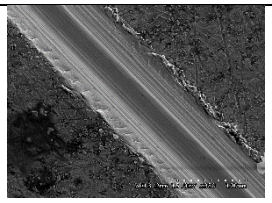
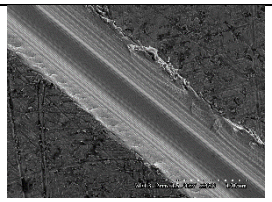
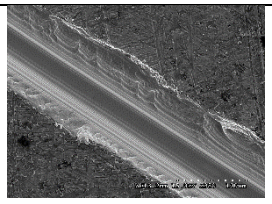
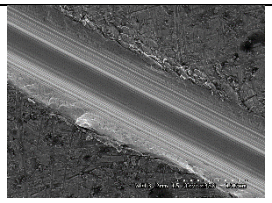
8		2	1	3	1
9		2	1	3	1
10		3	2	3	1
11		3	3	2	1
12		3	2	2	1
13		2	2	1	1
14		2	2	1	2
15		2	2	1	2

16		2	2	1	3
17		1	2	1	3
18		1	1	1	2
19		1	1	1	1
20		1	1	1	1
21		1	1	1	1
22		1	1	2	1
23		2	1	2	1

24		2	1	3	1
25		3	2	3	1
26		3	2	2	1
27		3	3	2	2
28		3	3	2	2
29		2	3	1	3
30		2	3	1	3
31		1	2	1	3

32		1	2	1	3
33		1	2	1	3
34		1	1	1	2
35		1	1	1	1
36		1	1	1	1
37		1	1	2	1
38		2	1	2	1
39		2	1	3	1

40		3	2	3	1
41		3	3	3	2
42		3	3	3	2
43		3	3	2	2
44		3	3	2	2
45		2	2	1	2
46		2	2	1	3
47		1	2	1	3

48		1	1	1	2
49		1	1	1	1
50		1	1	2	1
51		1	1	2	1
52		2	1	3	1
53		2	1	3	1
54		3	2	3	1
55		3	2	3	2

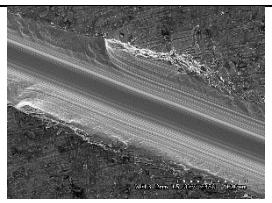
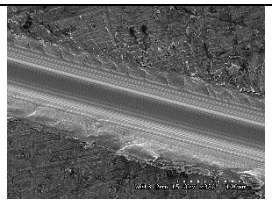
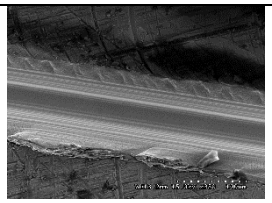
56		3	3	3	2
57		3	3	2	2
58		3	3	2	3
59		2	3	2	3

Table 7.8. Plastic deformation folds measurement

Channel no	Left burr	Right burr	Left ploughing	Right ploughing
1	3.74	12.33	7.20	42.68
2	5.34	0.00	10.64	35.75
3	0.00	14.36	6.25	10.94
4	7.79	11.87	6.19	8.70
5	4.53	8.54	5.88	8.61
6	12.49	13.54	5.93	9.22
7	15.57	9.26	7.50	9.50
8	12.48	9.96	11.74	8.98
9	8.15	6.82	19.64	10.61
10	8.15	4.84	15.93	11.83
11	16.92	8.61	21.04	13.84
12	17.76	18.24	30.74	20.56
13	9.91	15.70	27.66	25.57
14	9.22	11.30	7.20	42.68
15	8.26	10.84	19.64	25.62
16	3.74	12.33	8.38	25.31

Table 7.9. Channel width measurements, and calculated dimension based on left or right walls

Channel	Channel width [µm]	Left dimension [µm]	Right dimension [µm]
1	219.29	177.92	260.71
2	233.02	167.46	298.64
3	171.91	145.59	198.31
4	143.13	134.85	151.42
5	181.63	191.24	172.59
6	195.11	192.47	198.04
7	209.23	184.33	234.28
8	211.22	176.72	246.04
9	212.90	180.84	245.13
10	196.67	198.67	195.24
11	235.18	227.16	243.35
12	236.72	244.83	228.71
13	253.04	273.57	232.51
14	280.52	225.79	337.15
15	249.00	207.63	290.91
16	230.26	210.10	250.48
17	230.01	225.37	234.69
18	243.04	213.25	272.99
19	212.90	180.84	245.13
20	233.85	214.97	252.79
21	225.18	207.93	243.70
22	201.23	203.05	205.86
23	218.06	236.37	200.62
24	189.71	185.67	193.98

Table 7.10. Channel dimension measurements and estimations

Channel no	Channel width measure-ment [µm]	Dimension based on left measure-ment [µm]	Dimension based on right measure-ment [µm]	Ratio average/ width	Ratio average/ left	Ratio average/ right
1	110.51	96.42	124.67	1.05	0.92	1.18
2	107.30	98.65	116.02	1.02	0.94	1.10
3	99.51	90.38	108.76	0.95	0.86	1.03
4	91.90	90.48	93.32	0.87	0.86	0.89
5	91.60	88.21	95.04	0.87	0.84	0.90
6	92.03	91.07	93.01	0.87	0.87	0.88
7	94.20	93.42	95.11	0.89	0.89	0.90
8	97.61	100.80	94.53	0.93	0.96	0.90
9	105.93	116.43	95.46	1.01	1.11	0.91
10	101.69	103.99	100.32	0.97	0.99	0.95
11	107.89	107.57	109.56	1.03	1.02	1.04
12	114.93	113.99	116.02	1.09	1.08	1.10
13	127.77	125.62	130.07	1.21	1.19	1.24
14	117.27	112.08	122.50	1.11	1.06	1.16
15	118.70	108.95	128.72	1.13	1.04	1.22
Average	**105.26**	**102.54**	**108.21**			
16	117.45	187.74	122.47	0.96	1.53	1.00
17	117.66	98.03	137.32	0.96	0.80	1.12
18	118.58	108.98	128.28	0.97	0.89	1.04
19	110.69	114.64	106.84	0.90	0.93	0.87
20	108.75	107.63	109.89	0.89	0.88	0.89
21	115.10	115.40	114.88	0.94	0.94	0.94
22	104.34	99.83	108.89	0.85	0.81	0.89
23	125.40	128.01	123.06	1.02	1.04	1.00
24	123.31	121.38	125.37	1.00	0.99	1.02
25	133.44	133.11	133.81	1.09	1.08	1.09

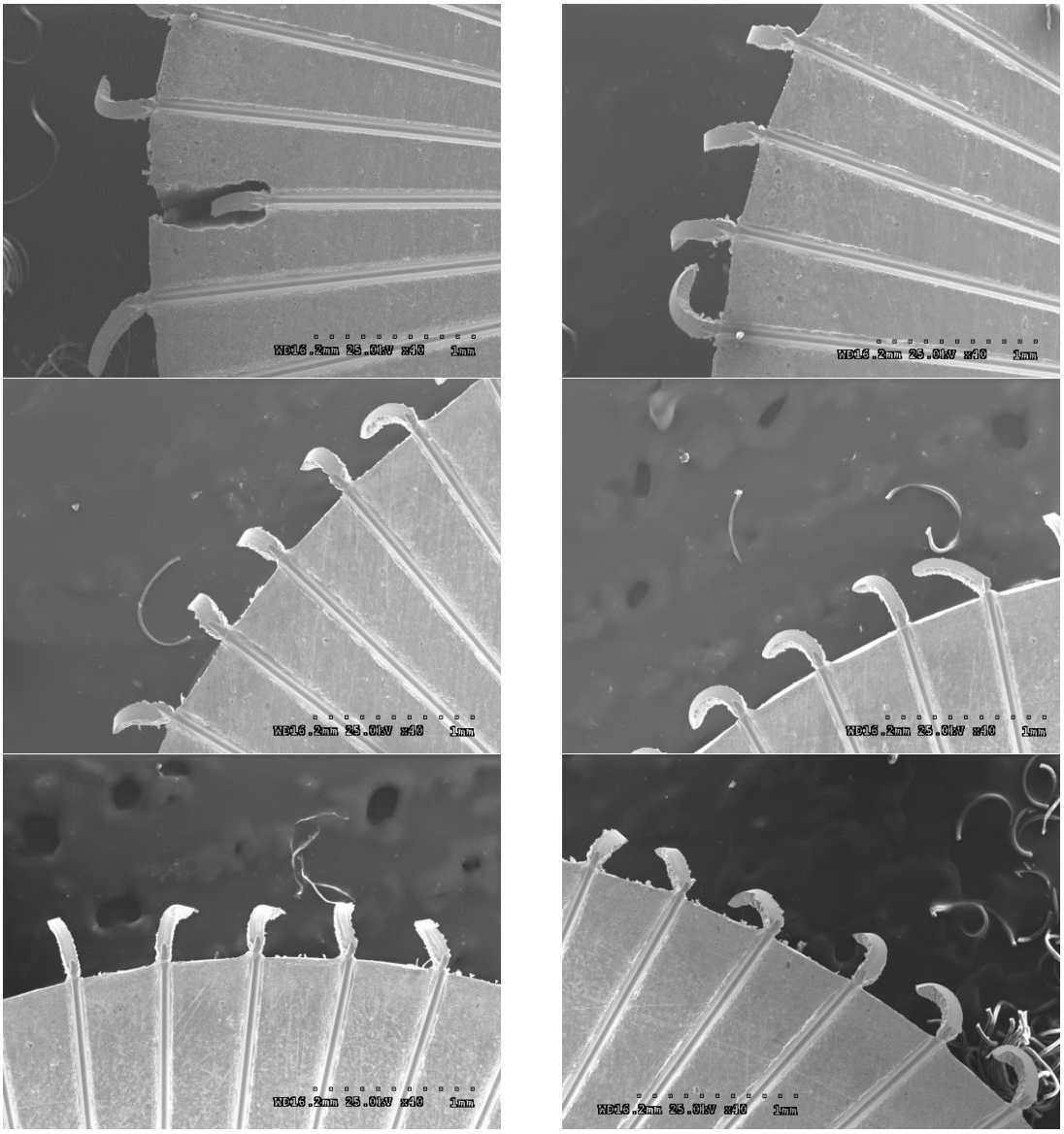
26	134.75	142.79	126.89	1.10	1.16	1.03
27	127.37	122.19	132.82	1.04	0.99	1.08
28	146.66	152.85	140.94	1.19	1.24	1.15
29	128.02	119.25	136.84	1.04	0.97	1.11
30	131.07	119.71	142.47	1.07	0.97	1.16
Average	**122.84**	**124.77**	**126.05**			
31	121.54	119.60	123.53	0.96	0.95	0.98
32	136.32	129.85	142.89	1.08	1.03	1.13
33	114.89	107.49	122.97	0.91	0.85	0.97
34	111.71	109.60	113.87	0.89	0.87	0.90
35	113.32	117.02	109.92	0.90	0.93	0.87
36	120.70	118.75	122.74	0.96	0.94	0.97
37	120.87	118.10	124.33	0.96	0.94	0.99
38	127.95	134.93	123.18	1.01	1.07	0.98
39	125.26	135.31	116.71	0.99	1.07	0.92
40	146.35	148.43	145.80	1.16	1.18	1.16
41	143.86	151.44	137.78	1.14	1.20	1.09
42	135.20	135.30	135.42	1.07	1.07	1.07
43	129.20	129.17	129.46	1.02	1.02	1.03
44	125.84	125.78	126.08	1.00	1.00	1.00
45	119.81	121.89	117.89	0.95	0.97	0.93
Average	**126.19**	**126.84**	**126.17**			
46	111.33	125.48	97.26	0.99	1.12	0.87
47	106.31	117.06	95.71	0.95	1.05	0.85
48	102.86	105.71	100.03	0.92	0.94	0.89
49	100.24	102.96	97.58	0.90	0.92	0.87
50	100.63	101.36	99.97	0.90	0.91	0.89
51	99.64	99.48	100.00	0.89	0.89	0.89
52	110.80	104.50	117.24	0.99	0.93	1.05
53	111.25	115.13	107.56	0.99	1.03	0.96
54	116.00	113.49	119.53	1.04	1.01	1.07
55	128.75	124.64	133.98	1.15	1.11	1.20
56	121.47	121.82	121.59	1.08	1.09	1.09

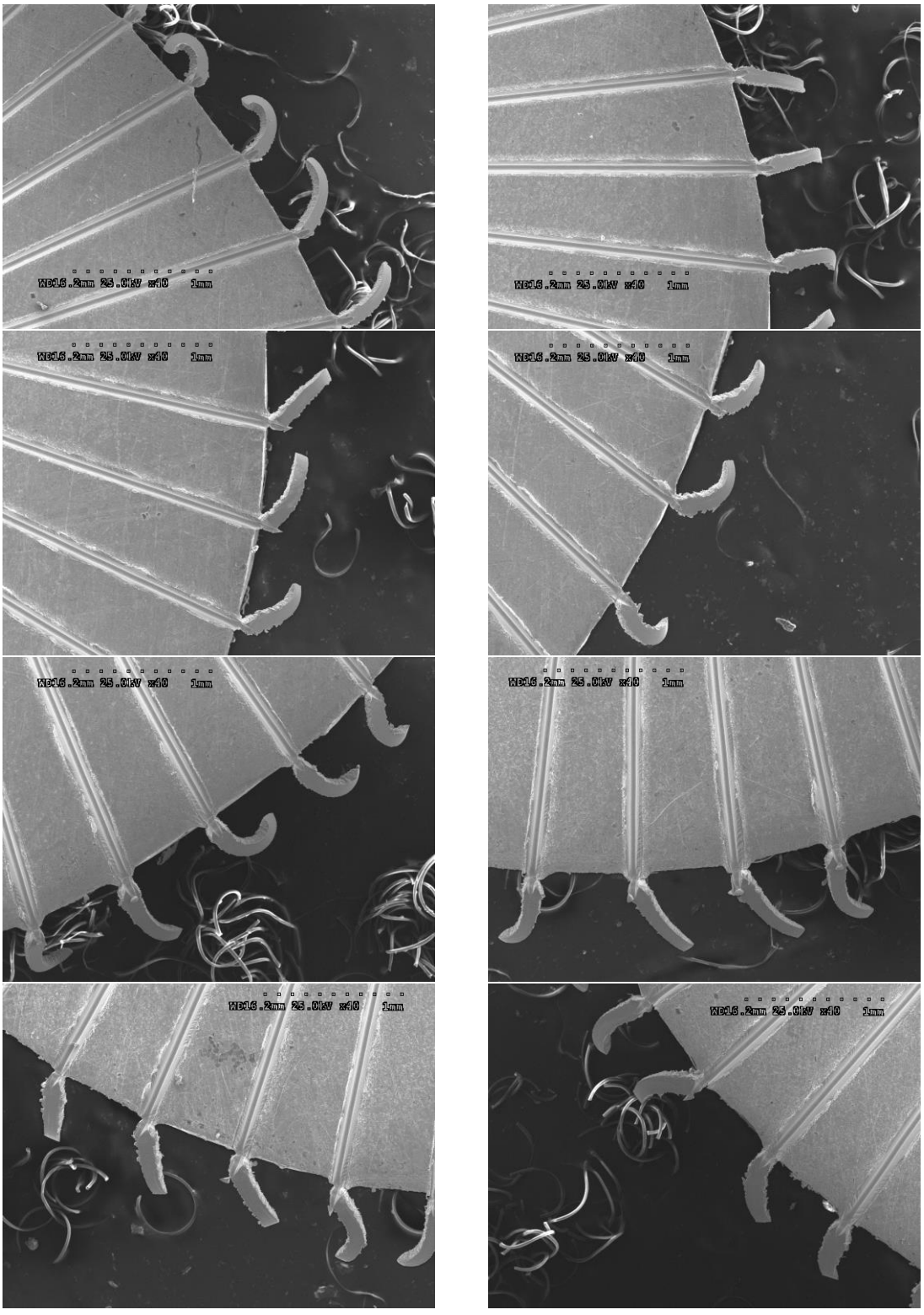
57	118.93	118.96	119.00	1.06	1.06	1.06
58	121.99	123.09	121.09	1.09	1.10	1.08
59	117.23	127.05	107.47	1.05	1.13	0.96
Average	**111.96**	**114.34**	**109.86**			

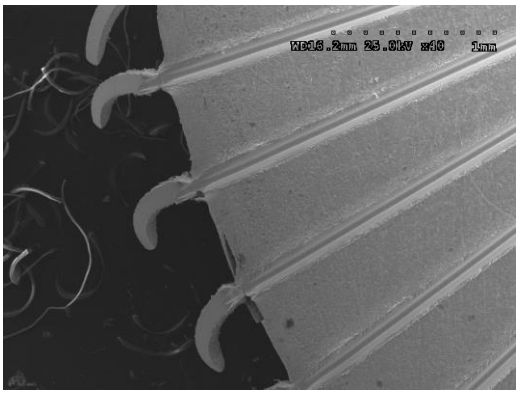
Table 7.14. Depth of cut measurement by different equipment

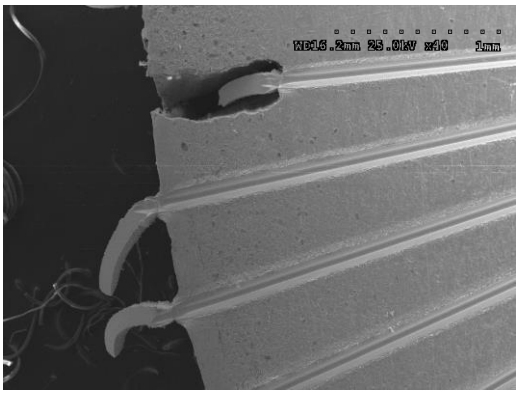
		Olympus microscope DSX110	Veeco NP-FEX interferometer
		Depth of cut (µm)	Depth of cut (µm)
Channel 1	Top	43	52.42
	Centre	40	53
	End	39	N/A
Channel 2	Top	33	44.88
	Centre	46	50.2
	End	45	49.14
Channel 3	Top	38	46.16
	Centre	46	50.57
	End	45	50.08
Channel 4	Top	37	46.36
	Centre	35	48.98
	End	43	49.39
Channel 5	Top	37	46.4
	Centre	42	48.27
	End	45	49.71
Channel 6	Top	45	46.47
	Centre	44	48.7
	End	45	49.1
Channel 7	Top	31	46.43
	Centre	37	48.56
	End	40	49.01
Channel 8	Top	33	46.96
	Centre	33	48.98
	End	34	47.39

APPENDIX B. 2ND PHASE SINGLE CRYSTAL 60 CHANNEL MICRO-MACHINING. CHIP RESULTS




WD16.2mm 25.0kV x40 1mm


WD16.2mm 25.0kV x40 1mm


WD16.2mm 25.0kV x40 1mm

APPENDIX C. DEPTH OF CUT AND SURFACE ROUGHNESS INVESTIGATION

As a last analysis, the depth of cut of the channels has been analysed in order to understand whether test piece misalignment or consistent errors have been registered, thus altering material phenomena results.

Surface roughness 2D and 3D parameters have been investigated in order to determine whether there is a correlation between crystallographic anisotropy and measured surface results. Depth of cut was determined prior to this step, in order to understand whether the variation in channel depth contributed to differences in the quality of the surface obtained.

For the 60-channel single crystal workpiece, the depth of cut was measured with two instruments: the Olympus microscope and the Veeco interferometer. Based on Table, top, middle and end channel measurements have been plotted to determine which equipment provides more consistent results. This allowed a comparison between the error introduced by measuring equipment, and the Veeco interferometer has been found to provide more accurate results.

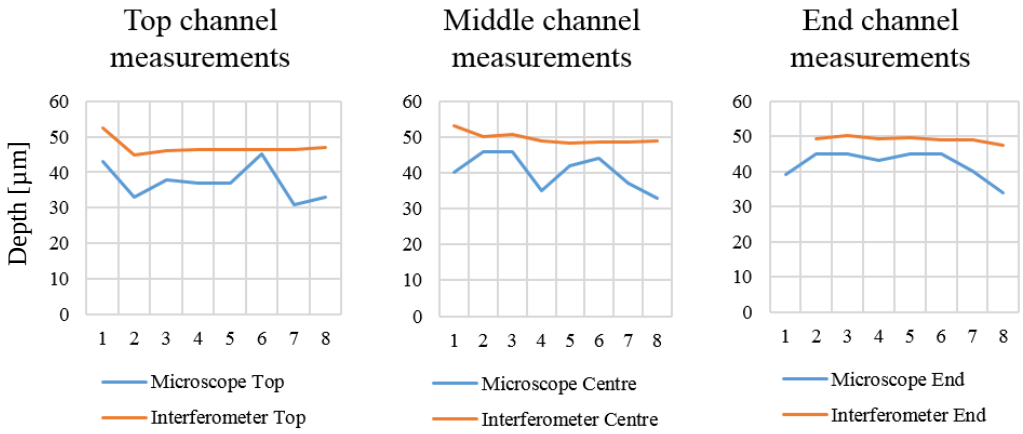


Figure C.1. Microscope vs. Interferometer channel depth assessment

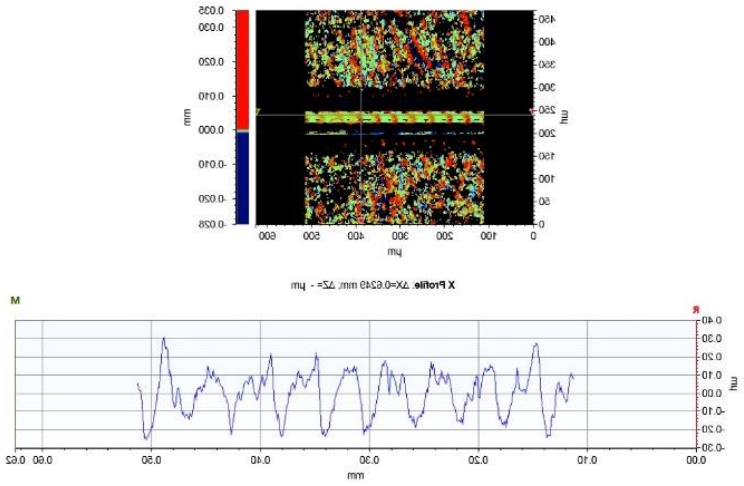


Figure C.2. Tool tracks observed on surface roughness analysis

More than just estimating the depth of cut, surface roughness and tool tracks (as exemplified in the image above) have been estimated for a varying number of channels, with results indicated in the plots below.

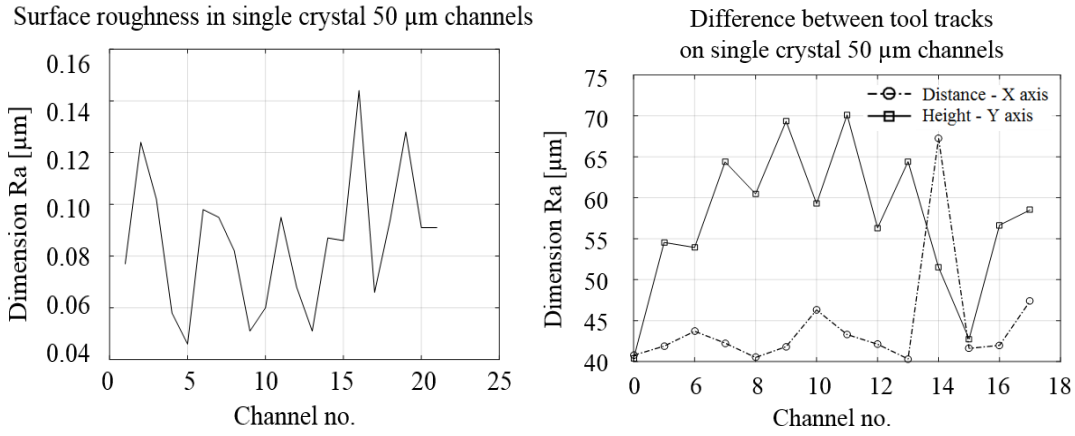


Figure C.3. Surface roughness and tool track estimations

Surface roughness is found to vary with four peaks within a 90° workpiece sector (channels 1-15). Dissimilarly, the difference between tool tracks can be seen as having an increase followed by a decrease in evolution, without evidence that these factors are related to crystallographic phenomena.

As a conclusion, the depth of cut was found to vary within reasonable limits when measured with the Veeco interferometer. No connection to crystallographic anisotropy has been established for neither surface roughness, now tool tracks spacing.

APPENDIX D. CONSIDERATIONS REGARDING SLIP DISLOCATION IN A 24-CHANNEL SINGLE CRYSTAL TEST PIECE MACHINED AT 200 μM DEPTH OF CUT

In all single crystal samples, ‘shadows’ or traces of material have been observed on the bottom and on the walls of the channels. They initially appeared as ‘micro-cracks’, due to their form. In the next section, it was investigated whether the scanning electron microscope would interfere with material observation.

The VP mode (backscattered electrons) of the SEM consists of high-energy electrons initiating in the electron beam, which are reflected out of the sample surface by elastic scattering interactions with specimen atoms. Elements with high atomic numbers reflect electrons to a higher degree than elements with low atomic numbers. Thus, elements with high atomic numbers appear brighter in SEM pictures, and contrast areas between different chemical compositions can be established. Backscattered electron diffraction is also used in crystallographic analysis. This mode is most useful in identifying different chemical compositions of the sample material, such as different phases in steel, or material inclusions.

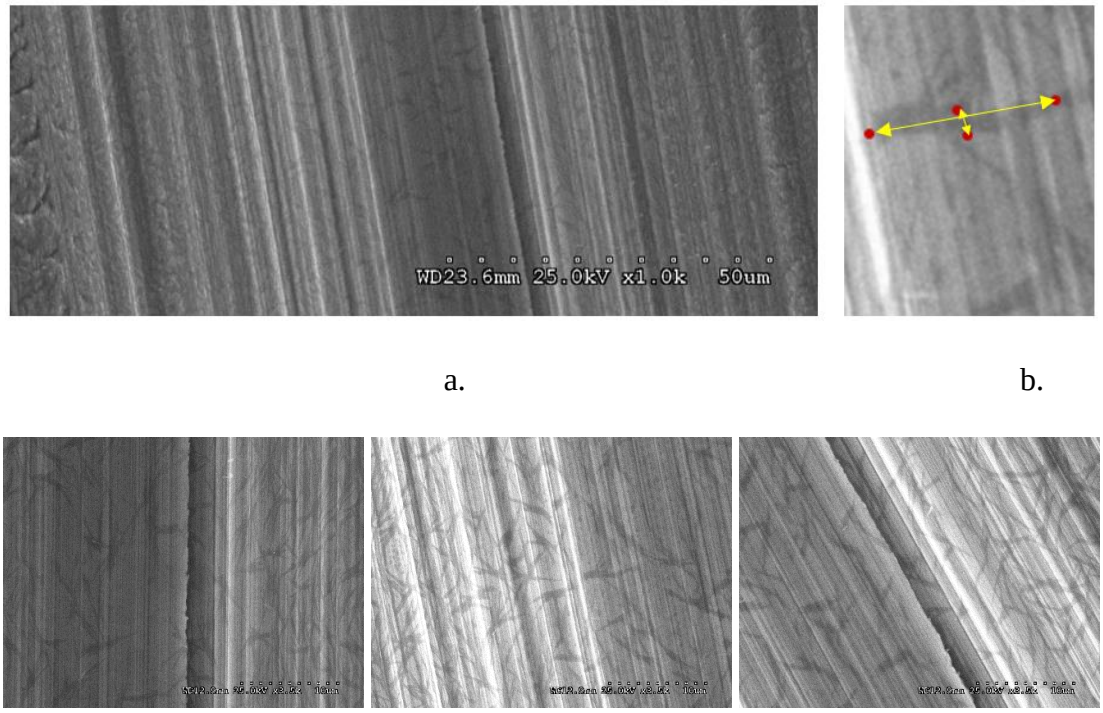
The SE mode (secondary electrons) of the SEM consists of electrons resulting from ionization products, as a result of another source of radiation (primary radiation) which exceeds the ionization potential. Signal brightness is governed by the number of electrons captured. For perpendicular surfaces, the electron beam reaches the detector uniformly around the axis of the beam, with electrons lost around the reflection. If the angle of the beam increases, the beam inclination leads to an increased contact surface with the detector (as a section of the inclined reflection). The higher contact area means that less electrons are lost from the beam, thus more secondary electrons end up being produced. Sharp edges of material and inclined surface appear brighter than horizontal

plane surfaces. This mode is best used in surfaces with very different topographies: the steeper a surface, the brighter it appears, while flat surfaces appear darker.

When analysing the shadows in the images obtained, the SEM mode can indicate different material phenomena. The backscattered electrons would indicate areas of different chemical composition, while secondary electrons would indicate flat surfaces or actual micro-cracks (both VP and SE mode are available on the Hitachi scanning electron microscope).

Examining data files that are supporting the images, SE mode was found in all image generation.

Slip dislocation lines consideration



a. b.

c. d. e.

Figure D.1. Slip dislocations prevalent in 50 μm single crystal channels: a. Channel 2, indicating overall slip dislocations, including on channel walls; b. Measurements of dislocation size at the bottom of the channel; c. Channel 1; d. Channel 3 detail; e. Channel 6.

This proves the fact that the sample material does not have a different chemical composition as a result of micro-cutting induced phenomena (a fact reinforced by the fact that copper is a one-phase material). However, upon closed investigation in the

Figures below (particularly Figure D.1b) the shadows are most likely not micro-cracks, as they do not exhibit edges around the darker areas, which would happen in the case of cracks.

To further inspect whether the shadows correspond to fissures in the material, white-light interferometry was used to analyse the bottom of the channels, as shown below in Figure D.2. The downside of using white-light interferometry is that it cannot capture inclined surfaces, only flat areas that perfectly reflect the beam. However, this is what would be expected in the case of material fissures. In the images, it is possible to see different levels on the sides of the channel analogous to the walls, and a flat surface of approximately 10-15 µm at the bottom. The flat surface presents a few 'dimples', but these do not match the vast areas of 'micro-cracks', and are more likely the result of material processing rather than specific material deformation.

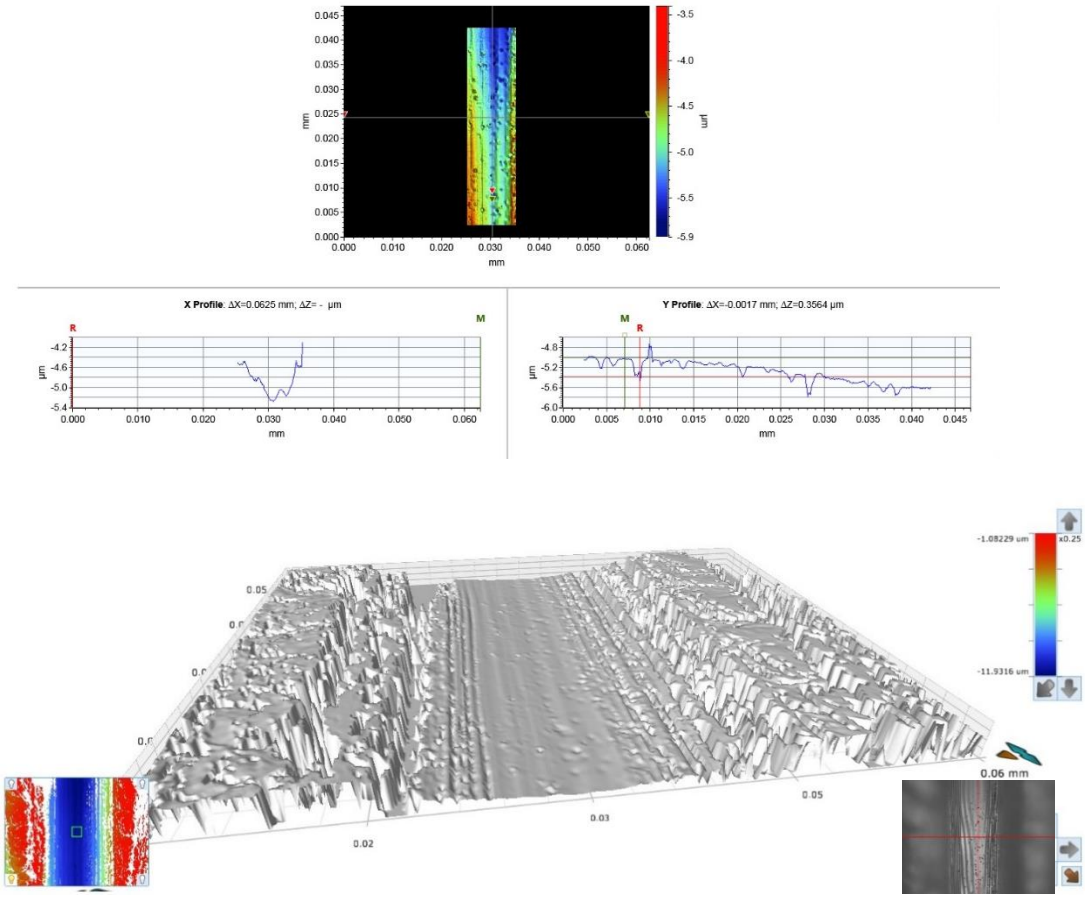


Figure D.2. White-light interferometry analysis

As a conclusion, the shadows observed on the material are not the result of material inclusions, they do not indicate different level of the material surface (such as in fissures), and are not correlated with any observed processing effects.

The most likely assumption is that the shadows are related to material microstructure, namely slip dislocations found in single crystal materials. An estimation and correlation between known crystallographic structure in the (001) plane and the number or size of these marks is attempted in the following steps.

Initially, the length and width of a few individual slip dislocations are measured with an image analysis software, and a comparison between slip dislocation arising at 50 µm and 200 µm depth of cut is made. Results of measurements are found in the tables below:

Table 7.11. Single crystal copper micro-machined at 50 µm depth of cut

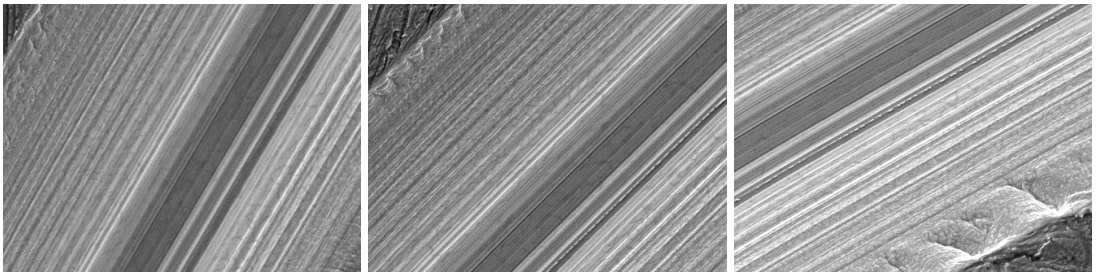
Channel	Slip dislocation length	Slip dislocation width
1 Right	4.332	0.54
1 Left	6.35	0.69
2	5.60	0.58
5	6.47	0.79
Average	5.69	0.65

Table 7.12. Single crystal copper micro-machined at 200 µm depth of cut

Channel	Slip dislocation length	Slip dislocation width
1	10.55	1.13
2	12.35	1.06
14	12.13	1.25
21	8.50	1.23
22	9.67	1.56
23	9.23	1.31
24	11.55	1.40
Average	10.57	1.28

The ratio between the averages obtained at 200 µm depth of cut and the ones at 50 µm depth of cut are 1.858 for the slip dislocation length, respectively 1.9594 for the width.

Next, the differences between individual channels with different crystallographic orientations are explored.



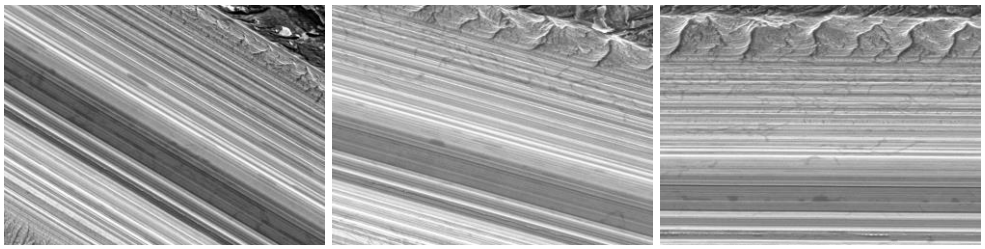
a. b. c.

Figure D.3. Slip dislocations observed on the bottom and walls of 200 µm single crystal channels: a. Channel 21; b. Channel 22; c. Channel 23.

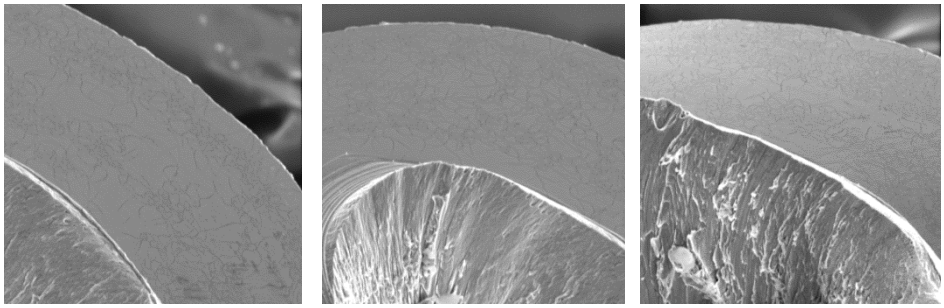
On the 24-channel sample, differences between the decreasing number of slip dislocations is observed. The density of slip dislocations is most easily observed at the bottom of the channel, since there is a very high density of dislocations on the walls of channels, and on the material plastic deformation folds themselves. Far less dislocations are present in Channels 1, 2 and 3, as seen in Figure D.4a.-c.

More notably, a strong correlation between the number of slip dislocations appearing on bottom of the channel and on the surface of the chip at the chip-tool interaction is established. Based on these observation, a commentary on the density of slip dislocations occurring on the (001) crystallographic plane is made based on the slip dislocation observed on the SEM images of chips.

The lowest density of slip dislocation has been observed on chips 3 and 5. The highest densities have been observed to cover the entire surface of chips; this can be observed in the images presented for consecutive chips 21, 22, 23, 24, 1, 2, 3, where all surfaces are covered in slip lines. Chip 21-24 present highly dense concentrations of lines.



a. b. c.



d. e. f.

Figure D.4. Correlation between dislocation slip lines observed in micro-machined channel and on the chips: a. channel 3; b. channel 2; c. channel 1; d. chip 3; e. chip 2; f. chip 1.

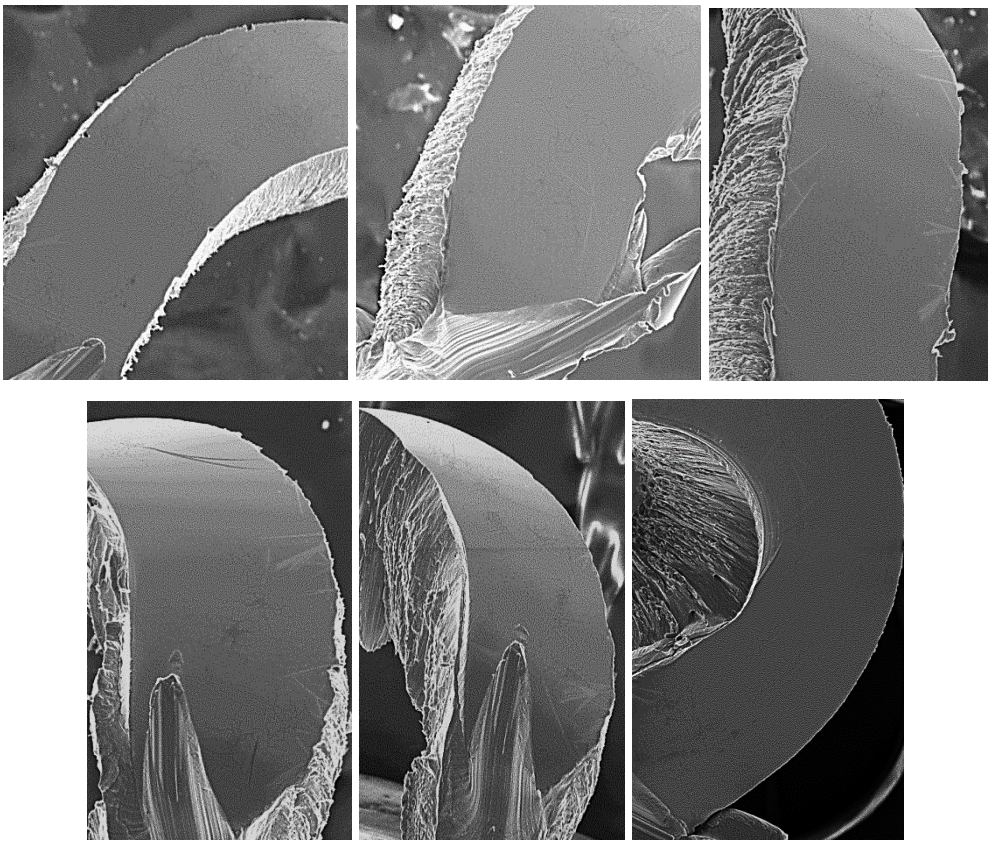


Figure D.5. Plane surface of chips emerging from channels 4 – 9

Due to difficulty in assessing the area occupied by slip dislocation, an estimation is made for chip 1-3 as to having 20+ intersecting clusters. As such, 13 chip out of 24 have been investigated and it has been observed that the highest density is found in chip 21-24, with moderate densities in chips 1-4 and 9, and low numbers in chip 5-8.

Table 7.13. Results of slip dislocation estimations

Channel	Clusters of slip dislocation
1	100 % surface, dense ~ 30
2	100 % surface, moderate ~ 25
3	50 % surface right, 7 left ~20
4	15
5	8
6	3
7	5
8	9
9	12

The densities of slip dislocation clusters observed in the 24-channel sample are not found to correspond to the four-fold evolution of the radial component of the cutting force. However, a correlation between a sector of the Fy tangential component of the cutting force and the slip dislocation density is observed and further analysed.

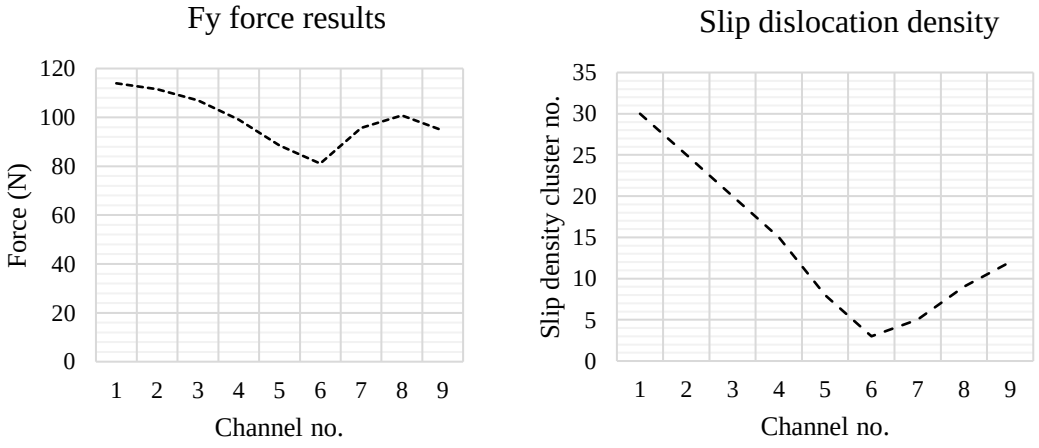


Figure D.6. Comparison of Fy force profile and slip dislocation numbers

For a section of 9 channels presenting the lower values of the cutting force Fy in Chapter 5 results, it is possible to see a minimum achieved in the similar manner as the density of observed slip lines. To the same extent, the high number of dislocation observed on chips 21-24 would correspond to the higher Fy values on the graph. A partial correlation can be established between the Fy component of the cutting force and the number of slip lines observed on the back of the chip.

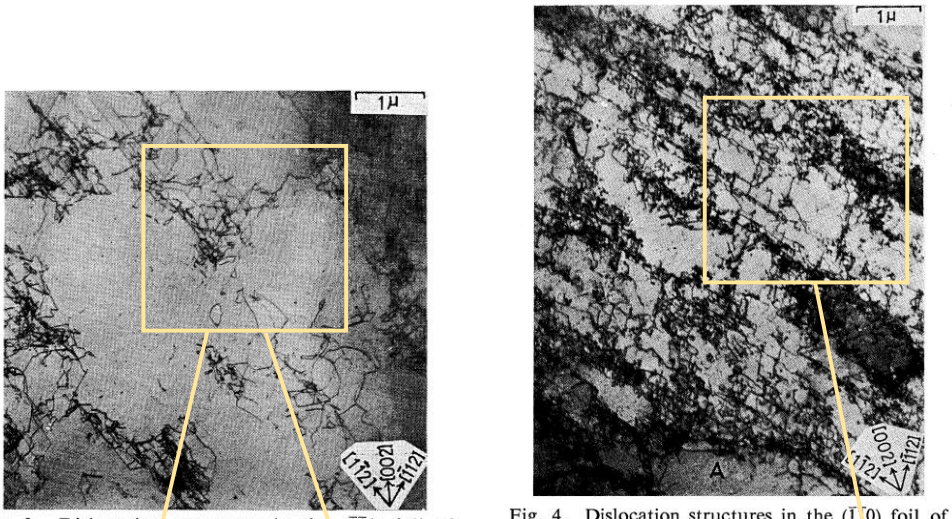


Fig. 3. Dislocation structures in the $(\bar{1}\bar{1}0)$ foil of the [145] crystal deformed to 1.8 kg/mm², No. 1.

Fig. 4. Dislocation structures in the $(\bar{1}\bar{1}0)$ foil of the [145] crystal deformed to 7.1 kg/mm², No. 3. The regions marked by *A* is a broadened cell.

Figure D.7. From: Kawasaki (1974) Figure 3:143 and 4:144. Orientation dependence of dislocation structures in cyclically deformed Cu-16 At. Pct Al alloy single crystals

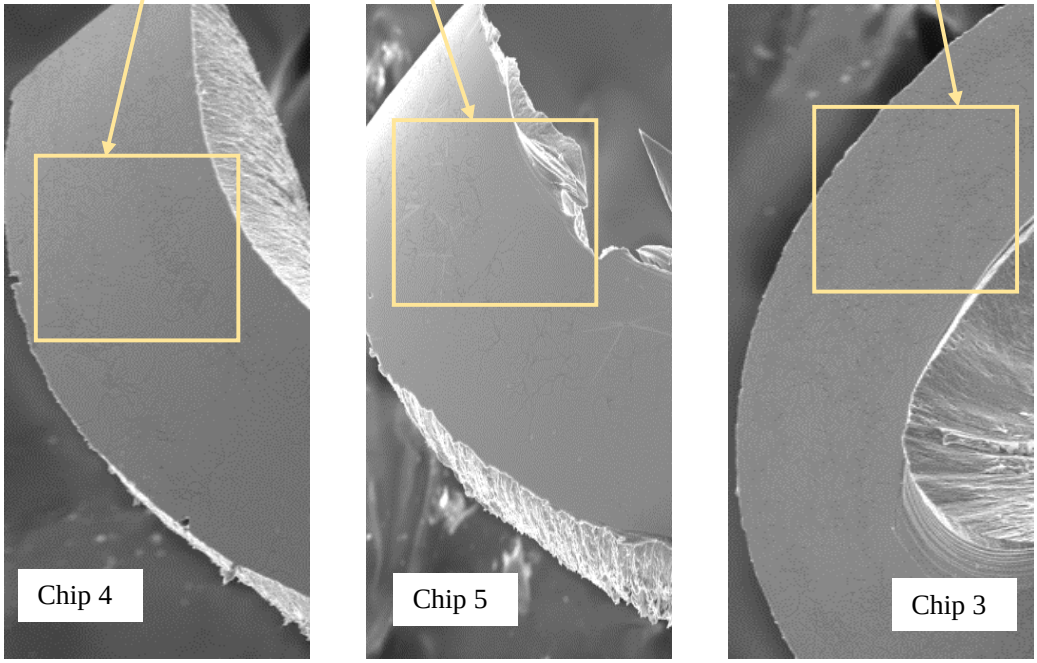


Figure D.8. Dislocations identified on the under surface of the chip

Validation of this assumption will be further made by taking more accurate SEM images of the chips, by breaking them so that they can be positioned perpendicular under the electron beam, under optimal analysing conditions. At the moment, only part of the chips and channels were possible to observe. Limitation of the analysis comes from SEM conditions under which electrons are captured better on some orientations of the test piece. Future analysis will establish whether slip dislocation lines and their density with respect to the entire chip surface follow the entire evolution of the Fy component of the cutting force. This would be unexpected, as the main driving factor in chip and burr formation has been the Fx component of the cutting force, due to establishing a correlation between chip morphologies and burr and ploughing formation in a four-fold pattern.

Discussion

In multigrain copper, bending/deformation of the workpiece can cause work hardening (or strain hardening) as deforming copper introduces dislocations in the material structure. The dislocations interfere with machining by making the material harder and stronger. Copper melting temperature is 1085°C, while annealing can take place at 400°C. During annealing, strain-free grains of material are created, while dislocations disappear; this changes the shape of the material and recovers its softness. Both processes involve substantial material transformation.

In single grain copper machining, dislocation densities have been observed at the top surface of the machined channel and at the chip-tool interface, and they correspond more to the tangential component of the cutting force Fy, rather than the radial component Fx.